

# Topics in Crystal Shape Dynamics

**Dissertation**  
zur Erlangung des akademischen Grades  
**Doktoringenieur**  
**(Dr.-Ing.)**

von: Dipl.-Ing. Christian Borchert  
geb. am: 25. April 1983  
in: Cloppenburg

genehmigt durch die Fakultät für Verfahrens- und Systemtechnik  
der Otto-von-Guericke-Universität Magdeburg

Gutachter: Prof. Dr.-Ing. habil. Kai Sundmacher  
Prof. Doraiswami Ramkrishna, Ph.D.  
Prof. Dr.-Ing. habil. Heiko Briesen

eingereicht am: 25. April 2012  
Promotionskolloquium am: 20. Juli 2012



## Abstract

The topic of this work is the dynamic modeling and observation of polyhedral, growing crystals. This is motivated by the fact that besides size, shape is an important product property for particulate materials in various industries. Due to the underlying anisotropic molecular crystal structure, growth proceeds at different rates in different directions. Therefore, crystals assume a non-spherical, polyhedral, though, under ideal conditions also a symmetric shape. The work at hand is essentially divided into three major parts. At first, a system-theoretic framework is introduced and applied to describe the evolution of single crystals and of crystal populations. In the second part the extraction of shape information from suspension images is discussed. This data is finally used to determine growth kinetics enabling the description of the conducted experiments with the developed models.

It is shown that models describing the development of a single crystal exhibit hybrid dynamics if the number of faces changes. In order to transfer this property to the population level, the class of systems that can be captured with population balances is widened to hybrid systems. Such systems are capable of performing switches in their velocity field or jumps in their state space. It is pointed out that different crystal morphologies exist in different parts of the state space, the so called morphology cones. On the bounding elements of the morphology cone hybrid dynamics is induced. It turns out that the morphology cones do not cover the whole state space and thus the computational time for the solution of evolution equations is reduced.

The shape evolution modeling studies are then augmented by the development of a crystal shape observation scheme. 3D shape descriptors of crystal populations cannot be measured directly with current devices. Therefore, an image processing routine is assembled that reduces 2D grayscale images of the crystal suspension so that individual particle projections are extracted. The estimation scheme to obtain the 3D shape is validated against synthetic (in-silico) image data. It is shown that the time-dependent shape distribution function of the synthetic images is reconstructed accurately. Also growth kinetics that control the shape evolution can be extracted from the image data. Since this is successfully tested on synthetic image data, the method is applied to observe the batch cooling crystallization of potassium dihydrogen phosphate. Two experiments are used to determine the supersaturation-dependent, face-specific growth rates. The obtained growth rates are cross-validated against the mass balance and independently conducted experiments.

Employing the developed techniques allows for a rigorous population balance modeling of crystals taking polyhedral shape into account. On the basis of the image-based crystal observation scheme, it is possible to determine face-specific growth rates. The so equipped population balance model can be included in a process model for crystallization and used to reproduce and predict the outcome of crystallization experiments.

## Zusammenfassung

Die vorliegende Arbeit behandelt die dynamische Modellierung und Beobachtung wachsender Kristallpolyeder. Da neben der Größe auch die Kristallform eine bedeutende Produkteigenschaft darstellt, ist dieses Thema für Verständnis und Optimierung von Kristallisationsprozessen relevant. Kristalle wachsen aufgrund ihrer anisotropen molekularen Struktur in unterschiedlichen Richtungen mit verschiedenen Geschwindigkeiten. Daher nehmen sie eine nicht-sphärische, polyedrische, und unter idealen Bedingungen dennoch symmetrische Form an. Die vorliegende Arbeit gliedert sich in drei Teile. Zunächst werden systemtheoretische Methoden entwickelt, die zur Beschreibung der Entwicklung von Einzelkristallen und Kristallpopulationen eingesetzt werden. Im zweiten Teil werden Methoden zur Gewinnung quantitativer Forminformationen aus Bildern von Kristallsuspensionen vorgestellt. Die so extrahierten Daten werden dann zur Bestimmung von Wachstumskinetiken herangezogen, die die Beschreibung der durchgeführten Experimente mit Hilfe der entwickelten Modelle ermöglichen.

Es wird gezeigt, dass Modelle, die die Entwicklung eines einzelnen Kristalls beschreiben, hybride Dynamik aufweisen, wenn sich die Anzahl der wachsenden Flächen ändert. Um die Dynamik auf die Populationsebene zu übertragen, wird die Systemklasse, die mit populationsdynamischen Modellen beschrieben werden kann, um hybride Systeme erweitert. Diese Systeme können instantane Änderungen im Geschwindigkeitsfeld oder Sprünge innerhalb ihres Zustandsraumes aufweisen. Es wird gezeigt, dass unterschiedliche Kristallmorphologien in verschiedenen konvexen, polyedrischen Kegeln – den sogenannten Morphologiekegeln – des Zustandsraums erzeugt werden und auf ihren begrenzenden Elementen hybride Dynamik erzeugt wird. Die Morphologiekegel decken nicht den gesamten Zustandsraum ab, weshalb das Rechengebiet zur Lösung von Evolutionsgleichungen signifikant reduziert und die Simulation beschleunigt wird.

Die Untersuchungen zur Kristallformdynamik werden dann um einen Algorithmus zur Messung von Kristallformen erweitert. Die 3D Form kann für Kristallpopulationen mit verfügbaren Mitteln nicht direkt gemessen werden. Daher wird eine Bildverarbeitungsvorschrift entwickelt, die 2D Graustufenbilder einer Kristallsuspension so abstrahiert, dass Projektionen einzelner Kristalle extrahiert werden können. Der Schätzalgorithmus zur Bestimmung der 3D Form wird gegen synthetische Bilddaten getestet. Darüberhinaus werden die – die Formentwicklung kontrollierenden – Wachstumskinetiken extrahiert. Da die Methode für Testdaten gute Ergebnisse liefert, wird sie zur Beobachtung einer Batch-Kühlungskristallisation von Kaliumdihydrogenphosphat angewendet. Mit Hilfe von zwei Experimenten werden flächenspezifische Wachstumsraten in Abhängigkeit der Übersättigung bestimmt. Die ermittelten Wachstumsraten halten einer Vergleichsprüfung gegen die Massenbilanz und unabhängigen Experimenten stand.

Die in dieser Arbeit entwickelten Methoden erlauben eine rigorose populationsdynamische Modellierung polyedrischer Kristalle. Auf Basis der ausgearbeiteten Formschätzmethode ist es möglich, flächenspezifische Wachstumsraten aus Experimenten zu bestimmen. Die damit parametrisierte Populationbilanz kann in einem Prozessmodell für Kristallisation genutzt werden, um den Verlauf von Experimenten zu beschreiben und vorherzusagen.

## Acknowledgements

This work has been taken out from 2007 till 2011 at the Max Planck Institute for Dynamics of Complex Technical Systems in Magdeburg. I would like to thank the Max Planck Society and in the end the German tax payer for establishing and financing this splendid research institute.

Personally, I thank at first Kai Sundmacher for supervising the thesis and creating the framework in which the work has been taken out. It has been a valuable experience to be part of his group, seeing people working on a broad spectrum of problems in process engineering. Since nearly a decade, a great deal of my professional development has been enabled by his guidance and support. Full commitment to the engineering sciences and willingness to move beyond personal boundaries and those of the discipline is the most important lecture I learnt from him.

As a young undergraduate student I met Doraiswami "Ramki" Ramkrishna first in 2006 when I spent nine months at Purdue. Working with him has been a shaping experience in many ways. He has encouraged me to enforce this research direction and to fight the mission through. His confidence in dealing with people and an unambiguous though unpretentious attitude of leadership has become an anchor point in my own coordinate system. It was an honor to have him on my committee.

On my first working day as a PhD student at the Max Planck Institute I met Heiko Briesen who launched a research group in population balance systems that day. He has been an important advisor in technical discussions and with regard to professional development. I am glad he could serve on my committee.

Furthermore, I thank Helmut Weiß for being a decent head of the committee.

Over the years I had the luck to meet many brilliant people at the Max Planck Institute. Everyone of them has particular splendid qualities. To my office comrade Michael Fricke I am grateful for being a permanent discussion partner and for being an even-tempered and modest close colleague. To Bianka Stein I am grateful for her creative ideas, dedicated work and good conversations. Richard Hanke-Rauschenbach has been of the utmost influence on me in activating the last and decisive reserves, in leading groups and being always open-minded and keeping a healthy portion of naivety. Peter Heidebrecht is the most dedicated teacher I've had at university. Furthermore, I thank Erik Temmel for proofreading of the manuscript and for an excellent collaboration without which the experimental part of this thesis would not have reached its state. We've had great discussions together with Holger Eisenschmidt who I also thank for proofreading and continuing the work. For being great colleagues I thank also Florian Karst, Sascha Rollié, Janine Holzmann, Kongmeng Ye, Hannsjörg Freund, Andreas Peschel, Andreas Voigt, Anett Raasch, Boris Bensmann, Astrid Bornhöft, Kaidi Gao, Linzhu Gou, Timm Faulwasser, Alexander Zinser, Matthias Eicke. Over the years I've had good discussions with Naim Bajinca, Meenesh Singh, Alexander Reinhold, Martin Behrendt, Martin Dietrich, Heike Lorenz, Luise Borchert and Jayanta Chakraborty.

To my parents Willi and Brigitte and my brothers Matthias and Johannes I want to express my deepest thankfulness for unconditional support and just being there.

I dedicate this work to the memory of my beloved aunt Helga Vaske, 1959-2008.



# Contents

<b>Abstract</b>	<b>iii</b>
<b>Zusammenfassung</b>	<b>iv</b>
<b>Preface</b>	<b>v</b>
<b>Notation</b>	<b>xiv</b>
<b>1 Introduction</b>	<b>1</b>
1.1 Aim of this Work . . . . .	4
1.2 This Thesis in a Nutshell . . . . .	6
<b>2 Evolution of Individuals and Populations</b>	<b>9</b>
2.1 The Notion of Population Balances . . . . .	10
2.2 The Property State Vector . . . . .	12
2.3 The Continuous Phase Vector . . . . .	13
2.4 Evolution of the Property State Vector . . . . .	14
2.4.1 Continuously Evolving Systems . . . . .	15
2.4.2 Systems with Discontinuous Right-Hand Side . . . . .	15
2.4.2.1 Case T ( $\rightarrow   \rightarrow$ ): Transition Surface . . . . .	20
2.4.2.2 Case S ( $\rightarrow \uparrow \leftarrow$ ): Stable Surface . . . . .	20
2.4.2.3 Case U ( $\leftarrow \uparrow \rightarrow$ ): Unstable Surface . . . . .	21
2.4.2.4 Case T <sub>os</sub> ( $\leftarrow   \times$ ): One-Sided Transition Surface . . . . .	21
2.4.2.5 Case S <sub>os</sub> ( $\rightarrow \uparrow \times$ ): One-Sided Stable Surface . . . . .	22
2.4.2.6 Case U <sub>os</sub> ( $\leftarrow \uparrow \times$ ): One-Sided Unstable Surface . . . . .	22
2.4.2.7 Interim Summary: Discontinuous Evolution . . . . .	22
2.4.3 Jumping Systems . . . . .	23
2.4.3.1 Case T <sub>j</sub> ( $\rightarrow   \rightarrow \rightarrow$ ): Transition Jump . . . . .	25
2.4.3.2 Case S <sub>j</sub> ( $\rightarrow   \rightarrow \uparrow$ ): Jump into Stable Surface . . . . .	26
2.4.3.3 Case U <sub>j</sub> ( $\leftarrow   \leftarrow$ ): Jump from Unstable Surface . . . . .	26
2.5 The Number Density Function . . . . .	27
2.6 Evolution of the Number Density Function . . . . .	30
2.6.1 Population Balance Model for Continuous Flow . . . . .	32
2.6.2 Population Balance Model for Discontinuous Evolution . . . . .	33
2.6.2.1 Population Case T ( $\rightarrow   \rightarrow$ ): Transition Surface . . . . .	33
2.6.2.2 Population Case S ( $\rightarrow \uparrow \leftarrow$ ): Stable Surface . . . . .	33
2.6.2.3 Population Case U ( $\leftarrow \uparrow \rightarrow$ ): Unstable Surface . . . . .	35

2.6.2.4	Population Case $T_{os}$ ( $\leftarrow \times$ ): One-Sided Transition Surface . . . . .	36
2.6.2.5	Population Case $S_{os}$ ( $\rightarrow \uparrow \times$ ): One-Sided Stable Surface . . . . .	36
2.6.2.6	Population Case $U_{os}$ ( $\leftarrow \uparrow \times$ ): One-Sided Unstable Surface . . . . .	37
2.6.3	Population Balance Model for Jumping Systems . . . . .	37
2.6.3.1	Population Case $T_j$ ( $\rightarrow   \rightarrow   \rightarrow$ ): Transition Jump . . . . .	37
2.6.3.2	Population Case $S_j$ ( $\rightarrow   \rightarrow \uparrow$ ): Jump in Stable Surface . . . . .	38
2.6.3.3	Population Case $U_j$ ( $\leftarrow   \leftarrow  $ ): Jump from Unstable Surface . . . . .	39
2.7	Summary . . . . .	40
<b>3</b>	<b>Single Crystal Shape Evolution Model and State Space Analysis</b>	<b>41</b>
3.1	Shape Model . . . . .	41
3.1.1	Elements of Convex Crystals . . . . .	43
3.1.2	Morphological Features . . . . .	45
3.1.3	Morphology Cone in $h$ -Space . . . . .	48
3.1.4	Morphological Variations . . . . .	49
3.1.4.1	Faces of the Morphology Cone . . . . .	49
3.1.4.2	Surrounding Morphology Cones . . . . .	50
3.1.4.3	Joint Morphology Cone . . . . .	51
3.1.5	Symmetry . . . . .	52
3.1.6	Morphology Cone Computations at a Glance . . . . .	53
3.1.7	Example: Potassium Alum . . . . .	54
3.2	Shape Evolution . . . . .	56
3.2.1	Displacement of Real and Virtual Faces . . . . .	56
3.2.2	Continuation of the Potassium Alum example . . . . .	58
3.2.2.1	Disappearance of Crystal Faces . . . . .	58
3.2.2.2	Appearance of Crystal Faces . . . . .	60
3.2.2.3	The Representation of Crystal Shape Evolution as a Hybrid System . . . . .	60
3.2.3	Analytical Solution for Constant Growth Rates . . . . .	62
3.3	Measures . . . . .	63
3.4	A more Complex Example – 4D Paracetamol Crystal . . . . .	64
3.4.1	Geometry of Monoclinic Paracetamol . . . . .	64
3.4.2	A Simple Process Model . . . . .	66
3.4.3	Case Study – Variation of the Cooling Policy . . . . .	70
3.5	Conclusion . . . . .	72
<b>4</b>	<b>Shape Evolution of Crystal Populations</b>	<b>73</b>
4.1	Evolving Potassium Dihydrogen Phosphate (KDP) Populations . . . . .	73
4.1.1	Potassium Dihydrogen Phosphate . . . . .	74
4.1.1.1	Kinetic Parameters from Literature . . . . .	76
4.1.1.2	Kinetic Parameters Determined in Ch. 6 . . . . .	77
4.1.1.3	Accessible Morphology Domain . . . . .	77
4.1.2	Population Balance Model for KDP . . . . .	78
4.1.3	Numerical Scheme . . . . .	79
4.1.3.1	Seeds . . . . .	80
4.1.3.2	Discretization of the Seed Region . . . . .	81



4.1.3.3	Nuclei . . . . .	83
4.1.3.4	The Discretized Population Balance . . . . .	84
4.1.4	Simulation Results . . . . .	84
4.1.4.1	Simulation with Literature Parameters . . . . .	85
4.1.4.2	Simulation with Estimated Parameters . . . . .	88
4.2	Evolving Crystal Populations with Varying Number of Faces – An Example . . . . .	91
4.2.1	Cubic Crystal Model and Single Crystal Evolution Revisited . . . . .	91
4.2.2	Population Balance Model for Cubic Crystals . . . . .	99
4.2.2.1	Modeling with Discontinuous Right Hand Sides . . . . .	99
4.2.2.2	Modeling with Jumps in State Space . . . . .	101
4.3	Population Balance Model for Faceted Crystals – Generalization . . . . .	102
4.3.1	Case 1 – Jump from Unstable Surface . . . . .	105
4.3.2	Case 2 – Jump into Stable Surface . . . . .	105
4.4	Summary . . . . .	106
<b>5</b>	<b>Observation of Crystal Shape</b>	<b>107</b>
5.1	Crystal Observation . . . . .	108
5.1.1	Tomography . . . . .	109
5.1.2	Optical Sectioning . . . . .	110
5.1.3	2D Observation . . . . .	111
5.1.3.1	Simple 2D Observation . . . . .	112
5.1.3.2	Estimation of the 3D State from the 2D Projection . . . . .	113
5.2	Shape Descriptors . . . . .	115
5.2.1	2D Boundary Curve . . . . .	116
5.2.2	Signature . . . . .	118
5.2.3	Sampled Signature . . . . .	119
5.2.4	Abstraction of the Signature: The Fourier Transform . . . . .	120
5.3	Shape Estimation Scheme . . . . .	121
5.3.1	Shape Estimator Setup . . . . .	122
5.3.2	Performance of the Estimator . . . . .	123
5.3.2.1	Projection on Plane with Infinite Resolution . . . . .	125
5.3.2.2	Crystals Projected on Plane with Finite Resolution . . . . .	125
5.3.2.3	Projection on Plane with Finite Resolution and Blurred Boundaries . . . . .	131
5.3.2.4	Asymmetric Crystals Projected on Plane with Finite Resolution . . . . .	132
5.3.2.5	Asymmetric Crystals Projected on Plane with Finite Resolution and Blurred Boundaries . . . . .	133
5.4	Application to Real Images . . . . .	134
5.4.1	Image Acquisition . . . . .	134
5.4.2	Image Analysis . . . . .	134
5.4.2.1	Image Enhancement . . . . .	135
5.4.2.2	Adaptive Background Image . . . . .	136
5.4.2.3	Binarization and Region Filling . . . . .	137
5.4.2.4	Feature Extraction and Distributions . . . . .	138
5.4.2.5	Density Estimation with Kernel Functions . . . . .	139
5.4.3	Two Case Studies on KDP Crystal Populations . . . . .	140
5.4.3.1	KDP Growth at High Supersaturations (Exp. 1) . . . . .	144

5.4.3.2	KDP Growth at Low Supersaturations (Exp. 2)	149
5.5	Summary	153
<b>6</b>	<b>Connecting Observation and Simulation</b>	<b>155</b>
6.1	Identifiability Analysis	155
6.1.1	Synthetic Data	156
6.1.2	Parameter Estimation and its Verification Using Synthetic Data for Potassium Dihydrogen Phosphate	156
6.2	Application to Potassium Dihydrogen Phosphate Crystallization	161
6.3	Conclusions	161
<b>7</b>	<b>Summary, Conclusion, and Outlook</b>	<b>165</b>
7.1	Summary	165
7.2	Conclusion	167
7.3	Outlook	168
	<b>Bibliography</b>	<b>180</b>
	<b>List of Figures</b>	<b>183</b>
	<b>List of Tables</b>	<b>185</b>
	<b>Publications</b>	<b>187</b>
	<b>Curriculum Vitae</b>	<b>191</b>

# Notation

## Latin Symbols

$a_I$	relative weight of current image	
$a_B$	relative weight of previous background image	
$A$	area of crystal surface	$m^2$
$A$	area of crystal projection	$m^2$
$b$	number of conditions	
$b$	exponent in the nucleation law for $B$	
$B$	nucleation rate	$\#/s$
$\hat{\mathbf{b}}$	outer unit normal on the boundary of $\Omega$	
$\mathbf{b}_j$	$j$ -th discrete coordinate of projection boundary	$m$
$\mathcal{B}$	boundary of $\mathcal{P}$	
$\mathbf{B}$	boundary matrix of morpholgoy cone	
$\mathbf{B}$	discretized boundary of particle projection	$m$
$B_{x,y}$	intensity level of background image	
$C$	circularity	
$\mathbf{d}$	descriptor vector	
$\hat{\mathbf{d}}$	estimated descriptor vector	
$\mathbf{d}_i$	$i$ th row of $\mathbf{D}$	
$D$	circle-equivalent diameter	
$\mathbf{D}$	velocity delimiter matrix	
$e_{jk,est}$	relative error of the estimation for the $j$ -th particles with regard to $k$ -th quantity	
$E_{x,y}$	intensity level of enhanced image	
$\mathcal{E}_{ij}$	edge between faces $i$ and $j$	
$\mathcal{E}_{ij,kl}$	$\mathcal{E}_{ij}$ bounded by faces $k$ and $l$	
$\mathcal{E}_{ij,kl}^{i \rightarrow \emptyset}$	$\mathcal{E}_{ij,kl}$ , whose disappearance involves the disappearance of face $i$	
$\mathcal{E}_{ij,kl}^{\curvearrowright}$	$\mathcal{E}_{ij,kl}$ , whose disappearance is followed by the appearance of an edge between $k$ and $l$	
$f$	number density	$\#/[x]$
$\hat{f}$	estimated number density	
$\mathbf{f}_{descr}$	function to obtain descriptor vector from shape and orientation	
$\mathbf{f}_{est}$	function to obtain the shape vector from descriptor vector	
$\mathbf{F}$	velocity function for mesh equilibration	
$\mathcal{F}$	$i$ th crystal face	
$g$	grayscale level	
$g_i$	growth exponent of the growth law for $G_i$	
$G_i$	growth rate of face $i$ and $i$ th component of $\mathbf{G}$	
$\mathbf{G}$	growth vector	
$h$	production density	$\#/s/[x]$
$h_i$	distance of the $i$ th face to the crystal center	$m$
$\mathbf{h}$	geometrical state vector	$m$
$\mathbf{h}_{ijk}$	vector with three components of $\mathbf{h}$	$m$
$\mathbf{h}_{nuc}$	nucleation state	$m$
$\mathbf{H}$	bandwidth matrix	

$I_{x,y}$	intensity level of original image	
$I_{\text{thres}}$	threshold grayscale value	
$J$	jacobian	
$k$	index	
$k_i$	kinetic coefficient in the growth law for $G_i$	m/s
$k_{\text{nuc}}$	kinetic coefficient in the nucleation rate law	$\#/\text{m}^3/\text{m}^3/\text{s}$
$K$	kernel function	
$L_{x,y}$	logical image	
$m$	mass	kg
$m$	number of C-morphologies	
$\mathcal{M}$	joint morphology cone	
$\mathcal{M}_\lambda$	morphology cone of $\lambda$ th C-morphology	
$\mathcal{M}_{\lambda,j}$	$j$ S- or T- morphology of $\mathcal{M}_\lambda$	
$\mathcal{M}'_{\lambda,j}$	projection of $\mathcal{M}_{\lambda,j}$	
$n$	number of faces	
$n_{\text{lut}}$	number of entries in lookup table	
$n_{\text{lut},\mathbf{h}}$	number of variations of the $\mathbf{h}$ -vector in lookup table	
$n_{\text{lut},\psi}$	number of variations of the $\mathbf{h}$ -vector in lookup table	
$n_{\text{nuc}}$	number of pivots for nucleated crystal population	
$n_{\mathcal{P}}$	number of projected crystal vertices that make up the convex hull	
$n_{\text{seed}}$	number of pivots for seed crystal population	
$\hat{\mathbf{n}}$	unit normal on a surface in state space	
$\mathbf{n}_i^T$	$i$ th row of $\mathbf{N}$ , unit normal of $i$ th face	
$O$	convexity	
$N$	number of particles	
$\dot{N}$	number flux	
$\mathbf{N}$	matrix with face normals (rows)	
$\mathbf{N}_{ijk}$	matrix with rows $ijk$ of $\mathbf{N}$	
$\mathbf{p}$	node for the mesh generation	
$\hat{\mathbf{p}}$	velocity direction vector of unit length	
$\mathbf{p}_j$	projection of crystal vertex	
$P$	perimeter	m
$\mathbf{P}$	joint projection and rotation matrix	
$\mathcal{P}$	projection of $\mathcal{S}$	
$r$	distance between centroid and boundary of the particle projection	m
$r_1$	side-length of the quadratic pyramid's base plane of KDP	m
$r_2$	distance between the pyramid's apices of KDP	m
$r_i$	component of $\mathbf{r}$	
$\mathbf{r}$	3-D space coordinate	
$\mathbf{r}$	vector of distances of the discretized boundary of the crystal projection	m
$R$	fixed region in $\Omega$	
$R_j$	$j$ -th Fourier coefficient	
$s$	surface function $\sigma$ solved for $x_n$	
$S$	fixed surface in $\Omega$	
$S$	solidity	

$\mathcal{S}$	crystal polyhedron	
$t$	time	s
$t_{\text{cross},k}$	instant when $k$ -th nucleation pivot leaves circle around $\mathbf{h}_{\text{nuc}}$	
$T$	temperature	K
$\mathbf{v}_j$	coordinates of $j$ -th vertex	m
$\mathbf{v}_{ijk}$	coordinates of $\mathcal{V}_{ijk}$	m
$V$	volume in property state space or physical space	
$\mathcal{V}_{ijk}$	vertex formed by faces $ijk$	
$\mathbf{w}_{ij,kl}$	computed weights of the edge $\mathcal{E}_{ij,kl}$	
$w$	mass ratio between solute and solvent in fluid phase	
$x$	first component of $\mathbf{x}$ (coord. on proj. plane)	m
$x$	sample point	
$x_i$	$i$ -th component of the property vector	
$\mathbf{x}$	property vector	
$\mathbf{x}$	coordinate on projection plane	m
$\mathbf{x}'$	vector with $n - 1$ components of the property vector $\mathbf{x}$	
$\dot{X}_i$	$i$ -th component of the velocity field in $\mathbf{x}$ -space	
$\dot{\mathbf{X}}$	velocity field in $\mathbf{x}$ -space	
$y$	second component of $\mathbf{x}$ (coord. on proj. plane)	m
$Y_i$	$i$ -th component of the environmental state vector	
$\mathbf{Y}$	environmental state vector	
$\mathbf{z}$	surface-intrinsic coordinate system in $\Sigma$	
$\dot{\mathbf{Z}}$	velocity in surface coordinates	

## Greek Symbols

$\alpha$	angle
$\alpha_j$	weight of $j$ -th vertex
$\Gamma$	spatial domain
$\delta$	Dirac delta
$\epsilon_{\text{nuc}}$	numerical parameter controlling the distance between nucleation pivots
$\theta$	angle
$\theta$	Euler angle
$\boldsymbol{\mu}$	vector of mean values
$\nu$	number of preliminary nodes
$\rho$	density
$\sigma$	indicator function defining $\Sigma$
$\sigma$	standard deviation
$\Sigma$	surface domain in property state space
$\lambda$	weight
$\lambda$	morphology index
$\Lambda$	material control volume in state space
$\xi$	jump function
$\phi$	Euler angle
$\psi$	Euler angle
$\Omega$	domain in property state space

## Superscripts

T	transpose
$\Sigma$	quantity on $\Sigma$
$\emptyset$	disappearance of a face
$\curvearrowright$	transition to new edge-configuration
$<$	inequality (less than zero)
<b>0</b>	equality (equal zero)
$-$	quantity related to that part of the state space where $\sigma < 0$
$+$	quantity related to that part of the state space where $\sigma > 0$

## Subscripts

0	initial value
$\{hkl\}$	related to crystallographic forms $\{hkl\}$
$[hkl]$	related to crystallographic direction $[hkl]$
c	centroid
cry	crystal/crystalline
cry, pop	crystal population
dis	dissolved
est	estimation/estimated value
H <sub>2</sub> O	quantity related to water
$i, j$	indices
j	jump
KDP	quantity related to KDP (potassium dihydrogen phosphate)
lut	lookup table
mod	model
nuc	nucleation/nucleated particles
particles	particles/all particles
P	Projection
S	related to surface S
sat	saturation
sc	scaled
seed	quantity related to the seed crystals
ss	steady state
true	true value
$\mathbf{x}'$	function given in $\mathbf{x}'$ -coordinates
$\mathbf{z}$	function given in $\mathbf{z}$ -coordinates
$\Lambda$	quantity related to $\Lambda$
$\Sigma$	quantity related to $\Sigma$
$\psi$	vector of Euler angles
$\emptyset$	disappearance of a face

# Chapter 1

## Introduction

About 60% of all products manufactured by major chemical companies are delivered as solids, among them many crystalline materials (Wintermantel, 1999). Virtually all pharmaceutical production processes involve a crystallization step and most active pharmaceutical ingredients are administered in a crystalline form (Variankaval et al., 2008). Crystalline pharmaceuticals, but also agrochemicals, cosmetics and other specialty chemicals are high value-added products for which crystal shape is an important quality factor. In fact, the availability of the adequate crystal shape is of interest wherever crystals are used, for example in nanotechnology (Barnard, 2009; Damm et al., 2012; Chemseddine and Moritz, 1999; Körmer et al., 2012), catalysis (Christopher and Linic, 2008; Dellamorte et al., 2009; Lee et al., 2009; Selloni, 2008; Yang et al., 2008; Yang and Liu, 2009), photo-catalysis (Zhang et al., 2010), solar cells (Wu et al., 2008), optical applications (Iskandar, 2009), pharmaceuticals (Tiwary, 2007; Sun and Grant, 2001; Blagden et al., 2007; Rasenack and Muller, 2002) and bio (medical) systems (Meldrum and Coelfen, 2008; Gupta and Gupta, 2005; Chow et al., 2011). Therefore, the focus of research in industrial crystal production aims ever more at controlling not only the crystal size but also crystal shape (Wintermantel, 1999; Charpentier, 2009).

Depending on the particular system and application, substances can crystallize from different fluid phases, for instance from a gas phase, from the melt, within an amorphous solid or from a solution. Most often, crystallization systems are multicomponent and multiphase systems. Solution crystallization is widely used as a separation and purification step in industrial practice. It can also be the first step in a series of operations to formulate a final product. In most of the cases the particle size and shape distribution needs to meet certain specifications depending on the further downstream processing (washing, filtration, drying) or end product specifications (Fujiwara et al., 2002; Mullin, 2001). Though it is well known that properties of dispersed phase products are strongly linked to their shape, process systems engineering research was so far focused on particle size and size distributions and only during the last years efforts have been started to include quantitative measures for shape and shape distributions, e.g. Zhang et al. (2006); Bajcinca et al. (2010); Borchert and Sundmacher (2011b); Briesen (2006); Chakraborty et al. (2010); Briesen (2007); Kempkes (2009); Ma and Braatz (2000); Ma et al. (2002b). An overview on crystal

shape engineering and recent advances with a special focus on solution crystallization has been published by Doherty and coworkers (Lovette et al., 2008).

Crystal shape is the result of the kinetic processes of growth and/or dissolution. That is, the harvesting of crystals from crystallizers yields kinetically rather than thermodynamically controlled crystal shapes. Hence, the mastering of the growth mechanism is the key to shape control. This is traditionally achieved by chemical means, i.e., by the usage of additives (Peltier et al., 2010; Radenovic et al., 2003) or by changing the solvent (Lahav and Leiserowitz, 2001; Davey et al., 1982). In the same manner impurities can shift the shape in an undesired way (Mullin et al., 1970; Sizemore and Doherty, 2009). Recently developed concepts to combine cycles of growth and dissolution have been discussed in order to expand the attainable region of crystal morphologies by avoiding the application of additives or different solvents (Snyder et al., 2007; Bajcinca et al., 2010). Changing the level of supersaturation is yet another method for systems which exhibit a clear dependency of the relative growth rate between different facets on the level of supersaturation (Yang et al., 2006; Ristic et al., 2001; Sangwal, 1998; Boerrigter et al., 2002; Mullin et al., 1970).

Models investigating different aspects of crystal growth range from the atomistic to the crystal population level. Geometric models of crystal growth track the advancement of the boundary of a whole crystal and assume that the boundary velocity depends only on local conditions (Taylor et al., 1992). Among these models, those describing the evolution of convex, faceted crystals are the simplest ones since they involve only a few ordinary differential equations. Growth models for polyhedral convex crystals have been used in the scientific and engineering literature for decades. For example, Prywer has published a series of papers which discuss the shape evolution of different crystal systems and analyze growth rate ratios of different faces that lead to morphological changes, that is, the disappearance of faces and edges (Prywer, 2005, 2002, 1996). Doherty and coworkers have published a series of papers in which, beside the derivation of growth kinetics, polyhedral shape evolution models are used that account for morphological changes (Gadewar and Doherty, 2004; Zhang et al., 2006; Snyder and Doherty, 2007). Even though polyhedral shape evolution models are not capable to model dendritic growth as it often appears for example in precipitation processes, they can be applied to the wide class of crystallization systems in which convex polyhedral crystal growth can be observed. The only challenge during the integration of polyhedral crystal growth models is the tracking of discrete events like the appearance and disappearance of edges and faces, events that constitute morphological changes (Zhang et al., 2006). Though the integration of these models, while continuously checking for discrete events, is a simple and computationally not very intensive task if the growth of only one crystal must be simulated, this is a quite expensive exercise if many crystal growth trajectories have to be computed. This is of course the case for crystal populations as they appear in industrial crystallizers.

For multi-scale modeling, the concept of the population balance equation facilitates the lifting of single particle dynamics to the level of a collection of a huge number of particles, a so called population. Population balances are partial differential (or partial integro differential) equations that capture the dynamics of a number density in the particle property state space. Classically, the population balance is used in crystallization for the modeling of the evolution of the size distribution (Ramkr-



ishna, 2000; Randolph and Larsen, 1988). The incorporation of shape information in process-level models using the population balance has been proposed by various authors. For instance, Matthews and Rawlings (1998); Zhang and Doherty (2004); Borchert et al. (2009) include shape information to a model based on a 1D population balance, by linking the development of the shape factor directly to size. More rigorous approaches treat the shape distribution evolution as a multivariate problem that involves a multidimensional population balance equation, e.g. Cardew (1985); Ma et al. (2002a,b, 2008); Briesen (2006); Borchert and Sundmacher (2011b).

When it comes to model identification on the population level, adequate sensors are required that track the dynamics of a crystallization process with respect to the quantities of interest. Probes that are capable of measuring the particle size distribution deliver a wealth of information with which a model can be calibrated. However, if only size information is available, nothing is known about the shape of the particles. That is, it can for instance not be distinguished directly whether an increase in size is attributed to aggregation or growth. Of course, from the shape of the size distribution curve and its evolution, mechanisms can be distinguished or even identified (Ramkrishna, 2000). But size distribution measurements rely also on a shape model for the particles (e.g. spherical) and thus, the result is biased by this assumption. Even though a model parametrized with these data may be capable of reflecting the size or even shape distribution evolution accurately or may even be extrapolative with respect to the specific probe, it is of major interest to extract distribution data from more advanced devices. In recent years, online probes that permit the imaging of bypassing particles have been discussed in the literature, see for example De Anda et al. (2005); Li et al. (2006); Kempkes (2009); Kempkes et al. (2010); Patience and Rawlings (2001b); Larsen and Rawlings (2009); Glicksman et al. (1994). The improvement of the quality of the measurements can in principle be afforded via the enhancement of the image quality or further development of the post-processing algorithms. That is, either the hardware of the sensor is improved, or processing algorithms for image analysis are equipped with advanced techniques in order to apply it to data acquired from (commercially) available equipment. The concatenation of so retrieved, information-rich population data to detailed population models promises model synthesis of high-quality.

The motivation for shape manipulation, enhancement, modeling and observation can be manifold. Sometimes only in its adequate crystal shape substances can be used for specific applications. Another goal could be the maximization of raw material usage because having assumed a specific shape, the material's performance is enhanced. If the crystalline material is only an intermediate in a production process, the formulation of a different shape can improve the handling of the solid which in turn increases the throughput of a plant or reduces the investment or operating costs. Though this is a strong motivation, the engineering interest, however, shall not only be driven by such economic factors but also by the spirit to push the boundaries of technological feasibility a bit further.

## 1.1 Aim of this Work

The understanding of a complex process like crystallization is the prerequisite for its rational improvement. This requires a realistic and thus physically interpretable model and appropriate measurement techniques. Shape is an important and ubiquitous issue in crystallization. The aim of this work is thus, to provide a modest contribution to the model formulation and observation in the wide field of crystal shape dynamics. In particular, this involves, among others, the treatment of the following questions:

- How can the crystal property shape be included in process models for crystallization, both on the single crystal and on the population level?
- Given a set of crystallographic faces, how many different morphologies can theoretically be produced from this set?
- If the morphology has to be determined that is produced by a specific crystal state vector: Is it possible to circumvent the computation of the crystal polyhedron? Or is it even possible to compute geometric quantities without computing the polyhedron?
- How is a morphology switch reflected in the crystal's state space during shape evolution? How are morphology switches reflected in the dynamic equations for shape evolution on the single crystal and on the population level?
- Are special model structures required to capture morphology switches?
- Can the crystal shape distribution be observed during a whole crystallization experiment?
- How can crystal projections be related easily to the crystal's 3D body in order to quantify the shape of a crystal? Can this information be used to determine the shape distribution of a population? And how reliable is this information?
- Can growth rates be estimated from measured shape distributions? And is it possible to assure the reliability of the estimation procedure?

Clearly, there are numerous other questions in crystal shape engineering which are not addressed here. The undeniably important subject of process control and optimization for instance is not discussed. Models that derive the equilibrium crystal shape or even growth rates from the molecular crystal structure are not a topic of this work. The complex interaction between the crystalline phase and the surrounding fluid is no matter of concern. This interaction also governs the growth process on the molecular level which is disregarded like the importance of additives to influence growth mechanisms. Only polyhedral crystals are considered, albeit many crystalline materials do not assume this kind of shape. Spatial variations within a crystallizer which undoubtedly impair the controllability on shape are not taken into account. The list of topics that cannot be found in this work could be prolonged arbitrarily. Themes that are addressed are outlined in the following section.

Questions you may have:	Can you find an answer to that here?	How you should read this thesis:
<ul style="list-style-type: none"><li>I have convex crystals in my process. How can I model their shape evolution?</li><li>Can I set up a simple model for the dynamics of the shape distribution?</li><li>How can images which I take from my suspension be processed?</li><li>Can the information which I extract from the image be used/compared to the information which I get from the model?</li><li>How can I identify face-specific growth kinetics?</li><li>Can you model and observe arbitrarily complex crystal shapes?</li><li>Can I find techniques to determine which additives (or other solvent) may lead to different shapes?</li><li>What about polymorphs?</li></ul>	<ul style="list-style-type: none"><li>For a single crystal you can use ordinary differential equations; have a look at Ch. 3. If this is too much theory at the moment, get started with the article of Zhang et al. (2006).</li><li>Yes you can! For this you need a population balance. Take a look at the introductory examples in Ch. 4. If you are not familiar with population balances, ask a modeler or get started with an introductory text, e.g. Randolph and Larson (1988).</li><li>This topic is addressed in Ch. 5. Of course, there are some ready to use solutions but here you see how to retrieve the information from an image that you really want.</li><li>Yes, but that is usually not delivered by tools you get off the shelf. For the case of convex crystals this is taken out in Ch. 5.</li><li>At first you need to track the shape evolution as described in Ch. 5. Then you turn to Ch. 6 where the estimation of growth rates is discussed.</li><li>No, in this work we focus on single convex crystals. They can involve an arbitrary number of faces but the model treatment does not apply to aggregates, fragments or irregular growth.</li><li>No. This thesis is only concerned with the modeling and identification of crystallization systems.</li><li>Polymorphism, understood as the change of the underlying molecular crystal structure (lattice) is not addressed here.</li></ul>	<p><b>Modeling:</b> You should make yourself familiar with the single crystal model in Sec. 3.2. It is not necessary that you study all the technical details but capture the ideas. A good starting point would be Fig. 3.4 which is half the thesis. If you are interested in single crystal shape evolution, continue with Ch. 3. If you want to set up a simple population balance model, turn directly to the examples given in Sec. 4.1 (no faces disappear) and Sec. 4.2 (faces disappear). If your system is qualitatively more complex than the 2D examples, i.e., you cannot directly transfer the equations, you need to continue with Sec. 4.3. But for this you have to fully understand the concepts of Ch.s 2 and 3. Without a sound modeling background this can become very time-intensive.</p> <p><b>Experimental techniques:</b> If your goal is to grasp the shape distribution in more quantitative terms without modeling the process, you can get started with Ch. 5. For the shape estimation scheme you may need some background information on the shape model from Sec. 3.2. Ch. 6 helps you to squeeze out kinetic data from the observed shape evolution.</p>

Figure 1.1: Dissertation guide particularly for readers with few modeling experience who are nonetheless interested in quantitative techniques.

## 1.2 This Thesis in a Nutshell

In this thesis, the general model formulation independent of a particular system stands in the foreground. Thus, the classical order to present at first experimental methods, the outcome of experiments and finally a model that is employed to interpret the experimental findings is not followed. In a sense, the horse is put before the cart because we start with general methods for model formulation, then turn to models for shape development and evolution of shape distributions. After this, the topic of shape observation is again addressed from a rather analytical point of view until the experiments using a simple model system are described at the very end. The parameters derived from the experiments, in particular the growth laws, are, however, already used throughout the theoretical parts.

In Ch. 2 general methods for the model formulation of dynamic systems are given. Of course, this is done in view of later applications. The notion of individuals and populations evolving over time and interacting with the environment is introduced. The special focus of this chapter lies in the formal description of hybrid dynamical systems. Differential equations for the state of individuals of such systems involve, beside the continuous evolution, instantaneous switches of their state development or even jumps in the state itself. The task of population balances is the incorporation of detailed information about individuals on a larger scale, i.e. huge populations of individuals. The lifting of detailed knowledge on the evolution of single hybrid dynamical systems to the population level is addressed.

In Ch. 3 an extensive dissection of the equations describing the shape of convex crystals and its evolution is given. Starting with the natural half-space representation of a convex polyhedral crystal, the state space is divided into morphology cones in which combinatorially similar shapes exist. On the faces of the morphology cones or by moving from one morphology cone to another, structural changes on the crystal surface can be observed, for example disappearance of faces or edges. Therefore, the knowledge of the morphology cones makes the exhaustive computation of the crystal polyhedron in every time step of the integration – which would alternatively reveal structural changes – unnecessary. It turns out that the evolution of a single crystal undergoing morphological changes can be interpreted as a hybrid dynamical system. Also the computation of crystal volume and surface area for a crystal of a given state can be directly performed without computing the polyhedron. A practical implementation of the methodology is carried out and applied to the shape evolution of paracetamol.

In Ch. 4 the application of the methods developed in Ch. 2 for the derivation of multivariate population balance equations for continuous and hybrid systems are applied to the special case of crystal shape evolution. At first, a model substance, which does not undergo morphological changes, is introduced that is in later chapters also used in experiments. The continuous population balance is solved with parameters that are determined in Ch. 6 on the basis of data collected in Ch. 5. More challenging from the theoretical point of view are systems in which morphological changes occur. The basic methodology is sketched along a simple 2D example. Using the state space analysis of Ch. 3 and the model formulation given in Ch. 2, the general procedure to derive systems of multivariate population balances incorporating shape evolution in a rigorous manner is given.

In Ch. 5 the model formulation themes are left and we concentrate on the connection between the world of models and the real world. For the topic at hand, this means that crystal shapes that can be seen in crystallization experiments must be measured. The method of choice would be a highly sophisticated 3D sensor which perfectly grasps the exact crystal shape. It is argued that such a sensor is not available for measurements that shall be taken directly during the crystallization. Instead, a flow-through microscope is used which, however, only delivers projections of the crystals within the suspension. A technique is developed that relates the boundary of the crystal projection to its actual 3D state using a model of the crystal shape. The proposed procedure is validated against synthetic data and subsequently applied to observe the shape evolution in experiments.

In Ch. 6 the results of Ch. 5 are used to estimate the growth kinetics from experiments. The procedure is validated by simulating the data acquisition and processing steps in-silico. On the basis of this synthetic data, the growth kinetics used in the simulation can be recovered accurately which gives confidence in the principle practicability of the scheme. Application of the method to data, which has been extracted from experiments in Ch. 5, allows for the determination of the growth kinetics. The growth laws are shown to reproduce not only the crystal geometry development but also the supersaturation dynamics when used in simulations that are presented already in Ch. 4. The outcome of independently conducted experiments is predicted as well.

In Ch. 7 the thesis is summarized and concluded. Also an outlook on major topics, that may play a role in future developments, is given.



*We propose to consider first the single elements of our subject, then each branch or part, and, last of all, the whole, in all its relations – therefore to advance from the simple to the complex. But it is necessary for us to commence with a glance at the nature of the whole, because it is particularly necessary that in the consideration of any of the parts the whole should be kept constantly in view.*

---

Carl von Clausewitz

*On War*

Book I – On the Nature of War

## Chapter 2

# Evolution of Individuals and Populations

*Evolution* is defined as “one of a set of prescribed movements”, “a process of change in a certain direction” or “a process of continuous change from a lower, simpler, or worse to a higher, more complex, or better state” (Webster, 2003, → evolution). The term evolution is most strongly bound to Darwin’s work on the “theory that the various types of animals and plants have their origin in other preexisting types” (Webster, 2003, → evolution). It clearly carries the notion of processes that aim at enhancing a system to a – however defined – better state. In this sense an objective has to be defined as a measure for the improvement due to evolution. Yet, this kind of measure is not included in this chapter. An alternative, more neutral term would be the word “development”, which is equally qualified to replace “evolution” in the title of this chapter. However, “evolution” reflects in a most appropriate way the purpose for which the models are developed for, that is, for the conduction of a process, which induces an optimal environment for the development of a population into the direction of a better state – which is evolution as used in everyday language.

An *individual* “exists as an indivisible whole” and “as a distinct entity” (Webster, 2003, → individual). This can be a person, a cell or a particle. In the later chapters of this thesis we shall be concerned with faceted crystals. Individuals are characterized by a state. The state is a point in the state space and as such recognized as a point particle in the state space. That is, the term *particle* in this chapter does not necessarily refer to a physical particle but is merely a point moving in the state space. The state is in general subject to change over time, that is, it evolves. The movement of the particle is associated with the evolution of a specific individual. The evolution of an individual is governed by (i) its state, (ii) the interaction with the environment and (iii) direct interaction with other individuals. The latter implies the existence of other individuals which make up a population.

A *population* is “the total of individuals occupying an area or making up a whole” (Webster, 2003, → population). It is a collection of individuals which are subject to evolve over time and thus the population evolves in the state space. If the population size is large and the number of individuals within a small volume changes almost continuously when the volume is moved through space at a particular configuration, a distribution density, for instance a number density, can be used to describe the

population structure. Population balance equations are a natural implement to model the change of the distribution of a population in an environment.

In view of Clausewitz' quote cited at the beginning of this chapter first the individuals are considered, then specific types of the evolution of individuals and, last of all, the evolution of the whole population and its interaction with its environment. This structure mainly follows the book by Ramkrishna (2000). Before the individuals are discussed, however, a look at the whole is taken and in Sec. 2.1 the attention is drawn to the concept of population balances. In Sec. 2.2 the nature of the state vector of an individual as used in this work is presented. The state of the environment which is a continuous phase is introduced in Sec. 2.3. Sec. 2.4 discusses in a rather detailed way the evolution of individuals which can proceed continuously, discontinuously or can even involve jumps in the state space. The latter two cases are more complex to transfer to the population case, thus a separate part on the number density function is included in Sec. 2.5 before the dynamical evolution of the population in terms of population balances is discussed in Sec. 2.6. Sec. 2.7 summarizes the chapter.

## 2.1 The Notion of Population Balances

Process engineering is concerned with the processing of materials to convert them into more valuable materials. The raw material as well as the product is either fluid (gas or liquid) or solid (amorphous or crystalline). For the purpose of engineering analysis, the processing system is characterized by state variables. Fluids are quantified by composition, temperature, velocity and pressure. The dynamical evolution of these state variables can be described by equations derived from conservation laws for energy, momentum and mass which – equipped with thermodynamic relationships and a proper quantification of kinetic processes – furnish a complete model of the fluid system. For a solid, in principle the same is true. However, a solid phase embedded in a continuous phase in a processing system is most often not a single homogeneous entity but composed of a huge number of individual particles. Then we also speak of a *dispersed* system.<sup>1</sup> From the macroscopic engineering point of view it is most often adequate to look at an individual of the dispersed phase as an entity that is sufficiently described by a finite number of scalar state variables, for example (like for the continuous phase) composition, temperature, velocity and pressure. But as a single particle is small compared to the overall system, it is assumed that these state variables are not spatially distributed within the particle. As such, it is also not necessary to describe the particle-fluid boundary in any detail. However, one is in principle interested in approximate geometrical and other extensive features of the individuals, for example their size and shape. By taking these properties into account, counting the number of individuals and describing the dynamical behavior in a continuous framework, one arrives at the population balance.

Under a population we understand a collection of individuals. At first, a quantitative measure for the size of the population is required, that is, the number of individuals. If no further information about the individuals are at hand, the dynamical evolution of the number of individuals suffices to model the system. The dynamical

---

<sup>1</sup>That is not to say that dispersed systems necessarily involve a solid phase. For example, non-miscible fluids forming an emulsion are dispersed system as well.



evolution of the population size is then captured by an ordinary differential equation. With this implement it is possible to model the interaction between different populations. The Lotka-Volterra equations for predator-prey dynamics is the most prominent example (Aulbach, 1997). Though such systems can exhibit complex dynamical behavior, from the practical point of view it is more interesting to study *structured* populations, i.e., the individual is characterized by at least one *property*, for instance size, shape, composition or the like. Property state vectors can be seen as points in the *property state space* or *phase space*. Within it, the distribution of individuals can be characterized by a *number density function*, which is an expedient tool to describe large systems with many individuals instead of tracking the state of each individual. The evolution of the number density is specified by the population balance. This framework allows not only an efficient population modeling but due to the inherent consideration of a whole population, the modeling of interactions between individuals as for example fusion, fission, breakage and aggregation can be integrated in a most elegant way.

The discussion above started with the distinction between fluid materials and populations of solid materials and this is also historically the adequate point of entry into the field of population balances in process engineering. Population balances have most prominently been applied for the modeling of solids and dispersed phase processes. In chemical engineering the seminal work of Hulburt and Katz (1964) introduced the general multivariate population balance equation from a statistical mechanics perspective. In the same year Randolph (1964) published the concept of the general population balance in a shorter note as well employing a continuum mechanical framework (Jakobsen, 2008). The focus of Hulburt and Katz (1964) has been laid on particle processes in which the population distribution undergoes nucleation, growth and agglomeration. The distribution dynamics equation (population balance) is derived as a Liouville equation from the equations of motion in the phase space. Beside the generality of the formulation, applicable to a wide range of (continuously evolving) state vectors in the phase space, their work stands out because the dependency of the particle evolution of the environmental state evolving according to the classical transport equations is included. Also the recognition that the application of population balances may be 'overdetailed' is admitted which motivated the introduction of the still nowadays widely used concept to derive evolution equations of the moments of the property distributions. Though the paper of Hulburt and Katz (1964) is mostly seen as the nucleation point of population balances, the concept has been applied earlier to special cases. For instance, Randolph and Larson (1962) use a 1D population balance for the modeling of mixed suspension crystallizers in which nucleation and growth is included. The particle size in this work (as mostly in population balance modeling for crystallization) is assumed to take values in the whole  $\mathbb{R}^+$  and thus the population balance is a partial differential equation. On the other hand Smoluchowski (1917) describes the coagulation of colloidal systems under the assumption of a monodisperse initial population. Hence, the new particles produced have a mass of  $n$  times the mass of the initial particles. Therefore, the property coordinate can be reduced to the positive integers which results, for the dynamical description of the distribution on the sites of the property coordinate, in a set of ordinary differential equations rather than in a partial differential equation. However, this set of ordinary differential equations may also be considered a population balance and

is widely used for problems in particle technology (Rollié, 2010) and polymerization (Wulkow, 1990) where individuals are assembled from uniform building blocks.

As outlined by Jakobsen (2008), application examples of the population balance beyond chemical engineering range from aerosol dynamics and atmospheric sciences (Williams and Loyalka, 1991; Friedlander, 2000; Yong and Seinfeld, 1992; Singh et al., 2005; Gelbard and Seinfeld, 1980, 1978; Gelbard et al., 1980; Shekar et al., 2012), over multiphase droplet flow dynamics (Kolev, 1993, 2002), flame synthesis (Shekar et al., 2012), and bubbly two-phase flow in nuclear engineering (Lavalle et al., 1994). Among the most important application fields of population balances are liquid-liquid dispersions, e.g. Coualoglou and Tavlarides (1977); Gerstlaue (1999), gas-liquid dispersions as for instance described by Carrica et al. (1999); Chen et al. (2005) and Lehr and Mewes (2001), and granulation, e.g. Peglow (2005); Hounslow et al. (2001). The usability of the population balance equation in chemical engineering beyond particle technology has been recognized right from the start of the field. Fredrickson and Tsuchiya (1963) derive the population balance in terms of the age distribution of microorganisms undergoing a continuous development in their life cycle. Furthermore, binary fission of older cells producing new cells of age zero reflect the dynamic process of birth and death of individuals. Though a significant progress in the field of biological reactor modeling, the generality of the presented approach is limited since age is taken as the only independent property coordinate determining the full state vector in terms of the metabolic state. In Fredrickson et al. (1967) the population balance in the full multivariate physiological phase space is derived for the case of a unicellular system. In this paper is it exemplary shown how the knowledge of the behavior of a single entity and its interaction with the environment can be incorporated in a population framework in order to derive a structured model of the complex process of population evolution. In their own words: They "have tried to show how information gleaned from analysis of subcellular phenomena can be used to describe and predict the behavior of cells and cell populations. The foregoing statement does not imply that such information will be sufficient to effect a synthesis; clearly, it is necessary for synthesis" (Fredrickson et al., 1967).

In this spirit the work at hand builds up on the theory of population balance equations for continuous systems and develops a population balance approach for entities which undergo continuous as well as discrete dynamics. This framework is later applied to the case of populations of faceted crystals which posses this combined continuous and discrete (hybrid) dynamical model structure.

## 2.2 The Property State Vector

An individual is characterized by a state vector composed of *external* coordinates  $\mathbf{r}$  denoting the spatial position and *internal* coordinates  $\mathbf{x}$  quantifying the actual particle state, for example size, shape and/or composition (Ramkrishna, 2000):

$$\mathbf{r} = \begin{pmatrix} r_1 \\ \vdots \\ r_3 \end{pmatrix} \in \Gamma \subset \mathbb{R}^3, \quad \mathbf{x} = \begin{pmatrix} x_1 \\ \vdots \\ x_n \end{pmatrix} \in \Omega \subset \mathbb{R}^n. \quad (2.1)$$

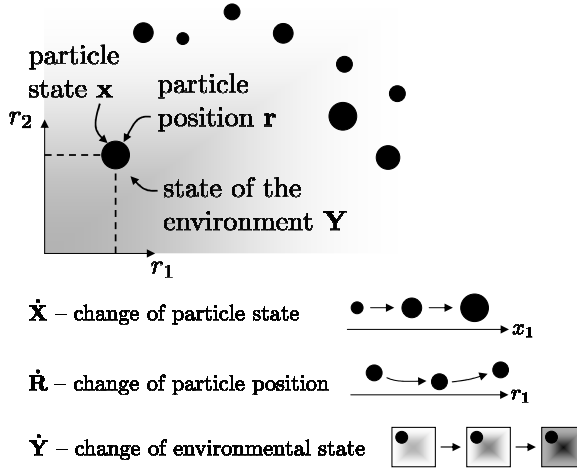


**Figure 2.1:** Property state, position and environmental state of a particle and its evolution.

The domain  $\Gamma$  is bound by the physical region in which a particle can move. The domain  $\Omega$  is a subset of the state space continuum  $\mathbb{R}^n$  in which the internal states take their values. In general,  $\mathbf{x}$  could also contain discrete or complex values but this is not discussed in the following.

The selection of properties to be accommodated in  $\mathbf{x}$  depends on the process and the purpose that the model is developed for. It is necessary that the number of state variables is straitened to a sensible amount that reflects the condition of the particle in an adequate manner. For the sake of identifiability, some of the state variables or (nonlinear) combinations of them should – in the real world – be accessible by measurements; at best for a huge number of individuals. But often, direct population distribution measurements or moments of the same suffice. Of course, only state variables that are subject to change during the process are included in  $\mathbf{x}$ , i.e., the nature of the underlying processes driving the movement of a state variable have to be modeled as well.

Clearly, in different contexts, the modeling of a system will lead to very different choices of the internal state variables, for instance the crystal sizes in different directions or the physiological state vector of a cell. Very often, it is also admissible to neglect the spatial position  $\mathbf{r}$  completely which is also done in the remainder of this work.

## 2.3 The Continuous Phase Vector

The particle is embedded in a fluid phase continuum whose state, denoted by (see Ramkrishna, 2000)

$$\mathbf{Y}(\mathbf{r}, t) = \begin{pmatrix} Y_1(\mathbf{r}, t) \\ \vdots \\ Y_c(\mathbf{r}, t) \end{pmatrix} \in \Omega_Y \subset \mathbb{R}^c, \quad (2.2)$$

is in general a time- and space-dependent function and involves quantities like composition, temperature and velocity. The evolution equations for these variables can be derived from the classical conservation laws for mass, energy and momentum (Bird et al., 2002; Jischa, 1982). It may not always be necessary to follow the fluid phase state in any detail. Rather, those states are selected that control the evolution of the particle state  $\mathbf{x}$ . The environmental state  $\mathbf{Y}$  sometimes varies significantly in space so that different individuals within a population are surrounded by different environments. But the spatial variation on the scale of the particle size is usually assumed to be negligible, i.e.,  $\mathbf{Y}$  does not vary on different sides of an individual. Very often, the spatial variation of  $\mathbf{Y}$  is negligible. And particularly in designed identification experiments, the change of  $\mathbf{Y}$  in time is small compared to the evolution of the particle state so that its dynamics must not always be reflected in a first order model.

In the remainder of this work, the spatial dependency of the continuous phase and the spatial coordinates of the individuals are not further considered. Their evolution in time, however, is retained and of course constitutes a core concept of the whole work.

## 2.4 Evolution of the Property State Vector

The change of the particle state is assumed to be at least piecewise continuous in time and deterministic, i.e., at a point in state space, the direction of movement is unambiguous. Particle trajectories in  $\Omega$  are controlled by the continuous phase variables and current state. Hence, a trajectory is a function that is a solution to a differential equation whose right-hand side is obtained from a velocity field

$$\frac{d\mathbf{x}}{dt} = \dot{\mathbf{X}}(\mathbf{x}, \mathbf{Y}, t) = \begin{pmatrix} \dot{X}_1(\mathbf{x}, \mathbf{Y}, t) \\ \vdots \\ \dot{X}_n(\mathbf{x}, \mathbf{Y}, t) \end{pmatrix}, \quad (2.3)$$

which is most often an explicit function of the environmental and particle state. An explicit time-dependency is uncommon and usually does not result from a rigorous physical model but from pretended environmental state trajectories. For the sake of brevity, the dependencies of the different variables may not be written out or only the dependency of interest is indicated while the others are hidden. For instance, the shorthand notation for  $\dot{\mathbf{X}}(\mathbf{x}, \mathbf{Y}, t)$  for the case when only the dependency on  $\mathbf{Y}$  is important but other dependencies can exist is  $\dot{\mathbf{X}}(\mathbf{Y}, \cdot)$ .

In the simplest case the state evolves within  $\Omega$  in accordance to a velocity field, which is continuously differentiable, see the hereafter directly following Sec. 2.4.1. Slightly more complex are trajectories with sharp bends, i.e., the velocity field switches at a point instantaneously. These systems are known as differential equations with discontinuous right-hand sides<sup>2</sup> and introduced in Sec. 2.4.2. A generalization of switching systems is the notion of systems that can perform state jumps. They make up the class of hybrid dynamical systems (Lunze, 2002) presented in Sec. 2.4.3.

---

<sup>2</sup>Systems with discontinuous right-hand side are also known as *Fillipov-Systems* and *sliding mode systems*.

### 2.4.1 Continuously Evolving Systems

The state  $\mathbf{x}$  of a particle evolves in accordance to a velocity field  $\dot{\mathbf{X}}$ , which is a smooth function in  $\Omega$ , that is, the partial derivatives

$$\frac{\partial^n \dot{X}_j}{\partial x_1 \dots \partial x_n}, \quad j = 1 \dots n, \quad (2.4)$$

exist. A trajectory starting at  $\mathbf{x}_0$  is a solution to the ordinary differential equation

$$\frac{d\mathbf{x}}{dt} = \dot{\mathbf{X}}, \quad \mathbf{x}(t=0) = \mathbf{x}_0, \quad (2.5)$$

which may be coupled to other algebraic or differential equations from which the necessary values for variables are obtained which are used to evaluate the right-hand side. The analytical solution for systems of the type (2.5) is known in general only for the linear (in the state variables) case (Aulbach, 1997; Bronstein et al., 2001). Nonlinear right-hand sides can lead to interesting dynamical behavior and are anything but trivial. For example, multiple steady-states can exist which can be stable, unstable or saddle points. Even limit cycles can occur and exhibit challenging dynamical behavior if the control of such a system must be achieved. Solutions in closed form can usually not be obtained, but according to the theorems of Peano and Picard-Lindelöf<sup>3</sup>, the local existence and uniqueness of the solution is guaranteed (Aulbach, 1997). For physical systems it is most often possible to integrate the system (2.5) together with accompanying (possibly algebraic) equations for  $\mathbf{Y}$  numerically and achieve a solution. For the numerical techniques the reader is referred to the standard literature, for instance Bronstein et al. (2001), Deuflhard and Bornemann (2002) and Shampine (1994).

### 2.4.2 Systems with Discontinuous Right-Hand Side

Differential equations whose right-hand side  $\dot{\mathbf{X}}$  shows qualitatively different behavior in different parts of the state space  $\Omega$  are encountered in many engineering problems (Fillippov, 1988). Examples are found for the model description of mechanical systems and hybrid control systems. In later chapters of this thesis, the evolution of faceted crystals is described by such a set of differential equations whose right-hand side switches if the shape undergoes qualitative changes. Ch. 3 and particularly Sec. 3.2.1 discusses this for single crystals whereas Ch. 4 adopts this concept also for crystal populations. However, because the general derivation of the discontinuous nature of the right-hand sides of dynamic crystal shape models requires a more elaborate introduction and because the statements given below apply to a whole class of such systems, we proceed with an easier comprehensible, motivational example taken from mechanics.

**Motivational Example: Cart-Wall Collision** Consider a system presented by van der Schaft and Schumacher (2000) and Imura and van der Schaft (2000): A cart colliding

<sup>3</sup>The Theorem of Picard-Lindelöf is also called Cauchy-Lipschitz Theorem.

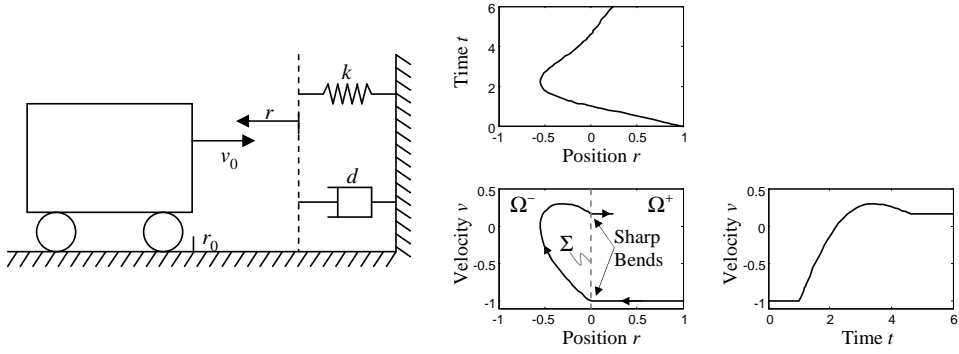


**Figure 2.2:** Collision of a cart to an elastic wall (left) (redrawn from Imura and van der Schaft, 2000). Trajectory with two sharp bends due to the discontinuity of the velocity field (right).

to an elastic wall as shown in Fig. 2.2 (left). The cart's system state is made up by the position and velocity:

$$\mathbf{x} = \begin{pmatrix} r \\ v \end{pmatrix}. \quad (2.6)$$

Its movement can be described by the differential equations

$$\frac{d\mathbf{x}}{dt} = \begin{bmatrix} 0 & 1 \\ 0 & 0 \end{bmatrix} \mathbf{x}, \quad \mathbf{x}(t=0) = \begin{pmatrix} r_0 > 0 \\ v_0 < 0 \end{pmatrix}, \quad \text{for } r \geq 0, \quad (2.7a)$$

$$\frac{d\mathbf{x}}{dt} = \begin{bmatrix} 0 & 1 \\ -k & -d \end{bmatrix} \mathbf{x}, \quad \mathbf{x}(t|_{r=0}) = \begin{pmatrix} 0 \\ v_0 \end{pmatrix}, \quad \text{for } r \leq 0. \quad (2.7b)$$

Though the system is not complicated to integrate if the collision event can be detected (MathWorks, 2011), at  $t|_{r=0}$  the velocity of the system is not differentiable and in principle governed by both differential equations. Before the wall is hit, the system is governed by Eq. (2.7a). It moves towards the wall with a constant velocity until after  $r = 0$  the dynamics is controlled by Eq. (2.7b) and thus decelerated by the spring-damper system. A typical trajectory<sup>4</sup> that passes twice through the surface  $r = 0$  is shown in Fig. 2.2 (right). It can be seen clearly that the trajectory in  $\mathbf{x}$ -space has sharp bends reflecting the discontinuity of the right-hand side.

A manifold of the kind  $\Sigma = \{\mathbf{x} : r = 0\}$ , see the state space plot in Fig. 2.2, is in the following recognized as a *switching surface* separating the state space into parts, denoted here by  $\Omega^-$  and  $\Omega^+$ , in which different system structures exist (van der Schaft and Schumacher, 2000; Lunze, 2002). These systems can be interpreted as *hybrid dynamical systems*, which are not capable of performing jumps in the state space. However, in this work the terms *system with discontinuous right-hand side* or *switching system* is preferred. The standard theory on existence and uniqueness for ordinary differential equations cannot be applied directly to switching systems (Aulbach, 1997; Fillippov, 1988; van der Schaft and Schumacher, 2000). In fact, a vast amount of literature is concerned to show existence and uniqueness of solutions to equations with discontinuous right-hand side, e.g. (Fillippov, 1988; van der Schaft and Schumacher, 2000). The present work, however, is not focused on this topic but rather numerical solu-

<sup>4</sup>Parameters:  $k = 1, d = 1$ . Initial condition  $\mathbf{x}^T = (1, -1)$ . Simulation time  $0 \leq t \leq 6$ .

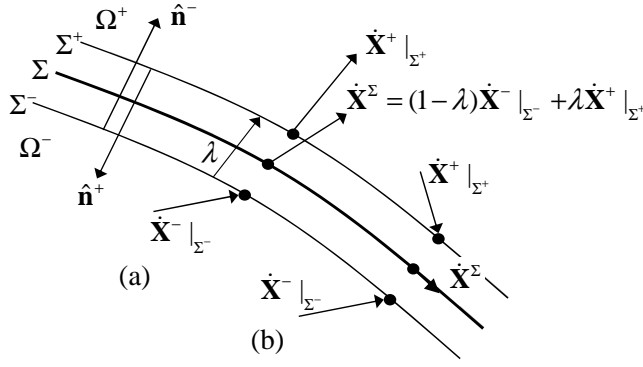


**Figure 2.3:** Division of the state space  $\Omega$  into a region  $\Omega^-$  in which the velocity field is  $\dot{\mathbf{x}}^-$  and a region  $\Omega^+$  where the field is  $\dot{\mathbf{x}}^+$ . Both parts are separated by the switching surface  $\Sigma$  of codimension 1. The surface  $\Sigma$  is imagined to be encased by a hull infinitesimally close to  $\Sigma$ . The parameter  $\lambda \in [0, 1]$  serves to connect the velocity fields in a consistent way if a trajectory just passes through the surface (a). If a particle trajectory moves on  $\Sigma$ , a velocity field  $\dot{\mathbf{x}}^\Sigma$  must be defined, which is at best obtained directly from the physical modeling or has to be defined in a consistent way (b).

tions to such systems are taken and by employing physical background information it is judged whether the so obtained integration is qualitatively correct. For this, it is important to tie the limit values of the velocity fields for switches (e.g. between Eq.s (2.7a) and (2.7b)) in a consistent way at the switching surface. In the example of the cart colliding to the elastic wall, the right hand side of Eq. (2.7b) can be defined to apply only for  $r < 0$  which makes practically no difference in the solution compared to the case with  $r \leq 0$ . This is also due to the fact that the system passes directly through the surface  $r = 0$  and does not move within it.

**The More Abstract Perspective** A more general view on a switching surface in the state space is depicted in Fig. 2.3. Rather than studying immediately an arbitrary number of switching surfaces, the situation with a single one is analyzed. The domain  $\Omega$  is partitioned into regions  $\Omega^-$  and  $\Omega^+$  which are separated by an  $(n-1)$ -D switching surface, denoted by  $\Sigma$ . This surface is encased by parts of the boundaries of the regions, that is  $\Sigma^- \subset \partial\Omega^-$  and  $\Sigma^+ \subset \partial\Omega^+$ . The nature of the other domain boundaries are of no concern for the current discussion. In order to specify  $\Sigma$ , an indicator function  $\sigma$  is introduced that is negative in  $\Omega^-$ , positive in  $\Omega^+$  and zero on  $\Sigma$ . The surface  $\Sigma$  is thus defined as a point set:

$$\Sigma = \{\mathbf{x} : \sigma(\mathbf{x}) = 0\}. \quad (2.8a)$$

Its hull, which is infinitesimally close to  $\Sigma$ , is given by

$$\Sigma^- = \{\mathbf{x} : \sigma(\mathbf{x}) = 0^-\} \quad (2.8b)$$

$$\Sigma^+ = \{\mathbf{x} : \sigma(\mathbf{x}) = 0^+\}, \quad (2.8c)$$

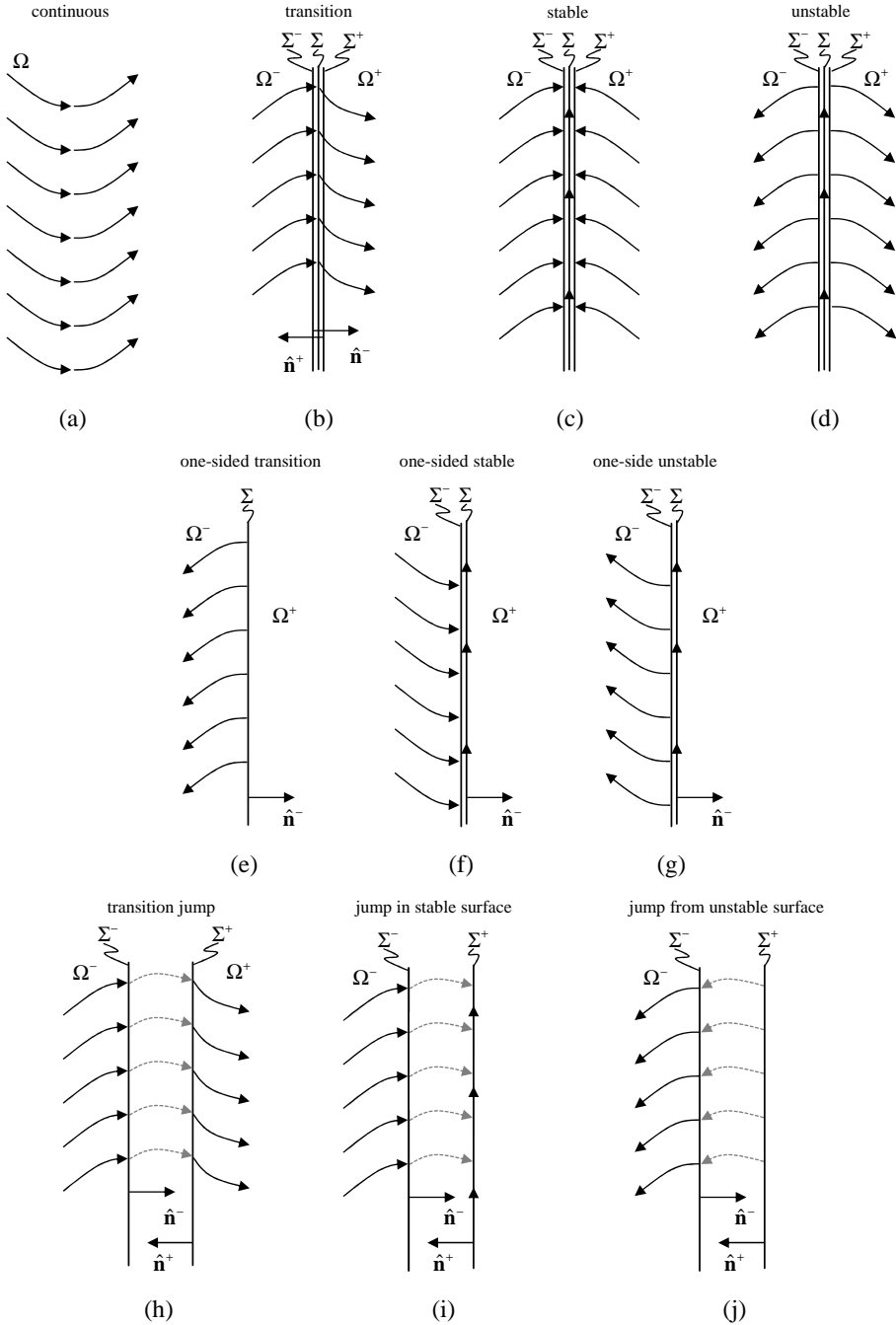


**Figure 2.4:** State space with continuous velocity field (a), with discontinuous velocity fields (b) to (d), one-sided discontinuous velocity fields (e) to (g) and jumping systems (h) to (j). Detailed explanations for the single trajectory case can be found in Sec.s 2.4.2.1-2.4.2.6 and Sec.s 2.4.3.1-2.4.3.3.



and thus (due to the continuity and differentiability of  $\sigma$ ) parallel to  $\Sigma = 0$ . The unit normal pointing from  $\Omega^-$  away is (Slattery et al., 2007; Aris, 1989)

$$\hat{\mathbf{n}}^- = \frac{1}{|\nabla_{\mathbf{x}} \sigma|_{\Sigma}} \nabla_{\mathbf{x}} \sigma|_{\Sigma}, \quad (2.9)$$

where  $\nabla_{\mathbf{x}}$  is the Nabla operator in  $\mathbf{x}$ -space. The outer unit normal of  $\Omega^+$  is  $\hat{\mathbf{n}}^+ = -\hat{\mathbf{n}}^-$ , see Fig. 2.3.

A particle in  $\Omega^-$  moves in accordance to the velocity field  $\dot{\mathbf{X}}^-$  and correspondingly in  $\Omega^+$  with  $\dot{\mathbf{X}}^+$ . Before the velocity in  $\Sigma$  is discussed we consider the particle velocities at the hull encasing  $\Sigma$ . There, the velocities are given in agreement with the continuously differentiable fields in the interior of  $\Omega^-$  and  $\Omega^+$ :

$$\dot{\mathbf{X}}^-|_{\Sigma^-} = \lim_{\sigma(\mathbf{x}) \rightarrow 0^-} \dot{\mathbf{X}}^-(\mathbf{x}, \cdot) \quad (2.10a)$$

$$\dot{\mathbf{X}}^+|_{\Sigma^+} = \lim_{\sigma(\mathbf{x}) \rightarrow 0^+} \dot{\mathbf{X}}^+(\mathbf{x}, \cdot), \quad (2.10b)$$

see Fig. 2.3. The reachability of the surface  $\Sigma$  clearly depends on the orientation of  $\dot{\mathbf{X}}^-|_{\Sigma^-}$  and  $\dot{\mathbf{X}}^+|_{\Sigma^+}$ . Let

$$\hat{\mathbf{p}}^- = \frac{1}{|\dot{\mathbf{X}}^-|_{\Sigma^-}} \dot{\mathbf{X}}^-|_{\Sigma^-}, \text{ and} \quad (2.11a)$$

$$\hat{\mathbf{p}}^+ = \frac{1}{|\dot{\mathbf{X}}^+|_{\Sigma^+}} \dot{\mathbf{X}}^+|_{\Sigma^+} \quad (2.11b)$$

be unit vectors, called velocity direction vectors, which point in the direction of the vector fields  $\dot{\mathbf{X}}^-|_{\Sigma^-}$  and  $\dot{\mathbf{X}}^+|_{\Sigma^+}$ , respectively. If the dot product between an outer unit normal surface vector and a velocity direction vector in the interior is positive, the inter-vectorial angle is acute, that is, the velocity vector points into the same half-plane and thus towards the surface. Therefore, the surface is reachable by a particle moving in accordance to the velocity field. If the dot product is negative, the surface is not reachable. For the velocities around the surface introduced above this means:

$$\hat{\mathbf{p}}^- \cdot \hat{\mathbf{n}}^- > 0 \rightarrow \Sigma \text{ is reachable from } \Omega^-, \quad (2.12a)$$

$$\hat{\mathbf{p}}^- \cdot \hat{\mathbf{n}}^- \leq 0 \rightarrow \Sigma \text{ is not reachable from } \Omega^-, \quad (2.12b)$$

$$\hat{\mathbf{p}}^+ \cdot \hat{\mathbf{n}}^+ > 0 \rightarrow \Sigma \text{ is reachable from } \Omega^+, \quad (2.12c)$$

$$\hat{\mathbf{p}}^+ \cdot \hat{\mathbf{n}}^+ \leq 0 \rightarrow \Sigma \text{ is not reachable from } \Omega^+, \quad (2.12d)$$

$$\dot{\mathbf{X}}^{\Sigma} \cdot \hat{\mathbf{n}}^+ = 0 \rightarrow \text{trajectories stay in } \Sigma. \quad (2.12e)$$

If the surface  $\Sigma$  has been reached and the path of the particle is continued therein (see the case-by-case analysis below) as for instance shown in Fig. 2.3 (b), its velocity is given by  $\dot{\mathbf{X}}^{\Sigma}$ . The origin of the field  $\dot{\mathbf{X}}^{\Sigma}$  may be given directly from the physical model or it is a projection of one of the neighboring higher-dimensional vector fields or a weighted sum thereof.

As indicated previously, it is in principle possible to produce different configurations arising from the direction of the vector fields  $\dot{\mathbf{X}}^-$ ,  $\dot{\mathbf{X}}^{\Sigma}$  and  $\dot{\mathbf{X}}^+$  and the orientations  $\hat{\mathbf{n}}^-$  and  $\hat{\mathbf{n}}^+$  of the surface. Some local cases are depicted in Fig. 2.4 which will be discussed in the following. For this, we use symbols having the following meaning:

horizontal arrows ( $\leftarrow$  and  $\rightarrow$ ) indicate the velocity direction in the domain  $\Omega^-$  or  $\Omega^+$ . A vertical line ( $|$ ) stands for the surface  $\Sigma$  on which the particle does not move but is passed directly through without staying in it. An upright arrow ( $\uparrow$ ) denotes a surface on which the particles can move. A cross-sign ( $\times$ ) stands for a domain in which no velocity field is defined, for example because a state vector in this domain has no physical meaning.

At first, the accumulation-free transition surface, abbreviated by T ( $\rightarrow | \rightarrow$ ), is discussed in Sec. 2.4.2.1. Then the case is sketched for which a particle is driven into the surface and trapped therein, the so called stable surface S ( $\rightarrow \uparrow \leftarrow$ ), see Sec. 2.4.2.2. Opposite to this situation is the unstable surface U ( $\leftarrow \uparrow \rightarrow$ ), on which particles can in principle move but are pushed away upon a slight deviation from it, see Sec. 2.4.2.3. In Sec.s 2.4.2.4 to 2.4.2.6 three special cases of the preceding generic situations are sketched in which one side across the dividing surface is not reachable. This is particularly interesting for later applications and the formulation of shape evolution equations in Ch.s 3 and 4.

#### 2.4.2.1 Case T ( $\rightarrow | \rightarrow$ ): Transition Surface

Consider the case sketched in Fig.s 2.3 (a) and 2.4 (b). The particle starts in  $\Omega^-$  with state  $\mathbf{x}_0$  and subsequently moves in accordance to the field  $\dot{\mathbf{X}}^-$  pointing towards  $\Sigma$  if the condition in Eq. (2.12a) is fulfilled. It reaches  $\Sigma^-$ , moves to  $\Sigma^+$  and continues directly in  $\Omega^+$  if the constraint given in Eq. (2.12d) can be met, see also Fig. 2.3 (a). The reverse situation where the trajectory is started in  $\Omega^+$ , passed through  $\Sigma$  and continued in  $\Omega^-$  is qualitatively identical if the direction of the velocity fields with respect to the orientation of the surface is reversed as well. Since the particles pass directly through the surface, this case is in the following referred to as *transition surface*. The differential equation describing the evolution of this system is given by

$$\frac{d\mathbf{x}}{dt} = \begin{cases} \dot{\mathbf{X}}^- & \text{for } \mathbf{x} \in \Omega^- \\ \dot{\mathbf{X}}^\Sigma & \text{for } \mathbf{x} \in \Sigma \\ \dot{\mathbf{X}}^+ & \text{for } \mathbf{x} \in \Omega^+ \end{cases}, \quad \mathbf{x}(t=0) = \mathbf{x}_0 \in \Omega, \quad (2.13)$$

where the velocity in  $\Sigma$  is

$$\dot{\mathbf{X}}^\Sigma = (1 - \lambda)\dot{\mathbf{X}}^-|_{\Sigma^-} + \lambda\dot{\mathbf{X}}^+|_{\Sigma^+}, \quad 0 \leq \lambda \leq 1. \quad (2.14)$$

The parameter  $\lambda$  can be chosen in a way that reflects the physical behavior of the system at best. For the practical solution the choice should make no difference.

#### 2.4.2.2 Case S ( $\rightarrow \uparrow \leftarrow$ ): Stable Surface

Contrary to the previous case, the particle starts either in  $\Omega^-$  or  $\Omega^+$  and moves with the velocity  $\dot{\mathbf{X}}^-$  or  $\dot{\mathbf{X}}^+$ , respectively, which point towards  $\Sigma$ . That is, the conditions (2.12a), (2.12c) and (2.12e) must be fulfilled in order to realize this situation, see Fig.s 2.3 (b) and 2.4 (c). Thus, the trajectory enters  $\Sigma$  and continues its path therein,

moving with  $\dot{\mathbf{X}}^\Sigma$ . Due to the fact that in this case particles remain in  $\Sigma$ , this setup is referred to as *stable surface*. The differential equation is qualitatively given by

$$\frac{d\mathbf{x}}{dt} = \begin{cases} \dot{\mathbf{X}}^- & \text{for } \mathbf{x} \in \Omega^- \\ \dot{\mathbf{X}}^\Sigma & \text{for } \mathbf{x} \in \Sigma \\ \dot{\mathbf{X}}^+ & \text{for } \mathbf{x} \in \Omega^+ \end{cases}, \quad \mathbf{x}(t=0) = \mathbf{x}_0 \in \Omega, \quad (2.15)$$

where  $\dot{\mathbf{X}}^\Sigma$  is a velocity field of the sliding mode (trajectory within  $\Sigma$ ) which follows directly from the physical model. If this does not follow directly from the model, a weighted sum of the projected fields  $\dot{\mathbf{X}}^-$  and  $\dot{\mathbf{X}}^+$  could generate a reasonable velocity field which shall be consistent with the physical situation.

#### 2.4.2.3 Case U ( $\leftarrow \uparrow \rightarrow$ ): Unstable Surface

The reverse setting to the previous case (Fig. 2.4 (d)) is given when the fields  $\dot{\mathbf{X}}^-$  and  $\dot{\mathbf{X}}^+$  point from  $\Sigma$  away (conditions (2.12b) and (2.12d)) and a trajectory that is in  $\Sigma$  remains therein (condition (2.12e)) but particles from within  $\Omega^-$  and  $\Omega^+$  are not attracted by  $\Sigma$ . The differential equation for this system is determined by the initial condition since the domain in which the particle is started cannot be left:

$$\frac{d\mathbf{x}}{dt} = \dot{\mathbf{X}}^- \quad \text{for } \mathbf{x}(t=0) = \mathbf{x}_0 \in \Omega^-, \quad (2.16a)$$

$$\frac{d\mathbf{x}}{dt} = \dot{\mathbf{X}}^\Sigma \quad \text{for } \mathbf{x}(t=0) = \mathbf{x}_0 \in \Sigma, \quad (2.16b)$$

$$\frac{d\mathbf{x}}{dt} = \dot{\mathbf{X}}^+ \quad \text{for } \mathbf{x}(t=0) = \mathbf{x}_0 \in \Omega^+. \quad (2.16c)$$

A trajectory is not attracted by  $\Sigma$  but in fact pushed to the interior of  $\Omega^-$  or  $\Omega^+$  once it slightly deviates from  $\Sigma$ , for example driven by a small disturbance. Hence, this configuration is referred to as *unstable surface*.

#### 2.4.2.4 Case T<sub>os</sub> ( $\leftarrow | \times$ ): One-Sided Transition Surface

A special case of the transition surface, see Sec. 2.4.2.1, occurs when particles starting in  $\Sigma$  move directly to the interior of  $\Omega^-$ , that is, the condition (2.12b) must be fulfilled. This situation is depicted in Fig. 2.4 (e). The velocity in  $\Sigma$  is determined by the limit value of  $\dot{\mathbf{X}}^-$ :

$$\dot{\mathbf{X}}^\Sigma = \dot{\mathbf{X}}^-|_{\Sigma^-}, \quad (2.17)$$

so that particles starting on  $\Sigma$  move – due to the validity and invalidity of Eq.s (2.12b) and (2.12e), respectively – directly into  $\Omega^-$ . Within the domain  $\Omega^+$  no velocity field is defined, i.e., this part of the state space cannot be entered by trajectories, for example because it does not reflect physically sensible states. In this case the differential equation reads

$$\frac{d\mathbf{x}}{dt} = \dot{\mathbf{X}}^-, \quad \mathbf{x}(t=0) = \mathbf{x}_0 \in \Omega^- \cup \Sigma. \quad (2.18)$$

Actually, this formulation makes sense only if indeed the particle is being started on  $\Sigma$ . This can for instance happen due to the conversion of a stable surface to a transition surface. That is, the continuation of the path that has been covered till the conversion within  $\Sigma$  is relaunched by (2.18) to continue in  $\Omega^-$ . If, however, the par-

ticle is started directly in  $\Omega^-$ , the system is simply an ordinary differential equation not necessitating the notion of the transition surface.

#### 2.4.2.5 Case $S_{os} (\rightarrow \uparrow \times)$ : One-Sided Stable Surface

If on the other hand the field  $\dot{\mathbf{X}}^-$  points towards  $\Sigma$  (see Eq. (2.12a)) and a particle entering  $\Sigma$  continues therein but in  $\Omega^+$  no velocity field is defined, the evolution of the system is a special case of the stable surface as described in Sec. 2.4.2.2:

$$\frac{d\mathbf{x}}{dt} = \begin{cases} \dot{\mathbf{X}}^- & \text{for } \mathbf{x} \in \Omega^- \\ \dot{\mathbf{X}}^\Sigma & \text{for } \mathbf{x} \in \Sigma. \end{cases}, \quad \mathbf{x}(t=0) = \mathbf{x}_0 \in \Omega^- \cup \Sigma. \quad (2.19)$$

This means that particles starting in  $\Omega^-$  move into  $\Sigma$  and stay therein while moving with the velocity  $\dot{\mathbf{X}}^\Sigma$ . If a particle starts in  $\Sigma$ , it remains in this surface and moves with  $\dot{\mathbf{X}}^\Sigma$  as well. In Fig. 2.4 (f) a sketch of the velocity field is depicted.

#### 2.4.2.6 Case $U_{os} (\leftarrow \uparrow \times)$ : One-Sided Unstable Surface

Like the stable surface, also the unstable surface as discussed in Sec. 2.4.2.3 can degenerate so that solutions starting in  $\Sigma$  stay in this domain. A trajectory that is started in  $\Omega^-$ , however, does not reach  $\Sigma$  since – presuming that the inequality (2.12b) is fulfilled – the velocity field points to the interior of  $\Omega^-$ , see Fig. 2.4 (g). As for the two degenerate cases discussed above, the opposite domain  $\Omega^+$  across  $\Sigma$  shall not be reachable. The differential equations for the state evolution are derived from Eq. (2.16):

$$\frac{d\mathbf{x}}{dt} = \dot{\mathbf{X}}^- \quad \text{for } \mathbf{x}(t=0) = \mathbf{x}_0 \in \Omega^- \quad (2.20a)$$

$$\frac{d\mathbf{x}}{dt} = \dot{\mathbf{X}}^\Sigma \quad \text{for } \mathbf{x}(t=0) = \mathbf{x}_0 \in \Sigma. \quad (2.20b)$$

#### 2.4.2.7 Interim Summary: Discontinuous Evolution

In the preceding Sec.s 2.4.2.1-2.4.2.6 the evolution equations for the trajectory of a particle have been formulated for the case that the state space is separated by a surface  $\Sigma$  of codimension 1 at which a qualitative change of the velocity (i.e., the right hand side of the differential equation) occurs. Clearly, switches between the cases can in principle emerge because the environmental conditions  $\mathbf{Y}$  and other variables controlling the velocity field are in general subject to evolve over time and with it the velocity fields. This must of course be tracked when such a system is integrated. Furthermore, it is imaginable that the velocity fields behave differently in different parts of the state space, that is, combinations of the cases presented above can be easily constructed.

The notion of switching surfaces does not complete our perception of hybrid systems. In the following section, yet another mechanism of an irregular (hybrid) state evolution is discussed: If the trajectory reaching the surface  $\Sigma$  is not continued locally but restarted at a different position in the state space, it performs a jump.

### 2.4.3 Jumping Systems

**Motivational Example: Bouncing Ball** An exemplary system performing jumps in the state space is the bouncing ball which is also discussed by Kofman (2004). A tutorial in the Matlab documentation (MathWorks, 2011) provides a readily implemented code of this system which has also been used here. The simplest version of this model describes the free fall of a ball (without friction) and the subsequent reflection at a solid surface at which a portion  $(1 - \gamma)$  of the kinetic energy is absorbed. The system state includes the height and velocity of the ball as depicted in Fig. 2.5 (a):

$$\mathbf{x} = \begin{pmatrix} h \\ v \end{pmatrix}. \quad (2.21)$$

The movement is governed by the following equations:

$$\frac{d\mathbf{x}}{dt} = \begin{bmatrix} 0 & 1 \\ 0 & 0 \end{bmatrix} \mathbf{x} + \begin{pmatrix} 0 \\ -g \end{pmatrix} \quad \text{for } h > 0 \quad (2.22a)$$

$$\mathbf{x}|_{\Sigma^-} = \mathbf{x}(t_j^-) \quad \text{for } h = 0 \quad (2.22b)$$

$$\mathbf{x}|_{\Sigma^+} = \begin{bmatrix} 1 & 0 \\ 0 & -\gamma \end{bmatrix} \mathbf{x}|_{\Sigma^-} \quad \text{for } h = 0, \quad (2.22c)$$

where  $t_j^-$  refers to the instant preceding the jumping time for an infinitesimal interval. A typical development of velocity and height is depicted in Figs 2.5 (b) and (c), respectively: At height  $h = 20$  the ball is released and subsequently accelerates constantly due to gravity, i.e., the evolution is dictated by Eq. (2.22a). The trajectory in  $\mathbf{x}$ -space is depicted in Fig. 2.5 (d). Until the height  $h = 0$  is reached for the first time the upper curve in the left half makes up the trajectory. At  $h = 0$  the ball hits a solid surface. In view of the previously introduced notation, the domain  $\Sigma = \{\mathbf{x} : h = 0\}$  is a so called jump surface. When it is reached, the direction of the ball's velocity is instantaneously reversed and its magnitude reduced (factor  $\gamma$ ), see Eq.s (2.22b) and (2.22c). This is also shown in Fig. 2.5 (b) where at  $t = 2$  the velocity is displaced from  $v \approx -20$  to  $v \approx 15$ . In the state space this implicates a jump on the velocity axis, i.e., the trajectory dunking into  $\Sigma^- = \{\mathbf{x} : h = 0, v < 0\}$  is continued at a determined point in  $\Sigma^+ = \{\mathbf{x} : h = 0, v > 0\}$ . The (deterministic) transfer from a point in  $\Sigma^-$  to a point in  $\Sigma^+$  is called a jump and indicated in Fig. 2.5 (d) by the gray shaded, curved arrows below the  $v$  axis. For  $t > 2$  the path of the ball is continued such that it reaches a maximal height, moved again towards the solid boundary where it is again reflected to move up and so forth until the kinetic energy is fully dissipated and  $\mathbf{x}^T(t \rightarrow \infty) = (0, 0)$ .

This small introductory example shall serve to motivate that jumps in the state space can occur in various systems in mechanics but also in chemical engineering, electrical and control engineering and robotics. In fact, a vast amount of researchers investigate such systems under the topic *hybrid dynamic systems*, that is hybrid in the sense that continuous (differential equations) as well as discrete (automates) dynamics are involved. The lecture notes of Tomlin (2005) are a good starting point to get acquainted with the field; therein also a huge number of references on mathematical foundations and on applications of hybrid systems is given. The book edited by Engell et al. (2002) contains overview articles on modeling, simulation, analysis

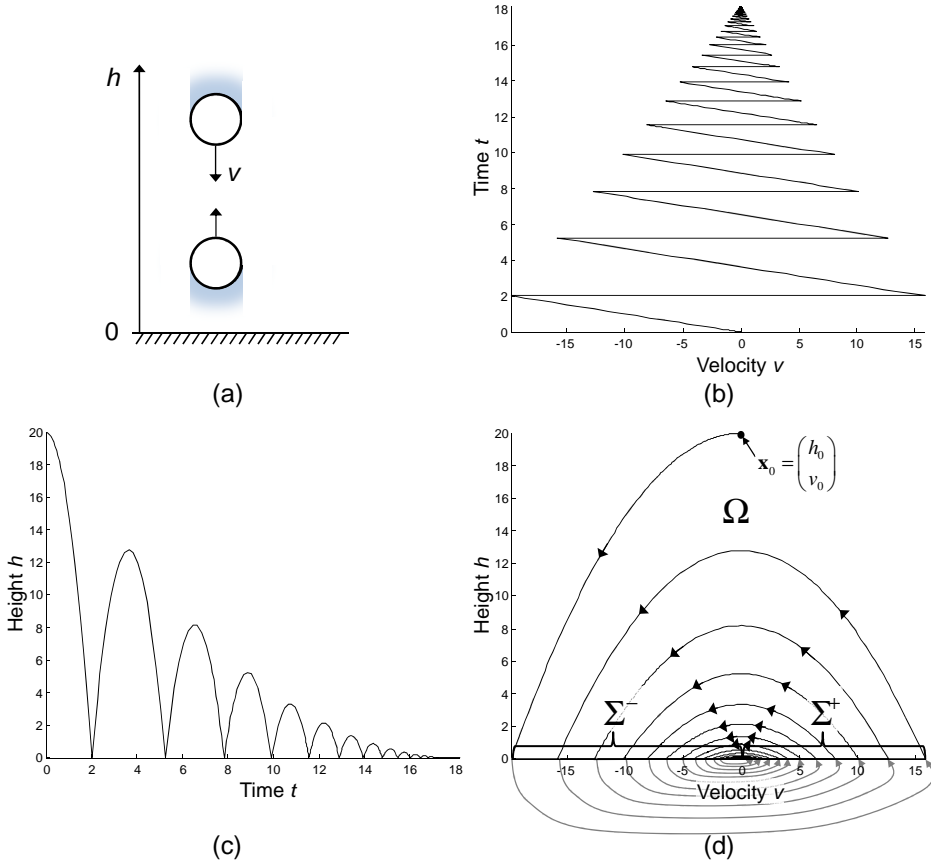


**Figure 2.5:** Bouncing ball. The ball is accelerated by gravitation and reflected at a solid wall (a). At the reflection point the velocity changes its sign and its magnitude is additionally decreased by a dissipation factor (b). The maximum height decreases over time (c). The trajectory in height-velocity-space performs jumps when the ball is reflected by the wall (d).

and controller synthesis from the theoretical point of view but contains application examples as well.

**The more General View** In the previous section, systems have been discussed whose path reaching the surface  $\Sigma$  is continued with a different velocity, i.e., the right-hand side of the differential equation can jump. The system class in this section is further widened since now jumps in the state are allowed as well (and not only in the velocity). This situation is depicted in Fig. 2.6. The state space is again decomposed into domains  $\Omega^-$  and  $\Omega^+$  which do (locally) not share a common boundary. In contrast to the preceding explanations, the boundaries  $\Sigma^-$  and  $\Sigma^+$  are separated and wrap a domain which is not accessible and where not necessarily a velocity field is defined similarly to the cases  $T_{os}$ ,  $S_{os}$  and  $U_{os}$  in Sec.s 2.4.2.4-2.4.2.6. But in contrast to these cases, the domain that is not accessible can in the following examples be jumped over. A particle starting in  $\Omega^-$  reaches the surface  $\Sigma^-$  if the conditions as stated in Eq. (2.12a) are met. From there the particle is instantaneously moved to a point  $x|_{\Sigma^+}$  on the surface  $\Sigma^+$  by a *jump-function*  $\xi_j^+$  whose argument is the state at

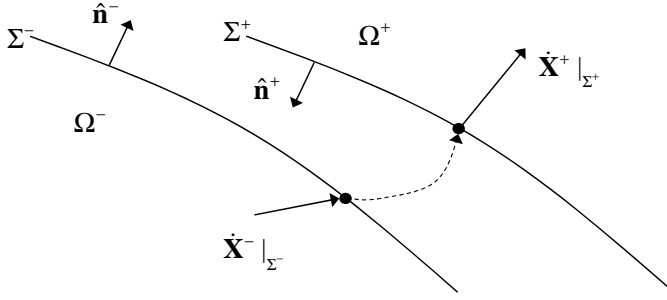


**Figure 2.6:** State space division for jumping systems.

the  $\Sigma^-$ -surface, denoted by  $\mathbf{x}|_{\Sigma^-}$ , and possibly other arguments, particularly environmental state variables. The instantaneous move from  $\Sigma^-$  to  $\Sigma^+$  is called a *jump in state space* and the time instant denoted by  $t_j$ . The instant preceding  $t_j$  for an infinitesimally small time interval is denoted by  $t_j^-$  whereas the instant following is  $t_j^+$ . Note that the superscripts + and - for  $t_j$  do not necessarily refer to  $\Sigma^-$  and  $\Sigma^+$ ; they rather indicate the sequence of the events.

Along the lines of the preceding Sec. 2.4.2, three cases are distinguished: The transition jump passing the trajectory to the boundary of the opposite domain where it is directly continued in the interior, see Sec. 2.4.3.1. In Sec. 2.4.3.2 the jump into a stable surface is presented whereas Sec. 2.4.3.3 discusses the case of the jump from an unstable surface to the boundary of a fully dimensional domain in which the trajectory is continued.

#### 2.4.3.1 Case $T_j (\rightarrow | \rightarrow | \rightarrow)$ : Transition Jump

The trajectory of the particle is started in  $\Omega^-$  and evolving with the velocity  $\dot{\mathbf{X}}^-$ . As depicted in Fig. 2.4 (h), the direction of  $\dot{\mathbf{X}}^-$  with respect to the orientation of the  $\Sigma^-$ -surface is such that trajectories dunk into  $\Sigma^-$ , i.e., the condition given in Eq. (2.12a) is fulfilled. After  $\Sigma^-$  is reached, the jump function  $\zeta^+$  is executed, i.e., the trajectory is instantaneously moved from a point on  $\Sigma^-$  to a determined point on  $\Sigma^+$ . The jump function with a + in the superscript refers to the transfer to  $\Sigma^+$ ; in principle, the reverse case is also possible when the orientation of the velocity fields is reversed. Formally, the instant preceding the jump time,  $t_j$ , for an infinitesimally short interval is denoted by  $t_j^-$ , whereas the instant following is referred to by  $t_j^+$ . After  $\Sigma^+$  is reached, the path is continued in the interior of  $\Omega^+$ , which necessitates that the velocity field  $\dot{\mathbf{X}}^+$  is oriented such that the condition given in Eq. (2.12d) is fulfilled. Using the introduced

notation, the dynamical equations including the discrete event of the jump can be expressed as

$$\frac{dx}{dt} = \dot{X}^- \quad \text{for } x \in \Omega^-, \text{ i.e. } 0 \leq t < t_j^-, \quad x(t=0) = x_0 \in \Omega^-, \quad (2.23a)$$

$$x|_{\Sigma^-} = x(t_j^-) \quad \text{for } x \in \Sigma^- \text{ at } t = t_j^-, \quad (2.23b)$$

$$x|_{\Sigma^+} = \zeta^+(x|_{\Sigma^-}, \cdot) \quad \text{for } x \in \Sigma^+ \text{ at } t = t_j^+, \quad (2.23c)$$

$$\frac{dx}{dt} = \dot{X}^+ \quad \text{for } x \in \Omega^+, \text{ i.e. } t > t_j^+, \quad x(t = t_j) = x|_{\Sigma^+}. \quad (2.23d)$$

The motivational example of the bouncing ball falls into this category with the simplification that the fully-dimensional region must not be separated into  $\Omega^-$  and  $\Omega^+$  since the continuous evolution equations before  $\Sigma^-$  and after  $\Sigma^+$  are the same and trajectories move in a joint domain,  $\Omega$ , which is not left, see Fig. 2.5 (d). This case shows a certain analogy to the transition surface case T described in Sec. 2.4.2.1, where the trajectory is passed over the surface. Hence, the prototype Eq.s (2.23) are referred to as transition jump or in shorthand notation  $T_j$ .

#### 2.4.3.2 Case $S_j$ ( $\rightarrow | \rightarrow \uparrow$ ): Jump into Stable Surface

After a jump, the continuation of the trajectory within a surface is also possible. The jump from the boundary  $\Sigma^-$ , following the movement in  $\Omega^-$ , into a surface  $\Sigma^+$  is sketched in Fig. 2.4 (i). The continuous movement succeeding the jump is continued within  $\Sigma^+$  in which the velocity field  $\dot{X}^\Sigma$  determines the evolution. The equations quantifying this situation are almost identical to Eq.s (2.23):

$$\frac{dx}{dt} = \dot{X}^- \quad \text{for } x \in \Omega^-, \text{ i.e. } 0 \leq t < t_j^-, \quad x(t=0) = x_0 \in \Omega^-, \quad (2.24a)$$

$$x|_{\Sigma^-} = x(t_j^-) \quad \text{for } x \in \Sigma^- \text{ at } t = t_j^-, \quad (2.24b)$$

$$x|_{\Sigma^+} = \zeta^+(x|_{\Sigma^-}, \cdot) \quad \text{for } x \in \Sigma^+ \text{ at } t = t_j^+, \quad (2.24c)$$

$$\frac{dx}{dt} = \dot{X}^{\Sigma^+} \quad \text{for } x \in \Sigma^+, \text{ i.e. } t > t_j^+, \quad x(t = t_j) = x|_{\Sigma^+}. \quad (2.24d)$$

Since the Eq.s (2.24) are similar to the stable surface (see Eq.s (2.15)) with the additional feature of the jump, the case is referred to as a *jump into stable surface* or in shorthand notation  $S_j$ .

#### 2.4.3.3 Case $U_j$ ( $\leftarrow | \leftarrow$ ): Jump from Unstable Surface

The reverse case to the jump into the stable surface is the jump from an unstable surface which may be compared to the simple unstable surface, see Sec. 2.4.2.3. The jump at  $t_j = 0$  from the surface  $\Sigma^+$  onto the boundary  $\Sigma^-$  of the domain  $\Omega^-$  is



shown in Fig. 2.4 (j). In principle, the governing equations are directly derived from the equations of the transition jump, Eq.s (2.23):

$$\mathbf{x}|_{\Sigma^+} = \mathbf{x}(t_j^-) \quad \text{for } \mathbf{x} \in \Sigma^+ \quad \text{at } t = t_j^- = 0^-, \quad \mathbf{x}(t=0) = \mathbf{x}_0 \in \Sigma^+, \quad (2.25a)$$

$$\mathbf{x}|_{\Sigma^-} = \xi^-(\mathbf{x}|_{\Sigma^+}, \cdot) \quad \text{for } \mathbf{x} \in \Sigma^- \quad \text{at } t = t_j^+ = 0^+ \quad (2.25b)$$

$$\frac{d\mathbf{x}}{dt} = \dot{\mathbf{X}}^- \quad \text{for } \mathbf{x} \in \Omega^-, \quad \text{i.e. } t > t_j^+, \quad \mathbf{x}(t = t_j) = \mathbf{x}|_{\Sigma^-}. \quad (2.25c)$$

Note that the jump function is furnished with a minus sign as a superscript because the jump is performed from  $\Sigma^+$  to  $\Sigma^-$ . In the sections above the jump was performed from  $\Sigma^-$  to  $\Sigma^+$ , i.e., the jump function was equipped with a plus sign. Because the mechanism is similar to the unstable surface explained in Sec. 2.4.2.3, this case is called *jump from unstable surface* and according to the previously developed abbreviated notation denoted by  $U_j$ .

## 2.5 The Number Density Function

While the preceding sections have dealt with single particles, from now on populations of particles are examined. In principle, this can be done in two different ways. The number of equations used to specify the evolution of a single particle can be increased so that every individual within the system is described separately. If the number of particles in the system, however, becomes large, the number of trajectories which must be computed becomes large and for practical applications the resulting set of equations is computationally expensive to solve. This problem can be remedied partly by choosing representative particles whose trajectories are computed. Neighboring particle trajectories are assumed to evolve in a similar way. Using this method, a number of problems in particle technology have been solved, particularly for the determination of particle trajectories in stirred vessels, e.g. Decker (2005). In a more rigorous way, the distribution of individuals in the state space is quantified by a *number distribution density* which upon multiplication with an infinitesimal volume of the state space yields the number of particles in state  $\mathbf{x}$ :

$$f(\mathbf{x}, t) dV_{\mathbf{x}}. \quad (2.26)$$

The volume measure  $dV_{\mathbf{x}}$  for a Cartesian state space is  $dx_1 dx_2 \dots dx_n$ . If the state space  $\Omega$  is not further partitioned, the overall number of particles in the system is obtained by integration over the whole domain:

$$N(t) = \int_{\Omega} f(\mathbf{x}, t) dV_{\mathbf{x}}. \quad (2.27)$$

In case that the state space – due to the discontinuous velocity field – is partitioned into regions  $\Omega^-$  and  $\Omega^+$ , separated by  $\Sigma$ , see Sec. 2.4.2 and Fig.s 2.4 and 2.7, the number density is separately defined in each part. The distribution of the particles in  $\Omega^+$  and  $\Omega^-$  is – as for the continuous case described above – given by a number density quantifying the number of particles within a unit volume in  $\mathbf{x}$ -space. On the

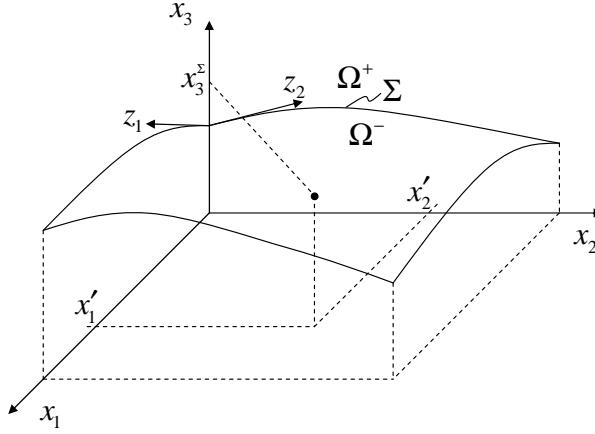


**Figure 2.7:** Surface intrinsic coordinates  $\mathbf{z}$ .

surface  $\Sigma$ , the distribution is specified by the number of particles per unit area on the surface:

$$f^-(\mathbf{x}, t) = \frac{\text{number of particles}}{\text{unit volume of } \Omega}, \quad \mathbf{x} \in \Omega^-, \quad (2.28a)$$

$$f^\Sigma(\mathbf{x}, t) = \frac{\text{number of particles}}{\text{unit area of } \Omega}, \quad \mathbf{x} \in \Sigma, \quad (2.28b)$$

$$f^+(\mathbf{x}, t) = \frac{\text{number of particles}}{\text{unit volume of } \Omega}, \quad \mathbf{x} \in \Omega^+. \quad (2.28c)$$

Hence, the total number of particles in the system is the sum of two volume integrals and a surface integral:

$$N = \underbrace{\int_{\Omega^-} f^- dV_{\mathbf{x}}}_{=N^-} + \underbrace{\int_{\Sigma} f^\Sigma dA_{\mathbf{x}}}_{=N^\Sigma} + \underbrace{\int_{\Omega^+} f^+ dV_{\mathbf{x}}}_{=N^+}. \quad (2.29)$$

Actually,  $(n-1)$  coordinates within  $\Sigma$  suffice for the quantification of the surface number density. A local intrinsic (possibly curvilinear) surface system with coordinate vector  $\mathbf{z} \in \Omega_{\mathbf{z}} \subset \mathbb{R}^{n-1}$  allows to address every point on the surface, see Fig. 2.7. Clearly, a unit volume in  $\mathbf{z}$ -space has the dimension of a unit area in the full  $\mathbf{x}$ -space. That is, a number density function in  $\mathbf{z}$ -coordinates can be defined such that

$$f^\Sigma(\mathbf{x}, t) dA_{\mathbf{x}} = f_{\mathbf{z}}^\Sigma(\mathbf{z}, t) dV_{\mathbf{z}}. \quad (2.30)$$

The number of particles within the surface is then obtained by

$$N^\Sigma(t) = \int_{\Omega_{\mathbf{z}}} f_{\mathbf{z}}^\Sigma(\mathbf{z}, t) dV_{\mathbf{z}}. \quad (2.31)$$

Though the integration of the surface density is conveniently expressed in terms of the  $\mathbf{z}$ - rather than in  $\mathbf{x}$ -coordinates, for balancing it is necessary to revert to a common framework. The following derivations serve to facilitate the surface density in terms of  $\mathbf{x}$ -coordinates.

If the point set  $\sigma = 0$ , defining the surface  $\Sigma$ , see Eq. (2.8a), can be solved for one coordinate of  $\mathbf{x}$ , say without loss of generality  $x_n$ , and if  $\Sigma$  is not perpendicular to the  $x_n$ -direction,  $\sigma = 0$  can be organized to assume the form

$$x_n^\Sigma = s(\mathbf{x}'), \quad (2.32)$$

where  $\mathbf{x}' = (x_1, \dots, x_{n-1})^T$  are the remaining coordinates, see Fig. 2.7. That is, the full state vector on the surface is given as a function of  $\mathbf{x}'$ :

$$\mathbf{x}(\mathbf{x}') = \begin{pmatrix} \mathbf{x}' \\ x_n^\Sigma(\mathbf{x}') \end{pmatrix} \in \Sigma. \quad (2.33)$$

Yet another number density function  $f_{\mathbf{x}'}^\Sigma(\mathbf{x}', t)$  can be defined such that

$$f_{\mathbf{z}}^\Sigma(\mathbf{z}, t) dV_{\mathbf{z}} = f_{\mathbf{x}'}^\Sigma(\mathbf{x}', t) dV_{\mathbf{x}'}. \quad (2.34)$$

If (at least locally) the  $\mathbf{z}$ -coordinates can be obtained uniquely from the  $\mathbf{x}'$  coordinates, i.e.

$$\mathbf{z} = \mathbf{z}(\mathbf{x}'), \quad (2.35)$$

the function  $f_{\mathbf{x}'}^\Sigma(\mathbf{x}', t)$  is obtained by

$$f_{\mathbf{x}'}^\Sigma(\mathbf{x}', t) = f_{\mathbf{z}}^\Sigma(\mathbf{z}(\mathbf{x}'), t) |J(\mathbf{z}, \mathbf{x}')|, \quad (2.36)$$

where

$$|J(\mathbf{z}, \mathbf{x}')| = \left| \det \left( \frac{dV_{\mathbf{z}}}{dV_{\mathbf{x}'}} \right) \right| = \left| \det \left( \frac{\partial(z_1, \dots, z_{n-1})}{\partial(x_1, \dots, x_{n-1})} \right) \right|, \quad (2.37)$$

is the Jacobian matrix determinant, e.g. Bronstein et al. (2001), which can be interpreted as the ratio between unit areas in the  $\mathbf{z}$ - and  $\mathbf{x}$ -framework. Of course, also the reverse operation to (2.35) may be of use:

$$\mathbf{x}' = \mathbf{x}'(\mathbf{z}), \quad (2.38)$$

which enables us to express a point  $\mathbf{x}$  on  $\Sigma$  as a function of  $\mathbf{z}$ , see Eq. (2.33):

$$\mathbf{x}(\mathbf{z}) = \begin{pmatrix} \mathbf{x}'(\mathbf{z}) \\ x_n^\Sigma(\mathbf{x}'(\mathbf{z})) \end{pmatrix} \in \Sigma. \quad (2.39)$$

The number of particles within  $\Sigma$  is obtained by integration over the whole  $\mathbf{x}'$ -space

$$N^\Sigma(t) = \int_{\Omega_{\mathbf{x}'}} f_{\mathbf{z}}^\Sigma(\mathbf{z}(\mathbf{x}'), t) |J(\mathbf{z}, \mathbf{x}')| dV_{\mathbf{x}'}, \quad (2.40)$$

or simply

$$N^\Sigma(t) = \int_{\Omega_{\mathbf{x}'}} f_{\mathbf{x}'}^\Sigma(\mathbf{x}', t) dV_{\mathbf{x}'}. \quad (2.41)$$

This result is not affected if  $f_{\mathbf{x}'}^\Sigma$  is multiplied previously by a Dirac delta function  $\delta(x_n - x_n^\Sigma) = \delta(x_n - s(\mathbf{x}'))$  that lifts the number density to the surface, and an integration over the  $x_n$ -coordinate is additionally taken out:

$$N^\Sigma(t) = \int_{x_n^{\min}}^{x_n^{\max}} \int_{\Omega_{\mathbf{x}'}} f_{\mathbf{x}'}^\Sigma(\mathbf{x}', t) \delta(x_n - s(\mathbf{x}')) dV_{\mathbf{x}'} dx_n. \quad (2.42)$$

The integration over  $\Omega_{\mathbf{x}'}$  and the full range of  $x_n$  corresponds to the integration over  $\Omega_{\mathbf{x}}$  which is:

$$N^{\Sigma}(t) = \int_{\Omega_{\mathbf{x}}} f_{\mathbf{x}'}^{\Sigma}(\mathbf{x}', t) \delta(x_n - s(\mathbf{x}')) dV_{\mathbf{x}}. \quad (2.43)$$

The total number of particles, see Eq. (2.29), can thus be calculated by volume integration over the whole domain  $\Omega_{\mathbf{x}}$ :

$$N(t) = \int_{\Omega_{\mathbf{x}}} f^{-}(\mathbf{x}, t) + f_{\mathbf{x}'}^{\Sigma}(\mathbf{x}', t) \delta(x_n - s(\mathbf{x}')) + f^{+}(\mathbf{x}, t) dV_{\mathbf{x}}. \quad (2.44)$$

Comparison to Eq. (2.27) gives rise to the formal definition:

$$f(\mathbf{x}, t) = f^{-}(\mathbf{x}, t) + f_{\mathbf{x}'}^{\Sigma}(\mathbf{x}', t) \delta(x_n - s(\mathbf{x}')) + f^{+}(\mathbf{x}, t). \quad (2.45)$$

Or in view of Eq. (2.36)

$$f(\mathbf{x}, t) = f^{-}(\mathbf{x}, t) + f_{\mathbf{z}}^{\Sigma}(\mathbf{z}(\mathbf{x}'), t) \delta(x_n - s(\mathbf{x}')) |J(\mathbf{z}, \mathbf{x}')| + f^{+}(\mathbf{x}, t). \quad (2.46)$$

That is, the surface population density expressed in  $\mathbf{x}$ -coordinates is obtained from the one in  $\mathbf{z}$ -coordinates by

$$f^{\Sigma}(\mathbf{x}, t) = f_{\mathbf{z}}^{\Sigma}(\mathbf{z}(\mathbf{x}'), t) \delta(x_n - s(\mathbf{x}')) |J(\mathbf{z}, \mathbf{x}')|. \quad (2.47)$$

**Summary** In this section, the number density function for the different parts of the state space has been introduced. The functions  $f^{-}$  and  $f^{+}$  quantifying the populations in the fully dimensional regions  $\Omega^{-}$  and  $\Omega^{+}$  are measured in terms of the number of particles per unit volume of the state space. The surface number density  $f^{\Sigma}$  is given by the number per unit area. Surface-intrinsic coordinates  $\mathbf{z}$  with one component less than the full state vector  $\mathbf{x}$  actually suffice as an argument for the surface density.  $\mathbf{z}$  may be obtained also from  $n - 1$  coordinates of  $\mathbf{x}$ , denoted by  $\mathbf{x}'$ . Using Dirac delta functions, it is possible to express surface number densities in terms of the full state vector  $\mathbf{x}$ . With these utilities in mind, the field of dynamical evolution of the number distributions is harvested.

## 2.6 Evolution of the Number Density Function

This section is concerned with the evolution equations for the population's number density functions introduced above. Following the structure of Sec. 2.4 where the evolution of single individuals has been dissected, the first section of this part introduces the balance equation for continuously evolving populations, see Sec. 2.6.1. In Sec. 2.6.2 the population balances for state spaces divided by a surface are discussed for the above introduced classes of transition, stable and unstable surfaces. For the more complex cases of jumping systems, the evolution of the number densities is exposed in Sec. 2.6.3.

Before the different cases are discussed in detail, major parts of the employed notation are presented as well as frequently used and case-independent mathematical relationships. The equations are derived using classical balancing over a fixed, arbitrary region  $R$  which is a subset of the whole state space  $\Omega$ , see Fig. 2.8 (left). Within

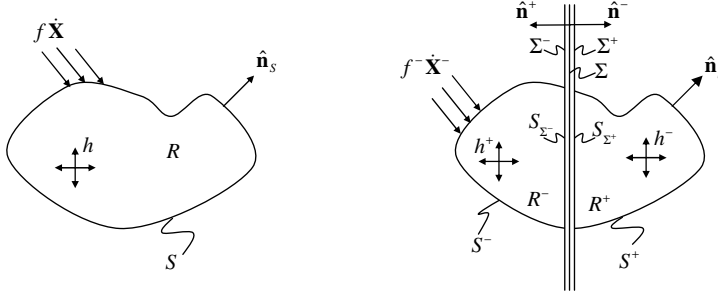


**Figure 2.8:** Balancing in state space for continuous evolution (left) and discontinuous evolution (right).

$R$ , overall  $N$  individuals reside. Integration of the number density function  $f(\mathbf{x}, t)$  over  $R$  gives this number:

$$N(t) = \int_R f(\mathbf{x}, t) dV_{\mathbf{x}}, \quad (2.48)$$

which is clearly a function of time, i.e. its time rate of change is

$$\frac{dN}{dt} = \frac{d}{dt} \int_R f(\mathbf{x}, t) dV_{\mathbf{x}}. \quad (2.49)$$

The integral on the right hand side can be reformulated using an extension of the classical transport theorem (Slattery, 1999) to arbitrary continuous state spaces (Ramkrishna, 2000) for stationary  $R$ :

$$\frac{dN}{dt} = \int_R \frac{\partial f}{\partial t}(\mathbf{x}, t) dV_{\mathbf{x}}. \quad (2.50)$$

In general, the number change within  $R$  is caused by the flux of particles across its boundary and by the production in the interior:

$$\frac{dN}{dt} = \dot{N}_{\text{Flux across boundary}} + \dot{N}_{\text{Production in } R}. \quad (2.51)$$

The number flux over the domain boundary  $S$  due to particle population movement with velocity  $\dot{\mathbf{X}}$  is:

$$(f\dot{\mathbf{X}}) \cdot (-\hat{n}_S). \quad (2.52)$$

where  $\hat{n}_S$  is the outer unit normal, see Fig. 2.8. Thus, the change of the number of particles due to in- and outflow to/from  $R$  is

$$\dot{N}_{\text{Flux across boundary}} = \int_S (f\dot{\mathbf{X}}) \cdot (-\hat{n}_S) dA_{\mathbf{x}}. \quad (2.53)$$

By the virtue of the Divergence Theorem, the surface integral can be reformulated to a volume integral:

$$\dot{N}_{\text{Flux across boundary}} = \int_R -\nabla_{\mathbf{x}} \cdot (f\dot{\mathbf{X}}) dV_{\mathbf{x}}. \quad (2.54)$$

The production density of individuals is denoted by  $h(\mathbf{x}, \mathbf{Y}, t)$  which contributes to the rate of change of  $N$  by

$$\dot{N}_{\text{Production in } R} = \int_R h(\mathbf{x}, \mathbf{Y}, t) dV_{\mathbf{x}}. \quad (2.55)$$

For a more general analysis, the argument of the production density must be expanded by the number density and – if existing – the number densities of other populations as well. Then it is feasible to model the impact of interactions between particles on the number density. This includes for instance aggregation and breakup of individuals. That is, particles located in one part of the state space can interact with remote particles, i.e., the evolution of the number density is not only governed by local operators (convective movement) but by global, integral operators, which possibly act on the full property state space, see for details Ramkrishna (2000); Randolph and Larsen (1988). For the remainder of this work, however, the effects are excluded. That is, the particle production density is only a function of the particle state, environmental conditions and possibly time. Then  $h$  can for instance represent the occurrence of new particles due to nucleation or feeding.

### 2.6.1 Population Balance Model for Continuous Flow

An arbitrary but contiguous region  $R$  in a state space  $\Omega$  that is not separated in the sense of Sec. 2.4 is balanced with regard to number conservation by

$$\frac{dN}{dt} = \dot{N}_{\text{Flux across } S} + \dot{N}_{\text{Production in } R}, \quad (2.56)$$

that is, in view of Eq.s (2.50), (2.54) and (2.55):

$$\int_R \frac{\partial}{\partial t} f(\mathbf{x}, t) dV_{\mathbf{x}} = \int_R -\nabla_{\mathbf{x}} \cdot (\dot{\mathbf{X}} f) dV_{\mathbf{x}} + \int_R h dV_{\mathbf{x}}. \quad (2.57)$$

Due to the arbitrariness of the choice of the region  $R$ , this equation must hold also locally:

$$\frac{\partial f}{\partial t} + \nabla_{\mathbf{x}} \cdot (\dot{\mathbf{X}} f) = h. \quad (2.58a)$$

The initial condition to this equation is denoted by  $f_0(\mathbf{x})$ . If the domain  $\Omega$  is open in some directions of the state space, it is formally separated into two parts. The closed boundary of  $\Omega$  is denoted by  $\partial\Omega$  with an outer unit normal  $\hat{\mathbf{b}}$ , whereas the open "boundary" is referred to by  $|\mathbf{x}| \rightarrow \infty$ . Across  $\partial\Omega$  particles flow with a flux density  $\dot{f}_{\text{in}}(\mathbf{x}, t)$ . For the open parts of  $\Omega$  it is pretended that the flux vanishes, the so called regularity condition Ramkrishna (2000). This is an adequate hypothesis for physical systems<sup>5</sup>. In summary, the Eq. (2.58a) must be solved subject to initial, boundary and regularity conditions

$$\text{I.C.: } f(\mathbf{x}, t = 0) = f_0(\mathbf{x}), \quad (2.58b)$$

$$\text{B.C.: } \hat{\mathbf{b}} \cdot \dot{\mathbf{X}} f = \dot{f}_{\text{in}}(\mathbf{x}, t), \quad \mathbf{x} \in \partial\Omega, \quad (2.58c)$$

$$\text{R.C.: } \dot{\mathbf{X}} f \rightarrow \mathbf{0}, \quad |\mathbf{x}| \rightarrow \infty, \quad (2.58d)$$

<sup>5</sup>For instance if the property is size, this assumption states that the particle cannot grow infinitely large.

see also Ramkrishna (2000).

## 2.6.2 Population Balance Model for Discontinuous Evolution

As in the preceding Sec. 2.4.2, let  $\Sigma$  be a surface of codimension 1, separating the  $n$ -dimensional domain  $\Omega$  into  $\Omega^-$  and  $\Omega^+$ , see Fig. 2.8 (right). The portion of  $R$  in  $\Omega^-$  is denoted by  $R^-$  and accordingly the portion within  $\Omega^+$  is  $R^+$ . If the region  $R$  is completely in either of the domains and its boundary does not share a part with the surface  $\Sigma$ , the population balances for the interior of  $\Omega^-$  and  $\Omega^+$  are directly derived from the continuous case, Eq. (2.58):

$$\frac{\partial f^-}{\partial t} + \nabla_{\mathbf{x}} \cdot (f^- \dot{\mathbf{X}}^-) = h^- \quad (2.59a)$$

$$\frac{\partial f^+}{\partial t} + \nabla_{\mathbf{x}} \cdot (f^+ \dot{\mathbf{X}}^+) = h^+, \quad (2.59b)$$

where  $h^-$  and  $h^+$  is the production density in  $\Omega^-$  and  $\Omega^+$ , respectively. The boundary and initial conditions are chosen with respect to the nature of the flow fields around  $\Sigma$  which is discussed case by case in the following. The transition, stable and unstable surfaces interacting with the number density of a population are discussed in Sec.s 2.6.2.1-2.6.2.3. From these equations the special cases of the one-sided transition, one-sided stable and one-sided unstable surface can be comprehended.

### 2.6.2.1 Population Case T ( $\rightarrow | \rightarrow$ ): Transition Surface

In Sec. 2.4.2.1 the single particle case for the transition surface has been discussed, see also Fig. 2.4 (b). The surface  $\Sigma$  in this configuration does not store particles. We consider the region  $R$ , which is separated by  $\Sigma$ . Let  $S_{\Sigma^-}$  be the portion of  $S^-$  that is shared with  $\Sigma^-$  and  $S_{\Sigma^+}$  the common surface of  $S^+$  and  $\Sigma^+$ , see Fig. 2.8 (right).  $S_{\Sigma}$  is the part of  $\Sigma$  between  $S_{\Sigma^-}$  and  $S_{\Sigma^+}$ . Since in  $\Sigma$  no particles reside, the flux across  $S_{\Sigma^-}$  must be balanced with the flux over  $S_{\Sigma^+}$  and the production within  $\Sigma$ , denoted by  $h^{\Sigma}$ :

$$\int_{S_{\Sigma^-}} (f^- \dot{\mathbf{X}}^-|_{\Sigma^-}) \cdot \mathbf{n}^- dA_{\mathbf{x}} + \int_{S_{\Sigma^+}} (f^+ \dot{\mathbf{X}}^+|_{\Sigma^+}) \cdot \mathbf{n}^+ dA_{\mathbf{x}} + \int_{S_{\Sigma}} h^{\Sigma} dA_{\mathbf{x}} = 0. \quad (2.60)$$

Because this relationship must hold for arbitrary  $S_{\Sigma}$  (and the respective surface sectors  $S_{\Sigma^-}$  and  $S_{\Sigma^+}$ ), it can be concluded that

$$(f^- \dot{\mathbf{X}}^-|_{\Sigma^-}) \cdot \mathbf{n}^- + (f^+ \dot{\mathbf{X}}^+|_{\Sigma^+}) \cdot \mathbf{n}^+ + h^{\Sigma} = 0 \quad \text{at } \mathbf{x} \in \Sigma. \quad (2.61)$$

This equation serves as the coupling boundary condition for the interior population balances (Eq. (2.59)) whose initial, remaining boundary and regularity conditions can be written similar to Eq.s (2.58) (b)-(d).

### 2.6.2.2 Population Case S ( $\rightarrow \uparrow \leftarrow$ ): Stable Surface

For the case of the stable surface (see the single particle case in Sec. 2.4.2.2), the populations in  $\Omega^-$  and  $\Omega^+$  move into  $\Sigma$  wherein they further exist and possibly con-

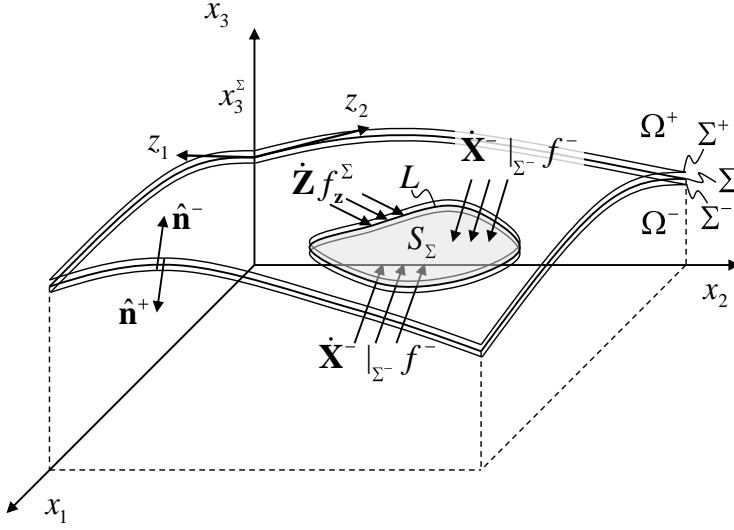


**Figure 2.9:** Control area  $S_\Sigma$  within the dividing surface.

tinue their evolution, see Fig. 2.4 (c). That is, particles in the control area  $S_\Sigma$  exist and their number is changed, as depicted in Fig. 2.9, due to (i) flux within the surface,  $\dot{N}_{\text{Flux across } L}^\Sigma$ , (ii) flux across  $S_{\Sigma^-}$  into  $S_\Sigma$  and over  $S_{\Sigma^+}$  into  $S_\Sigma$ , written as  $\dot{N}_{\text{Flux from } \Sigma^-}^\Sigma$  and  $\dot{N}_{\text{Flux from } \Sigma^+}^\Sigma$ , respectively, and (iii) production within  $\Sigma$ , denoted by  $\dot{N}_{\text{Production in } \Sigma}^\Sigma$ . That is overall:

$$\frac{dN^\Sigma}{dt} = \dot{N}_{\text{Flux across } L}^\Sigma + \dot{N}_{\text{Flux from } \Sigma^-}^\Sigma + \dot{N}_{\text{Flux from } \Sigma^+}^\Sigma + \dot{N}_{\text{Production in } \Sigma}^\Sigma. \quad (2.62)$$

In the following derivation the surface-intrinsic coordinates  $\mathbf{z}$  are used like during the introduction of the surface number density function, see Eq. (2.30). For the accumulation term we find upon differentiation of Eq. (2.31) with the help of the Transport Theorem for fixed regions:

$$\frac{dN^\Sigma}{dt} = \int_{S_\Sigma} \frac{\partial f_z^\Sigma}{\partial t}(\mathbf{z}, t) dV_z, \quad (2.63)$$

where  $f_z^\Sigma$  is used for the quantification of the surface number density. In this sense, the velocity within the surface,  $\dot{\mathbf{X}}^\Sigma$ , as used for the single particle case is transformed to a velocity vector  $\dot{\mathbf{Z}}$  with respect to the surface-intrinsic coordinates. Then the flux across the boundary  $L$  enclosing  $S_\Sigma$  within  $\Sigma$ , see Fig. 2.9, is obtained similar to Eq. (2.53):<sup>6</sup>

$$\dot{N}_{\text{Flux across } L}^\Sigma = \int_{S_\Sigma} -\nabla_z \cdot (\dot{\mathbf{Z}} f_z^\Sigma(\mathbf{z}, t)) dV_z. \quad (2.64)$$

The flux of the  $f^-$ -population across  $S_{\Sigma^-}$  into  $S_\Sigma$  is (see Fig. 2.9)

$$\dot{N}_{\text{Flux from } \Sigma^-}^\Sigma = \int_{S_{\Sigma^-}} (\dot{\mathbf{X}}^-|_{\Sigma^-} f^-(\mathbf{x}, t)) \cdot \hat{\mathbf{n}}^- dA_{\mathbf{x}}. \quad (2.65)$$

<sup>6</sup>Note that practical calculations with differential operators acting in curvilinear systems using indexed tensor notation involve the consideration of the curvature (Christoffel symbols).



Similarly, the flux over  $S_{\Sigma^+}$  into  $S_{\Sigma}$  is

$$\dot{N}_{\text{Flux from } \Sigma^+}^{\Sigma} = \int_{S_{\Sigma^+}} (\dot{\mathbf{X}}^+|_{\Sigma^+} f^+(\mathbf{x}, t)) \cdot \hat{\mathbf{n}}^+ dA_{\mathbf{x}}. \quad (2.66)$$

The production of individuals within  $S_{\Sigma}$  is obtained by integration of the surface production density over  $S_{\Sigma}$ :

$$\dot{N}_{\text{Production in } \Sigma}^{\Sigma} = \int_{S_{\Sigma}} h_{\mathbf{z}}^{\Sigma}(\mathbf{z}, t) dV_{\mathbf{z}}. \quad (2.67)$$

Inserting Eq.s (2.63), (2.64), (2.65), (2.66), (2.67) into Eq. (2.62) yields:

$$\begin{aligned} \int_{S_{\Sigma}} \frac{\partial f_{\mathbf{z}}^{\Sigma}}{\partial t}(\mathbf{z}, t) + \nabla_{\mathbf{z}} \cdot (\dot{\mathbf{Z}} f_{\mathbf{z}}^{\Sigma}(\mathbf{z}, t)) dV_{\mathbf{z}} &= \int_{S_{\Sigma^-}} (\dot{\mathbf{X}}^-|_{\Sigma^-} f^-(\mathbf{x}, t)) \cdot \hat{\mathbf{n}}^- dA_{\mathbf{x}} \\ &\dots + \int_{S_{\Sigma^+}} (\dot{\mathbf{X}}^+|_{\Sigma^+} f^+(\mathbf{x}, t)) \cdot \hat{\mathbf{n}}^+ dA_{\mathbf{x}} + \int_{S_{\Sigma}} h_{\mathbf{z}}^{\Sigma}(\mathbf{z}, t) dV_{\mathbf{z}}. \end{aligned} \quad (2.68)$$

By converting the first two integrals on the right-hand side to be taken over  $\Sigma$  using the transformation (2.39) we obtain

$$\begin{aligned} \int_{S_{\Sigma}} \frac{\partial f_{\mathbf{z}}^{\Sigma}}{\partial t}(\mathbf{z}, t) + \nabla_{\mathbf{z}} \cdot (\dot{\mathbf{Z}} f_{\mathbf{z}}^{\Sigma}(\mathbf{z}, t)) dV_{\mathbf{z}} &= \\ \dots \int_{S_{\Sigma}} (\dot{\mathbf{X}}^-(\mathbf{x}(\mathbf{z}))|_{\Sigma^-} f^-(\mathbf{x}(\mathbf{z}), t)) \cdot \hat{\mathbf{n}}^-(\mathbf{x}(\mathbf{z})) |J(\mathbf{x}', \mathbf{z})| \\ \dots + (\dot{\mathbf{X}}^+(\mathbf{x}(\mathbf{z}))|_{\Sigma^+} f^+(\mathbf{x}(\mathbf{z}), t)) \cdot \hat{\mathbf{n}}^+(\mathbf{x}(\mathbf{z})) |J(\mathbf{x}', \mathbf{z})| + h_{\mathbf{z}}^{\Sigma}(\mathbf{z}, t) dV_{\mathbf{z}}. \end{aligned} \quad (2.69)$$

Because this relationship must hold for arbitrary regions  $S_{\Sigma}$ , the integrand must fulfill the equation:

$$\begin{aligned} \frac{\partial f_{\mathbf{z}}^{\Sigma}}{\partial t}(\mathbf{z}, t) + \nabla_{\mathbf{z}} \cdot (\dot{\mathbf{Z}} f_{\mathbf{z}}^{\Sigma}(\mathbf{z}, t)) &= (\dot{\mathbf{X}}^-(\mathbf{x}(\mathbf{z}))|_{\Sigma^-} f^-(\mathbf{x}(\mathbf{z}), t)) \cdot \hat{\mathbf{n}}^-(\mathbf{x}(\mathbf{z})) |J(\mathbf{x}', \mathbf{z})| \\ &\dots + (\dot{\mathbf{X}}^+(\mathbf{x}(\mathbf{z}))|_{\Sigma^+} f^+(\mathbf{x}(\mathbf{z}), t)) \cdot \hat{\mathbf{n}}^+(\mathbf{x}(\mathbf{z})) |J(\mathbf{x}', \mathbf{z})| + h_{\mathbf{z}}^{\Sigma}(\mathbf{z}, t). \end{aligned} \quad (2.70)$$

This equation together with adequate boundary, initial and regularity conditions is directly coupled to the evolution equations for the density in the interior of  $\Omega^-$  and  $\Omega^+$ , see Eq.s (2.59).

### 2.6.2.3 Population Case U ( $\leftarrow \uparrow \rightarrow$ ): Unstable Surface

As in Sec. 2.4.2.3 we deal with a state space in which the velocity fields  $\dot{\mathbf{X}}^-$  and  $\dot{\mathbf{X}}^+$  point from  $\Sigma$  away, see Fig. 2.4 (d). Only particles that are already in  $\Sigma$  or produced directly therein make up the surface population. Following the explanations and notation for the stable surface in the previous section, the influx terms in Eq. (2.70) can be crossed out so that the population balance for the unstable surface immediately becomes:

$$\frac{\partial f_{\mathbf{z}}^{\Sigma}}{\partial t}(\mathbf{z}, t) + \nabla_{\mathbf{z}} \cdot (\dot{\mathbf{Z}} f_{\mathbf{z}}^{\Sigma}(\mathbf{z}, t)) = h_{\mathbf{z}}^{\Sigma}(\mathbf{z}, t). \quad (2.71)$$

This equation, equipped with proper boundary and initial conditions, must be solved simultaneously with the balances for  $f^-$  and  $f^+$ , Eq.s (2.59), however, it is not directly coupled to these functions.

### 2.6.2.4 Population Case $T_{os} (\leftarrow \times)$ : One-Sided Transition Surface

Let us revisit the case of a one-sided transition surface discussed for the single particle case in Sec. 2.4.2.4, see also Fig. 2.4 (e). The domain  $\Omega^+$  does not contain any particles, thus the number density  $f^+$  is not defined. Particles accommodated in  $\Sigma$  are instantaneously moved to the interior of the domain  $\Omega^-$ , thus the distribution density in  $\Sigma$  is zero except for  $t = 0$ :

$$f_z^\Sigma(\mathbf{z}, t) = \begin{cases} f_{z,0}^\Sigma(\mathbf{z}) & \text{for } t = 0 \\ 0 & \text{for } t > 0. \end{cases} \quad (2.72)$$

Within the domain  $\Omega^-$  the population balance is given by Eq. (2.58):

$$\frac{\partial f^-}{\partial t} + \nabla_{\mathbf{x}} \cdot (f^- \dot{\mathbf{X}}^-) = h^-. \quad (2.73)$$

At the  $\Sigma^-$  boundary of  $\Omega^-$ , the surface population is added to the  $f^-$  population instantaneously at  $t = 0$ . Thus, the initial condition for  $f^-$  consists of a part quantifying the population in the interior of  $\Omega^-$  as in Eq. (2.58c),  $f_0^-(\mathbf{x})$ , and the population transferred from  $\Sigma$ . Transformation of the  $f_z^\Sigma$  density to  $\mathbf{x}$ -coordinates using Eq. (2.47) yields the initial condition for the population balance for the domain  $\Omega^-$ :

$$f^-(\mathbf{x}, t = 0) = f_0^-(\mathbf{x}) + f_{z,0}^\Sigma(\mathbf{z}(\mathbf{x}')) \delta(x_n - s(\mathbf{x}')) |J(\mathbf{z}, \mathbf{x}')|. \quad (2.74)$$

It can be seen that for the case of  $f_0^-(\mathbf{x}) = 0$  and  $h^-(\mathbf{x}, t) = 0$  the population evolving in  $\Omega^-$  exists only on a surface of codimension 1 since the surface  $s(\mathbf{x}')$  in the dirac delta distribution, lifting  $f_{z,0}^\Sigma$  to the full  $\mathbf{x}$ -space, is moved with  $\dot{\mathbf{X}}^-$  according to Eq. (2.73).

In case that particles are being produced within the unstable surface at a production density  $h^\Sigma$ , the boundary condition to Eq. (2.73) must be augmented by balancing the production with the influx to  $\Omega^-$  following the derivation of Eq. (2.61):

$$(f^- \dot{\mathbf{X}}^-) \cdot \mathbf{n}^- + h^\Sigma = 0 \quad \text{at } \mathbf{x} \in \Sigma. \quad (2.75)$$

### 2.6.2.5 Population Case $S_{os} (\rightarrow \uparrow \times)$ : One-Sided Stable Surface

Recall the case of the one-sided stable surface for the single particle explained in Sec. 2.4.2.5. The population balance for  $f_z^\Sigma$  can be derived directly from the (two-sided) stable surface in Eq. (2.70) in Sec. 2.6.2.2, since only the feeding from the  $\Omega^+$ -side must be cleared:

$$\frac{\partial f_z^\Sigma}{\partial t}(\mathbf{z}, t) + \nabla_{\mathbf{z}} \cdot (\dot{\mathbf{Z}} f_z^\Sigma(\mathbf{z}, t)) = (\dot{\mathbf{X}}^-|_{\Sigma^-} f^-(\mathbf{x}, t)) \cdot \hat{\mathbf{n}}^- |J(\mathbf{x}', \mathbf{z})| + h_z^\Sigma(\mathbf{z}, t). \quad (2.76)$$

Due to unattainability of the domain  $\Omega^+$ , a number density function  $f^+$  is not defined. In  $\Omega^-$  the continuous case population balance applies, Eq. (2.59).

### 2.6.2.6 Population Case $U_{os} (\leftarrow \uparrow \times)$ : One-Sided Unstable Surface

In analogy to Sec. 2.4.2.6 for the single particle case we consider the surface on which a population can in principle exist and move but the flow field, existing in  $\Omega^-$  only, points from  $\Sigma$  away. The domain  $\Omega^+$  is assumed to be not accessible and thus the number density  $f^+$  is not defined. The dynamics of  $f^-$  is captured by the population balance (2.59), whereas the evolution in  $\Sigma$  is identical to the (two-sided) unstable surface, see Eq. (2.71):

$$\frac{\partial f_z^\Sigma}{\partial t}(\mathbf{z}, t) + \nabla_z \cdot (\dot{\mathbf{z}} f_z^\Sigma(\mathbf{z}, t)) = h_z^\Sigma(\mathbf{z}, t). \quad (2.77)$$

with the initial condition

$$f_z^\Sigma(\mathbf{z}, t = 0) = f_{z,0}^\Sigma(\mathbf{z}). \quad (2.78)$$

## 2.6.3 Population Balance Model for Jumping Systems

This section considers the population case for state spaces in which single particles can perform jumps as introduced in Sec.s 2.4.3.1-2.4.3.3, which are depicted in Fig.s 2.4 (h)-(j). Evolution equations for the population density involving jumps are structurally similar to the simple transition, stable and unstable cases considered above, except that jump functions of the type given in Eq. (2.23c) must be included. Like in the preceding parts, in the following Sec.s 2.6.3.1-2.6.3.3 the differential equations are derived for the transition jump, the jump into a stable surface and the jump from an unstable surface.

### 2.6.3.1 Population Case $T_j (\rightarrow | \rightarrow | \rightarrow)$ : Transition Jump

In setting up the population balance for transition jumps, see Fig. 2.4 (i), we follow the derivation of the population balance for the transition surface, Eq. (2.60), in Sec. 2.6.2.1. The integral flux into the surface  $\Sigma^-$  must be balanced with the flux feeding  $\Omega^+$  at  $\Sigma^+$ . Firstly, two fixed control surfaces  $S_{\Sigma^-}$  and  $S_{\Sigma^+}$  are defined, see Fig. 2.10, such that every transfer from the  $S_{\Sigma^-}$  is covered by the  $S_{\Sigma^+}$  region. Vice versa, all trajectories jumping into  $S_{\Sigma^+}$  originate in  $S_{\Sigma^-}$ . Upon number conservation, the amount of particles flowing into  $S_{\Sigma^-}$  emerge on  $S_{\Sigma^+}$  again:

$$\int_{S_{\Sigma^-}} (\dot{\mathbf{X}}^-(\mathbf{x}, \cdot) f^-(\mathbf{x}, t)) \cdot \mathbf{n}^-(\mathbf{x}) dA_{\mathbf{x}} = \int_{S_{\Sigma^+}} (\dot{\mathbf{X}}^+(\mathbf{x}, \cdot) f^+(\mathbf{x}, t)) \cdot \mathbf{n}^+(\mathbf{x}) dA_{\mathbf{x}}. \quad (2.79)$$

With the help of the jump function  $\mathbf{x}|_{\Sigma^+} = \xi^+(\mathbf{x}|_{\Sigma^-})$ , relating starting points of the jump on  $\Sigma^-$  to the end point on  $\Sigma^+$ , the integral on the r.h.s. can be taken over  $\Sigma^-$  instead of  $\Sigma^+$ :

$$\begin{aligned} \int_{S_{\Sigma^-}} (\dot{\mathbf{X}}^-(\mathbf{x}, \cdot) f^-(\mathbf{x}, t)) \cdot \mathbf{n}^-(\mathbf{x}) dA_{\mathbf{x}} = \\ \int_{S_{\Sigma^-}} (\dot{\mathbf{X}}^+(\xi^+(\mathbf{x}), \cdot) f^+(\xi^+(\mathbf{x}), t)) \cdot \mathbf{n}^+(\xi^+(\mathbf{x})) |J(\xi^+, \mathbf{x})| dA_{\mathbf{x}}, \end{aligned} \quad (2.80)$$

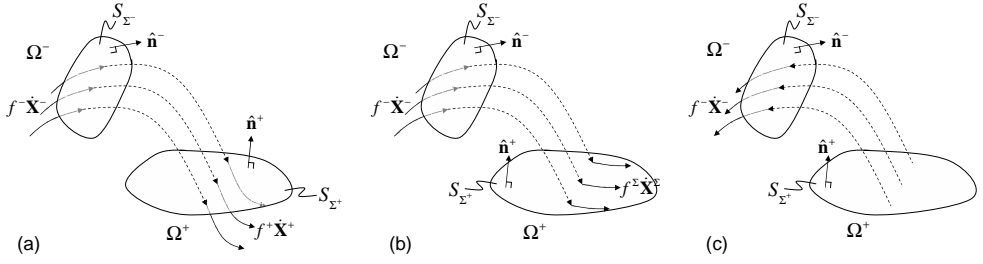


**Figure 2.10:** Population balance modeling for jumping systems: (a) transition jump, (b) jump in stable surface, (c) jump from unstable surface.

where  $J(\xi^+, \mathbf{x})$  is the Jacobian matrix determinant:

$$J(\xi^+, \mathbf{x}) = \det \left( \frac{\partial(\xi_1, \dots, \xi_n)}{\partial(x_1, \dots, x_n)} \right). \quad (2.81)$$

Due to the arbitrariness of the domain  $S_{\Sigma^-}$ , (2.80) must hold also locally:

$$\begin{aligned} (\dot{\mathbf{X}}^-(\mathbf{x}, \cdot) f^-(\mathbf{x}, t)) \cdot \hat{\mathbf{n}}^-(\mathbf{x}) = \\ (\dot{\mathbf{X}}^+(\xi^+(\mathbf{x}), \cdot) f^+(\xi^+(\mathbf{x}), t)) \cdot \hat{\mathbf{n}}^+(\xi^+(\mathbf{x})) |J(\xi^+, \mathbf{x})|, \quad \mathbf{x} \in \Sigma^-, \end{aligned} \quad (2.82)$$

which is the boundary condition for the population balances for the domains  $\Omega^-$  and  $\Omega^+$  which are given according to Eq.s (2.59) with the appropriate initial, boundary and regularity conditions.

### 2.6.3.2 Population Case $S_j (\rightarrow | \rightarrow \uparrow)$ : Jump in Stable Surface

The case of a population moving from  $\Omega^-$  into the boundary surface  $\Sigma^-$ , jumping into the surface  $\Sigma^+$  and continuing its evolution therein is depicted in Fig. 2.10 (b). Within  $\Omega^-$  the continuous population balance (2.59) can be applied. Within  $\Sigma^+$ , the integral version of the evolution equation for the one-sided stable surface, see Eq. (2.76), is taken as the prototype:

$$\int_{S_{\Sigma^+}} \frac{\partial f_{\mathbf{z}}^{\Sigma}}{\partial t}(\mathbf{z}, t) + \nabla_{\mathbf{z}} \cdot (\dot{\mathbf{z}} f_{\mathbf{z}}^{\Sigma}(\mathbf{z}, t)) dV_{\mathbf{z}} = \dot{N}_{\text{Flux from } \Sigma^-} + \int_{S_{\Sigma^+}} h_{\mathbf{z}}^{\Sigma}(\mathbf{z}, t) dV_{\mathbf{z}}. \quad (2.83)$$

The number of particles crossing the fixed control surface  $S_{\Sigma^-}$  per unit time is

$$\dot{N}_{\text{Flux from } \Sigma^-} = \int_{S_{\Sigma^-}} (\dot{\mathbf{X}} f^-(\mathbf{x}, t)) \cdot \hat{\mathbf{n}}^- dA_{\mathbf{x}}. \quad (2.84)$$

Instead of integrating over the  $\Sigma^-$  surface, a change of coordinates using the inverse of the jump function, see Eq. (2.24c),

$$\mathbf{x}|_{\Sigma^-} = \xi^-(\mathbf{x}|_{\Sigma^+}) = (\xi^+)^{-1}(\mathbf{x}|_{\Sigma^+}), \quad (2.85)$$

allows to calculate the flux by integration over  $\Sigma^+$  :

$$\dot{N}_{\text{Flux from } \Sigma^-} = \int_{S_{\Sigma^+}} (\dot{\mathbf{X}} f^-(\xi^-(\mathbf{x}), t)) \cdot \hat{\mathbf{n}}^-(\xi^{-1}(\mathbf{x})) |J(\xi^-, \mathbf{x})| dA_{\mathbf{x}}. \quad (2.86)$$

The point  $\mathbf{x}$  on  $\Sigma^+$  must now be expressed in terms of the  $\mathbf{z}$ -coordinate system for which it is partitioned into two parts:  $\mathbf{x}'(\mathbf{z})$  and  $x_n(\mathbf{x}'(\mathbf{z}))$ , see Eq. (2.39). Hence, switching to  $\mathbf{z}$  as the integration variable, Eq. (2.86) becomes

$$\dot{N}_{\text{Flux from } \Sigma^-} = \int_{S_{\Sigma^+}} (\dot{\mathbf{X}} f^-(\xi^-(\mathbf{x}(\mathbf{z})), t)) \cdot \hat{\mathbf{n}}^-(\xi^-(\mathbf{x}(\mathbf{z}))) |J(\xi^-, \mathbf{x}(\mathbf{z}))| |J(\mathbf{x}', \mathbf{z})| dV_{\mathbf{z}}. \quad (2.87)$$

Eq. (2.83) can be written fully under an  $S_{\Sigma^+}$  integral

$$\begin{aligned} \int_{S_{\Sigma^+}} \frac{\partial f_{\mathbf{z}}^{\Sigma}}{\partial t}(\mathbf{z}, t) + \nabla_{\mathbf{z}} \cdot (\dot{\mathbf{Z}} f_{\mathbf{z}}^{\Sigma}(\mathbf{z}, t)) dV_{\mathbf{z}} = \\ \dots + \int_{S_{\Sigma^+}} (\dot{\mathbf{X}} f^-(\xi^-(\mathbf{x}(\mathbf{z})), t)) \cdot \hat{\mathbf{n}}^-(\xi^-(\mathbf{x}(\mathbf{z}))) |J(\xi^-, \mathbf{x}(\mathbf{z}))| |J(\mathbf{x}', \mathbf{z})| + h_{\mathbf{z}}^{\Sigma}(\mathbf{z}, t) dV_{\mathbf{z}}. \end{aligned} \quad (2.88)$$

Since this equation must hold for arbitrary domains  $\Sigma$ , the integrand itself must fulfill this relationship as well:

$$\begin{aligned} \frac{\partial f_{\mathbf{z}}^{\Sigma}}{\partial t}(\mathbf{z}, t) + \nabla_{\mathbf{z}} \cdot (\dot{\mathbf{Z}} f_{\mathbf{z}}^{\Sigma}(\mathbf{z}, t)) = \\ \dots + (\dot{\mathbf{X}} f^-(\xi^-(\mathbf{x}(\mathbf{z})), t)) \cdot \hat{\mathbf{n}}^-(\xi^-(\mathbf{x}(\mathbf{z}))) |J(\xi^-, \mathbf{x}(\mathbf{z}))| |J(\mathbf{x}', \mathbf{z})| + h_{\mathbf{z}}^{\Sigma}(\mathbf{z}, t), \end{aligned} \quad (2.89)$$

which is the surface population balance for the case that the surface is fed by particles jumping into it.

### 2.6.3.3 Population Case $U_j$ ( $\leftarrow$ | $\leftarrow$ |): Jump from Unstable Surface

The jump from an unstable surface is sketched in Figs 2.4 (j) and 2.10 (c). If a population exists on the unstable surface  $\Sigma^+$  only at  $t = 0$ , i.e., no particles are being produced within  $\Sigma^+$ , this initial population must be transferred to  $\Sigma^-$  via the initial condition to the population balance for  $\Omega^-$ , given by Eq. (2.59). Similar to the one-sided transition surface, let the population density on  $\Sigma^+$  be given in a surface intrinsic coordinate system  $\mathbf{z}$ , denoted by  $f_{\mathbf{z},0}^{\Sigma^+}$ . Transformation to  $\mathbf{x}$ -coordinates and lifting this number density to the fully-dimensional  $\mathbf{x}$ -space yields

$$f_0^{\Sigma^+}(\mathbf{x}) = f_{\mathbf{z},0}^{\Sigma}(\mathbf{z}(\mathbf{x}')) \delta(x_n - s(\mathbf{x}')) |J(\mathbf{z}, \mathbf{x}')|, \quad (2.90)$$

see also Eq. (2.47). Using the jump function, see Eq. (2.25b),  $f_0^{\Sigma^+}(\mathbf{x})$  is shifted from  $\Sigma^+$  to  $\Sigma^-$ :

$$f_0^{\Sigma^-}(\mathbf{x}|\Sigma^-) = f_0^{\Sigma^+}(\mathbf{x}|\Sigma^+) |J(\xi^-, \mathbf{x})|. \quad (2.91)$$

As such it can be incorporated to the initial condition of Eq. (2.59), quantifying the density evolution in  $\Omega^-$ :

$$f^-(\mathbf{x}, t = 0) = f_0^-(\mathbf{x}) + f_0^{\Sigma^-}(\mathbf{x}). \quad (2.92)$$

If the production rate in  $\Sigma^+$  does not vanish, there is a flux from  $\Sigma^+$  into  $\Omega^-$  across  $\Sigma^-$ . In case that the production density is given in surface coordinates  $\mathbf{z}$ , the number of particles produced in the fixed control area  $S_{\Sigma^+}$  is given by

$$\dot{N}_{\text{Production Flux from } \Sigma^+} = \int_{S_{\Sigma^+}} h_{\mathbf{z}}^{\Sigma}(\mathbf{z}, t) dV_{\mathbf{z}}, \quad (2.93)$$

see also Fig. 2.10 (c). Switching to  $\mathbf{x}$ -coordinates yields

$$\dot{N}_{\text{Production Flux from } \Sigma^+} = \int_{S_{\Sigma^+}} h_{\mathbf{z}}^{\Sigma}(\mathbf{z}(\mathbf{x}'), t) |J(\mathbf{z}, \mathbf{x}')| dA_{\mathbf{x}}. \quad (2.94)$$

Replacing the integration domain to the opposite domain  $S_{\Sigma^-}$  using the inverse of the jump function, we obtain

$$\dot{N}_{\text{Production Flux from } \Sigma^+} = \int_{S_{\Sigma^-}} h_{\mathbf{z}}^{\Sigma}(\mathbf{z}(\mathbf{x}'), t) |J(\mathbf{z}, \mathbf{x}')| |J(\mathbf{x}, \xi^-)| dA_{\mathbf{x}}. \quad (2.95)$$

Equating this with the flux of the  $f^-$ -population across  $S_{\Sigma^-}$ , yields

$$\int_{S_{\Sigma^-}} (\dot{\mathbf{x}} f^-) \cdot (-\hat{\mathbf{n}}^-) dA_{\mathbf{x}} = \int_{S_{\Sigma^-}} h_{\mathbf{z}}^{\Sigma}(\mathbf{z}(\mathbf{x}'), t) |J(\mathbf{z}, \mathbf{x}')| |J(\mathbf{x}, \xi^-)| dA_{\mathbf{x}}, \quad (2.96)$$

which must hold for arbitrary choices of  $S_{\Sigma^-}$ , i.e.,

$$(\dot{\mathbf{x}} f^-) \cdot (-\hat{\mathbf{n}}^-) = h_{\mathbf{z}}^{\Sigma}(\mathbf{z}(\mathbf{x}'), t) |J(\mathbf{z}, \mathbf{x}')| |J(\mathbf{x}, \xi^-)|, \quad (2.97)$$

which is incorporated as the boundary condition for the population balance of  $f^-$ .

## 2.7 Summary

In this chapter, the differential equations for developing individuals and populations have been discussed with the special focus on the systematization of evolution equations that involve not only continuous development but also discrete events (hybrid systems). For this, the state space has been divided into three parts: two fully dimensional domains  $\Omega^-$  and  $\Omega^+$  and a surface  $\Sigma$  separating the former two. In principle, three different cases were introduced: (a)  $\Sigma$  acting as a transition surface, i.e., trajectories immediately pass through it, (b)  $\Sigma$  attracting trajectories from its environment, thus called a stable surface and (c)  $\Sigma$  pushing trajectories away. Either case can be clearly identified by comparing the direction of the velocity fields in the respective domain with the orientation of the dividing surface. The differential equations for such systems typically exhibit switches on the right hand side. A further generalization allows the separation of the domain boundaries of  $\Omega^-$  and  $\Omega^+$  between which trajectories can jump. From the evolution equation of a single entity and using classical balancing, general population balances have been derived that are capable of capturing the number density evolution of systems consisting of particles with switching right hand side and the ability to jump in state space. These generic equations shall serve in Ch. 4 to set up rigorous models for populations of faceted crystals. However, following the structure of this chapter, at first the evolution of single faceted crystals is analyzed in the next chapter.

*It is only safe to start detailed computations when the form of the solution is understood. To do otherwise is to invite an expensive output of meaningless numbers and to sacrifice one's birthright of rationality for a mess of digits.*

---

Rutherford Aris  
*Elementary Chemical Reactor Analysis*  
What is Chemical Reactor Analysis?

## Chapter 3

# Single Crystal Shape Evolution Model and State Space Analysis

General equations on the evolution of individuals have been presented in the preceding chapter. The concrete topic that is addressed in this thesis is crystal shape evolution. In this chapter we embark on an analysis of the geometric model of a polyhedral convex crystal. The state space of the crystal is divided into regions, so called morphology cones, in which different morphologies exist (Sec. 3.1). This analysis allows an elegant formulation and fast computation of the crystal shape trajectory (Sec. 3.2). The recognition of morphological regions makes it easy to compute crystal properties like volume and surface area directly from the state vector, i.e., by avoiding the computation of the crystal shape (Sec. 3.3). In Sec. 3.4, a more complex crystal system than the one developed in parallel in the previous sections is given. Finally, in Sec. 3.5 the chapter is concluded in brief.

### 3.1 Shape Model

The shape of a polyhedral convex crystal is given by

$$\mathcal{S} = \{\mathbf{r} : \mathbf{N} \mathbf{r} \leq \mathbf{h}\} , \quad (3.1)$$

where  $\mathbf{r}$  is a 3D vector of space coordinates, and

$$\mathbf{N} = \begin{bmatrix} \mathbf{n}_1^T \\ \vdots \\ \mathbf{n}_n^T \end{bmatrix} \in \mathbb{R}^{n \times 3} \quad (3.2)$$

is a matrix with the unit normals of the  $n$  faces on its rows. Throughout the paper skew intrinsic crystal coordinate systems with different unit vector's lengths are not used. Instead, all orientation vectors are transformed to a right-handed Cartesian coordinate system beforehand. The unit normals  $\mathbf{n}_i$  can be calculated from the Miller

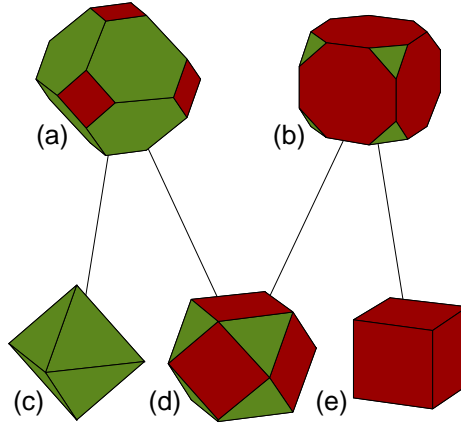


**Figure 3.1:** Morphologies of a symmetric cubic crystal with two different forms. The distance of the cubic  $\{100\}$  and octahedral  $\{111\}$  faces is  $h_1$  and  $h_2$ , respectively. For example, in pure water, NaCl crystals grow as cubes (e) but if urea or formamide is added,  $\{111\}$  faces are stabilized and shapes as shown in (a)-(d) can appear, see e.g. Radenovic et al. (2003).

indices of the crystal system, e.g. Schwarzenbach (2001); Zhang et al. (2006). The vector

$$\mathbf{h} = \begin{pmatrix} h_1 \\ \vdots \\ h_n \end{pmatrix} \in \mathbb{R}_+^{n \times 1} \quad (3.3)$$

contains the distances of the faces to a reference point which is without loss of generality assumed to lie within the crystal, i.e.  $h_j > 0$ .  $\mathbf{h}$  is called the *geometrical crystal state* since it is subject to variations due to growth, whereas the orientation of a face is fixed. The space in which the geometrical state exists is referred to as  $\mathbf{h}$ -space or simply state space. By varying the geometrical state, qualitatively different shapes can be generated. An example for a symmetric crystal with the distance of the cube and octahedral forms denoted by  $h_1$  and  $h_2$ , respectively, is given in Fig. 3.1. Particularly, special shapes can be obtained from which some faces have disappeared, i.e., Eq. (3.1) contains in this case redundant conditions. It is a central concern of this paper to deduce regions in  $\mathbf{h}$ -space in which qualitatively different shapes occur. As an example without detailed explanations given at this stage, take a look at Fig. 3.4 in which different crystal shapes are depicted obtained from various points in state space. Within the region  $\mathcal{M}_1$  for instance all shapes assume the form of the truncated octahedron, whereas this type of shape is not found in other parts of the  $\mathbf{h}$ -space. In the remainder we aim at partitioning arbitrary crystal shape space in such a way.

For the analysis below, often only subsets of the whole set of unit normal vectors and distances are needed. For example, if only the unit normals and distances of the faces  $i$ ,  $j$ , and  $k$  must be considered, the following notation is used:

$$\mathbf{N}_{ijk} = \begin{bmatrix} \mathbf{n}_i^T \\ \mathbf{n}_j^T \\ \mathbf{n}_k^T \end{bmatrix}, \quad \mathbf{h}_{ijk} = \begin{pmatrix} h_i \\ h_j \\ h_k \end{pmatrix}. \quad (3.4)$$



The equations which are given in this paper apply to arbitrary, in general unsymmetrical, convex polyhedra. But crystals usually exhibit a certain degree of symmetry which should also be exploited for a model formulation. In order to keep the following discussion as general as possible, the considerations given below are taken out without the notion of any symmetry. Resulting equations can be simplified for the symmetric case later as presented in Sec. 3.1.5.

The remainder of this section is organized as follows. At first, faces, edges and vertices of crystal shapes are introduced, see Sec. 3.1.1. Then in Sec. 3.1.2 the term crystal morphology is casted in a quantitative definition. Subsequently, the existence domain of a morphology in  $\mathbf{h}$ -space (a cone) is derived, see Sec. 3.1.3. In Sec. 3.1.4 the systematic search for all possible morphologies which can be obtained from a given set of crystal faces is described. Then, it is shown how to account for symmetry (Sec. 3.1.5) and the steps for the computation of morphological domains are summarized in Sec. 3.1.6. In Sec. 3.1.7 an example is discussed which can also be comprehended by pencil-and-paper geometry.

### 3.1.1 Elements of Convex Crystals

The convex hull of the 3D shape as defined by Eq. (3.1) comprises of faces, edges and vertices:

$$\mathcal{F}_i = \mathcal{S} \cap \{\mathbf{r} : \mathbf{n}_i \cdot \mathbf{r} = h_i\} \quad (3.5a)$$

$$\mathcal{E}_{ij} = \mathcal{S} \cap \{\mathbf{r} : \mathbf{N}_{ij}\mathbf{r} = \mathbf{h}_{ij}\} \quad (3.5b)$$

$$\mathcal{V}_{ijk} = \mathcal{S} \cap \{\mathbf{r} : \mathbf{N}_{ijk}\mathbf{r} = \mathbf{h}_{ijk}\} . \quad (3.5c)$$

Though the shape is defined by the geometrical state vector, only after computing these elements it becomes clear how the actual shape looks like, e.g. the area of faces and edges and their ratios. For example, it can happen that some inequality conditions in Eq. (3.1) are redundant. This means also that such a condition induces no face on  $\mathcal{S}$ . Faces which are in principle included in  $\mathbf{N}$  and  $\mathbf{h}$  but do not appear on the crystal surface are referred to as *virtual faces*. On the other hand, *real faces* do appear on the crystal surface (Zhang et al., 2006; Gadewar and Doherty, 2004; Johnsen, 1910).

The quantification of the crystal shape using linear inequalities, Eq. (3.1), is called halfspace ( $\mathcal{H}$ -) representation in polytope theory (Ziegler, 2006). Alternatively, the shape is also known when the coordinates of all vertices are known, because the polyhedron can be interpreted as the set of all possible convex combinations of the vertices. This is referred to by  $\mathcal{V}$ -representation (Ziegler, 2006). Even though, only the  $\mathcal{V}$ -representation allows a detailed analysis of the actual shape, there is no direct mapping known between  $\mathcal{H}$  and  $\mathcal{V}$ -representations, i.e., the shape must be calculated exhaustively, for instance by checking whether triplets of faces, e.g.  $ijk$ , meet at a vertex. The coordinates of a vertex follow directly from the definition in Eq. (3.5c):

$$\mathbf{v}_{ijk} = \mathbf{N}_{ijk}^{-1} \mathbf{h}_{ijk} , \quad (3.6)$$

which makes clear that a vertex can only be formed by three faces whose orientations are independent, i.e.,  $\det \mathbf{N}_{ijk} \neq 0$ . The intersection point of the planes  $i$ ,  $j$  and  $k$  constitutes a vertex on the crystal surface if the constraints in Eq. (3.1) can be met. In

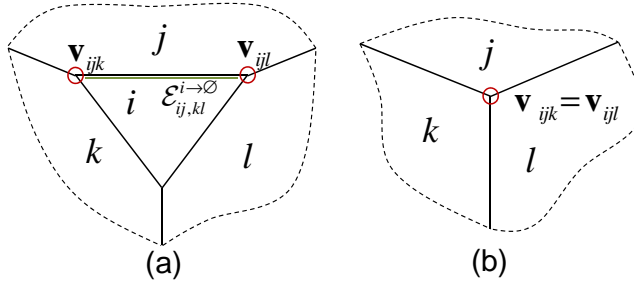


**Figure 3.2:** The edge  $\mathcal{E}_{ij,kl}^{i \rightarrow \emptyset}$  is defined by four faces where the unit normal of the face  $i$  is enclosed by the unit normals of the other faces, i.e., lies in the positive linear span (a). If the distance of the face  $i$  is increased so that the edge disappears, the face  $i$  disappears as well (b).

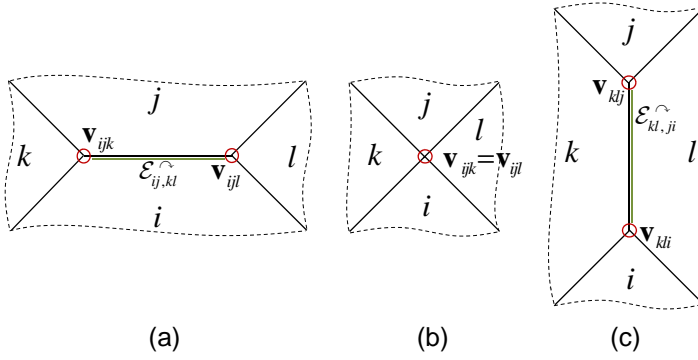


**Figure 3.3:** The edge  $\mathcal{E}_{ij,kl}^{\curvearrowright}$  is defined by four faces of which no unit normal lies in the positive linear span of the other three unit normal vectors. If the distance of one face, for example  $i$ , is varied such that the edge disappears, a four-compound vertex is formed on the crystal surface. If it is displaced even further, a new edge, denoted by  $\mathcal{E}_{kl,ji}^{\curvearrowright}$ , appears on the crystal surface.

computational geometry this problem is known as the vertex enumeration problem (Bremner et al., 1998; Ziegler, 2006). Of course, more than three faces can meet at a vertex. In Zhang et al. (2006) these vertices are called compound vertices, i.e., if  $n$  faces form a vertex, it is an  $n$ -compound vertex. Vertices made up by three faces are called simple vertices. Even though compound vertices appear quite often on (ideal) crystal shapes, a special treatment is not required for the following analysis because compound vertices can be seen as combined simple vertices. Only the additional treatment of the occurrence conditions of 4-compound vertices is essential because – as will be shown hereafter – 4-compound vertices constitute the generic geometric configuration for morphology changes.

Two vertices are said to be connected if their connecting line is an edge on the crystal surface. The edge is labeled using the index of the two faces which meet at the edge, e.g.  $\mathcal{E}_{ij}$ , see Eq. (3.5b). However, this point set is bounded by at least two more faces (indices  $k$  and  $l$ ) which detain the intersection line between  $i$  and  $j$  to be a finite line, see Figs. 3.2 and 3.3. This means, an edge is in the simplest case defined by four faces which form two simple connected vertices. Again, the primal setting with four

faces is sufficient to dissect, since edges at which more than four faces are involved can be seen as a combination of simple edges which are geometrically identical but combinatorially (i.e. which set of faces constitutes the simple edge) different. Therefore, it makes sense to introduce an alternative to the notation in Eq. (3.5b) disclosing the involvement of the four faces establishing a simple edge:

$$\mathcal{E}_{ij,kl} = \{ \mathbf{r} : \mathbf{v}_{ijk} + \alpha (\mathbf{v}_{ijl} - \mathbf{v}_{ijk}), 0 \leq \alpha \leq 1 \} . \quad (3.7)$$

The comma-separation between the index pairs  $ij$  and  $kl$  is used to clarify that the faces  $i$  and  $j$  intersect and faces  $k$  and  $l$  terminate the intersection line to become an edge. The two qualitatively different situations of faces defining an edge are sketched in Figs 3.2 and 3.3. In one case, the disappearance of an edge is followed by the occurrence of another edge like the transition from (a) to (c) in Fig. 3.3. In the other case, the disappearance of an edge goes along with the disappearance of a face and no new edge is formed, see Fig. 3.2. The two different situations are generic and can be distinguished by analyzing the orientation of the unit normals of the faces which are involved. The transition to a configuration with a new edge (Fig. 3.3) can only occur if  $\mathbf{n}_i$  does not lie in the positive linear span of the vectors  $\mathbf{n}_j$ ,  $\mathbf{n}_k$  and  $\mathbf{n}_l$ . On the other hand, the shift to a configuration lacking the face  $i$  requires that  $\mathbf{n}_i$  is within the positive linear span of  $\mathbf{n}_j$ ,  $\mathbf{n}_k$  and  $\mathbf{n}_l$ . That means,  $\mathbf{n}_i$  is a linear combination of  $\mathbf{n}_j$ ,  $\mathbf{n}_k$  and  $\mathbf{n}_l$ , where the combination coefficients, denoted by  $w_{ij}$ ,  $w_{ik}$  and  $w_{il}$ , are all positive:

$$\mathbf{n}_i = w_{ij}\mathbf{n}_j + w_{ik}\mathbf{n}_k + w_{il}\mathbf{n}_l . \quad (3.8)$$

Combining the weights to a vector  $\mathbf{w}_{ij,kl}^T = (w_{ij}, w_{ik}, w_{il})$ , they can be easily calculated in order to distinguish both situations:

$$\mathbf{w}_{ij,kl} = [\mathbf{n}_j \ \mathbf{n}_k \ \mathbf{n}_l]^{-1} \mathbf{n}_i . \quad (3.9)$$

An edge whose disappearance goes along with the disappearance of the  $i$ th face is denoted by  $\mathcal{E}_{ij,kl}^{i \rightarrow \emptyset}$ , whereas edges whose disappearance is followed by the appearance of another edge are denoted by  $\mathcal{E}_{ij,kl}^{\curvearrowright}$ . For  $\mathcal{E}_{ij,kl}^{i \rightarrow \emptyset}$  all coefficients in  $\mathbf{w}_{ij,kl}$  are positive (positive linear span) whereas for  $\mathcal{E}_{ij,kl}^{\curvearrowright}$  the coefficients have mixed signs:

$$\mathcal{E}_{ij,kl}^{i \rightarrow \emptyset} \rightarrow \mathbf{w}_{ij,kl} \geq \mathbf{0} \quad (3.10a)$$

$$\mathcal{E}_{ij,kl}^{\curvearrowright} \rightarrow \mathbf{w}_{ij,kl} \not\geq \mathbf{0} \quad (3.10b)$$

A similar index notation could be introduced for faces since the definition of the point set  $\mathcal{F}_i$  is bounded by other faces as well (at least three). However, this is not required for the remainder of this paper.

### 3.1.2 Morphological Features

For convex crystals, the number of faces and edges and their combinatorial arrangement is a palpable feature to distinguish morphologies. That is, the knowledge of faces and edges present on the surface enables for the identification of the morphology; we follow in this Borchardt-Ott (2009):

**Morphology** is the external boundary of a crystal comprising of faces and edges.

In Fig. 3.1 different crystal morphologies are shown which are produced with the same set of faces but different state vectors. Our goal is to determine the domain in  $\mathbf{h}$ -space in which a certain morphology exists. Types of crystal morphologies are described below:

**Complete Morphology (C-Morphology)** refers to crystal shapes comprising of all  $n$  real faces. Examples of two C-morphologies are in Fig. 3.1 (a) and (b).

**Submorphology (S-Morphology)** means crystal shapes with less than  $n$  real faces, i.e., some are virtual. Examples are the crystals shown in Fig. 3.1 (c) and (e) which are S-morphologies of the crystals depicted in (a) and (b), respectively. The crystal shown in Fig. 3.1 (d) is not an S-morphology because all faces can be found on the crystal surface and the shape is rather special since  $h_1$  and  $h_2$  must be chosen exactly in a way so that two cubic and two octahedral faces meet in one vertex.

**Transition Morphology (T-Morphology)** refers to crystal shapes which connect different morphologies or submorphologies with the same set of real faces. Their state vectors are chosen so that compound vertices on the crystal surface appear which clear edges from the crystal surface but no faces. An example is depicted in Fig. 3.1 (d).

Clearly, the differentiation whether a morphology is termed C- or S-morphology depends on the choice of the  $n$  faces which have been included in the analysis. A morphology recognized to be an S-morphology is in a different context a C-morphology if only a subset of faces is included into the analysis. For example, the C-morphologies shown in Fig. 3.1 are S-morphologies if yet another face is considered in the analysis as for example depicted in Fig. 3.7. T-morphologies, as will be shown later, are classified as such regardless of the maximum number of faces.

From the definition above it follows that morphology boundaries in the  $\mathbf{h}$ -space must be located where faces and edges appear or disappear. We restrict ourselves for the following analysis (until Sec. 3.1.3) to identify disappearance from C-morphologies since the knowledge of their existence domain unfolds the existence domain of associated S- and T-morphologies. The detection of T-morphologies also discloses the boundaries to other domains of C- or S-morphologies. Without having an a priori knowledge of how many morphologies can be generated from a given set of faces we also aim at determining the morphological variations which can occur.

The disappearance of a face is accompanied by the disappearance of edges (Prywer, 1996, 2002). Hence, it is sufficient to study the disappearance of edges. Before we analyze this in more detail, we cast the term C-morphology in a more formal definition: The index set  $E_\lambda$  contains all quads of faces, e.g.  $ij, kl$ , which form an edge on a given shape of the  $\lambda$ th C-morphology. Every C-morphology of the overall  $m$  possible C-morphologies has a different index set  $E_\lambda$ .

Practically, the index set  $E_\lambda$  is obtained from calculating a representative shape of the morphology. This can for instance be done by checking the set of faces involved in the formation of a pair of vertices, for instance  $\mathbf{v}_{ijk}$  and  $\mathbf{v}_{nml}$ . In general, this means a set of six faces  $\{i, j, k, l, m, n\}$ . If two elements of this set occur twice, for instance

$i = n$  and  $j = m$  and if the distance between  $\mathbf{v}_{ijk}$  and  $\mathbf{v}_{nml} = \mathbf{v}_{ijl}$  is greater than zero, the two vertices are connected by an edge  $\mathcal{E}_{ij,kl}$ . By exhaustively running through all pairs of vertices, the full set of edges  $E_\lambda$  can be determined:

$$E_\lambda = \{ij, kl : |\mathbf{v}_{ijk} - \mathbf{v}_{ijl}| > 0\}. \quad (3.11)$$

For reasons which become clear below, the set of edges is split into a subset of edges whose disappearance is accompanied by the disappearance of faces,  $E_\lambda^\emptyset$ , and a subset of edges whose disappearance is followed by the occurrence of a compound vertex or thereafter another edge,  $E_\lambda^\curvearrowright$ . See also the discussion at the end of Sec. 3.1.1.

An edge is bound by two vertices which are each made up of three faces  $ijk$  and  $ijl$ , see Fig.s 3.2 and 3.3. It is assumed for the following analysis that the vectors  $\mathbf{n}_i$ ,  $\mathbf{n}_j$  and  $\mathbf{n}_k$  constitute a right-handed system, i.e.,  $\det \mathbf{N}_{ijk} > 0$ , and correspondingly  $\mathbf{n}_i$ ,  $\mathbf{n}_j$  and  $\mathbf{n}_l$  establish a left-handed system, i.e.,  $\det \mathbf{N}_{ijl} < 0$ . The coordinates of the vertices are

$$\mathbf{v}_{ijk} = \mathbf{N}_{ijk}^{-1} \mathbf{h}_{ijk} \quad (3.12a)$$

$$\mathbf{v}_{ijl} = \mathbf{N}_{ijl}^{-1} \mathbf{h}_{ijl}. \quad (3.12b)$$

If the distances  $h_i$ ,  $h_j$ ,  $h_k$  and  $h_l$  are varied such that both vertices merge to a single vertex (the coordinates coincide) the following equation must be fulfilled:

$$\mathbf{N}_{ijk}^{-1} \mathbf{h}_{ijk} = \mathbf{N}_{ijl}^{-1} \mathbf{h}_{ijl}. \quad (3.13)$$

In Fig.s 3.2 and 3.3 this means a transition from (a) to (b) which both are structural changes of the shape, that is, a morphological change. A closer look at Eq. (3.13) reveals that they are linearly dependent, i.e., one scalar equation suffices to describe the condition give above:

$$\beta_{ij,kl} \cdot \mathbf{h}_{ijkl} = 0, \quad (3.14)$$

where

$$\beta_{ij,kl} = \begin{pmatrix} - \det \mathbf{N}_{jkl} \\ \det \mathbf{N}_{ikl} \\ - \det \mathbf{N}_{ijl} \\ \det \mathbf{N}_{ijk} \end{pmatrix}. \quad (3.15)$$

The operator  $\cdot$  in Eq. (3.14) produces the scalar product between the two vectors standing left and right from it. The set of points fulfilling Eq. (3.14) is a 3D plane in the space spanned by the coordinates  $h_i$ ,  $h_j$ ,  $h_k$  and  $h_l$  ( $\mathbf{h}_{ijkl}$ -space), where  $\beta_{ij,kl}$  is the unit normal of the plane. It separates the  $\mathbf{h}_{ijkl}$ -space into a part in which the edge  $\mathcal{E}_{ij,kl}$  can occur and another one in which it cannot. If the signs for the vector  $\beta_{ij,kl}$  are chosen as in Eq. (3.15),  $\beta_{ij,kl}$  points away from the halfspace in which  $\mathcal{E}_{ij,kl}$  can exist. The choice of the sign is insofar important, as we wish to produce only *outer* normal vectors which is for instance helpful to keep the definition equation for the morphology domain compact and to facilitate later the search for new morphological domains. The conditional equation (3.14) can be extended to the full  $\mathbf{h}$ -space by ex-

panding  $\beta_{ij,kl}$  to an  $n$ -dimensional vector with zeros except on the positions  $i, j, k$  and  $l$ :

$$\mathbf{b}_{ij,kl} = \begin{pmatrix} 0 \\ \vdots \\ -\det \mathbf{N}_{jkl} \\ \vdots \\ \det \mathbf{N}_{ikl} \\ \vdots \\ -\det \mathbf{N}_{ijl} \\ \vdots \\ \det \mathbf{N}_{ijk} \\ \vdots \\ 0 \end{pmatrix} \begin{pmatrix} 1 \\ \vdots \\ i \\ \vdots \\ j \\ \vdots \\ k \\ \vdots \\ l \\ \vdots \\ n \end{pmatrix}. \quad (3.16)$$

This vector is called a *boundary vector*. The necessary condition that the edge  $\mathcal{E}_{ij,kl}$  exists is:

$$\mathbf{b}_{ij,kl} \cdot \mathbf{h} < 0. \quad (3.17)$$

Since the edges have been classified into those whose disappearance is accompanied by the disappearance of the  $i$ th face (superscript  $i \rightarrow \emptyset$ ) and those whose disappearance involves the occurrence of a compound vertex and a new edge (superscript  $\curvearrowright$ ), these indices are inherited by  $\mathbf{b}_{ij,kl}$  if this distinction is required:

$$\begin{aligned} \mathbf{b}_{ij,kl}^{\curvearrowright} &\rightarrow (ij, kl) \in E_{\lambda}^{\curvearrowright} \\ \mathbf{b}_{ij,kl}^{i \rightarrow \emptyset} &\rightarrow (ij, kl) \in E_{\lambda}^{\emptyset} \end{aligned} \quad (3.18)$$

### 3.1.3 Morphology Cone in $\mathbf{h}$ -Space

If the existence conditions after Eq. (3.17) are known for all edges of the C-morphology  $\lambda$ , the existence domain of this morphology in  $\mathbf{h}$ -space is

$$\mathcal{M}_{\lambda} = \{\mathbf{h} : \mathbf{B}_{\lambda} \mathbf{h} < \mathbf{0}\}, \quad (3.19)$$

where the rows of  $\mathbf{B}_{\lambda}$  are boundary vectors, see Eq.s (3.16), (3.17):

$$\mathbf{B}_{\lambda} = \left[ \mathbf{b}_{ij,kl}^T \right]_{ij,kl \in E_{\lambda}} \in \mathbb{R}^{b_{\lambda} \times n}, \quad (3.20)$$

where  $b_{\lambda}$  is the number of boundary vectors which of course equals the number of edges on the crystal surface.  $\mathbf{B}_{\lambda}$  is called a *boundary matrix*. The domain  $\mathcal{M}_{\lambda}$  is a cone in  $\mathbf{h}$ -space whose apex is the origin, see for example Fig. 3.4.

The boundary matrix defining the morphology cone can be split into two parts which reflects the classification between boundaries in  $\mathbf{h}$ -space where faces disappear (superscript  $\emptyset$ ) or the edge configuration changes (superscript  $\curvearrowright$ ):

$$\mathbf{B}_{\lambda}^{\emptyset} = \left[ \mathbf{b}_{ij,kl}^T \right]_{ij,kl \in E_{\lambda}^{\emptyset}} \in \mathbb{R}^{b_{\lambda}^{\emptyset} \times n} \quad (3.21a)$$

$$\mathbf{B}_{\lambda}^{\curvearrowright} = \left[ \mathbf{b}_{ij,kl}^T \right]_{ij,kl \in E_{\lambda}^{\curvearrowright}} \in \mathbb{R}^{b_{\lambda}^{\curvearrowright} \times n}. \quad (3.21b)$$



ogy. In order to keep a consistent notation, the index sets  $E_{\lambda,j}^<$  and  $E_{\lambda,j}^0$  are introduced with which the boundary matrices can be assembled in a similar way to Eq.s (3.20) and (3.21):

$$\mathbf{B}_{\lambda,j}^< = \left[ \mathbf{b}_{ij,kl}^T \right]_{ij,kl \in E_{\lambda,j}^<} \in \mathbb{R}^{b_{\lambda,j}^< \times n} \quad (3.23a)$$

$$\mathbf{B}_{\lambda,j}^0 = \left[ \mathbf{b}_{ij,kl}^T \right]_{ij,kl \in E_{\lambda,j}^0} \in \mathbb{R}^{b_{\lambda,j}^0 \times n}. \quad (3.23b)$$

As discussed before, the disappearance of edges on the crystal boundary is termed a morphological change. That is to say, on the faces of the morphology cone we find morphologies which differ from the morphology that can be found in the interior of the cone. However, they are in a sense not so different because only edges (and possibly faces) have disappeared but no new edges can be found on the shape. Therefore, the morphologies existing in the domain  $\mathcal{M}_{\lambda,j}$  are recognized as special species of the  $\lambda$ th morphology. In Sec. 3.1.2 these subspecies have been termed S- and T-morphologies. T-morphologies comprise at least one equality condition from the set  $E_{\lambda}^<$ , i.e., they comprise a compound vertex which occurs only due to the morphological transition from one edge configuration to another one as depicted in Fig. 3.3. S-morphologies contain only conditions from the set  $E_{\lambda}^{\emptyset}$  which corresponds to a disappearing face as depicted in Fig. 3.2:

$$\begin{aligned} \text{if } E_{\lambda,j}^0 \subset E_{\lambda}^{\emptyset} & \rightarrow \mathcal{M}_{\lambda,j} \text{ is an S-morphology} \\ \text{if } E_{\lambda,j}^0 \cap E_{\lambda}^< \neq \emptyset & \rightarrow \mathcal{M}_{\lambda,j} \text{ is a T-morphology} \end{aligned} \quad (3.24)$$

An example depicting these cases in  $\mathbf{h}$ -space is given in Fig. 3.4. On the faces of the morphology cone  $\mathcal{M}_1$  we find two subspecies of that morphology: the cuboctahedron on the upper face is a T-morphology and the octahedron below is an S-morphology. In the interior of  $\mathcal{M}_1$  the truncated octahedron exists of which two examples are depicted (C-morphology). All three shapes look qualitatively different, however, they can be described by the same set of edges. But for the two boundary morphologies the length of one of the two kinds of edges is zero. The example in Fig. 3.4 also indicates that in the neighborhood of the morphology cone other morphologies can exist across boundaries on which T-morphologies exist. In the here considered example this is the region  $\mathcal{M}_2$  in which the truncated cube exists above the morphology cone  $\mathcal{M}_1$ .

### 3.1.4.2 Surrounding Morphology Cones

An  $(n-1)$ -dimensional facet of the morphology cone on which a T-morphology exists is

$$\mathcal{M}_{\lambda,j} = \mathcal{M}_{\lambda} \cap \left\{ \mathbf{h} : \mathbf{b}_{ij,kl}^{\wedge} \cdot \mathbf{h} = 0 \right\}. \quad (3.25)$$

An example is the line  $\mathcal{M}_{1,1}$  between the 2D domains  $\mathcal{M}_1$  and  $\mathcal{M}_2$  in Fig. 3.4 on which the cuboctahedra exist. The outer unit normal of  $\mathcal{M}_1$  at this boundary is denoted  $\mathbf{b}_{22,11}$  and points to the interior of a new morphology cone  $\mathcal{M}_2$ . If only  $\mathcal{M}_1$  is known but recognized that on  $\mathcal{M}_{1,1}$  transition morphologies exist, a new C-morphology is found by moving from the boundary domain away in the direction of the outer unit normal. Let the vector  $\mathbf{h}_{\lambda,j}$  ( $\mathbf{h}_{1,1}$  in Fig. 3.4) be located in the interior of that boundary



domain. It is the starting point to find a representative state vector of a neighboring C-morphology:

$$\mathbf{h}_{\lambda+1} = \mathbf{h}_{\lambda,j} + \epsilon \mathbf{b}_{ij,kl}^{\curvearrowright} \in \mathcal{M}_{\lambda+1}, \quad (3.26)$$

where  $\epsilon$  is a small positive number so that one moves not too far away from the boundary, thus avoids to miss the morphology cone lying across. In our computations we have chosen  $\mathbf{h}_{\lambda,j}$  so that its magnitude is unity and  $\epsilon = 0.05$ . From the shape configuration produced by this vector, the associated morphology cone  $\mathcal{M}_{\lambda+1}$  can be determined as described above, starting with the computation of all vertices and the edges,  $E_{\lambda}$ , following therefrom, subsequently the boundaries for the existence of the edges are derived, see Eq. (3.16), and finally the morphology cone  $\mathcal{M}_{j+1}$  ( $\mathcal{M}_2$  in Fig. 3.4).

### 3.1.4.3 Joint Morphology Cone

In this way, all morphologies can be found by determining all morphology cones. Starting with a state vector, e.g.  $\mathbf{h}_1 = \mathbf{1}$ , a shape which exhibits all  $n$  possible faces, the morphology cone  $\mathcal{M}_1$  is determined as described in Sec.s 3.1.2 and 3.1.3. The faces of the cones of the newly found morphologies are again checked for other morphologies which lie across of them until no new morphologies can be found. The union of the set of all morphology cones is called the *joint morphology cone* and is denoted by

$$\mathcal{M} = \bigcup_{i=1}^m \mathcal{M}_{\lambda}, \quad (3.27)$$

where  $m$  is the number of C-morphologies which can occur using the set of crystal faces stored in  $\mathbf{N}$ . A facet of the morphology cone can now be classified to belong to the interior of the joint morphology cone or it is a facet of the joint morphology cone as well. The conditions which make up the facets of the joint morphology cone, denoted by  $\mathbf{B}^{\emptyset}$ , lead to the disappearance of a face on the crystal shape. That is, the joint morphology cone is defined by

$$\mathcal{M} = \{ \mathbf{h} : \mathbf{B}^{\emptyset} \mathbf{h} < \mathbf{0} \}, \quad (3.28)$$

where

$$\mathbf{B}^{\emptyset} = [\mathbf{b}_{ij,kl}]_{ij,kl \in E^{\emptyset}} \in \mathbb{R}^{b^{\emptyset} \times n}, \quad E^{\emptyset} = \bigcup_{j=1}^m E_{\lambda}^{\emptyset}. \quad (3.29)$$

With the help of the boundary vectors stored in the matrix

$$\mathbf{B}^{\curvearrowright} = [\mathbf{b}_{ij,kl}]_{ij,kl \in E^{\curvearrowright}} \in \mathbb{R}^{b^{\curvearrowright} \times n}, \quad E^{\curvearrowright} = \bigcup_{j=1}^m E_{\lambda}^{\curvearrowright}. \quad (3.30)$$

standing for the transition between different edge configurations, the morphology cone is partitioned into regions in which different morphologies are assumed by the crystal.

### 3.1.5 Symmetry

One of the most essential features of crystals is that the molecules of the crystallized material form a regular pattern. The different lattice patterns which can be formed with building blocks (molecules) of different symmetry features in 3D space are known as the 230 space groups. The symmetry of the external shape of crystals expresses to a certain degree the underlying symmetry and regular arrangement on the molecular level. Since translational operations are omitted for external shapes, overall 32 crystallographic point groups can be found representing all possible combinations of crystallographic symmetry operations Borchardt-Ott (2009).

Because of the regular arrangement, the crystal structure looks the same from different but related perspectives. That is, along these related directions the properties, for instance the surface structure, of the material are the same. Directions normal to crystal faces and featuring the same surface structure are combined to a crystal form. The faces of a crystal form are related to each other by symmetry operations (McWeeny, 1963). Overall, there exist 48 different kinds of forms, tabulated for instance in Borchardt-Ott (2009).

If the crystal grows under ideal conditions, i.e., the environment of the crystal is the same in every direction, the growth rate of every face of a form is the same. If the distances of all faces of a form are equal at the beginning, they remain equal under ideal conditions. Hence, it is then sufficient to keep track of the distance  $h_i$  of only one face of a form. The geometrical state vector for the ideal symmetric case is denoted by  $\mathbf{h}_{\text{sy}} \in \mathbb{R}^{n_{\text{sy}}}$ , where  $n_{\text{sy}}$  is the number of crystal forms. The full state vector is obtained from the symmetric state vector by

$$\mathbf{h} = \mathbf{M} \mathbf{h}_{\text{sy}}, \quad (3.31)$$

where  $\mathbf{M} \in \mathbb{R}^{n \times n_{\text{sy}}}$  is a mapping matrix with ones on positions where the  $i$ th face (row) belongs to the  $j$ th form (column) and zero otherwise. The inequality conditions for the existence of particular edges, Eq. (3.17), can be rewritten:

$$\underbrace{\mathbf{b}_{ij,kl}^{\text{sy}}}_{=\mathbf{M}\mathbf{b}_{ij,kl}} \cdot \mathbf{h}_{\text{sy}} < 0. \quad (3.32)$$

By converting all conditions to the symmetrical case, the morphology cones and with it all possible morphological variations of the symmetric crystal are obtained exactly in the way as described in the preceding sections. However, it occurs that a condition is obtained multiple times due to the symmetry reduction from the asymmetric case. The set of conditions (or the matrix  $\mathbf{B}_\lambda$ ) should be reduced such that a condition appears only once. A condition is classified to be an edge transition condition (superscript  $\sim$ ) if all conditions of the asymmetric case which are associated with this symmetric condition are transition conditions. If only one of the associated conditions of the asymmetric case is a face-disappearance condition (superscript  $\emptyset$ ), the symmetric condition is classified as a face-disappearance condition. It is furthermore assumed in the following that redundant conditions are removed from the matrix  $\mathbf{B}_\lambda$ . For example, a morphological change that implies for the symmetrical case necessarily additionally other morphological changes involves redundant conditions which do not form a facets on the morphology cone.

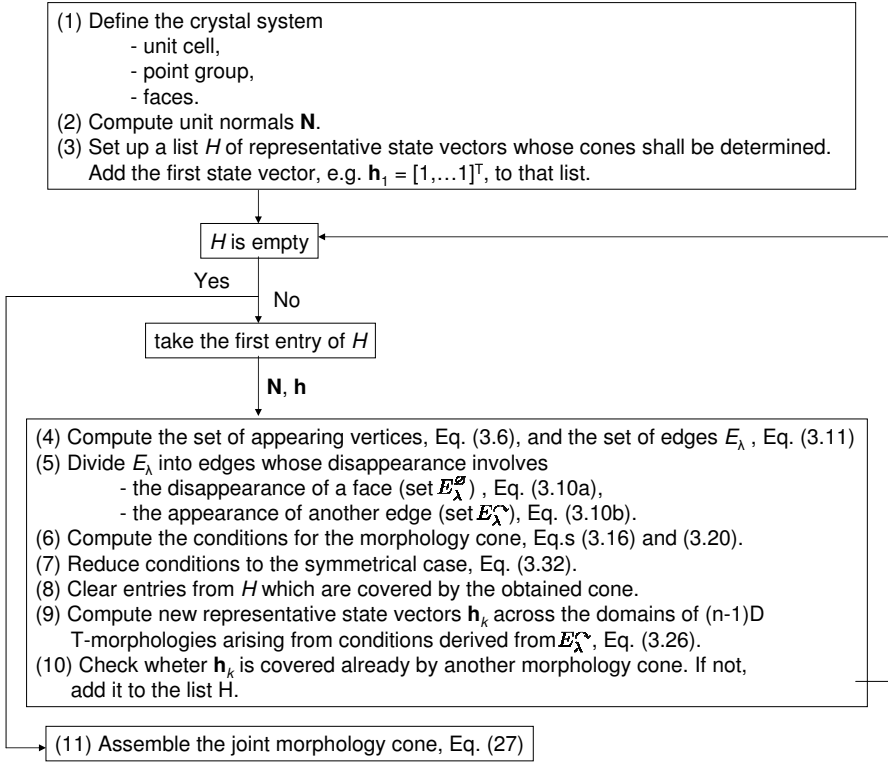


**Figure 3.5:** Workflow of the computation of the morphology cone.

### 3.1.6 Morphology Cone Computations at a Glance

The determination of the morphology cone involves many different calculations. The order of the topics and formulae presented in this section follows not exactly the order as they should be used in a computer program. To facilitate the practical applicability of the presented material, an overview of the major steps is depicted in Fig. 3.5. Starting with the definition of basic crystallographic data, the unit normals of the crystal faces are determined and a list of state vectors, denoted by  $H$ , is introduced for which the morphology cones shall be determined. The first entry of that list can be chosen arbitrarily but the shape produced from that state must exhibit all crystal faces, i.e.  $\mathbf{h} = (1, \dots, 1)^T$  is a self-evident choice. Of that list the first (and at this stage only) state vector is passed to a routine which computes the crystal vertices and edges, and thus the set  $E_\lambda$ . With the help of this set, the morphology cones are determined ( $\mathbf{B}$ -matrices). Then the conditions are reduced to the (possibly) symmetric case and entries of the list  $H$  are cleared if they are contained in the just determined cone (this is of course not the case if the first cone is calculated). Across the boundaries on which T-morphologies are found, new candidate states for the list  $H$  are calculated which are added to  $H$  if they are not covered by a cone that has been found previously. Then the procedure is started again for the next entry of  $H$  until the list is empty. That is, the joint morphology cone can be assembled. We strongly conjecture that this procedure *guarantees* locating all possible C-morphologies and thus the joint morphology cone. However, a rigorous mathematical proof has not been established.

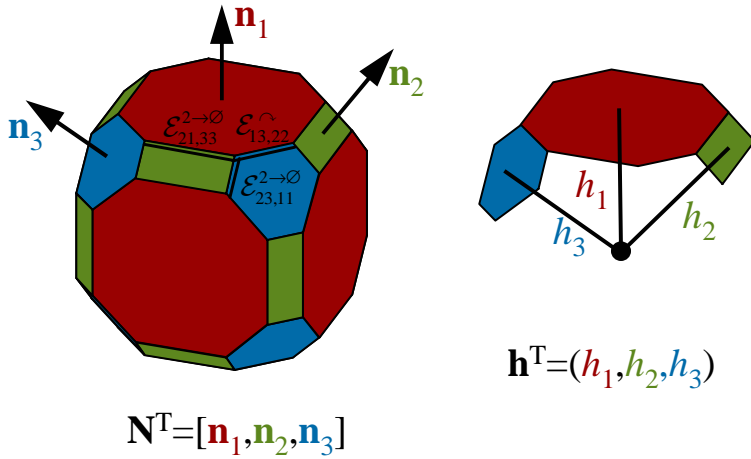


**Figure 3.6:** Potassium alum with forms cube (1), rhombic dodecahedron (2) and octahedron (3). All faces of one form are assumed to have the same distance to the crystal center. Thus, a 3D state vector,  $\mathbf{h}$ , suffices to quantify the shape.

### 3.1.7 Example: Potassium Alum

In order to clarify the usage of the equations presented in this section, an example is examined which can easily be reassessed using elementary geometry. Potassium alum crystallizes in the space group  $\text{Pa}\bar{3}$  (cubic crystal system) and thus possesses point group symmetry  $m\bar{3}$ . We consider only the forms  $\{100\}$  (cube),  $\{110\}$  (rhombic dodecahedron), and  $\{111\}$  (octahedron), that is, the three mirror planes perpendicular to the unit cell axes are sufficient to capture the symmetry exhibited by these three special forms. Note that the general form of this point group is the pyritohedron.

We follow the procedure described above and start to find all morphologies by analyzing a particular shape where all faces are present (C-morphology), see Fig. 3.6. For the symmetrical case three types of edges can be found, that is:

$$E_1 = \{13, 22; 21, 33; 23, 11\} . \quad (3.33)$$

With this information the morphology at hand is defined, in the sense of Sec. 3.1.2. Using Eq. (3.9) and the distinction of cases given in Eq. (3.10), we find for the symmetric case:

$$\begin{aligned} \mathbf{w}_{13,22} &= (-\sqrt{3}, \sqrt{2}, \sqrt{2})^T \rightarrow \mathcal{E}_{13,22}^{0 \rightarrow 2} \\ \mathbf{w}_{21,33} &= \frac{1}{4} (0, \sqrt{6}, \sqrt{6})^T \rightarrow \mathcal{E}_{21,33}^{2 \rightarrow 0} \\ \mathbf{w}_{23,11} &= \frac{1}{2} (0, \sqrt{2}, \sqrt{2})^T \rightarrow \mathcal{E}_{23,11}^{2 \rightarrow 0} \end{aligned} \quad (3.34)$$

That is, if the edges  $\mathcal{E}_{13,22}$  vanish, the crystal undergoes a morphological transition to a different C-morphology because if (only) this edge disappears no face disappears. Without paying attention to the quantification of the boundaries in state space, in Fig. 3.7 this would mean a transition of the morphology from (e) to (f). If the edge  $\mathcal{E}_{21,33}$  disappears from the surface, the values of  $\mathbf{w}_{21,33}$  indicate that faces of the rhombic dodecahedron ( $h_2$ ) disappear which is also immediately clear by looking at the crystal shape. In Fig. 3.7 this is a transition from (e) to (b). Upon disappearance of

the edge  $\mathcal{E}_{23,11}$ , the faces of the rhombic dodecahedron ( $h_2$ ) disappear as well and this would mean a transition from (e) to (d).

The next step in our analysis is the determination of the morphological boundaries. It is easily shown that for the symmetrical case, see Eq.s (3.15), (3.16) and (3.32):

$$\begin{aligned} \mathbf{b}_{13,22}^{\curvearrowright} &= \left( \sqrt{\frac{1}{12}}, -\sqrt{\frac{2}{3}}, \frac{1}{2} \right)^T \\ \mathbf{b}_{21,33}^{2 \rightarrow \emptyset} &= \left( 0, \sqrt{\frac{2}{5}}, -\sqrt{\frac{3}{5}} \right)^T \\ \mathbf{b}_{23,11}^{2 \rightarrow \emptyset} &= \frac{1}{2} \left( -\sqrt{\frac{2}{3}}, \sqrt{\frac{1}{3}}, 0 \right)^T \end{aligned} \quad (3.35)$$

Therefore, the first morphology cone is

$$\mathcal{M}_1 = \{ \mathbf{h} : \mathbf{B}_1 \mathbf{h} < \mathbf{0} \}, \quad \mathbf{B}_1 = \begin{bmatrix} (\mathbf{b}_{13,22}^{\curvearrowright})^T \\ (\mathbf{b}_{21,33}^{2 \rightarrow \emptyset})^T \\ (\mathbf{b}_{23,11}^{2 \rightarrow \emptyset})^T \end{bmatrix}. \quad (3.36)$$

The projection of this cone into  $(h_1/h_3, h_2/h_3)$ -space is a triangular region as depicted in Fig. 3.7. Using Eq. (3.26), a representative shape of the morphology cone which lies across the morphological domain with unit normal  $\mathbf{b}_{13,22}^{\curvearrowright}$  can be found. In a similar way as for the first morphology cone, three kinds of edges can be found, denoted by  $\mathcal{E}_{22,13}$ ,  $\mathcal{E}_{12,22}$  and  $\mathcal{E}_{32,22}$  which determine the morphological boundaries of the second morphology cone as

$$\begin{aligned} \mathbf{b}_{22,13}^{\curvearrowright} &= \left( -\sqrt{\frac{1}{12}}, \sqrt{\frac{2}{3}}, -\frac{1}{2} \right)^T \\ \mathbf{b}_{12,22}^{1 \rightarrow \emptyset} &= \left( \sqrt{\frac{1}{3}}, -\sqrt{\frac{2}{3}}, 0 \right)^T \\ \mathbf{b}_{32,22}^{3 \rightarrow \emptyset} &= \left( 0, -\sqrt{\frac{3}{5}}, \sqrt{\frac{2}{5}} \right)^T \end{aligned} \quad (3.37)$$

Similarly to Eq. (3.36), the point set contained by the second morphology cone can be defined. In Fig. 3.7 this second morphology cone is sketched along with occurring S- and T-morphologies. The joint morphology cone, see Eq. (3.28), is described only by those boundaries which involve the disappearance of a face (superscript  $\emptyset$ ), i.e.:

$$\mathcal{M} = \{ \mathbf{h} : \mathbf{B}^{\emptyset} \mathbf{h} \leq \mathbf{0} \}, \quad \mathbf{B}^{\emptyset} = \begin{bmatrix} (\mathbf{b}_{12,22}^{1 \rightarrow \emptyset})^T \\ (\mathbf{b}_{21,33}^{2 \rightarrow \emptyset})^T \\ (\mathbf{b}_{23,11}^{2 \rightarrow \emptyset})^T \\ (\mathbf{b}_{32,22}^{3 \rightarrow \emptyset})^T \end{bmatrix}. \quad (3.38)$$

Now we have analysed the accessible region in the state space in a sufficient detail in order to describe the crystal shape evolution adequately.

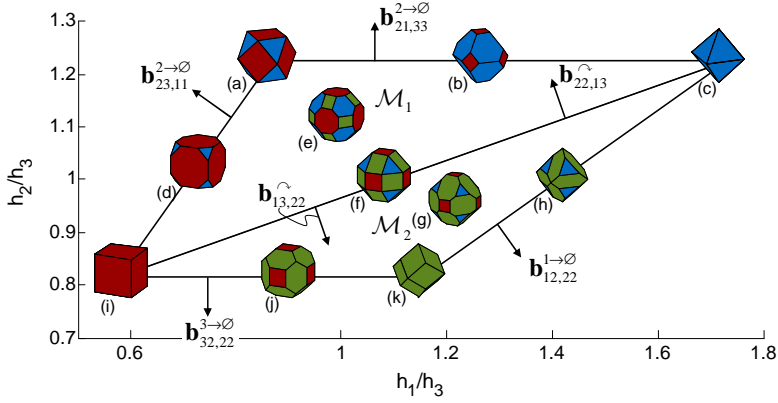


**Figure 3.7:** Morphologies of potassium alum.  $h_1$ :  $\{100\}$  red cubic faces;  $h_2$ :  $\{110\}$  green faces;  $h_3$ :  $\{111\}$  blue octahedral faces. The classification as introduced in Sec. 3.1.2: C-morphologies: (e), (g); S-morphologies: (b), (c), (d), (h), (i), (j), (k); T-morphologies: (a), (f).

## 3.2 Shape Evolution

The following section shows how to handle the shape evolution equation in a way which exploits the notion of different morphological domains. Different morphologies with virtual faces evolve in a different way which is expressed by a special matrix in the evolution equation, see Sec. 3.2.1. This is clarified by an example given in Sec. 3.2.2. In Sec. 3.2.3 the analytical solution to the shape evolution equation is presented for the case of constant growth rates.

### 3.2.1 Displacement of Real and Virtual Faces

The crystal shape as defined in Eq. (3.1) is time-dependent, i.e., the distances of the faces undergo a dynamical evolution. The mode of this evolution is determined by the perpendicular growth velocities of the faces:

$$\mathbf{G}(\mathbf{Y}, \mathbf{h}) = \begin{pmatrix} G_1 \\ \vdots \\ G_n \end{pmatrix}, \quad (3.39)$$

where  $\mathbf{Y}$  is the state vector of the surrounding continuous phase and involves particularly the supersaturation. Very often, the dependency of  $\mathbf{G}$  on  $\mathbf{h}$  is neglected and in fact it is one of the most challenging problems in crystal research to quantify this dependency along with the dependency on  $\mathbf{Y}$ . However, in the following we take the growth rates as given. As long as a face is real, its advancement is indeed governed by the growth rate:

$$\frac{dh_i}{dt} = G_i \quad \text{if } i \text{ is a real face.} \quad (3.40)$$

But when the face has become virtual, its displacement is dictated by the advancement of the vertex at which the virtual face touches the crystal (Gadewar and Doherty, 2004; Zhang et al., 2006). The distance of the virtual face  $i$  which lies on a

vertex made up by the faces  $jkl$ , see Fig. 3.2 (b), is given by Eq. (3.14) which can be reformulated to

$$h_i = \mathbf{d}_{i,jkl}^T \mathbf{h} \quad (3.41)$$

where

$$\mathbf{d}_{i,jkl} = \frac{1}{\det \mathbf{N}_{jkl}} \begin{pmatrix} 0 \\ \vdots \\ -\det \mathbf{N}_{ikl} \\ \vdots \\ \det \mathbf{N}_{ijl} \\ \vdots \\ -\det \mathbf{N}_{ijk} \\ \vdots \\ 0 \end{pmatrix} \begin{pmatrix} 1 \\ \vdots \\ j \\ \vdots \\ k \\ \vdots \\ l \\ \vdots \\ n \end{pmatrix}. \quad (3.42)$$

Compare this vector also to  $\mathbf{b}_{ij,kl}$  given in Eq. (3.16). It can be seen that  $\mathbf{d}_{i,jkl}$  is obtained from  $\mathbf{b}_{ij,kl}$  by dividing  $\mathbf{b}_{ij,kl}$  through its  $i$ th element and setting the  $i$ th element to zero. In order to keep the distance of a virtual face such that it remains on the vertex (and does not move away from the crystal), its evolution is determined by the velocity of the vertex:

$$\frac{dh_i}{dt} = \mathbf{d}_{i,jkl}^T \mathbf{G} \quad \text{if } i \text{ is a virtual and } jkl \text{ are real faces.} \quad (3.43)$$

The virtual face appears on the crystal surface if the growth rate  $G_i$  becomes smaller than the displacement rate given in the previous equation Johnsen (1910); Zhang et al. (2006). In order to obtain a compact notation, we introduce morphology-dependent matrices which are assembled depending on which faces are real:

$$\mathbf{D}(\mathbf{h}, \mathbf{G}) = \begin{bmatrix} \mathbf{d}_1(\mathbf{h}, \mathbf{G})^T \\ \vdots \\ \mathbf{d}_n(\mathbf{h}, \mathbf{G})^T \end{bmatrix}^\infty \in \mathbb{R}^{n \times n}, \quad (3.44)$$

where

$$\mathbf{d}_i(\mathbf{h}, \mathbf{G}) = \begin{cases} \mathbf{d}_{i,jkl} & \text{if } i \text{ is virtual for the state } \mathbf{h} \text{ and } G_i > \mathbf{d}_{i,jkl}^T \mathbf{G} \\ \mathbf{e}_i & \text{if } i \text{ is real or } G_i < \mathbf{d}_{i,jkl}^T \mathbf{G} \end{cases}, \quad (3.45)$$

where  $\mathbf{e}_i$  is the basis vector for which the  $i$ th entry is one and all others are zero.  $\mathbf{D}$  is called the *velocity delimiter matrix* which must in principle be defined for every morphology individually. Clearly, for C-morphologies on which all  $n$  faces are real, the velocity delimiter matrix is the identity matrix:  $\mathbf{D} = \mathbf{E}_n$ . Note also the power to infinity of the matrix on the r.h.s. of Eq. (3.44). The necessity of this operation and properties of the velocity delimiter matrix are discussed in the following section when the previously started example is further developed.

In general, when the disappearance of faces is considered, the state vector evolves according to the differential equation

$$\frac{d\mathbf{h}}{dt} = \mathbf{D}(\mathbf{h}, \mathbf{G}) \mathbf{G}, \quad \mathbf{h}(t=0) = \mathbf{h}_0, \quad (3.46)$$

which is a system of ordinary differential equations with discontinuous (switching) right-hand side. As such it can also be interpreted as a hybrid dynamic system since it exhibits continuous as well as discrete dynamic behavior. In general, these systems are difficult to solve but in the example at hand, the integration becomes only a little more difficult than solving conventional ODEs, since the state vector  $\mathbf{h}$  keeps its dimensionality and does not perform any jumps within the state space. In general, the integration across a discrete event can lead to incorrect or inaccurate results due to a loss in differentiability of the continuous state across the event. This means that the fourth- and fifth-order approximations commonly used by most ODE solvers will not be fourth- or fifth-order accurate across an event, and can be no more accurate than first order in time. Supported by our experiences with the practical implementation of Eq. (3.46) using Matlab's ODE solvers "ode23" and "ode45" we conjecture that a numerically stable ODE-solver accurately solves the particular hybrid systems considered in this paper.

### 3.2.2 Continuation of the Potassium Alum example

The shape evolution equation (3.46) is now discussed by continuing the previously started analysis on the cubic crystal with three kinds of faces as shown in Fig. 3.6. This is done in two steps. At first, the mechanism of disappearance of faces is exemplified and then the appearance of faces.

#### 3.2.2.1 Disappearance of Crystal Faces

The initial morphology is given by

$$\mathbf{h}_0 = (1, 0.9, 0.8)^T. \quad (3.47)$$

Note that units are dropped in this illustrative example.  $\mathbf{h}_0$  lies in the interior of  $\mathcal{M}_1$ , see Eq. (3.36), and thus all three kinds of faces are real on the crystal surface which means that  $\mathbf{D}(\mathbf{h}_0, \mathbf{G}) = \mathbf{E}_3$ . The growth rates are set constant to

$$\mathbf{G} = (0.5, 3, 2)^T. \quad (3.48)$$

The steady-state morphology is easily shown to be the cube which means that only  $h_1$ -faces are present on the crystal surface. The joint morphology cone, see Eq. (3.38), bounds the state vector so that the  $h_2$ -faces lie on the edges of the cube and the  $h_3$ -faces on the vertices. The steady state morphology is thus

$$\mathbf{h}_{ss} \propto (1, \sqrt{2}, \sqrt{3})^T. \quad (3.49)$$

The task is to integrate the differential equation (3.46) for  $0 \leq t \leq 1$ .

The trajectory in  $(h_1/h_3, h_2/h_3)$ -space together with some selected shapes along the trajectory is depicted in Fig. 3.8. Initially, all three faces are present until at  $t \approx 0.145$  the boundary  $\mathbf{b}_{21,33}^{2 \rightarrow \emptyset} \cdot \mathbf{h} = 0$ , see Eq. (3.35), is hit. Before this event, the faces are displaced with the natural growth rate  $\mathbf{G}$ , which means:

$$\frac{d\mathbf{h}}{dt} = \mathbf{E}_3 \mathbf{G} \quad \text{until } \mathbf{b}_{21,33}^{2 \rightarrow \emptyset} \cdot \mathbf{h} = 0 \text{ at } t \approx 0.145. \quad (3.50)$$



From then on the  $h_2$ -faces are not present on the crystal surfaces any longer. They lie on the edge between two  $h_3$ -faces of the truncated octahedron. Using Eq. (3.45) and reducing it to the symmetrical case (similar to the normal vector of the boundary as shown in Eq. (3.32)), the  $h_2$ -faces are displaced with  $\frac{dh_2}{dt} = \mathbf{d}_{2,133}^T \mathbf{G}$  where  $\mathbf{d}_{2,133}^T = (0, 0, \frac{\sqrt{3}}{\sqrt{2}})$ . Thus, the shape evolution is given by

$$\frac{d\mathbf{h}}{dt} = \begin{bmatrix} 1 & 0 & 0 \\ 0 & 0 & \frac{\sqrt{3}}{\sqrt{2}} \\ 0 & 0 & 1 \end{bmatrix} \mathbf{G} \quad \text{until } \mathbf{b}_{23,11}^{2 \rightarrow \emptyset} \cdot \mathbf{h} = 0 \text{ at } t \approx 0.249.$$

At the intersection of the boundaries  $\mathbf{b}_{21,33}^{2 \rightarrow \emptyset} \cdot \mathbf{h} = 0$  and  $\mathbf{b}_{23,11}^{2 \rightarrow \emptyset} \cdot \mathbf{h} = 0$  the cuboctahedron appears and the transformation from the truncated octahedron to the truncated cube takes place. The virtual  $h_2$ -faces on the truncated cube, however, lie on the edge between two  $h_1$ -faces, that is, the shape evolution now proceeds according to

$$\frac{d\mathbf{h}}{dt} = \begin{bmatrix} 1 & 0 & 0 \\ \sqrt{2} & 0 & 0 \\ 0 & 0 & 1 \end{bmatrix} \mathbf{G} \quad \text{until } \mathbf{b}_{32,22}^{3 \rightarrow \emptyset} \cdot \mathbf{h} = 0 \text{ at } t \approx 0.822.$$

The crystal is on the path towards the cube because the octahedral  $h_3$ -faces grow out. At the boundary  $\mathbf{b}_{32,22}^{3 \rightarrow \emptyset} \cdot \mathbf{h} = 0$  the  $h_3$ -faces have disappeared from the crystal surface and their displacement is – if only the boundary  $\mathbf{b}_{32,22}^{3 \rightarrow \emptyset} \cdot \mathbf{h} = 0$  is considered – now dictated by the displacement of the  $h_2$ -faces because  $\mathbf{d}_{3,222}^T = (0, \frac{\sqrt{3}}{\sqrt{2}}, 0)$ , see also Fig. 3.7, i.e.,

$$\frac{dh_3}{dt} = \frac{\sqrt{3}}{\sqrt{2}} \frac{dh_2}{dt}. \quad (3.51)$$

However, at the intersection of  $\mathbf{b}_{32,22}^{3 \rightarrow \emptyset} \cdot \mathbf{h} = 0$  and  $\mathbf{b}_{23,11}^{2 \rightarrow \emptyset} \cdot \mathbf{h} = 0$ , the displacement of the (virtual)  $h_2$ -faces is itself dictated by the displacement of the (real)  $h_1$ -faces:

$$\frac{dh_2}{dt} = \sqrt{2} G_1. \quad (3.52)$$

Therefore, the displacement of the  $h_3$ -faces is given by inserting Eq. (3.52) into Eq. (3.51):

$$\frac{dh_3}{dt} = \sqrt{3} G_1. \quad (3.53)$$

The evolution equation for the crystal shape after the trajectory has hit the boundary  $\mathbf{b}_{32,22}^{3 \rightarrow \emptyset} \cdot \mathbf{h} = 0$  is

$$\frac{d\mathbf{h}}{dt} = \begin{bmatrix} 1 & 0 & 0 \\ \sqrt{2} & 0 & 0 \\ \sqrt{3} & 0 & 0 \end{bmatrix} \mathbf{G} = \begin{bmatrix} 1 & 0 & 0 \\ \sqrt{2} & 0 & 0 \\ 0 & \frac{\sqrt{3}}{\sqrt{2}} & 0 \end{bmatrix}^\infty \mathbf{G}, \quad (3.54)$$

which is – as indicated on the rightmost side – also obtained from multiplying the “raw” matrix  $\mathbf{D}$  with itself infinitely many times (in general). In this particular case it is sufficient to do this once but for more complex cases it can happen that the limit value must be determined (which is practically done by using 1000 instead of  $\infty$ ). In general, the matrix  $\mathbf{D}$  is a projection matrix and thus idempotent, which means that  $\mathbf{D}\mathbf{D} = \mathbf{D}$ , see Zurmühl and Falk (1996).

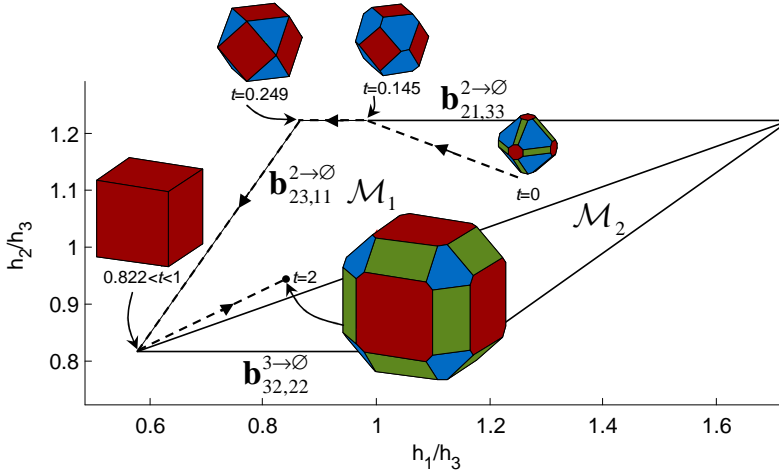


Figure 3.8: Shape evolution of a cubic crystal with disappearing and reappearing faces.

If the last part of the trajectory has been integrated according to Eq. (3.54) the state vector at the end of the integration interval is

$$\mathbf{h}(t = 1) \approx (1.500, 2.121, 2.598)^T. \quad (3.55)$$

### 3.2.2.2 Appearance of Crystal Faces

Let us now assume that, at  $t = 1$ , the crystal with the state vector  $\mathbf{h}(t = 1)$ , Eq. (3.55), is moved to an environment leading to the growth-rate vector

$$\mathbf{G} = (1, 0.7, 0.4)^T. \quad (3.56)$$

which means that the ‘real’ growth rates of the (currently virtual)  $h_2$ - and  $h_3$ -faces,  $G_2$  and  $G_3$ , are slower than the displacement rate following from Eq. (3.54). Therefore, the  $h_2$ - and  $h_3$ -faces appear again on the crystal surface and thus the velocity delimiter matrix becomes the unity matrix again. Integrating this differential equation until  $t = 2$  yields a trajectory moving into the interior of the region  $\mathcal{M}_1$ . The resulting crystal shape is shown at the bottom of Fig. 3.8.

### 3.2.2.3 The Representation of Crystal Shape Evolution as a Hybrid System

The switching between different velocity delimiter matrices makes Eq. (3.46) a hybrid system in which the geometrical state is the continuous state variable and the morphology, respectively the velocity delimiter matrix and the coefficients for the volume evaluation (see Sec. 3.3), are the discrete states. Also the guard conditions are given with which a discrete event (switch to a different morphology) is detected by the crossing or reaching of morphological boundaries (Eq. (3.14)) or if the velocity of a virtual face falls below a critical value (Eq. (3.45)) and thus a morphological boundary is left. In Fig. 3.9 a typical graphical representation of the example crystal as a hybrid system is depicted. The discrete states (morphologies) are connected by conditions

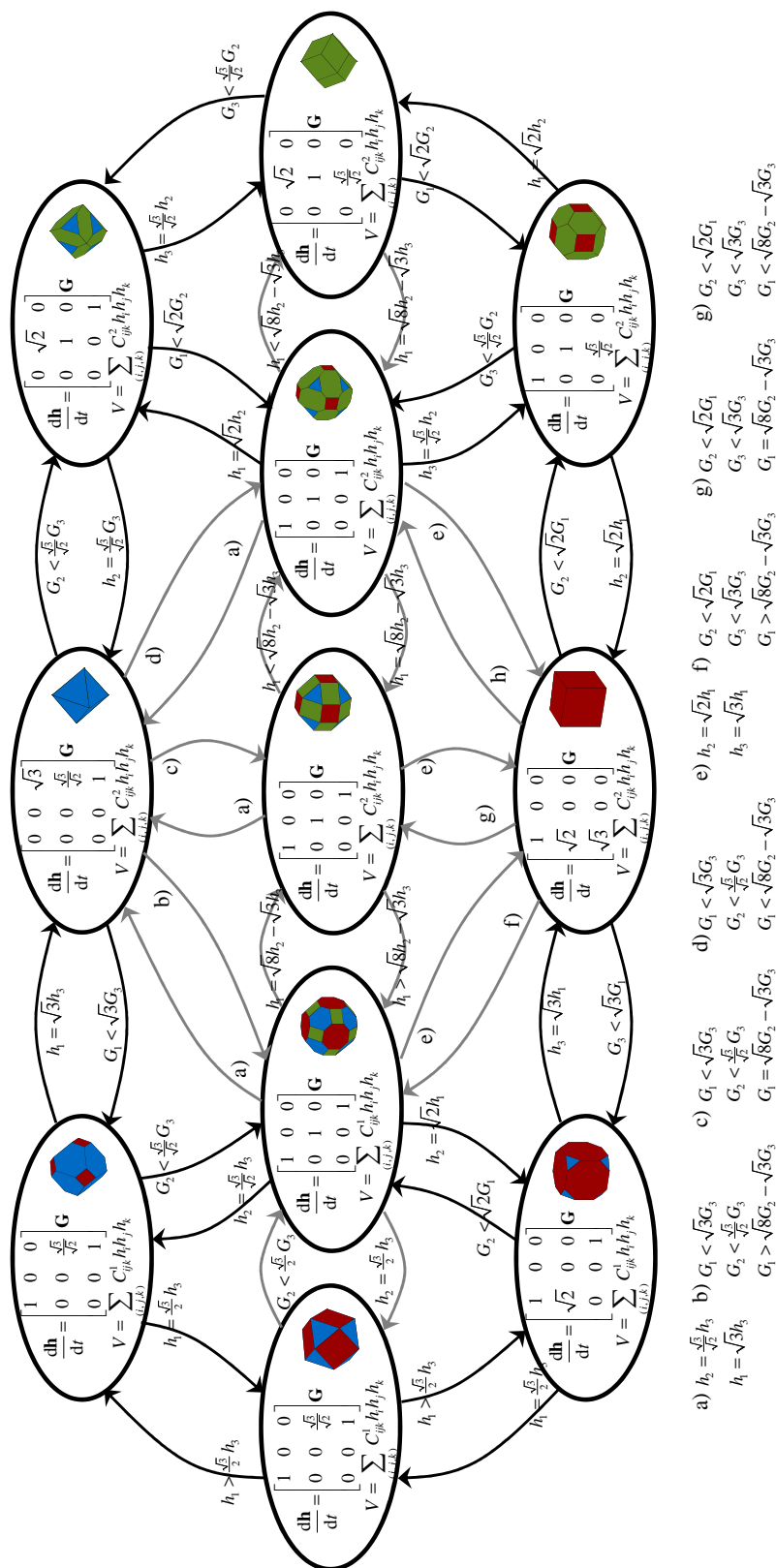


**Figure 3.9:** The shape evolution equation can be interpreted as a hybrid system.

at which the switch (arrows) between different discrete states is recognized. Details on hybrid systems can be found in Matveev and Savkin (2000); van der Schaft and Schumacher (2000); Lunze (2002).

### 3.2.3 Analytical Solution for Constant Growth Rates

The analytical solution to the differential equation (3.46) under the constraint of a constant growth vector and constant velocity delimiter matrix is

$$\mathbf{h}(\mathbf{h}_0, \mathbf{G}, t) = \mathbf{h}_0 + \mathbf{D}(\mathbf{h}_0, \mathbf{G})\mathbf{G}t \in \mathcal{M}_{\lambda,j}. \quad (3.57)$$

But in general, a morphological boundary will be hit and the above solution applies only until before another boundary is reached. If the trajectory leaves a morphological domain, the matrix  $\mathbf{D}$  changes instantaneously. This can be checked directly using the conditions  $\mathbf{B}_{\lambda,j}^<\mathbf{h}$  which are less than zero for  $\mathbf{h} \in \mathcal{M}_{\lambda,j}$ . The instances when the rows of  $\mathbf{B}_{\lambda,j}^<\mathbf{h}$  become zero are obtained by multiplying Eq. (3.57) with  $\mathbf{B}_{\lambda,j}^<$ :

$$\underbrace{\mathbf{B}_{\lambda,j}^<\mathbf{h}_0}_{=\mathbf{p}} + \underbrace{\mathbf{B}_{\lambda,j}^<\mathbf{D}(\mathbf{h}_0, \mathbf{G})\mathbf{G}t}_{=\mathbf{q}} = \mathbf{0}, \quad (3.58)$$

which gives a set of  $b_{\lambda,j}^<$  time intervals after which the (next) boundary is reached. Of these times the smallest positive one, denoted by  $\Delta t_1$ , is chosen and the solution after Eq. (3.57) is applied in this time interval. This procedure must be repeated, say  $n_s$  times, until the desired end-time has been reached. The solution can be assembled of the so obtained sections:

$$\mathbf{h}_{\text{an}}(\mathbf{h}_0, \mathbf{G}) = \mathbf{h}_0 + \sum_{j=1}^{n_s} \mathbf{D}(\mathbf{h}_{j-1}, \mathbf{G})\mathbf{G}\Delta t_j \quad (3.59a)$$

where

$$\mathbf{h}_j = \mathbf{h}_{j-1} + \mathbf{D}(\mathbf{h}_{j-1}, \mathbf{G})\mathbf{G}\Delta t_j \quad (3.59b)$$

$$\Delta t_j = \min_k \left\{ t : t = -\frac{p_{k,j}}{q_{k,j}}, t \geq 0, k = 1 \dots b_{\lambda,j}^< \right\} \quad (3.59c)$$

$$\mathbf{G} = \text{const.} \quad (3.59d)$$

The quantities  $p_{k,j}$  and  $q_{k,j}$  are components of the vectors

$$\mathbf{p}_j = \mathbf{B}_{\lambda,j}^<\mathbf{h}_{j-1} \quad (3.59e)$$

$$\mathbf{q}_j = \mathbf{B}_{\lambda,j}^<\mathbf{D}(\mathbf{h}_{j-1}, \mathbf{G})\mathbf{G} \quad (3.59f)$$

compare also to Eq. (3.58). Though it is unrealistic that the growth rates can be kept constant in a crystallization process, this solution can be helpful when a nonlinear supersaturation profile is decomposed into *piecewise* constant supersaturation segments.

### 3.3 Measures

From the geometrical state vector all geometrical quantities can in principle be calculated of which volume and surface area are the most important ones. In Borchert et al. (2009) a practical method is presented which allows the calculation of the crystal volume. The crystal faces are partitioned into triangles, which are the base planes of polyhedra that involve the crystal center from where the distances  $h_i$  are measured. The volume of such a polyhedron is readily found if the coordinates of the vertices are given (see Fig. 3.10 and Borchert et al. (2009); Bronstein et al. (2001)):

$$V_{ijk,pqr} = \frac{1}{6} \det [\mathbf{v}_{ijk} \mathbf{v}_{ipq} \mathbf{v}_{iqr}] . \quad (3.60)$$

Insertion of the vertex coordinates, Eq. (3.5c), gives a third order polynomial in  $\mathbf{h}$ :

$$V_{i,jk,pqr} = h_i \frac{ \begin{aligned} & ( h_i \det \mathbf{N}_{jkq} - h_j \det \mathbf{N}_{ikq} + \\ & \quad h_k \det \mathbf{N}_{ijq} - h_q \det \mathbf{N}_{ijk} ) \\ & ( h_i \det \mathbf{N}_{pqr} - h_p \det \mathbf{N}_{iqr} + \\ & \quad h_q \det \mathbf{N}_{ipr} - h_r \det \mathbf{N}_{ipq} ) \end{aligned} }{ 6 \det \mathbf{N}_{ijk} \det \mathbf{N}_{ipq} \det \mathbf{N}_{iqr} } . \quad (3.61)$$

The signs are given for the case that the order of the indices is such that  $\det \mathbf{N}_{ijk} > 0$ ,  $\det \mathbf{N}_{ipq} > 0$  and  $\det \mathbf{N}_{iqr} > 0$ . It can be seen here already that the determination of the volume from the  $\mathbf{h}$ -vector is morphology-dependent. The marked triangle on the  $i$ th face shown in Fig. 3.10 disappears if the edge that is formed between the faces  $i$  and  $q$  (and bound by  $r$  and  $p$ ) collapses to a 4-compound vertex. This morphological transition is also reflected in the above equation in the second factor of the numerator. The expression equals (except for the sign) the condition given in Eq. (3.14) which indicates a morphological transition and becomes zero in this case. Similar considerations can be inquired about the first term of the numerator of Eq. (3.61). Therefore, the shorthand notation for the above equation is:

$$V_{i,jk,pqr} = h_i \frac{ (\beta_{ij,kq} \cdot \mathbf{h}_{ij,kq}) (\beta_{ip,qr} \cdot \mathbf{h}_{ip,qr}) }{ 6 \det \mathbf{N}_{ijk} \det \mathbf{N}_{ipq} \det \mathbf{N}_{iqr} } . \quad (3.62)$$

The tetrahedra volumes can be summed up and the coefficients of the third order polynomial can easily be determined to calculate the volume of a convex crystal:

$$V^\lambda = \sum_{(i,j,k)} C_{ijk}^\lambda h_i h_j h_k . \quad (3.63)$$

This formula is different for every C-morphology because for every morphology the faces must be triangulated in a different way. However, for S- and T-morphologies the coefficients are inherited from the enclosed C-morphology except that some terms cancel each other out, i.e., terms in the numerator of Eq. (3.62) become zero when a morphological boundary is reached.

The surface area of the crystal can be determined directly using the coefficients of the volume equation (3.63). If the above equation is compared to the classical equa-

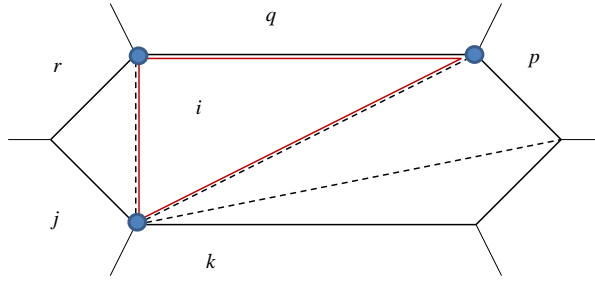


**Figure 3.10:** The volume of a polyhedron can be obtained by decomposing it into tetrahedra whose common vertex is the crystal center from where the distances  $h_i$  are measured.

tion for the determination of the volume of a polyhedron,  $V = \frac{1}{3} \sum_i A_i h_i$ , it follows that Cardew (1985)

$$A_i^\lambda = 3 \sum_{(j,k)} C_{ijk}^\lambda h_j h_k. \quad (3.64)$$

### 3.4 A more Complex Example – 4D Paracetamol Crystal

The analysis taken out so far is useful for a better understanding of the structure of the accessible region in  $\mathbf{h}$ -space. It is possible to calculate for example the volume directly if the state is known – without calculating the vertices of the crystal polyhedron. For simple systems as discussed in the previous sections this can of course also be done manually but as the crystal coordinate systems become skew and the number of faces increases, it is advantageous to take out the above calculations with a computer program. As an example for such a slightly more complex example we discuss the evolution of paracetamol.

For this, a state space analysis is taken out as described in the previous sections, see Sec. 3.4.1. Then in Sec. 3.4.2 a simple process model for the (batch) growth of a single crystal is presented. The solution of the model under variation of the cooling policy is discussed in Sec. 3.4.3.

#### 3.4.1 Geometry of Monoclinic Paracetamol

Monoclinic paracetamol has space group symmetry  $P2_1/a$  (unit cell parameters  $a = 12.651 \text{ \AA}$ ,  $b = 8.887 \text{ \AA}$ ,  $c = 7.236 \text{ \AA}$ ,  $\beta = 114.848^\circ$ ) and thus exhibits point-group symmetry  $2/m$  (Boerrigter et al., 2002). The symmetry elements of this space group are an inversion center, a twofold rotation axis and a mirror plane, see Fig. 3.11. In an article by Ristic et al. (2001) face-specific growth rates as a function of supersaturation have been determined for the forms  $\{1, 1, 0\}$ ,  $\{2, 0, 1\}$ ,  $\{0, 1, 1\}$ , and  $\{0, 0, 1\}$ . Their distances to the crystal center are denoted by  $h_1$ ,  $h_2$ ,  $h_3$ ,  $h_4$ , respectively, see the upper crystal shape in Fig. 3.11. If these forms are taken into account for a state space analysis as described in the above sections, it is found, that overall 13 qualitatively different C-

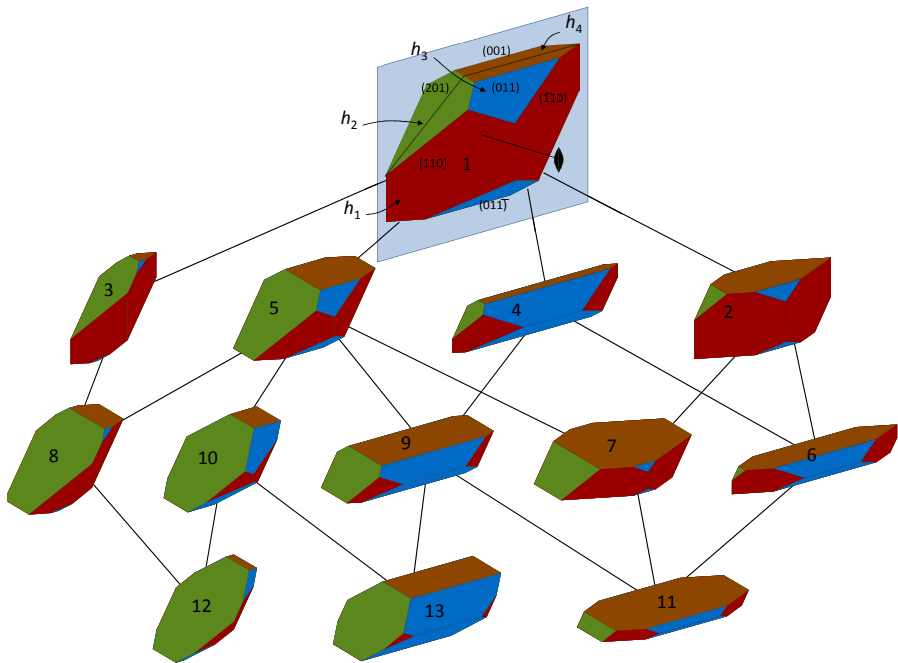


Figure 3.11: The 13 C-morphologies of Paracetamol.

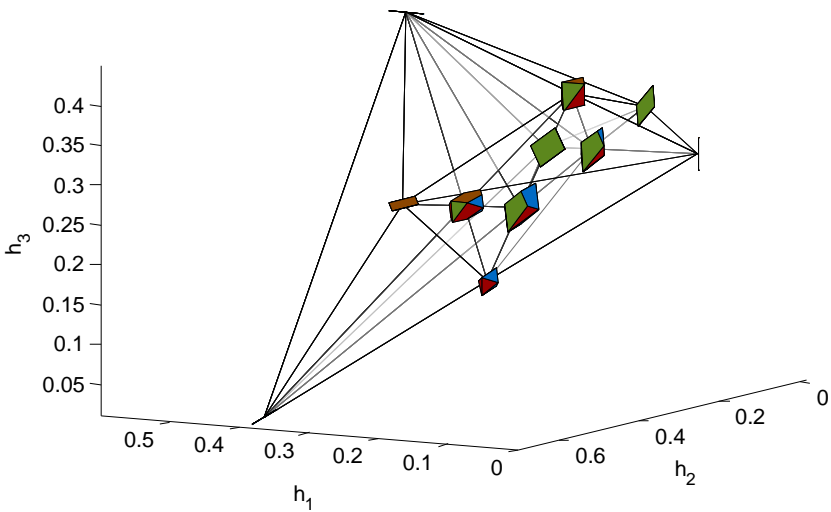


Figure 3.12: The facets of the paracetamol morphology cone in 4D  $h$ -space are 3D polyhedra (mostly tetrahedra) as can be seen from the projection of the morphology cone into the subspace spanned by  $h_1$ ,  $h_2$  and  $h_3$ . The morphologies shown lie on the edges of the morphology cone.

morphologies are obtained which are shown in Fig. 3.11. In Fig. 3.12 the projection of the morphology cone into the space spanned by  $h_1$ ,  $h_2$ , and  $h_3$  is shown along with the (partially degenerated) crystal shapes existing on the edges of the morphology cones. The matrices  $\mathbf{B}^\circ$  and  $\mathbf{B}^\sim$  of the joint morphology cone, see Eq.s (3.29), (3.30), are given in Tab. 3.1. Additionally, the outer boundary normals (rows of  $\mathbf{B}^\circ$  and  $\mathbf{B}^\sim$ ) of the 13 morphology domains are given. In Tab. 3.2 the coefficients required to determine volume and surface area are presented for the C-morphologies which occur in the case study.

### 3.4.2 A Simple Process Model

A paracetamol crystal is assumed to be surrounded by a liquid phase consisting of water and paracetamol dissolved therein. The system is cooled below the saturation temperature and thus a supersaturation is built up which induces crystal growth.

The dynamic evolution of the state of the crystal is captured by Eq. (3.46). Let  $m_{L,A}$  be the mass of dissolved paracetamol,  $m_{L,B}$  the mass of water and  $T$  the temperature which is assumed to not vary spatially within the whole system (crystal and liquid). The volume of the crystal is denoted by  $V_S$  and its density is  $\rho_S$ . If the mass of the solvent is assumed to be constant, the dynamic evolution of the liquid phase composition is fully captured by the differential equation for the solute which describes the transfer of dissolved paracetamol to the solid phase:

$$\frac{dm_{L,A}}{dt} = -\rho_S \mathbf{G} \cdot \nabla_{\mathbf{h}} V_S(\mathbf{h}). \quad (3.65)$$

For the practical implementation Eq. (3.64) is used since

$$\frac{\partial V}{\partial h_i} = A_i. \quad (3.66)$$

The face-specific growth rates of paracetamol were measured by Ristic et al. (2001). We have used polynomials to fit the growth laws (values are given in Tab. 3.3):

$$G_1 = \begin{cases} g_{1,1}\sigma & \sigma < 0.1076 \\ g_{1,2}\sigma^2 + g_{1,3}\sigma + g_{1,4} & \text{otherwise} \end{cases} \quad (3.67a)$$

$$G_2 = g_{2,1}\sigma^3 + g_{2,2}\sigma^2 + g_{2,3}\sigma \quad (3.67b)$$

$$G_3 = g_{3,1}\sigma^3 + g_{3,2}\sigma^2 + g_{3,3}\sigma \quad (3.67c)$$

$$G_4 = \begin{cases} g_{4,1}\sigma^2 + g_{4,2}\sigma & \sigma < 0.0533 \\ g_{4,3}\sigma^3 + g_{4,4}\sigma^2 + g_{4,5}\sigma & \text{otherwise} \end{cases}. \quad (3.67d)$$

The supersaturation is defined as:

$$\sigma = \frac{x - x_{\text{sat}}}{x_{\text{sat}}}. \quad (3.68)$$

The equilibrium mole fraction is given by Hojjati and Rohani (2006)

$$\ln x_{\text{sat}} = b_1 + \frac{b_2}{T} + b_3 \ln T, \quad (3.69)$$



**Table 3.1:** Boundary matrices of the joint morphology cone of paracetamol (left). The boundary matrices of the thirteen C-morphologies can be assembled from the boundary matrices of the joint morphology using only selected rows (right)

Transition and disappearance boundary matrices												No.	Boundary vectors (rows)
$\mathbf{B}^{\sim} = \begin{bmatrix} -0.714 & 0.598 & 0 & 0.363 & (1) \\ -0.609 & 0 & 0.793 & 0 & (2) \\ -0.523 & 0.438 & 0.681 & -0.266 & (3) \\ -0.426 & -0.714 & 0.555 & 0 & (4) \\ -0.418 & 0.35 & 0.544 & -0.637 & (5) \\ 0 & -1 & 0 & 0 & (6) \\ 0 & 0 & 0 & -1 & (7) \\ 0.418 & -0.35 & -0.544 & 0.637 & (8) \\ 0.426 & 0.714 & -0.555 & 0 & (9) \\ 0.523 & -0.438 & -0.681 & 0.266 & (10) \\ 0.609 & 0 & -0.793 & 0 & (11) \\ 0.714 & -0.598 & 0 & -0.363 & (12) \end{bmatrix}$												1	(7), (8), (10), (16), (17)
												2	(1), (6), (12), (16), (17)
												3	(4), (10), (13), (17)
												4	(3), (8), (10), (17)
												5	(2), (7), (8), (14), (16)
												6	(1), (3), (12), (17)
												7	(2), (6), (12), (16)
												8	(2), (4), (13), (14)
												9	(2), (3), (8), (14)
												10	(5), (7), (10), (16)
												11	(2), (3), (11), (12)
												12	(5), (9), (10), (13)
												13	(3), (5), (10), (15)

$$\mathbf{B}^{\emptyset} = \begin{bmatrix} -0.714 & 0.598 & 0 & -0.363 & (13) \\ -0.523 & -0.438 & 0.681 & -0.266 & (14) \\ -0.518 & 0 & 0.674 & -0.526 & (15) \\ 0 & 0 & -0.788 & 0.615 & (16) \\ 0.543 & -0.454 & -0.706 & 0 & (17) \end{bmatrix}$$



Table 3.3: Parameters for the simulation of the paracetamol system.

$[b_1, b_2, b_3]$	$[-298.59288, 10495.900, 45.11344]$
$[N_A, N_B]$	$[151.17 \text{ kg/kmol}, 18.02 \text{ kg/kmol}]$
$[g_{1,1}, g_{1,2}, g_{1,3}, g_{1,4}]$	$[1.041 \times 10^{-8}, 2.125 \times 10^{-6}, -2.142 \times 10^{-7}, -4.366 \times 10^{-10}]$
$[g_{2,1}, g_{2,2}, g_{2,3}]$	$[-5.883 \times 10^{-6}, 1.847 \times 10^{-6}, -1.131 \times 10^{-9}]$
$[g_{3,1}, g_{3,2}, g_{3,3}]$	$[-2.238 \times 10^{-6}, 7.461 \times 10^{-7}, 5.940 \times 10^{-8}]$
$[g_{4,1}, g_{4,2}, g_{4,3}, g_{4,4}, g_{4,5}]$	$[-1.272 \times 10^{-8}, 2.431 \times 10^{-8}, -5.699 \times 10^{-6}, 1.867 \times 10^{-6}, -5.975 \times 10^{-8}]$

where

$$x = \frac{m_{L,A}}{m_{L,A} + \frac{N_A}{N_B} m_{L,B}}. \quad (3.70)$$

The temperature in the system is assumed to be perfectly controllable and given by

$$T = T_0 - (T_0 - T_f) \left( \frac{t}{t_f} \right)^p, \quad (3.71)$$

where  $T_0$  and  $T_f$  are the initial and final temperature, respectively,  $t_f$  is the end-time and  $p$  is a parameter which determines the shape of the temperature curve.

### 3.4.3 Case Study – Variation of the Cooling Policy

The numerical solution to the shape evolution equation (3.46) together with the mass balance (3.65) has been computed. The parameter  $p$  of the temperature profiles according to Eq. (3.71) has been varied between 1 and 4. The initial conditions, temperature and supersaturation profiles, as well as the resulting crystal shapes are shown in Fig. 3.13. It can be seen that the plate-like initial crystal shape which is typically produced under high-supersaturation conditions Garekani et al. (1999); Ristic et al. (2001) develops to a more compact crystal. For the linear cooling profile ( $p = 1$ ) the  $h_2$ - and  $h_3$ -faces grow out. The supersaturation profile for this case is such that at a relatively early stage a maximum is reached. After this the supersaturation is kept around 0.1 and decreases slowly. In this regime  $G_2$  and  $G_3$  are large compared to  $G_1$  and  $G_4$ . For higher values of  $p$  the maximum of the supersaturation is shifted to later times and the supersaturation at the end of the process is increased as  $p$  is increased. However, the growth rate  $G_1$  compared to all other growth rates is significantly increased at higher supersaturations. Therefore, the  $h_2$ - and  $h_3$ -faces occur. This is clearly seen for the final crystal shape which is produced from the temperature profile with  $p = 4$ . Here, the fraction of  $h_2$ - and  $h_3$ -surfaces is almost 22%.

The practical implications of the different cooling strategies is not a direct concern of this section. This example shall only serve to show the applicability of the results which have been produced in the above sections. Of course, the results we have shown here could have been obtained also by using the shape evolution equation and constructing the crystal polyhedron in every time step to check whether a structural evolution like disappearance of faces has happened in order to correctly integrate the system. It would also be necessary to compute the surface area from the crystal polyhedron when the coupling to the mass balance is included. The computation of the crystal polyhedron can in principle be done by exhaustively checking all intersections between crystal planes. Alternatively, a primal-dual method for computing the vertices can be used Bremner et al. (1998). However, using the techniques described above, the computation of the polyhedron is avoided and only the preprocessing of the boundaries in state space, coefficients for volume computation and velocity delimiter matrices must be performed prior to the integration. By this, the CPU-time (measured with the Matlab functions tic-toc) for integration of the paracetamol system (2.64 s on a 3GHz Intel Core Duo with Windows XP and Matlab R2010b) is reduced by a factor 134 compared to the exhaustive checking (353 s) and reduced by a factor of 5.5 compared to a primal-dual method (14.26 s). The ode-solver (ode23 in

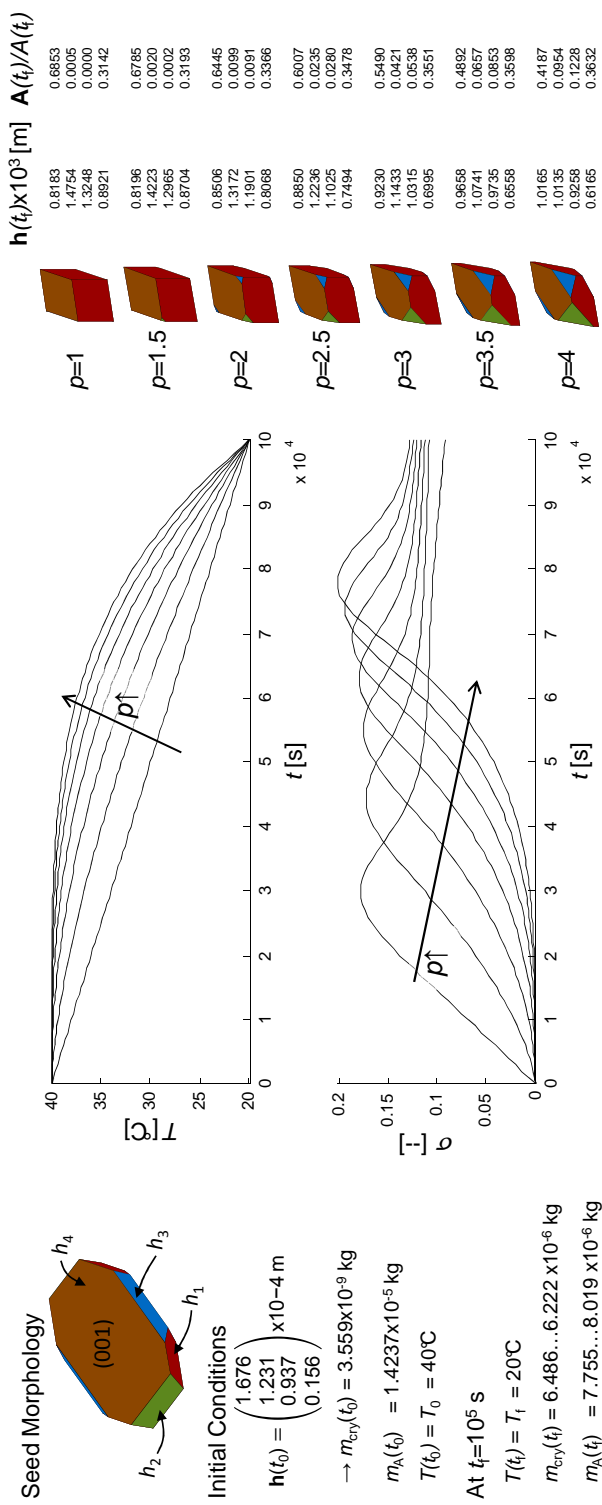


**Figure 3.13:** Simulation of paracetamol growth with different temperature profiles. The selection of the parameter  $p$  defines the shape of the temperature profile, see Eq. (3.71).

Matlab) was set to a maximum time step of 100 s. The determination of the morphology cones and volume evaluation coefficients requires circa 3 s, i.e. it is computationally advantageous to determine the morphology cones and to avoid the computation of the polyhedron even for the determination of a single crystal shape trajectory.

### 3.5 Conclusion

In this chapter the shape evolution of convex, polyhedral crystals has been discussed with regard to an elegant and efficient way of formulating the model equations accounting for appearance and disappearance of crystal faces. Previous models required the thorough detection of discrete events (face and edge appearance or disappearance) in every integration step. With the approach introduced above the shape analysis is separated from the integration of the evolution equations and can be taken out in a preprocessing step. The shape analysis as discussed in this paper is an algorithm which enables the computation of all theoretically possible shapes which can be obtained from a given set of faces. Due to the possibly high dimensionality of the resulting state space the complexity of that analysis increases fast. Therefore, only symmetric crystals can be analysed in a justifiable time.

Practically, the results of this chapter can be used to implement differential equations for crystal shape evolution in an efficient way. Albeit this may not be required if a single crystal trajectory has to be calculated, the computational benefit is of great value if many crystal trajectories must be integrated. This is the case in optimization tasks and in the case of crystal populations in mass crystallizers.

More important is that from the methodological point of view, the analysis of the state space gains a deeper insight into the shape evolution process. The transparency with which the hybrid dynamic equations of shape evolution are formulated paces the way towards a profound framework for large populations of convex crystals.

*What I cannot create I do not understand.*

---

Richard P. Feynman

Photograph of his blackboard at the time of his death  
shown in Stephen Hawking's *The Universe in a Nutshell*

## Chapter 4

# Shape Evolution of Crystal Populations

In the previous chapter we have learned how a *single* faceted crystal evolves and travels through  $\mathbf{h}$ -space. It enters different regions in which distinguished geometrical properties occur, that is particularly the presence of certain edges and faces on the crystal surface. The growth of the crystal influences the dynamics of its environment, especially the concentration in the surrounding continuous phase. In this chapter it will be dissected how an essential part of the dynamics of a whole *population* of faceted crystals can be synthesized from insights we have gained on the dynamics of a single crystal. The population balance that has been discussed in Ch. 2 is the natural implement to characterize the dynamics of the number density in  $\mathbf{h}$ -space.

At first, the population balance is introduced for an example system: Potassium dihydrogen phosphate (KDP) crystal populations are modeled in Sec. 4.1. This system is relatively simple to handle since for the process conditions we shall consider, the number of real crystallographic faces is constant. An algorithm for the computation of numerical solutions is developed along this 2D system. The kinetic coefficients required as input to the population balance model are identified in Ch. 6 on the basis of experiments presented in Ch. 5 where KDP crystallization from water is observed. Disappearance and appearance of crystal faces enables the structuring of the state space as it has been shown in the preceding chapter. In Ch. 2 generic equations have been developed which enable the incorporation of these structures in a population balance model. This is – as the second step – exemplified for a simple 2D system in Sec. 4.2. Sec. 4.3 discusses the generalization of the concept to  $n$ D state spaces. Sec. 4.4 summarizes this chapter in brief.

### 4.1 Evolving Potassium Dihydrogen Phosphate (KDP) Populations

Potassium dihydrogen phosphate (KDP) is a popular model substance for crystal research for several reasons. It is well soluble in water, not hazardous, cheap and it produces well developed faceted crystals. This is especially due to the relatively high

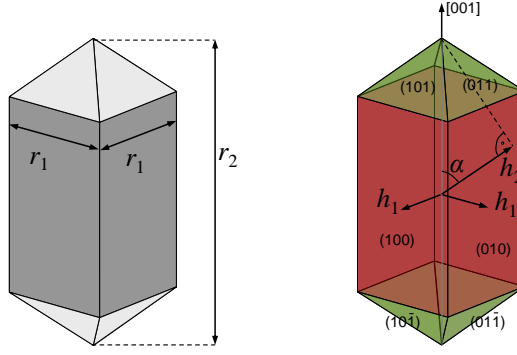


**Figure 4.1:** Quantification of the crystal shape according to Ma and Braatz (2001) and Gunawan et al. (2002) (left) and as used in this work (right).

hardness which avoids abrasion at stirrers and in sampling loops. The identification of the kinetic parameters for KDP solution crystallization has been discussed by Gunawan et al. (2002). For this, a population balance model along with a mass balance is fitted to experimental data of a whole crystallization experiment. The parameters identified involve face-specific growth rates and a nucleation rate. Ma et al. (2002a) employ these parameters for simulation studies with a high resolution algorithm. In Ma et al. (2002b) the model is further refined by compartmentalization of the crystallizer and optimal control studies are taken out.

Hereafter, the crystal system KDP is introduced, Sec. 4.1.1, and the population balance model derived, similar to the above cited works of Braatz and coworkers, see Sec. 4.1.2. Albeit the aforementioned high resolution scheme provides accurate solutions, as an alternative, a further development of the popular 1D moving pivot technique of Kumar and Ramkrishna for pure growth and nucleation processes is developed in Sec. 4.1.3. Finally, in Sec. 4.1.4, simulation results are presented for a reference experiment which is further discussed in Ch. 6.

#### 4.1.1 Potassium Dihydrogen Phosphate

Potassium dihydrogen phosphate (KDP) crystallizes in space group  $I\bar{4}2d$  (Yang et al., 2006) and thus has point-group symmetry  $\bar{4}2m$  (Borchardt-Ott, 2009); the lengths of the crystallographic axis are  $a = 74.51$  nm and  $c = 69.73$  nm (Mathew and Wong-Ng, 1995). KDP grown from water is bound by the crystallographic faces  $\{001\}$  and  $\{011\}$  (Yang et al., 2006), as depicted in Fig. 4.1. Assuming that the crystal exhibits perfect symmetry, the geometry is quantified by a 2D state vector containing the distances to the prismatic  $\{001\}$  and pyramidal  $\{011\}$  faces:

$$\mathbf{h} = \begin{pmatrix} h_1 \\ h_2 \end{pmatrix} = \begin{pmatrix} h_{\{001\}} \\ h_{\{011\}} \end{pmatrix}, \quad (4.1)$$



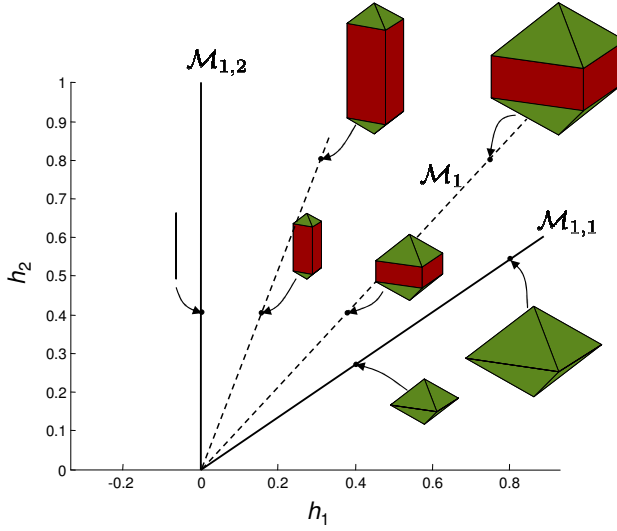


Figure 4.2: Morphology cone of KDP.

see Fig. 4.1 (right). Using the partitioning of the state space introduced in the previous chapter, the region of the state space in which both pyramidal and prismatic faces are real is given by the morphology cone

$$\mathcal{M}_1 = \{\mathbf{h} : \mathbf{B}\mathbf{h} < \mathbf{0}\}, \quad \mathbf{B} \approx \begin{bmatrix} 0.5638 & -0.8259 \\ -1 & 0 \end{bmatrix}, \quad (4.2)$$

which is depicted in Fig. 4.2. It can be seen that on the two bounding lines of the morphology cone, the prismatic ( $\mathcal{M}_{1,1}$ , upper row of  $\mathbf{B}$ ) and pyramidal ( $\mathcal{M}_{1,2}$ , lower row of  $\mathbf{B}$ ) crystal faces disappear. Clearly, the disappearance of the pyramidal faces corresponds to the disappearance of the crystal, see the indicated 'line' crystal beneath  $\mathcal{M}_{1,2}$ . Within the morphology cone, the crystal habit varies. For instance, more compact shapes are found above the  $\mathcal{M}_{1,1}$  boundary, see the two shapes drawn on the lower dotted line in Fig. 4.2 (this line does not stand for a morphological manifold but shall serve to lead the eye). On the upper dotted line (lower  $h_1$ -values), crystals are more elongated while the height is kept constant in comparison to the crystals on the lower gray line.

An alternative to the  $\mathbf{h}$ -vector is to measure the side length of the pyramid's base square,  $r_1$ , and the distance between the pyramid's apices,  $r_2$ , as used by Ma and Braatz (2001) and Gunawan et al. (2002), see Fig. 4.1. The transformation between  $\mathbf{h}$ - and  $\mathbf{r}$ -representation is

$$\begin{pmatrix} h_1 \\ h_2 \end{pmatrix} = \begin{pmatrix} \frac{1}{2}r_1 \\ \frac{\cos \alpha}{2}r_2 \end{pmatrix}, \quad \cos \alpha = \mathbf{n}_{\{001\}} \cdot \mathbf{n}_{[010]} \approx 0.73073, \quad (4.3)$$

see also Fig. 4.1. As a side note it should be mentioned that the formula for the volume calculations used by Ma et al. (2002a,b):

$$V_{\text{cry}}(\mathbf{r}) = \frac{1}{3}r_1^3 + (r_2 - r_1)r_1^2, \quad (4.4)$$

is not correct. They assume an angle of  $135^\circ$  between the pyramidal and prismatic faces but its value is actually  $\approx 133.02^\circ$ . The error which is made by this assumption is small, but for the sake of completeness we give here the right formula:

$$V_{\text{cry}}(\mathbf{r}) = r_1^2 r_2 - \frac{2c}{3a} r_1^3, \quad (4.5)$$

where  $a$  and  $c$  are the lengths of the crystallographic axes, see the work of Zinser (2010). Using the volume computation scheme applicable to crystals described by  $\mathbf{h}$ -vectors, see Sec. 3.3, the volume is obtained by

$$V_{\text{cry}}(\mathbf{h}) \approx 10.9479 h_1^2 h_2 - 4.9825 h_1^3. \quad (4.6)$$

#### 4.1.1.1 Kinetic Parameters from Literature

In Gunawan et al. (2002) the growth and nucleation rates in the  $\mathbf{r}$ -framework, denoted by  $\mathbf{G}^r = (G_1^r, G_2^r)^T$  as a function of supersaturation have been determined. In two simulation studies (Ma et al., 2002a,b), authors of the same group refer to Gunawan et al. (2002) for the kinetic parameters which are, however, not the same. Since the simulation work appeared later, we assume that the kinetic data given in (Ma et al., 2002a,b) is appropriate. The growth rates in the  $\mathbf{r}$ -framework are:

$$G_1^r = k_1^r \sigma^{g_1^r}, \quad k_1^r = 12.21 \times 10^{-6} \text{ m/s}, \quad g_1^r = 1.48, \quad (4.7a)$$

$$G_2^r = k_2^r \sigma^{g_2^r}, \quad k_2^r = 100.75 \times 10^{-6} \text{ m/s}, \quad g_2^r = 1.74. \quad (4.7b)$$

Transformation to the  $\mathbf{h}$ -framework using Eq. (4.3) yields:

$$G_1 = k_1 \sigma^{g_1}, \quad k_1 = 6.105 \times 10^{-6} \text{ m/s}, \quad g_1 = 1.48, \quad (4.8a)$$

$$G_2 = k_2 \sigma^{g_2}, \quad k_2 = 36.8105 \times 10^{-6} \text{ m/s}, \quad g_2 = 1.74, \quad (4.8b)$$

which is depicted in Fig. 4.3. Gunawan et al. (2002) observed large amounts of nuclei in their experiments and estimated the following nucleation rate<sup>1</sup> (the values again taken from the later papers of Ma et al. (2002a,b) and not from Gunawan et al. (2002) wherein their determination is described):

$$B_{\text{nuc}} = k_{\text{nuc}} \sigma^b V_{\text{cry, pop}} V, \quad k_{\text{nuc}} = 3.75 \times 10^{13} \#/\text{m}^3/\text{m}^3/\text{s}, \quad b = 2.04, \quad (4.9)$$

where

$$V_{\text{cry, pop}}(t) = \int_{\mathcal{M}_1} f(\mathbf{h}, t) V_{\text{cry}}(\mathbf{h}) d\mathbf{h}_1 d\mathbf{h}_2 \quad (4.10)$$

is the volume of the crystalline phase and  $V$  is the volume of the overall system (crystalline plus continuous phase). The dependency of the nucleation rate on the mass of the crystal population accounts for the fact that in the environment of a crystalline phase, nucleation is more probable to occur (Mullin, 2001).

<sup>1</sup>Note that the value for  $k_{\text{nuc}}$  given in Eq. (4.9) has been divided by the volume of the system and thus this volume multiplication is added because the system volume in Ma et al. (2002b,a) is different from the value used in the simulations and experiments of this work.

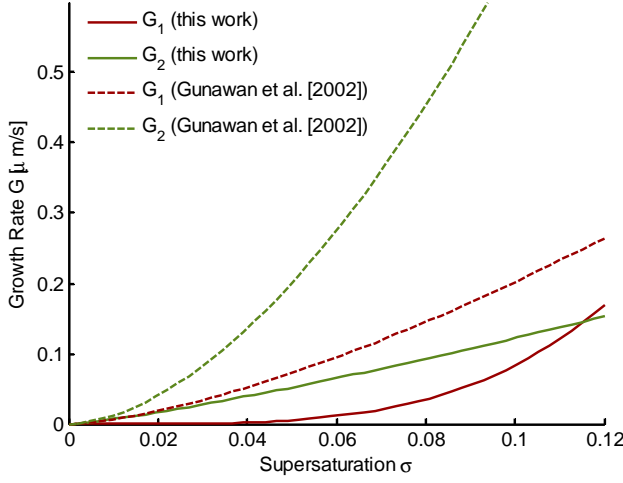


**Figure 4.3:** Comparison of the KDP growth kinetics measured by Gunawan et al. (2002) and determined in this work.

#### 4.1.1.2 Kinetic Parameters Determined in Ch. 6

In Ch. 6 of this work the following growth rates have been determined (Fig. 4.3):

$$G_1 = k_1 \sigma^{g_1}, \quad k_1 = 643.2 \times 10^{-6} \text{ m/s}, \quad g_1 = 3.89, \quad (4.11a)$$

$$G_2 = k_2 \sigma^{g_2}, \quad k_2 = 2.07 \times 10^{-6} \text{ m/s}, \quad g_2 = 1.23. \quad (4.11b)$$

In the experiments which were used for the estimation of the growth rates, the amount nucleation was relatively low. Therefore, the nucleation rate could not be determined with the sufficient accuracy. As the simulation studies in Sec. 4.1.4.2 suggest, this is also not necessary, since the state of the continuous phase could be predicted well even for a process model that neglects nucleation and includes only growth of the seed population.

#### 4.1.1.3 Accessible Morphology Domain

In principle it is possible that the prismatic  $\{001\}$  faces disappear from the crystal surface. However, if only growth is considered and only crystals with shapes within the interior of  $\mathcal{M}_1$  are seeded and all nuclei occur within  $\mathcal{M}_1$ , the faces of the morphology cone cannot be reached if  $G_2 > 0.6827G_1^2$ . This is the case for both growth laws (Eq.s (4.8), (4.11)) within large parts of the supersaturation observed in the experiments and simulations. Also, if the crystals are far away from the morphological boundary and if  $G_2 \leq 0.6827G_1$  only for relatively short times, the boundary will not be reached. This was the case in all experiments and simulations we show in the following. Hence, for practical calculations none of the morphological boundaries will

<sup>2</sup>The value 0.6827 is obtained from dividing 0.5638 by 0.8259 the entries of the boundary matrix **B** see Eq. (4.2).

be reached which means for the shape evolution of a single crystal that the differential equation for the crystal state is simply given by

$$\frac{d}{dt} \begin{pmatrix} h_1 \\ h_2 \end{pmatrix} = \begin{pmatrix} k_1 \sigma^{g_1} \\ k_2 \sigma^{g_2} \end{pmatrix}, \quad (4.12)$$

i.e., the velocity delimiter matrix  $\mathbf{D}$ , with which switches between morphological domains are accounted for according to Ch. 3, can be omitted.

### 4.1.2 Population Balance Model for KDP

Because Eq. (4.12) is a continuously evolving system, the population balance equation reads for a batch crystallizer, according to Sec. 2.6.1, see also Cardew (1985); Ma et al. (2002a); Ramkrishna (2000),

$$\frac{\partial f}{\partial t} + \nabla_{\mathbf{h}} \cdot (\mathbf{G}f) = B_{\text{nuc}} \delta(\mathbf{h} - \mathbf{h}_{\text{nuc}}), \quad t > 0, \mathbf{h} \in \mathcal{M}_1, \quad (4.13)$$

subject to the initial, boundary and regularity conditions

$$\text{I.C. : } f(t = 0, \mathbf{h}) = f_{\text{seed}}(\mathbf{h}), \quad (4.14a)$$

$$\text{R.C. : } f(t, \mathbf{h}) \rightarrow 0, \quad |\mathbf{h}| \rightarrow \infty, \quad (4.14b)$$

$$\text{B.C. : } \mathbf{b} \cdot \mathbf{G}f = 0, \quad \mathbf{h} \in \mathcal{M}_{1,1} \cup \mathcal{M}_{1,2}. \quad (4.14c)$$

The right hand side of Eq. (4.13) accounts for nucleation which is assumed to occur at a specified point  $\mathbf{h}_{\text{nuc}}$ . Clearly, the nucleation as well as the growth rate depend on the supersaturation which is in this work considered to be induced by cooling of the solution below the equilibrium. Mullin (2001) has measured the solubility of KDP in water; supplemented by own measurements in the relevant temperature interval, the solubility has been fitted to a parabolic curve:

$$w_{\text{KDP,sat}}(T) = 5.5843 \times 10^{-5} T^2 - 0.028159 T + 3.6832, \quad (4.15)$$

see also Fig. 4.4.  $w_{\text{KDP,sat}}$  is the ratio of the maximally soluble mass of KDP per unit mass of water, thus has the unit  $[\text{kg}_{\text{KDP}}/\text{kg}_{\text{H}_2\text{O}}]$ .

Mass balances for the batch crystallization must account for the transfer of dissolved KDP (dis) to the crystalline state (cry) due to growth (gr) and nucleation (nuc), whereas the amount of solvent (water) does not change:

$$\frac{dm_{\text{H}_2\text{O}}}{dt} = 0, \quad m_{\text{H}_2\text{O}}(t = 0) = m_{\text{H}_2\text{O},0}, \quad (4.16a)$$

$$\frac{dm_{\text{KDP,cry}}}{dt} = \dot{m}_{\text{KDP,gr}} + \dot{m}_{\text{KDP,nuc}}, \quad m_{\text{KDP,cry}}(t = 0) = m_{\text{KDP,cry},0}, \quad (4.16b)$$

$$\frac{dm_{\text{KDP,dis}}}{dt} = -\dot{m}_{\text{KDP,gr}} - \dot{m}_{\text{KDP,nuc}}, \quad m_{\text{KDP,dis}}(t = 0) = m_{\text{KDP,dis},0}. \quad (4.16c)$$

The amount of crystal mass is also obtained from the number density:

$$m_{\text{KDP,cry}} = \rho_{\text{cry}} \int_{\mathcal{M}_1} V_{\text{cry}}(\mathbf{h}) f(\mathbf{h}, t) dV_{\mathbf{h}}, \quad (4.17)$$

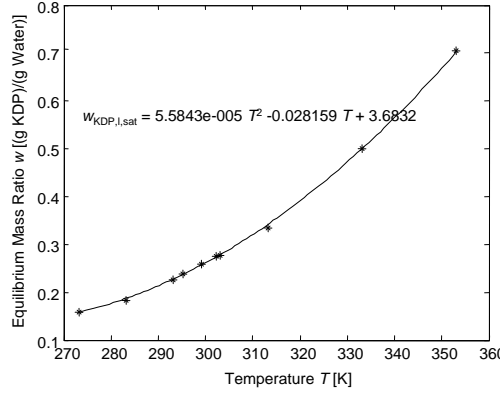


**Figure 4.4:** Solubility of KDP in water, data points taken from Mullin (2001) and own measurements.

that is, Eq. (4.16b) can be omitted if  $f$  is known. Recognizing that the r.h.s. of Eq. (4.16b) equals the r.h.s. of Eq. (4.16c) except for the sign, the amount of dissolved KDP can be calculated as:

$$m_{\text{KDP},\text{dis}} = m_{\text{KDP},\text{dis},0} - (m_{\text{KDP},\text{cry}} - m_{\text{KDP},\text{cry},0}) . \quad (4.18)$$

The concentration of the dissolved KDP in the fluid phase is in this work defined by the mass-ratio of KDP and solvent (Mullin, 2001):

$$w_{\text{KDP}} = \frac{m_{\text{KDP},\text{dis}}}{m_{\text{H}_2\text{O}}} = \left[ \frac{\text{kg}_{\text{KDP}}}{\text{kg}_{\text{H}_2\text{O}}} \right] . \quad (4.19)$$

The supersaturation is defined by (Mullin, 2001; Ma et al., 2002a):

$$\sigma = \frac{w_{\text{KDP}}}{w_{\text{KDP},\text{sat}}} - 1 . \quad (4.20)$$

The temperature is in general obtained from an energy balance. Within this work, however, temperature profiles are pretended which can be accurately realized by cooling the batch crystallizer with a thermostat if the heat of crystallization is small. For the remainder of this work, the heat of crystallization is neglected. The set of Eq.s (4.13), (4.14), (4.8) or (4.11), (4.9), (4.15), (4.17), (4.18), (4.19), (4.20) together with a temperature profile makes up the crystallizer model.

### 4.1.3 Numerical Scheme

In order to solve the population balance numerically, an extension of the well established moving pivot technique developed by Kumar and Ramkrishna (1996b, 1997) is employed. In principle, in this method, the evolution of representative particles, so called pivots, is tracked and additionally the change of the number of particles which are represented by the pivot. The collection of pivots is regarded as a moving grid, thus covers different parts of the state space at different instances. The region in which nucleation occurs may thus not be contained in the region of the original

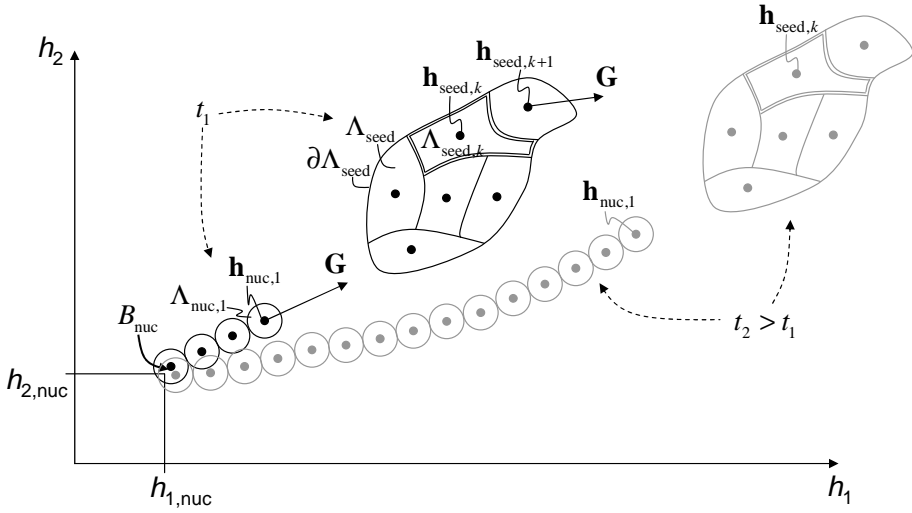


**Figure 4.5:** Numerical scheme at two instances. The region in which the seed population exists is partitioned into finite cells which are each represented by a state in their interior. The representative states (and thus the cell) is moved in accordance to the vector field  $\mathbf{G}$ . Nucleation is included by continuously adding new representative cells in the vicinity of the nucleation point. Also the nucleation cells move in accordance to  $\mathbf{G}$ , i.e., a new cell must be started when the nucleation point is not covered by the closest cell.

moving grid. Therefore, new pivots are continuously added around the nucleation point in order to absorb the nucleated particles (Kumar and Ramkrishna, 1997). For the multivariate case discussed in the following, the crystal distribution is separated into two parts: (i) crystals which have been seeded at  $t = 0$  and grow and (ii) crystals which nucleate during the crystallization process and subsequently grow. This separation is sketched in Fig. 4.5: The seed region  $\Lambda_{\text{seed}}$  only moves in the state space whereas the nucleation 'line region' is continuously expanding.

Discretization and growth of the seed crystal population is dissected in Sec.s 4.1.3.1 and 4.1.3.2. Sec. 4.1.3.3 explains how nucleation is captured by the numerical scheme.

#### 4.1.3.1 Seeds

Let the domain of interest in which the seeds are located at  $t = 0$  within  $\mathcal{M}_1$  be denoted by  $\Lambda_{\text{seed}}(t = 0)$  which is assumed to be a material control volume.  $\Lambda_{\text{seed}}$  is partitioned into  $n_{\text{seed}}$  cells  $\Lambda_{\text{seed},k}$  which cover  $\Lambda_{\text{seed}}$ , see Fig. 4.5. It can also be seen that every cell contains a representative so called pivot  $\mathbf{h}_{\text{seed},k}$ . The practical partitioning of  $\Lambda_{\text{seed}}$  at  $t = 0$  into cells is explained in a more detail in Sec. 4.1.3.2.

For  $t > 0$  the cells  $\Lambda_{\text{seed},k}$  are time-dependent and move according to the velocity field  $\mathbf{G}$ , i.e., they are – like  $\Lambda_{\text{seed}}$  – material control volumes. Integration of the population balance (4.13) over  $\Lambda_{\text{seed},k}$  yields

$$\int_{\Lambda_{\text{seed},k}} \frac{\partial f}{\partial t} + \nabla_{\mathbf{h}} \cdot (\mathbf{G}f) dV_{\mathbf{h}} = \int_{\Lambda_{\text{seed},k}} B_{\text{nuc}} \delta(\mathbf{h} - \mathbf{h}_{\text{nuc}}) dV_{\mathbf{h}}. \quad (4.21)$$

By the virtue of the transport theorem (Ramkrishna, 2000; Slattery, 1999) we obtain

$$\frac{d}{dt} \int_{\Lambda_{\text{seed},k}} f dV_{\mathbf{h}} = \int_{\Lambda_{\text{seed},k}} B_{\text{nuc}} \delta(\mathbf{h} - \mathbf{h}_{\text{nuc}}) dV_{\mathbf{h}}. \quad (4.22)$$

The number of particles within a cell is

$$N_{\text{seed},k} = \int_{\Lambda_{\text{seed},k}} f dV_{\mathbf{h}}, \quad (4.23)$$

i.e., Eq. (4.22) makes up an evolution equation for this quantity. Usually, the nuclei are significantly smaller than the seed particles, that is,  $\mathbf{h}_{\text{nuc}}$  is not located within  $\Lambda_{\text{seed}}$ . Hence, the integral on the r.h.s of Eq. (4.22) vanishes which gives the trivial differential equation

$$\frac{dN_{\text{seed},k}}{dt} = 0, \quad N_{\text{seed},k}(t=0) = N_{\text{seed},k,0}, \quad k = 1 \dots n_{\text{seed}}. \quad (4.24)$$

Additionally, the motion of the cells must be accounted for. It is assumed that all particles within  $\Lambda_{\text{seed},k}$  are concentrated on the representative pivot  $\mathbf{h}_{\text{seed},k}$ . This pivot can be interpreted as a representative state and moves like a single particle in accordance to the velocity field  $\mathbf{G}$ :

$$\frac{d\mathbf{h}_{\text{seed},k}}{dt} = \mathbf{G}, \quad \mathbf{h}_{\text{seed},k}(t=0) = \mathbf{h}_{\text{seed},k,0}, \quad k = 1 \dots n_{\text{seed}}. \quad (4.25)$$

#### 4.1.3.2 Discretization of the Seed Region

The representative pivots  $\mathbf{h}_{\text{seed},k,0}$  must be chosen in a way that they properly support the approximation of the original number density of the seeds. The projection of  $f_{\text{seed}}$  (see Eq. (4.14a)) on a regular, rectilinear or structured grid would allow a good numerical approximation. However, the number of grid points especially for higher-dimensional state spaces would be relatively large while the possibilities for local grid refinement are limited. Therefore, an unstructured mesh is used that is generated with an algorithm in Matlab along the ideas of Persson and Strang (2004) which is shortly sketched in the following paragraphs.

Firstly, the geometry of the region of interest must be represented. The choice of this region, denoted by  $\Lambda_{\text{seed}} \subset \mathcal{M}_1$ , is in our case only determined by the seed's number density function, i.e., only regions with sufficiently high number densities are taken into account. Preliminary nodes  $\mathbf{p}_{k,0}$ ,  $k = 1, \dots, \nu$  are distributed within the region and passed to a Delaunay triangulation routine which connects the nodes, see Fig. 4.6 (left). This formation is now considered to be a truss with nodes and elastic bars being the connecting lines between nodes. Due to an interaction between connected nodes, they are moved according to the differential equation

$$\frac{d\mathbf{p}}{d\tau} = \mathbf{F}(\mathbf{p}), \quad \mathbf{p}(\tau=0) = \mathbf{p}_0, \quad (4.26)$$

with  $\mathbf{p} = [\mathbf{p}_1, \dots, \mathbf{p}_{\nu}]$  and  $\mathbf{p}_0 = [\mathbf{p}_{1,0}, \dots, \mathbf{p}_{\nu,0}]$ . The velocity function  $\mathbf{F}$  allows to manipulate the mesh with regard to spacing between nodes. This function is chosen such that the equilibrium length between connected nodes is small in parts of the

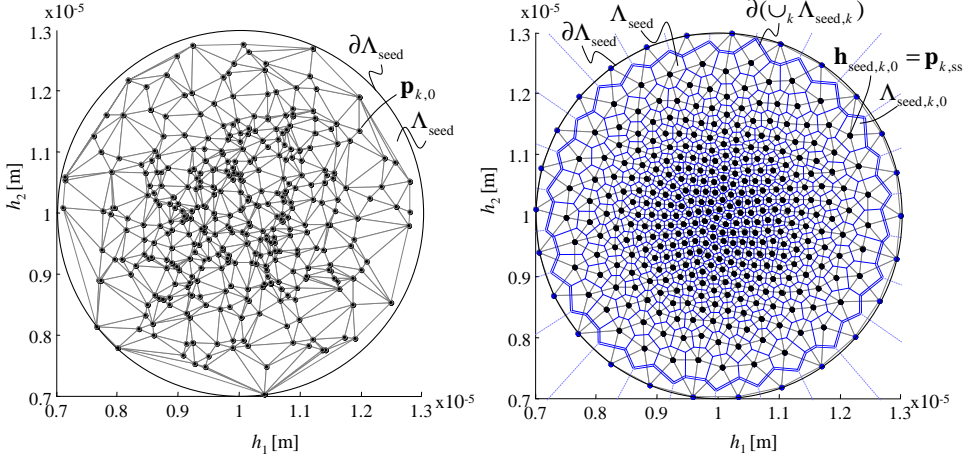


**Figure 4.6:** Meshing of the population region. Left: randomly distributed nodes. Right: equilibrated mesh.

state space with high number densities and sparsely covered with nodes in regions with lower densities. Note that  $\tau$  and  $\mathbf{F}$  have no physical meaning, though a physical analogy has been used for illustration.

The steady state solution of Eq. (4.26),  $\mathbf{F}(\mathbf{p}_{ss}) = \mathbf{0}$ , provides well distributed points  $\mathbf{p}_{k,ss}$ . A Voronoi tessellation is taken out, assigning cells to the nodes  $\mathbf{p}_{ss,k}$  as depicted in Fig. 4.6 (right). The  $n_{\text{seed}}$  cells of finite size<sup>3</sup> are taken as continuously evolving cells  $\Lambda_{\text{seed},k}$  covering nearly the whole region  $\Lambda_{\text{seed}}$ . The nodes  $\mathbf{p}_{ss,k}$  are now the previously introduced pivots  $\mathbf{h}_{\text{seed},k,0}$  and serve as the initial condition to Eq. (4.25). I.e., the remaining network of  $n_{\text{seed}} < \nu$  pivots covers almost the whole region  $\Lambda_{\text{seed}}$ , see Fig. 4.6 (right).

The initial conditions to the seed cell's number equation (4.24) is obtained by integrating the number density function over the cell domain:

$$N_{\text{seed},k,0} = \int_{\Lambda_k} f_{\text{seed}}(\mathbf{h}) dV_{\mathbf{h}}, \quad k = 1, \dots, n_{\text{seed}}. \quad (4.27)$$

With the cell volume

$$V_{\Lambda_{\text{seed},k}} = \int_{\Lambda_{\text{seed},k}} dV_{\mathbf{h}}, \quad (4.28)$$

The approximate number density within a cell is obtained by

$$\hat{f}_{\text{seed},k} = \frac{N_{\text{seed},k}}{V_{\Lambda,k}}, \quad k = 1 \dots n_{\text{seed}}. \quad (4.29)$$

An alternative point of view is to consider the particles being concentrated on the pivots, i.e., the approximated seed part of the number density function is a sum of moving Dirac delta distributions:

$$\hat{f}_{\text{seed}} = \sum_{k=1}^{n_{\text{seed}}} N_{\text{seed},k} \delta(\mathbf{h} - \mathbf{h}_{\text{seed},k}), \quad (4.30)$$

<sup>3</sup>If the mesh parameters are well chosen, this excludes nodes that were moved towards the boundary  $\partial\Lambda$ .



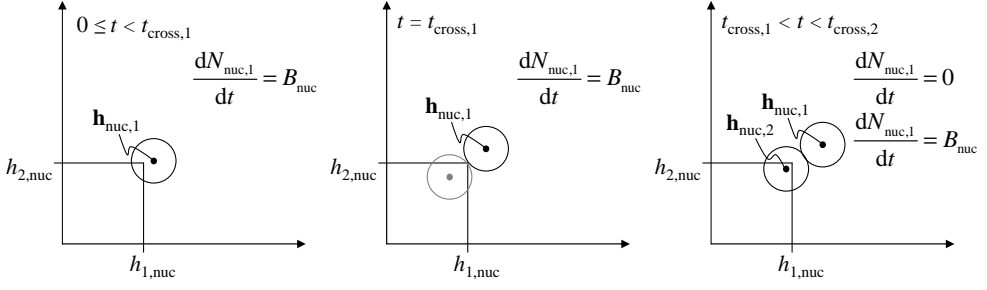


**Figure 4.7:** Numerical scheme to capture nucleation. Left: At the beginning, the nucleation point is covered by the cell  $\Lambda_{\text{nuc},1}$  with the representative state  $\mathbf{h}_{\text{nuc},1}$  which moves with the velocity  $\mathbf{G}$ . Middle: Until the boundary of the first cell crosses the nucleation point, the nuclei are fed to  $N_{\text{nuc},1}$ . Right: If the nucleation point is not covered by the preceding nucleation pivot, a new one is added.

see also Kumar and Ramkrishna (1996a, 1997); Chakraborty and Kumar (2007).

#### 4.1.3.3 Nuclei

Usually, the seed crystals are significantly larger than the nuclei, that is,  $\Lambda_{\text{seed}}$  does not include the domain in state space where nuclei occur. Therefore, a circular cell  $\Lambda_{\text{nuc},1}$  is introduced which covers the nucleation point, see Fig. 4.7 (left). The number of particles within that cell is denoted by  $N_{\text{nuc},1}$ . It is assumed that the number of particles carried by this pivot is initially zero. The evolution equation for  $N_{\text{nuc},1}$  is – similar to Eq. (4.22) – derived by integrating the population balance over  $\Lambda_{\text{nuc},1}$ :

$$\frac{dN_{\text{nuc},1}}{dt} = \int_{\Lambda_{\text{seed},k}(t)} B_{\text{nuc}} \delta(\mathbf{h} - \mathbf{h}_{\text{nuc}}) dV_{\mathbf{h}} \quad (4.31a)$$

$$= B_{\text{nuc}}, \quad N_{\text{nuc},1}(t=0) = 0, \quad 0 < t \leq t_{\text{cross},1}. \quad (4.31b)$$

For the integral on the right hand side the sifting property of the Dirac delta distribution (Bronstein et al., 2001) has been exploited. The time  $t_{\text{cross},1}$  denotes the instant at which the boundary of the cell  $\Lambda_{\text{nuc},1}$  crosses the nucleation point, see Fig. 4.7 (middle). This is the case because the material control volume  $\Lambda_{\text{nuc},1}$  is – like  $\Lambda_{\text{seed},k}$  – moved in accordance to  $\mathbf{G}$  which is reflected by displacing the representative pivot  $\mathbf{h}_{\text{nuc},1}$  according to the differential equation

$$\frac{d\mathbf{h}_{\text{nuc},1}}{dt} = \mathbf{G}, \quad \mathbf{h}_{\text{nuc},1}(t=0) = \mathbf{h}_{\text{nuc},1,0}, \quad (4.32)$$

where the starting point is chosen such that the distance to the nucleation point is small:

$$|\mathbf{h}_{\text{nuc}} - \mathbf{h}_{\text{nuc},1,0}| < \epsilon_{\text{nuc}}. \quad (4.33)$$

The distance  $\epsilon_{\text{nuc}}$  has – for the computations taken out in this work – been chosen to be equal to the radius of the cell, see Fig. 4.7 (middle). From Eq. (4.32) it follows

that  $\Lambda_{\text{nuc},1}$  moves from  $\mathbf{h}_{\text{nuc}}$  away and eventually covers  $\mathbf{h}_{\text{nuc}}$  not any longer. The integration region in Eq. (4.31a) does not include  $\mathbf{h}_{\text{nuc}}$  which results in:

$$\frac{dN_{\text{nuc},1}}{dt} = \int_{\Lambda_{\text{seed},k}(t)} B_{\text{nuc}} \delta(\mathbf{h} - \mathbf{h}_{\text{nuc}}) dV_{\mathbf{h}} \quad (4.34a)$$

$$= 0, \quad t > t_{\text{cross},1}. \quad (4.34b)$$

Therefore, a new material control volume  $\Lambda_{\text{nuc},2}$  is introduced that covers  $\mathbf{h}_{\text{nuc}}$  again. Then the differential equations describing the nucleation-induced part of the crystal population read:

$$\frac{d\mathbf{h}_{\text{nuc},1}}{dt} = \mathbf{G}, \quad \frac{dN_{\text{nuc},1}}{dt} = 0, \quad t_{\text{cross},1} < t, \quad (4.35a)$$

$$\frac{d\mathbf{h}_{\text{nuc},2}}{dt} = \mathbf{G}, \quad \frac{dN_{\text{nuc},2}}{dt} = B_{\text{nuc}} \quad t_{\text{cross},1} \leq t < t_{\text{cross},2}, \quad (4.35b)$$

which describe the nucleation until also the boundary of  $\Lambda_{\text{nuc},2}$  crosses the nucleation point. Then yet another  $\Lambda_{\text{nuc},3}$  is introduced and so forth until the process' end time is reached. That is, in general the differential equations capturing nucleation read:

$$\frac{d\mathbf{h}_{\text{nuc},k}}{dt} = \mathbf{G}, \quad \frac{dN_{\text{nuc},k}}{dt} = \begin{cases} B_{\text{nuc}} & t_{\text{cross},k-1} \leq t < t_{\text{cross},k} \\ 0 & t_{\text{cross},k} < t \end{cases} \quad k = 1 \dots n_{\text{nuc}}(t). \quad (4.36)$$

#### 4.1.3.4 The Discretized Population Balance

The discretized number density function can, according to the previous sections, be expressed as

$$\hat{f} = \sum_{k=1}^{n_{\text{nuc}}(t)} N_{\text{nuc},k} \delta(\mathbf{h} - \mathbf{h}_{\text{nuc},k}) + \sum_{k=1}^{n_{\text{seed}}} N_{\text{seed},k} \delta(\mathbf{h} - \mathbf{h}_{\text{seed},k}). \quad (4.37)$$

In summary, the differential equations for  $N_{\text{nuc},k}$ ,  $N_{\text{seed},k}$ ,  $\mathbf{h}_{\text{nuc},k}$  and  $\mathbf{h}_{\text{seed},k}$  read

$$\frac{d\mathbf{h}_{\text{nuc},k}}{dt} = \mathbf{G}, \quad \frac{dN_{\text{nuc},k}}{dt} = \begin{cases} B_{\text{nuc}} & t_{\text{cross},k-1} < t < t_{\text{cross},k} \\ 0 & t_{\text{cross},k} < t \end{cases} \quad k = 1 \dots n_{\text{nuc}}(t). \quad (4.38)$$

$$\frac{d\mathbf{h}_{\text{seed},k}}{dt} = \mathbf{G}, \quad \frac{dN_{\text{nuc},k}}{dt} = 0 \quad (4.39)$$

This set of ordinary differential equations can be implemented in Matlab and is solved in time with standard higher order Runge-Kutta schemes (ode23 or ode45 in Matlab). In the next section the above developed model is solved using this numerical procedure.

#### 4.1.4 Simulation Results

For the system KDP not only the model equations as described in Sec. 4.1 are presented but also experiments that have been performed. For these experiments the evolution of the number density function is extracted from intensity images, see for details Sec. 5.4.3. In these experiments a temperature trajectory is imposed that in-

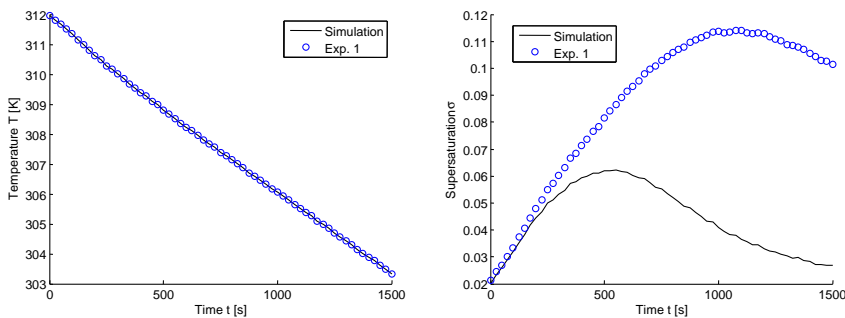


**Figure 4.8:** Temperature profile of Exp. 1 and the resulting supersaturation profile using the parameters from the literature presented in Sec. 4.1.1.1. The supersaturation can obviously not be reproduced well for the conditions of Exp. 1.

duces supersaturation in the fluid phase and causes the seed crystals to grow. In the following two sections the experimental temperature trajectories are retraced and the evolution of the shape distribution is calculated along with the induced supersaturation profile. At first, in Sec. 4.1.4.1, the simulation is taken out with growth and nucleation parameters from the literature, whereas the system with growth parameters identified in Ch. 6 without nucleation is solved.

#### 4.1.4.1 Simulation with Literature Parameters

The pretended temperature profile of Exp. 1, presented in Sec. 5.4.3.1, is depicted in Fig. 4.8 (left). Between the sampling points (circles), the temperature is evaluated by linear interpolation (line) for the simulation. The growth and nucleation parameter from the literature used for the simulation are specified in Eq.s (4.9) and (4.8). The resulting supersaturation profile is shown in Fig. 4.8 (right). The measured experimental results (circles) deviate significantly from the simulation (line), however, the qualitative development is similar. For  $t < 500$  s the supersaturation of the simulation increases as a result of the undercooling of the solution. Until  $t = 200$  s the slope is almost constant, as this is the case for the temperature profile, because the transfer of dissolved material to the crystalline phase by nucleation and growth is rather low. Subsequently, the driving force for growth and nucleation (supersaturation) is large enough to provoke significant transfer to the crystalline phase which results in a decrease of the slope of the supersaturation and for  $t > 500$  s even the decrease of supersaturation. The amount of crystalline material that grows onto the crystals originating either from the seed population or are produced by nucleation during the process is depicted in Fig. 4.9 (left). The mass fraction of crystals arising from nucleation is shown in Fig. 4.9 (right). In Sec. 5.4.3.1 this quantity is estimated from the images of the experiment (circles). It can be seen that the deviation between experiment and simulation is rather large. The amount of observed nucleated (and subsequently grown) crystals is about ten times larger in the simulation. With the deviations perceived in the supersaturation profile, Fig. 4.8 (right) it can be stated that the literature parameters do not furnish the population balance model adequately to reflect the observed dynamics. This is further supported by the simulated evolution of the number density function depicted in Fig. 4.10. Qualitatively, the evolution of

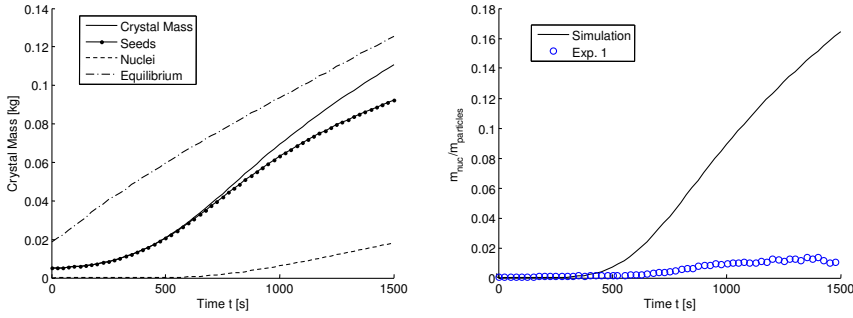


**Figure 4.9:** Crystal mass over time for the simulation of Exp. 1 using the parameters from the literature presented in Sec. 4.1.1.1. The mass of the (grown) nuclei is relatively large (left) and makes up well above 15% at the end of the batch. In the experiments the amount of nuclei has been estimated to be less than 1.5%, see also Fig. 5.29 for a more detailed view on the increase of the nuclei mass.

the mean state (thick black line) deviates from the observed mean path as the comparison to the measured trajectory, drawn as a gray line in the distribution plot at the bottom, indicates. The experimental mean shape is more compact than the one obtained by the simulation. Compare the simulated distribution evolution of Fig. 4.10 also to the measure one depicted in Fig. 5.24. The amount of nucleated particles as already indicated by Fig. 4.9 (right) is low which gives rise to the assumption that this effect can be neglected for a first order model which is solved in the following section.

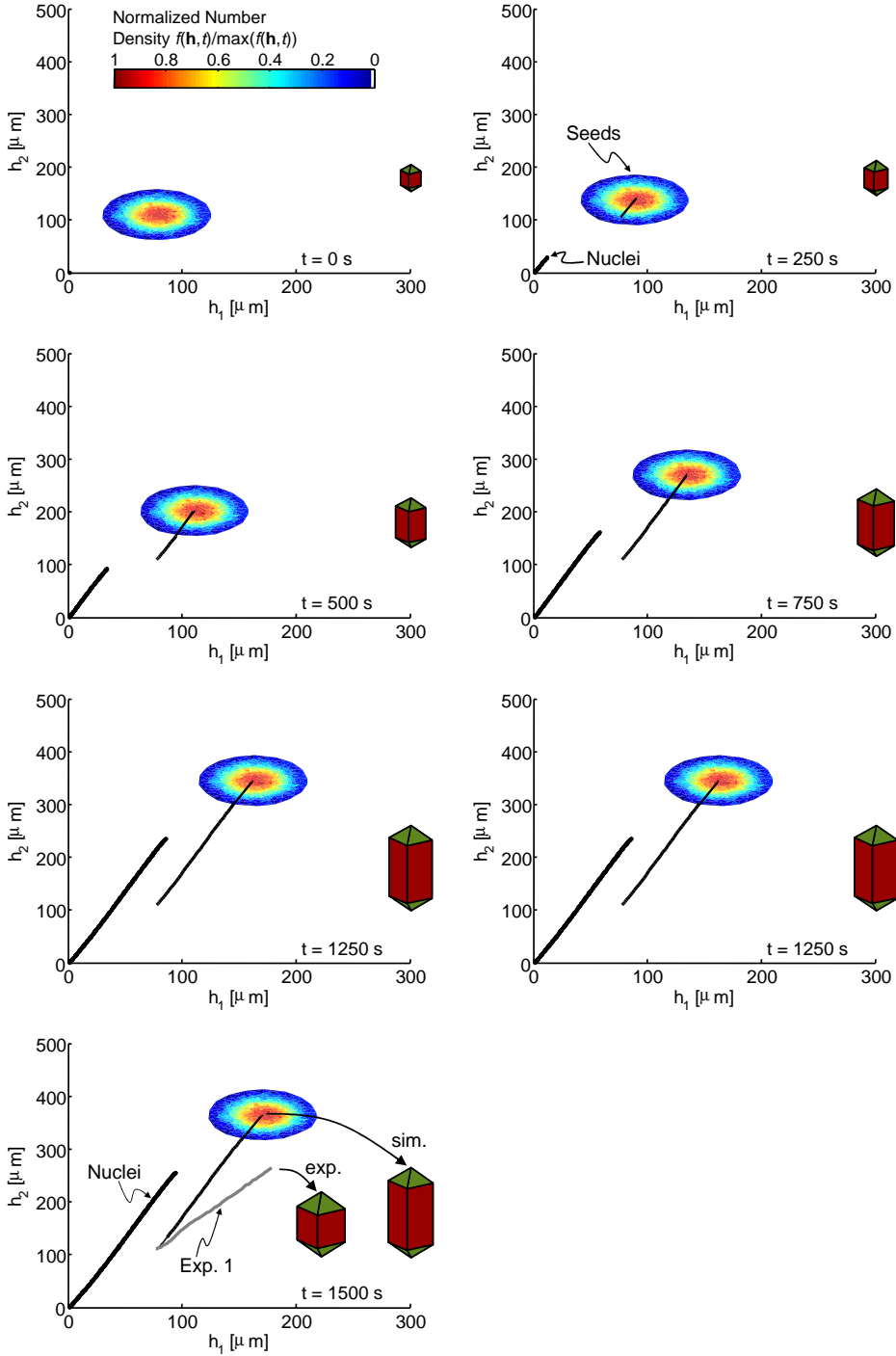


**Figure 4.10:** Evolution of the simulated shape distribution using the temperature profile of Exp. 1 and the parameters from the literature presented in Sec. 4.1.1.1. The mean state trajectory of the seeds is drawn as a thick black line ending in center of the seed distribution. At the right of each coordinate system the shape of the mean state is drawn. In the lower left the measured mean trajectory of the seeds is added as a gray line. It can be seen that the computed and the measured trajectory differs significantly. The black lines starting in the origin of the coordinate systems are the locations of the pivots with which the nuclei have been captured.

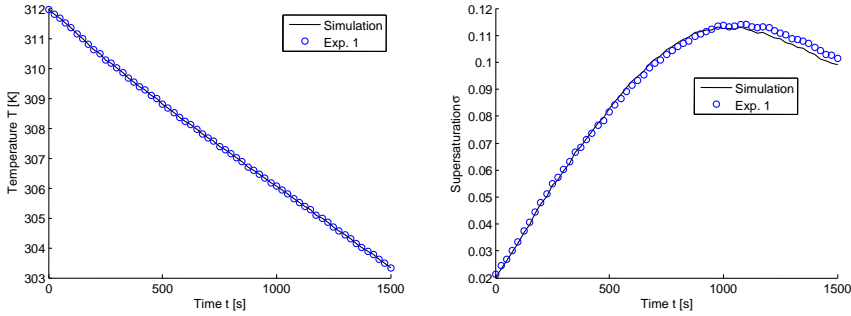


**Figure 4.11:** Temperature profile of Exp. 1 and the resulting supersaturation profile using the growth parameters determined in Ch. 6.

#### 4.1.4.2 Simulation with Estimated Parameters

The same temperature profile of Exp. 1 – like in the preceding section – is applied to a population balance model equipped with growth parameters determined in Ch. 6, see also Eq. (4.11). The experimental results suggest that the nucleation rate is low. Therefore, for this first-order model only growth is taken into account and nucleation neglected. It should be noted that for the determination of the growth rates in Ch. 6 the measured supersaturation profile and the trajectory of the mean state is directly used for the parameter estimation and not a full process model is fitted. That is in particular important because the mass balance of the continuous phase is not used in the estimation procedure but only the growth kinetics with respect to the geometry of the crystals is fitted to the measured values. In that sense, the simulation using a population balance model coupled to the mass balance constitutes a test whether the growth kinetics can not only reproduce the measured shape evolution using a pretended supersaturation profile but whether the supersaturation profile is correctly determined by the mass balance. The simulated supersaturation profile obtained in this way is depicted in Fig. 4.11 (right) which is close to the measured one. An additional simulation has been performed for the temperature profile that has been applied in Exp. 2. Also for this setup, the supersaturation evolution is reproduced well by the mass balance. The evolution of the simulated shape distribution for the simulation of Exp. 1 is depicted in Fig. 4.13. It can be seen that the simulated shape evolution agrees well with the measured evolution which is indicated in the bottom of Fig. 4.13 by the gray line. Similar results on the simulated mean state evolution are obtained for Exp. 2.

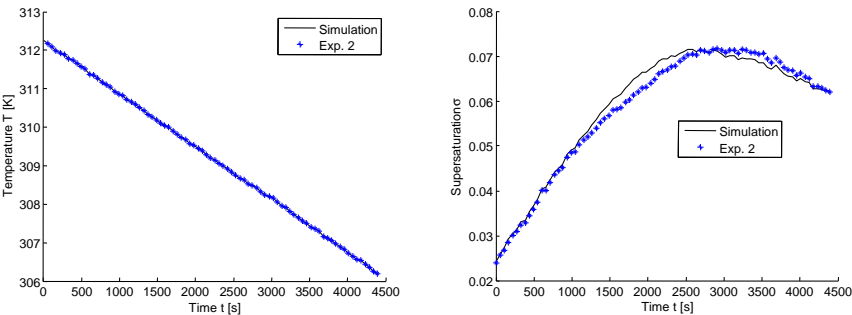


**Figure 4.12:** Temperature profile of Exp. 2 and the resulting supersaturation profile using the growth parameters determined in Ch. 6.

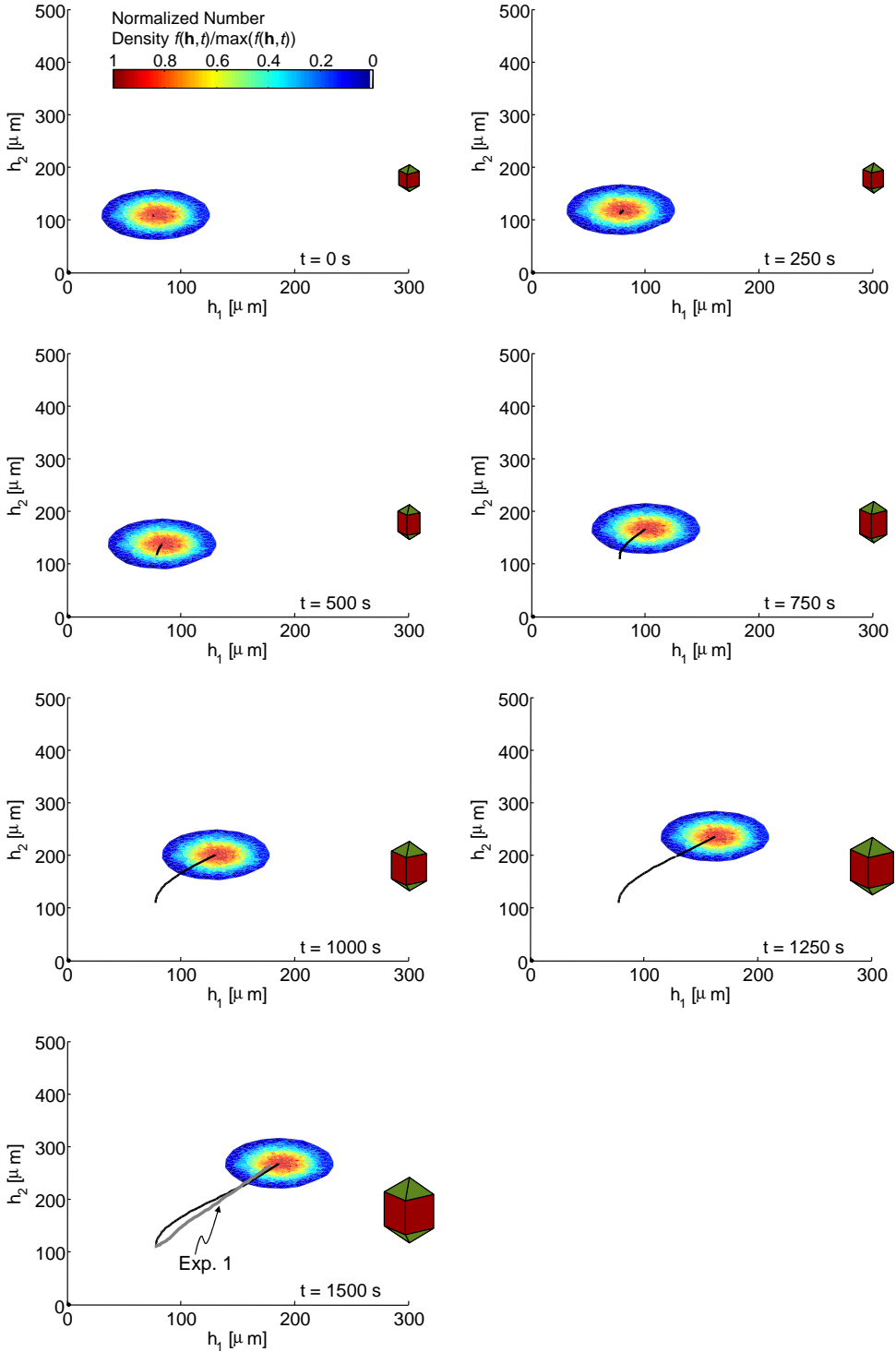


**Figure 4.13:** Evolution of the simulated shape distribution using the temperature profile of Exp. 1 and the parameters from Ch. 6. The mean state trajectory of the seeds is drawn as a thick black line ending in center of the seed distribution. At the right of each coordinate system the shape of the mean state is drawn. In the lower left the measured mean trajectory of the seeds is added as a gray line. It can be seen that the computed and the measured trajectory compare well.



## 4.2 Evolving Crystal Populations with Varying Number of Faces – An Example

In the previous section, the population balance model as well as a means for its numerical solution for the case of *continuously* evolving systems has been introduced. That is, the trajectories of the crystals were not subject to run into a morphological boundary which was for the general single crystal case pointed out in Ch. 3. In this section, a rather simple 2D example is worked out in which crystal faces can disappear. In Sec. 4.2.1 the crystal system is introduced and the evolution of a single crystal is revisited on the basis of this example. Sec. 4.2.2 introduces the population balance along the framework that has been developed in Ch. 2.

### 4.2.1 Cubic Crystal Model and Single Crystal Evolution Revisited

Various substances crystallize in the cubic system, for instance table salt, most metals such as copper, iron, gold and silver but also diamond (Borchardt and Turowski, 1999). In our example, the crystallographic faces  $\{001\}$  and  $\{111\}$  may occur leading to the following geometrical state vector:

$$\mathbf{h} = \begin{pmatrix} h_1 \\ h_2 \end{pmatrix} = \begin{pmatrix} h_{\{001\}} \\ h_{\{111\}} \end{pmatrix}, \quad (4.40)$$

see Fig. 4.14. Readers familiar with Ch. 3, can switch directly to the sentence before Eq. (4.41). It can be seen from Fig. 4.14 that under the variation of the  $\mathbf{h}$ -vector the shape of the crystal can be changed qualitatively. Take for instance the shape (d) (truncated cube) and move to the left on the horizontal line: If the distance  $h_2$  is increased relative to  $h_1$ , the area of the  $h_2$ -faces (or  $\{111\}$ -faces or octahedral faces) becomes smaller until they finally disappear which happens when  $h_2 = \sqrt{3}h_1$ , see the drawn shape (c) and the line on which such shapes exist. Note that the octahedral faces at the shape (c) do not belong to the crystal but lie on the corners of the cube in order to indicate that they are taken into account for the model, thus have the possibility to exist but are currently not present on the crystal. By moving from the point (c) directly towards the origin, the shape remains the same and becomes only smaller, see (a). In the following we restrict ourselves to confine the crystal states to the ones below the line  $h_2 = \sqrt{3}h_1$  because for all states above, the resulting shape would still be a cube. But whilst the (non existing, thus virtual, see Ch. 3)  $h_2$ -faces touch the corners of the cube on the line, they are distant from the cube for states above the line as the sketched shape (b) shall indicate. That is, all faces which cannot be seen on the crystal surface shall be tangential to the remaining crystal polyhedron and because of this, the accessible region in  $\mathbf{h}$ -space is restricted. If we move from the point (d) to the right, the crystal shape changes as well. When the point (e) (cuboctahedron) is reached, which is the case for  $h_1 = \sqrt{3}/2 h_2$ , the previously separated  $h_2$ -faces meet at a so called 4-compound vertex, i.e., the edge between the  $h_1$ -faces disappears. By moving even further towards (f), shapes are obtained on which an edge between the  $h_2$ -faces occurs (truncated octahedron). Keeping  $h_1$  constant and decreasing  $h_2$  produces shapes with smaller  $h_1$ -faces (g) until the (cubic)  $h_1$ -faces disappear and become virtual on the line  $h_1 = \sqrt{3}h_2$ , see shape (h). Below that line the virtual  $h_1$ -faces are distant from the octahedron, see (i), i.e., the region  $h_1 > \sqrt{3}h_2$  shall not be accessible

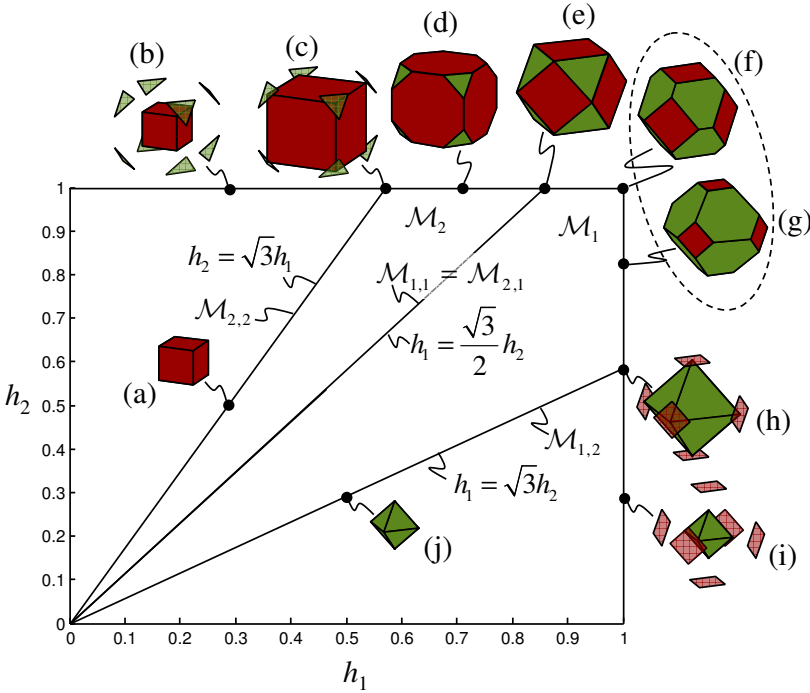


**Figure 4.14:** Left: The  $\mathbf{h}$ -vector is made up by the distance of the cubic faces ( $h_1$ ) and the octahedral faces ( $h_2$ ). Right: State space partitioning for the example of the cubic crystal system.

because the real crystal shape cannot vary in this domain and only the distance of the virtual faces is larger than zero. Clearly, by moving on the line  $h_1 = \sqrt{3}h_2$  from (h) towards the origin, the shape remains the same (octahedron) and only the size becomes smaller, see for example (j). The discussion on crystal shapes in different parts of the state space revolves around distinguished morphological features which can be seen on the crystal surface. In the basic example of this section, this analysis is driven by intuition but for more complex cases it is easily imaginable that the bookkeeping and imagination for the possible variations in higher-dimensional state spaces becomes difficult. Therefore, Ch. 3 addresses this topic in full generality and implements the necessary means to resolve the possible shape variations and restriction of the accessible domain for arbitrary cases.

Using the methods of Ch. 3 (or the intuitive investigation above), it turns out that there exist in principle five different morphology domains, i.e., two 2D morphology cones  $\mathcal{M}_1$  and  $\mathcal{M}_2$  (C-morphologies<sup>4</sup>) which are bound by two morphological subdo-

<sup>4</sup>C-morphology (or complete morphology) refers to the case where all faces can be seen on the shape, see Ch. 3.

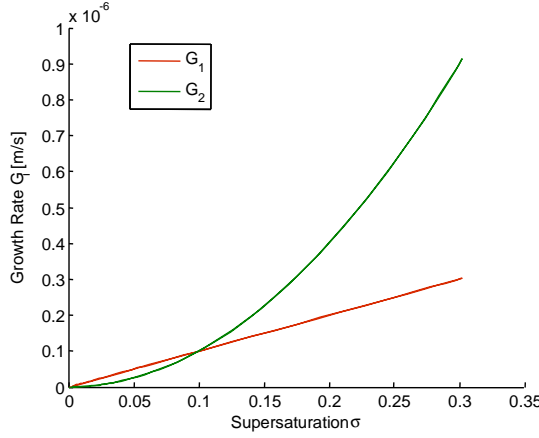


**Figure 4.15:** Growth rates for the example of the cubic crystal system, see Eq. (4.43).

mains  $\mathcal{M}_{2,2}$  and  $\mathcal{M}_{1,2}$  (S-morphology<sup>5</sup>) and a transition line  $\mathcal{M}_{1,1}$  (T-morphology<sup>6</sup>):

$$\mathcal{M}_{2,2} = \{ \mathbf{h} : h_2 = \sqrt{3}h_1 \} , \quad (4.41a)$$

$$\mathcal{M}_2 = \{ \mathbf{h} : h_1 < \sqrt{3}/2h_2, h_2 < \sqrt{3}h_1 \} , \quad (4.41b)$$

$$\mathcal{M}_{1,1} = \{ \mathbf{h} : h_1 = \sqrt{3}/2h_2 \} , \quad (4.41c)$$

$$\mathcal{M}_1 = \{ \mathbf{h} : h_1 > \sqrt{3}/2h_2, h_1 < \sqrt{3}h_2 \} , \quad (4.41d)$$

$$\mathcal{M}_{1,2} = \{ \mathbf{h} : h_1 = \sqrt{3}h_2 \} , \quad (4.41e)$$

see Fig. 4.14. The shape evolution for the case that all faces are present on the crystal surface is determined by the ordinary differential equation

$$\frac{d\mathbf{h}}{dt} = \mathbf{G} , \quad \mathbf{h}(t=0) = \mathbf{h}_0 , \quad (4.42)$$

where  $\mathbf{G}$  contains the growth rates normal to the crystal surface, see Eq. (3.39). Let the growth law for this example be defined by

$$G_1 = k_1 \sigma^{g_1} , \quad k_1 = 10^{-6} \text{ m/s} , \quad g_1 = 1 , \quad (4.43a)$$

$$G_2 = k_2 \sigma^{g_2} , \quad k_2 = 10^{-5} \text{ m/s} , \quad g_2 = 2 , \quad (4.43b)$$

see also Fig. 4.15. If not all faces can be seen on the crystal, as this is the case for the octahedron (h or j) in Fig. 4.14, the virtual, tangential faces must be displaced by a velocity that keeps the virtual faces virtual but at the corners of the crystal polyhedron. For this, the condition equation in Eq. (4.41a) is differentiated which yields the 2D

<sup>5</sup>S-morphology (or submorphology) means that only some faces can be seen on the shape and that their existence domain is adjacent to the domain in  $\mathbf{h}$ -space which is not accessible, see Ch. 3.

<sup>6</sup>T-morphologies (or transition morphologies) are special shapes which connect morphology regions (of C- or S-morphologies) in which the same set of crystal faces can be observed but in a different configuration, i.e., the transition between the truncated cube (d) and truncated octahedron (f) via the cuboctahedron (e), see details in Ch. 3.

system of ordinary differential equations whose dynamics is controlled by the scalar  $G_2$ :

$$\frac{dh_1}{dt} = \sqrt{3}G_2, \quad (4.44a)$$

$$\frac{dh_2}{dt} = G_2, \quad \text{for } \mathbf{h} \in \mathcal{M}_{1,2} \text{ and } G_1 \geq \sqrt{3}G_2, \quad (4.44b)$$

which means that the trajectory remains on the line  $\mathcal{M}_{1,2}$ . This is only the case if the natural growth rate of  $h_1$ ,  $G_1$ , is larger than the virtual displacement rate  $\sqrt{3}G_2$  in order to retard the movement across the accessible region (e.g. to the point (i) in Fig. 4.14). If however, the natural growth rate  $G_1$  becomes smaller than the virtual displacement rate, the  $h_1$ -faces reappear by setting

$$\frac{dh_1}{dt} = G_1 \quad \text{for } G_1 < \sqrt{3}G_2, \quad (4.45)$$

which means that the trajectory leaves  $\mathcal{M}_{1,2}$  and enters the domain  $\mathcal{M}_1$ . In general, the evolution equation for a single crystal can be formulated by switching the growth vector  $\mathbf{G}$  with the help of a state- and velocity-dependent so called velocity delimiter matrix  $\mathbf{D}(\mathbf{h}, \mathbf{G})$ , see also Eq. (3.46) in Ch. 3:

$$\frac{d\mathbf{h}}{dt} = \mathbf{D}(\mathbf{h}, \mathbf{G})\mathbf{G}, \quad (4.46)$$

where in the example at hand this is

$$\mathbf{D}(\mathbf{h}, \mathbf{G}) = \begin{cases} \begin{bmatrix} 1 & 0 \\ \sqrt{3} & 0 \end{bmatrix}, & \text{for } \mathbf{h} \in \mathcal{M}_{2,2}, \quad G_2 > \sqrt{3}G_1 \\ \begin{bmatrix} 1 & 0 \\ 0 & 1 \end{bmatrix}, & \text{for } \mathbf{h} \in \mathcal{M}_1 \cup \mathcal{M}_{1,1} \cup \mathcal{M}_2. \\ \begin{bmatrix} 0 & \sqrt{3} \\ 0 & 1 \end{bmatrix}, & \text{for } \mathbf{h} \in \mathcal{M}_{1,2}, \quad G_1 > \sqrt{3}G_2 \end{cases} \quad (4.47)$$

The technique to assemble such matrices for more complex cases is described in Sec. 3.2.

**Example Trajectory** For the system at hand we consider the shape evolution of a crystal with initial state

$$\mathbf{h}_0 = (50, 50)^T \times 10^{-6} \text{ m} \quad (4.48)$$

at a low supersaturation value of  $\sigma = 0.05$  which gives, according to Eq. (4.43), a constant growth rate vector of

$$\mathbf{G} = (5, 2.5)^T \times 10^{-8} \text{ m/s}. \quad (4.49)$$

Under these conditions the crystal shall grow for 10,000 s and for yet another 750 s at a high supersaturation value of  $\sigma = 0.3$  which gives a constant growth rate vector of

$$\mathbf{G} = (3, 9)^T \times 10^{-7} \text{ m/s}. \quad (4.50)$$

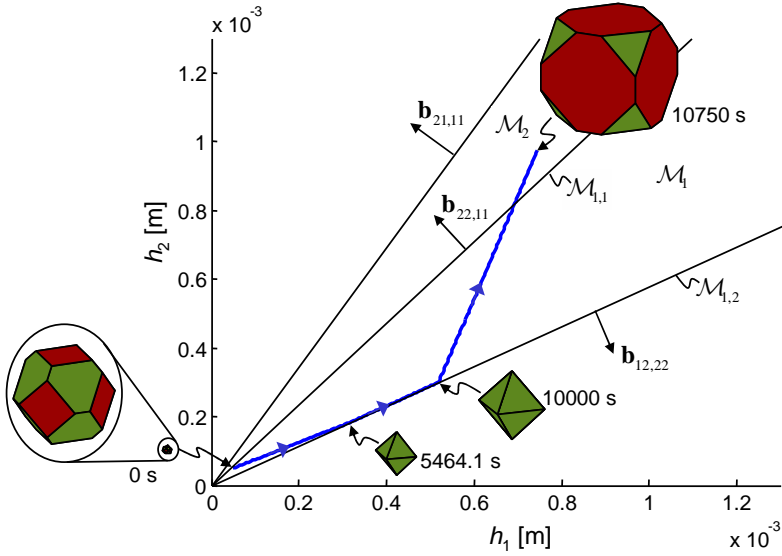


**Figure 4.16:** Trajectory in  $h$ -space for the example system under growth conditions as stated in Eq.s (4.49) and (4.50).

The resulting trajectory can be seen in Fig. 4.16. The initial state lies in the cone  $\mathcal{M}_1$  and moves towards the boundary  $\mathcal{M}_{1,2}$  until it reaches  $\mathcal{M}_{1,2}$  at  $t \approx 5464.2$  s. At this state, the  $h_1$ -faces have disappeared from the crystal surface and thus only the octahedral faces can be seen. If the path were continued with the velocities given in Eq. (4.49), the trajectory would cross  $\mathcal{M}_{1,2}$  and the cubic faces would become distant to the octahedron as shown in Fig. 4.14 (i). In order to prevent this, the cubic faces are displaced on  $\mathcal{M}_{1,2}$  as determined by the octahedral growth rates, see Eq. (4.44) or in more general terms according to Eq. (4.46) using the third velocity delimiter matrix of Eq. (4.47). The trajectory is continued on  $\mathcal{M}_{1,2}$  until the growth rate is switched to the values given in Eq. (4.50) which means that the natural growth rate of the cubic faces is smaller than its virtual displacement rate, i.e., Eq. (4.45) applies. Hence, the cubic faces reappear and the state evolution is continued as a truncated octahedron in the cone  $\mathcal{M}_1$ , crosses the T-morphology line  $\mathcal{M}_{1,1}$  and enters the region  $\mathcal{M}_2$  in which it assumes the shape of a truncated cube. From the slope of the trajectory it can be seen that if the simulation were continued even the upper boundary of  $\mathcal{M}_2$  would be reached, i.e., a transformation to a shape with only cubic faces would occur.

An alternative to keep the trajectory for the case of the octahedron for the interval  $5464.2 \text{ s} < t < 10,000 \text{ s}$  moving within the S-morphology line  $\mathcal{M}_{1,2}$  is to not further track the state of the virtual  $h_1$ -state but consider only the evolution of  $h_2$ . Instead of moving on the line  $\mathcal{M}_{1,2}$ , the trajectory is imagined to be instantaneously transferred to the  $h_2$ -coordinate or generally speaking to the line  $\mathcal{M}'_{1,2}$ . That is, it performs a jump as depicted in Fig. 4.17. The differential equation which must be solved for this configuration is simply

$$\frac{dh_2}{dt} = G_2, \quad (4.51)$$

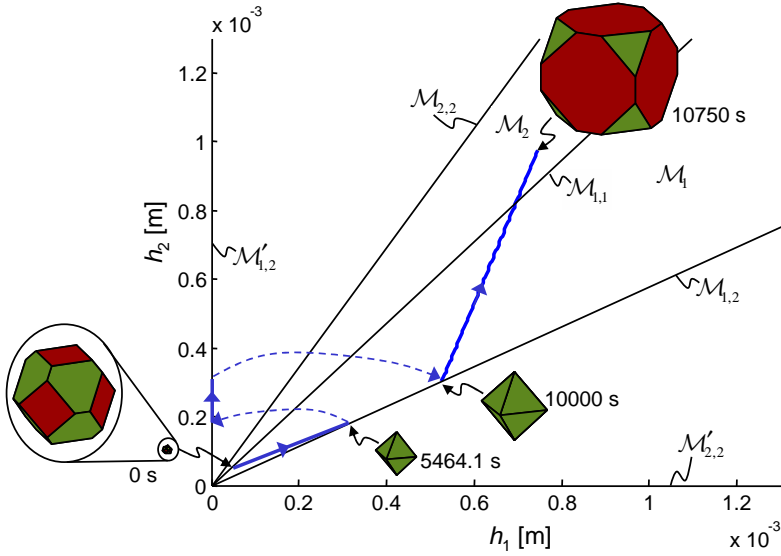


**Figure 4.17:** Trajectory in  $\mathbf{h}$ -space for the example system under growth conditions as stated in Eq.s (4.49) and (4.50) using a state jumps.

along with a trivial algebraic equation equipped with the condition that supervises the validity of its application:

$$h_1 = 0, \quad \text{for } \mathbf{h} \in \mathcal{M}'_{1,2} \text{ and } G_1 \geq \sqrt{3}G_2. \quad (4.52)$$

If the natural growth rate for  $G_1$  is again lower than its virtual displacement rate of  $\sqrt{3}G_2$  (as this is the case for  $t > 10,000$  s in the example), the state  $h_1$  is instantaneously shifted to  $h_1 = \sqrt{3}h_2$  in order to continue the evolution within  $\mathcal{M}_1$  starting at the appropriate point on  $\mathcal{M}_{1,2}$ , see Fig. 4.17. That means, instead of binding the crystal shape state on a morphological subdomain<sup>7</sup>, the trajectory is switched to and from the lower dimensional real part of the state space by performing jumps. At the moment, the notion of jumps in state space may be found to be more complicated but for the population case, which requires the definition of number densities in subspaces, it shall serve as a means for a more straightforward formulation of the dynamical model equations. This concludes the discussion on the example trajectory that also introduced state jumps which are easily imagined also for the morphological subdomain of the cube.

In the following the presented two approaches for the evolution of crystals with virtual faces are distinguished and termed *modeling with discontinuous right-hand sides* and *modeling with state jumps*. Both approaches have their advantages and drawbacks but model the same situation and lead to the same results.

It is clear that the growth vector  $\mathbf{G}$ , pointing into different directions, decides whether the morphological manifolds, e.g.  $\mathcal{M}_{1,2}$  or  $\mathcal{M}_{2,2}$ , can be reached. In order to classify the single crystal evolution equation, also in view of Ch. 2, it must be perceived whether the growth vector  $\mathbf{G}$  (velocity in state space) points towards or

<sup>7</sup>more precisely within the domain of an S-morphology

away from  $\mathcal{M}_{1,2}$  and/or  $\mathcal{M}_{2,2}$ . For that purpose, the unit normals of the domains are introduced, see Fig. 4.16:<sup>8</sup>

$$\mathbf{b}_{12,22} \rightarrow \text{unit normal on } \mathcal{M}_{1,2}, \quad (4.53a)$$

$$\mathbf{b}_{22,11} \rightarrow \text{unit normal on } \mathcal{M}_{1,1}, \quad (4.53b)$$

$$\mathbf{b}_{21,11} \rightarrow \text{unit normal on } \mathcal{M}_{2,2}, \quad (4.53c)$$

Depending on the orientation of  $\mathbf{G}$ , three cases can be distinguished as denoted in the *Condition* column of Table 4.1. The line  $\mathcal{M}_{1,1}$  is always simply crossed by the trajectories because none of the faces becomes virtual but only the transition from the truncated cube to the truncated octahedron (or vice versa) takes place. However, for the population balance model it is important to distinguish whether a crystal (or a full population) lies in  $\mathcal{M}_1$  or  $\mathcal{M}_2$  because for the coupling to the mass balance, the volume or volume change of the crystalline phase must be calculated. The coefficients for the volume evaluation are different for different morphological configurations, in fact we have (see also the formal procedure given in Sec. 3.3 or the work of Zinser (2010) using pencil-and-paper-geometry):

$$V(\mathbf{h}) = 4h_1^3 - 12\sqrt{3}h_1^2h_2 + 36h_1h_2^2 - 8\sqrt{3}h_2^3 \quad \text{for } \mathbf{h} \in \mathcal{M}_1 \cup \mathcal{M}_{1,2} \cup \mathcal{M}_{1,1}, \quad (4.54a)$$

$$V(\mathbf{h}) = -28h_1^3 + 36\sqrt{3}h_1^2h_2 - 36h_1h_2^2 + 4\sqrt{3}h_2^3 \quad \text{for } \mathbf{h} \in \mathcal{M}_2 \cup \mathcal{M}_{1,1} \cup \mathcal{M}_{2,2}. \quad (4.54b)$$

In the following, the three cases are further discussed in view of the classification in Ch. 2. For the modeling with discontinuous right-hand sides, this makes use of the following classification of the surfaces<sup>9</sup>  $\mathcal{M}_{1,2}$ ,  $\mathcal{M}_{1,1}$  and  $\mathcal{M}_{2,2}$  which are termed:

**one-sided stable** if trajectories move towards it from one side and stay therein,

**one-sided transition** if trajectories that are currently within the domain leave it by the following instant, and

**transition** if trajectories approach the region, pass through it and continue on the opposite side.

The three configurations for the example system are given in Tab. 4.1 in the column *Types of domains*. For all cases  $\mathcal{M}_{1,1}$  is a transition surface except for  $\mathbf{b}_{22,11} \cdot \mathbf{G} = 0$ . Revisiting the example trajectory shown in Fig. 4.16 reveals that the evolution in the interval  $0 < t < 10,000$  s (the growth rates given by (4.49)) must be assigned to Case 1 and the trajectory from  $10,000 \text{ s} \leq t \leq 10,750$  s to Case 3 of Tab. 4.1.

If the model is formulated with state jumps, the one-sided stable and one-sided transition surfaces are replaced by

**jump in stable surface** if trajectories jump into it when they reach the jump surface, and

<sup>8</sup>Details on the notation can be found in Ch. 3. The main idea behind the collection of numbers is that a morphological change is associated with the disappearance of an edge. For instance, if the edges bounding the area of the cubic faces on the truncated octahedron disappear, this means a transition to a pure octahedron. This edge is given the number 12,22 meaning that the edge lies between an  $h_1$ - and an  $h_2$ -face and is bound by two  $h_2$ -faces. Therefore, the unit normal of that region in state space is denoted by  $\mathbf{b}_{12,22}$ .

<sup>9</sup>Even though for the example at hand the mentioned domains are not surfaces as understood in everyday language, we use it nevertheless because we consider for the  $nD$  case a manifold of codimension one to be a surface in the state space.

Table 4.1: Dynamic characteristics of the shape domains.

	Condition	Types of domains	Types of domains for modeling with state jumps
<b>Case 1</b>	$\mathbf{b}_{12,22} \cdot \mathbf{G} < 0$ and $\mathbf{b}_{21,11} \cdot \mathbf{G} > 0$ → $\mathbf{G}$ points from $\mathcal{M}_{1,2}$ away and towards $\mathcal{M}_{2,2}$	$\mathcal{M}_{1,2}$ is a one-sided transition surface and $\mathcal{M}_{2,2}$ a one-sided stable surface	$\mathcal{M}'_{1,2}$ is an unstable surface from which particles jump directly to $\mathcal{M}_{1,2}$ and $\mathcal{M}'_{2,2}$ is a stable surface to which particles jump from $\mathcal{M}_{2,2}$
<b>Case 2</b>	$\mathbf{b}_{12,22} \cdot \mathbf{G} < 0$ and $\mathbf{b}_{21,11} \cdot \mathbf{G} < 0$ → $\mathbf{G}$ points from $\mathcal{M}_{1,2}$ and $\mathcal{M}_{2,2}$ away	$\mathcal{M}_{1,2}$ and $\mathcal{M}_{2,2}$ are both one- sided transition surfaces	$\mathcal{M}'_{1,2}$ and $\mathcal{M}'_{2,2}$ are both unstable, i.e., particles jump directly to $\mathcal{M}_{1,2}$ and $\mathcal{M}_{2,2}$ , respectively in order to continue their trajectories in the interior of the cone
<b>Case 3</b>	$\mathbf{b}_{12,22} \cdot \mathbf{G} > 0$ and $\mathbf{b}_{21,11} \cdot \mathbf{G} < 0$ → $\mathbf{G}$ points towards $\mathcal{M}_{1,2}$ and from $\mathcal{M}_{2,2}$ away	$\mathcal{M}_{1,2}$ is a one-sided stable sur- face and $\mathcal{M}_{2,2}$ a one-sided tran- sition surface	$\mathcal{M}'_{1,2}$ is a stable surface into which particles jump and subsequently evolve when reaching $\mathcal{M}_{1,2}$ and $\mathcal{M}'_{2,2}$ is an unstable surface from which particles jump to $\mathcal{M}_{2,2}$ in order to continue their path in $\mathcal{M}_2$



**jump from unstable surface** if trajectories leave the surface by jumping into another surface and continuing their evolution from there,

respectively. The three configurations for the example system (Fig. 4.17) are summarized in the last column of Table 4.1. As for the modeling with discontinuous right-hand sides,  $\mathcal{M}_{1,1}$  is a transition surface except for the special case  $\mathbf{b}_{22,11} \cdot \mathbf{G} = 0$ .

Using the notion of the three different cases either for the modeling with discontinuous right-hand sides or using state jumps, the derivation of the population balances that model the evolution of shape distributions rather than single crystal trajectories is tackled below.

## 4.2.2 Population Balance Model for Cubic Crystals

In contrast to the population model that was presented for potassium dihydrogen phosphate in Sec. 4.1.2, the state space of the cubic crystal example exhibits morphological manifolds on which crystals with either only cubic or octahedral faces exist,  $\mathcal{M}_{2,2}$  and  $\mathcal{M}_{1,2}$  (or  $\mathcal{M}'_{2,2}$  and  $\mathcal{M}'_{1,2}$  for the modeling with state jumps), respectively, and two different regions, namely  $\mathcal{M}_1$  and  $\mathcal{M}_2$  separated by  $\mathcal{M}_{1,1}$ , in which the crystal shape is qualitatively different. That is in particular, the volume computation, Eq.s (4.54), is different in the regions  $\mathcal{M}_1$  and  $\mathcal{M}_2$ . Therefore, in principle five different kinds of crystals exist:

**Octahedra** existing in  $\mathcal{M}_{1,2}$  (or alternatively  $\mathcal{M}'_{1,2}$  for modeling with state jumps),

**Truncated Octahedra** existing in  $\mathcal{M}_1$ ,

**Cuboctahedra** existing in  $\mathcal{M}_{1,1}$ ,

**Truncated Cubes** existing in  $\mathcal{M}_2$ , and

**Cubes** existing in  $\mathcal{M}_{2,2}$  (or  $\mathcal{M}'_{2,2}$  for modeling with state jumps).

The cuboctahedron existing in  $\mathcal{M}_{1,1}$  can of course exist steadily only for the special case  $\mathbf{b}_{22,11} \cdot \mathbf{G} = 0$ , otherwise this shape is only assumed during the transfer from  $\mathcal{M}_1$  to  $\mathcal{M}_2$  or vice versa. Number densities in  $\mathcal{M}_1$  and  $\mathcal{M}_2$  are in general 2D, whereas they are 1D in  $\mathcal{M}_{1,2}$  ( $\mathcal{M}'_{1,2}$ ) and  $\mathcal{M}_{2,2}$  ( $\mathcal{M}'_{2,2}$ ). Therefore, number densities are defined separately for the four crystal types:

$$f_{z_2}(z_2, t) \text{ (or } f_{h_2}(h_2, t) \text{ for model with jumps) for the octahedra (} h_2\text{-faces)} \quad (4.55a)$$

$$f_1(\mathbf{h}, t) \text{ for the truncated octahedra (existing in } \mathcal{M}_1) \quad (4.55b)$$

$$f_2(\mathbf{h}, t) \text{ for the truncated cubes (existing in } \mathcal{M}_2) \quad (4.55c)$$

$$f_{z_1}(z_1, t) \text{ (or } f_{h_1}(h_1, t) \text{ for model with state jumps) for the cubes (} h_1\text{-faces).} \quad (4.55d)$$

The introduction of the  $z$ 's in the subscripts of the number densities will be explained in Sec. 4.2.2.1.

### 4.2.2.1 Modeling with Discontinuous Right Hand Sides

We assume that the particles exist within the morphology cone or on its boundaries, i.e. the concept of state jumps is disregarded. Number densities are introduced as stated in (4.55). On the boundaries of the morphology cones, the densities are essen-

tially one-dimensional. For this, new coordinates are introduced whose basis vectors have the same length as the basis vectors of the  $\mathbf{h}$ -coordinates. That is, for a  $z$ -coordinates we find in general:

$$z = \sqrt{h_1^2 + h_2^2}. \quad (4.56)$$

Inserting the definition equations specifying the domains, Eq.s (4.41), yields

$$z_1 = 2h_1 \text{ (points on } \mathcal{M}_{2,2}) \quad (4.57)$$

$$z_2 = 2h_2 \text{ (points on } \mathcal{M}_{1,2}). \quad (4.58)$$

Without loss of generality we consider Case 1 (see Table 4.1) in which the growth vector points towards  $\mathcal{M}_{2,2}$ . The population balance for the interior domains  $\mathcal{M}_1$  and  $\mathcal{M}_2$  reads

$$\frac{\partial f_1}{\partial t} + \frac{\partial G_1 f_1}{\partial h_1} + \frac{\partial G_2 f_1}{\partial h_2} = \delta(\mathbf{h} - \mathbf{h}_{\text{nuc}}), \quad \text{for } \mathbf{h} \in \mathcal{M}_1 \quad (4.59a)$$

$$\frac{\partial f_2}{\partial t} + \frac{\partial G_1 f_2}{\partial h_1} + \frac{\partial G_2 f_2}{\partial h_2} = \delta(\mathbf{h} - \mathbf{h}_{\text{nuc}}), \quad \text{for } \mathbf{h} \in \mathcal{M}_2 \quad (4.59b)$$

subject to the initial conditions

$$f_1(\mathbf{h}, t = 0) = f_{1,0}(\mathbf{h}) \quad (4.59c)$$

$$f_2(\mathbf{h}, t = 0) = f_{2,0}(\mathbf{h}). \quad (4.59d)$$

Within the one-sided transition surface  $\mathcal{M}_{1,2}$  particles practically do not exist except if they are added at the beginning or later by nucleation. If the latter is not the case, we find according to Sec. 2.6.2,

$$f_{z_2}(z_2, t) = \begin{cases} f_{z_2,0}(z_2) & \text{for } t = 0 \\ 0 & \text{for } t > 0 \end{cases}. \quad (4.60)$$

The seed population in  $\mathcal{M}_{1,2}$  is added to the interior population of  $\mathcal{M}_1$  at  $t = 0$ , i.e. the initial condition (4.59d) is changed to:

$$f_1(\mathbf{h}, t) = f_{1,0}(\mathbf{h}) + f_{z_2,0}(z_2(h_2)) \delta(h_1 - \sqrt{3}h_2) \underbrace{\frac{\partial z_2}{\partial h_2}}_{=2}, \quad (4.61)$$

see also Eq. (2.74). The population balance for the one-sided stable surface  $\mathcal{M}_{1,2}$  to which particles are added, read, if nucleation in this region is omitted (see the derivation in Sec. 2.6.2.4, Eq. (2.76)):

$$\frac{\partial f_{z_1}}{\partial t} + \frac{\partial G_1^{z_1} f_{z_1}}{\partial z_1} = (\mathbf{G} f_2(\mathbf{h}, t))|_{\mathcal{M}_{2,2}} \cdot \mathbf{b}_{21,11} \quad (4.62)$$

with the initial condition

$$f_{z_1}(z_1, t = 0) = f_{z_1,0}(z_1). \quad (4.63)$$

The velocity in  $z_1$ -coordinates is directly obtained by differentiation of Eq. (4.57) with respect to time, i.e.

$$G_1^{z_1} = 2G_1. \quad (4.64)$$

The particles are directly passed through the transition surface  $\mathcal{M}_{1,1}$ . Therefore, it is not necessary that a number density is defined on this line. It serves only to couple the population balances for  $\mathcal{M}_1$  and  $\mathcal{M}_2$ . In view of Eq. (2.61) and under the assumption that nucleation does not take place directly within  $\mathcal{M}_{1,1}$ , the coupling equation is

$$((f_1 \mathbf{G}) - (f_2 \mathbf{G})) \cdot \mathbf{b}_{22,11} = 0 \quad \text{for } \mathbf{h} \in \mathcal{M}_{1,1}. \quad (4.65)$$

This completes the discussion on modeling with discontinuous right-hand sides for the moment until the implementation using state jumps is finished for this example. For the sake of brevity, only Case 1 is presented in detail since the other two cases do not add further complexity to the model equations and can be easily derived if the steps are followed equivalently.

#### 4.2.2.2 Modeling with Jumps in State Space

Introducing the coordinates  $z_1$  and  $z_2$  allows to track the evolution of the population directly on the facets of the morphology cone. However, the transformation to surface-intrinsic coordinates is disadvantageous because the original model formulation in terms of the  $\mathbf{h}$ -vector is lost. As discussed for the single crystal case, the introduction of state jumps avoids the introduction of new coordinates. In Tab. 4.1, the dynamic properties of the lower dimensional manifolds (see also Fig. 4.17) for the three different cases induced by the orientation of the growth vector  $\mathbf{G}$ . As for the previous model formulation, we consider only Case 1 since the other cases do not add further complexity and are easily derived likewise.

The population balance equation for the interior domains of the cone are given by Eq. (4.59). Their coupling on the common boundary  $\mathcal{M}_{1,1}$  is described by Eq. (4.65).  $\mathcal{M}'_{1,2}$  (see Fig. 4.17) being an unstable surface from which particles jump directly to  $\mathcal{M}_{1,2}$ , its dynamics reduced to the transfer of the seed population from  $\mathcal{M}'_{1,2}$  to  $\mathcal{M}_{1,2}$  if nucleation in  $\mathcal{M}'_{1,2}$  can be neglected. Following Sec. 2.6.3.3, the initial number density  $f_{h_2,0}(h_2)$  along the  $h_2$ -coordinate is lifted to a true 2D number density along the  $h_2$ -coordinate:

$$f_{h_2,0}(\mathbf{h}) = f_{h_2,0}(h_2) \delta(h_1 - \sqrt{3}h_2) \quad \mathbf{h} \in \mathcal{M}'_{1,2}, \quad (4.66)$$

derived from the general case stated in Eq. (2.90).<sup>10</sup> The jump from  $\mathcal{M}_{1,2}$  to the cone's facet  $\mathcal{M}'_{1,2}$  is given by

$$\mathbf{h}|_{\mathcal{M}'_{1,2}} = \underbrace{\begin{bmatrix} \mathbf{b}_{12,22}^T \\ 0 & 1 \end{bmatrix}}_{\Xi_{1,2}} \mathbf{h}|_{\mathcal{M}_{1,2}}, \quad (4.67)$$

where  $\mathbf{b}_{12,22}^T = \frac{1}{2}(1, -\sqrt{3})$ , see Fig. 4.16. However, for the present case, the jump is performed from  $\mathcal{M}'_{1,2}$  to  $\mathcal{M}_{1,2}$ , i.e. the transfer

$$\mathbf{h}|_{\mathcal{M}_{1,2}} = \Xi_{1,2}^{-1} \mathbf{h}|_{\mathcal{M}'_{1,2}} \quad (4.68)$$

<sup>10</sup>Note that the surface intrinsic coordinates,  $\mathbf{z} \in \mathbb{R}^{n-1}$  in Eq. (2.90), is  $h_2$  in the present case, i.e., the Jacobian matrix determinant is unity.

is required. In view of Eq.s (2.91) and (2.92), this yields

$$f_1(\mathbf{h}, t = 0) = f_{1,0}(\mathbf{h}) + f_{h_2,0}(h_2) \underbrace{\delta(h_1 - \sqrt{3}h_2) \det(\Xi_{1,2}^{-1})}_{=2}. \quad (4.69)$$

According to Tab. 4.1 (Case 1)  $\mathcal{M}'_{2,2}$  is a stable surface to which particles jump from  $\mathcal{M}_{2,2}$ . The relationship between a point on  $\mathcal{M}'_{2,2}$  to the corresponding position on  $\mathcal{M}_{2,2}$  is given by

$$\mathbf{h}|_{\mathcal{M}'_{2,2}} = \underbrace{\begin{bmatrix} 0 & 1 \\ \mathbf{b}_{21,11}^T & \end{bmatrix}}_{\Xi_{2,2}} \mathbf{h}|_{\mathcal{M}_{2,2}}, \quad (4.70)$$

where  $\mathbf{b}_{21,11}^T = \frac{1}{2}(-\sqrt{3}, 1)$ . Using Eq. (2.89), the evolution of the number density is given by

$$\frac{\partial f_{h_1}}{\partial t} + \frac{\partial G_1 f_{h_1}}{\partial h_1} = (\mathbf{G} f_2(\mathbf{h}, t))|_{\mathcal{M}_{2,2}} \cdot \mathbf{b}_{21,11} \underbrace{\det(\Xi_{2,2})}_{=\frac{1}{2}}, \quad (4.71)$$

when nucleation is ignored. This completes the derivation of the population balances required to represent the dynamics of the number density if the particles are modeled to not exist on the boundaries of the morphology cone but rather jump into linear manifolds on the coordinate axis. The similarity of the approaches becomes evident when the population balances are compared. Obviously, the population balances for the interior domains of the cone are equal. Comparing the transfer of the number density from an unstable manifold, as stated in Eq.s (4.61) and (4.84), it becomes clear that both approaches yield the same modified initial condition for the number density in  $\mathcal{M}_1$ , except that the number density on the lower dimensional manifold is directly given in terms of the  $\mathbf{h}$ -coordinate system for the modeling with state jumps. Comparing the population balances for  $\mathcal{M}'_{2,2}$  and  $\mathcal{M}_{2,2}$ , see Eq.s (4.62) and (4.86), it turns out that with the transformation

$$z_1 = 2h_1 \quad (4.72a)$$

$$f_{z_1} = 2f_{h_1} \quad (4.72b)$$

Eq. (4.62) can be converted to Eq. (4.86). The advantage of the formulation using state jumps for the derivation, Eq. (4.86), is that the resulting equations are directly given in terms of  $\mathbf{h}$ -coordinates rather than in surface-specific coordinates,  $\mathbf{z}$ , on the facets of the morphology cone. For that reason the derivation of the generalized population balances, see next section, applicable to  $n$ -dimensional state spaces is taken out directly using state jumps.

### 4.3 Population Balance Model for Faceted Crystals – Generalization

The generalization of the concept of population balances taking appearing and disappearing crystal faces into account can be sketched by following the procedure given for the 2D example of the previous section. At first, a single crystal analysis as de-

scribed in Ch. 3 must be taken out. This procedure requires as inputs only the orientation vectors of the crystal's face normals, collected in the matrix  $\mathbf{N}$  (Eq. (3.2)), and possibly the symmetry relationships expressed by a mapping matrix  $\mathbf{M}$  (see Eq. (3.31)). From this, the morphology cones and the joint morphology cones are derived. This involves in particular the determination of the normals of the facets of the morphology cones which are divided into two groups. The first one surrounds the joint morphology cone and the other one divides the joint morphology cone into the several morphology cones. On the former cone facets, states are found whose crystal shapes exhibit less faces than in the interior of the cone, i.e. this group of normal vectors is collected in the matrix  $\mathbf{B}^\varnothing$ , see Eq. (3.29). The latter ones, their normals being combined in  $\mathbf{B}^\curvearrowright$ , see Eq. (3.30), serve as transition manifolds between morphologically distinct regions in the state space. The region of a morphology cone is denoted by

$$\mathcal{M}_\lambda = \{\mathbf{h} : \mathbf{B}_\lambda^\varnothing \mathbf{h} < 0, \mathbf{B}_\lambda^\curvearrowright \mathbf{h} < 0\} \quad (4.73a)$$

$$= \{\mathbf{h} : \mathbf{B}_\lambda \mathbf{h} < 0\}, \quad (4.73b)$$

where  $\mathbf{B}_\lambda^\varnothing$  and  $\mathbf{B}_\lambda^\curvearrowright$  contain rows of the joint morphology cone matrices  $\mathbf{B}^\varnothing$  and  $\mathbf{B}^\curvearrowright$ , respectively, see Sec. 3.1.  $\mathbf{B}_\lambda$  is the matrix obtained from stacking  $\mathbf{B}_\lambda^\varnothing$  and  $\mathbf{B}_\lambda^\curvearrowright$ , see Eq. (3.20). The  $(n-1)$ -dimensional facets of this cone can be either transition surfaces, i.e., involve the fulfillment of a condition that a compound vertex appears

$$\mathcal{M}_{\lambda,j}^\curvearrowright = \{\mathbf{h} : \mathbf{B}_\lambda \mathbf{h} < 0\} \cap \{\mathbf{h} : \mathbf{b}_{\lambda,j}^\curvearrowright \cdot \mathbf{h} = 0\} \quad (4.74a)$$

or a condition that implies the disappearance of a face

$$\mathcal{M}_{\lambda,k}^\varnothing = \{\mathbf{h} : \mathbf{B}_\lambda \mathbf{h} < 0\} \cap \{\mathbf{h} : \mathbf{b}_{\lambda,k}^{i \rightarrow \varnothing} \cdot \mathbf{h} = 0\}. \quad (4.74b)$$

The notation for the unit normals of the cone facets is here adapted in accordance to the linear facet enumeration scheme, i.e.  $\mathbf{b}_{\lambda,j}^\curvearrowright$  and  $\mathbf{b}_{\lambda,k}^{i \rightarrow \varnothing}$  rather than  $\mathbf{b}_{ij,kl}^\curvearrowright$  and  $\mathbf{b}_{ij,kl}^{i \rightarrow \varnothing}$  as in Sec. 3.1. For the 2D example discussed in the previous section, the morphology cones  $\mathcal{M}_1$  and  $\mathcal{M}_2$  were each enclosed by one transition and one disappearance facet. Though in higher dimensions the number of such facets is larger, and  $(n-1)$ -dimensional facets are themselves bound by  $(n-2)$ -dimensional facets and so forth, for the generic derivation of the model equations it suffices to consider an  $n$ -dimensional cone  $\mathcal{M}_\lambda$  and two representative facets  $\mathcal{M}_{\lambda,k}^\varnothing$ ,  $\mathcal{M}_{\lambda,j}^\curvearrowright$ . The latter one constituting the boundary to a neighboring morphology cone  $\mathcal{M}_{\lambda+1}$  as depicted in Fig. 4.18. Without loss of generality we assume that if a particle reaches  $\mathcal{M}_{\lambda,k}^\varnothing$  the  $i$ -th face disappears. As it was shown for the 2D example in the previous section, the modeling using state jumps from and into lower dimensional subspaces spanned by the basis vectors (rather those spanned by the cone edges) yields model equations directly in terms of  $\mathbf{h}$ -coordinates and the introduction of a separate coordinates system,  $\mathbf{z}$ -coordinates, on the cone facet can be spared out.

In principle, the growth vector  $\mathbf{G}$  can point towards a facet or away from it generating two generic cases, see Fig. 4.18, yielding different sets of equations for the number density evolution. Both cases are further specified in Tab. 4.2. The transition from or to the cone  $\mathcal{M}_\lambda$  through the facet  $\mathcal{M}_{\lambda,j}^\curvearrowright$  occurs in any case. Case 1 involves the transition of particles existing in  $\mathcal{M}_{\lambda,k}^\varnothing$  to  $\mathcal{M}_{\lambda,k}^\varnothing$  whereas for Case 2 the reverse sit-



### 4.3.1 Case 1 – Jump from Unstable Surface

The population balances for the fully dimensional interior domain  $\mathcal{M}_\lambda$  and  $\mathcal{M}_{\lambda+1}$  are directly derived from the general continuous case as given in Eq. (2.58a):

$$\frac{\partial f_\lambda}{\partial t} + \nabla_{\mathbf{h}} \cdot (\mathbf{G} f_\lambda) = 0, \quad \text{for } \mathbf{h} \in \mathcal{M}_\lambda \quad (4.77)$$

$$\frac{\partial f_{\lambda+1}}{\partial t} + \nabla_{\mathbf{h}} \cdot (\mathbf{G} f_{\lambda+1}) = 0, \quad \text{for } \mathbf{h} \in \mathcal{M}_{\lambda+1}, \quad (4.78)$$

where their coupling at the cone facet  $\mathcal{M}_{\lambda,j}^\curvearrowright$  is according to Eq. (2.61)

$$(f_\lambda \mathbf{G} - f_{\lambda+1} \mathbf{G}) \cdot \mathbf{b}_{\lambda,j}^\curvearrowright = 0 \quad \text{for } \mathbf{h} \in \mathcal{M}_{\lambda,j} \quad (4.79)$$

The initial populations within  $\mathcal{M}_\lambda$  and  $\mathcal{M}_{\lambda+1}$  are denoted as  $f_{\lambda,0}$  and  $f_{\lambda+1,0}$ . The initial population accommodated in  $\mathcal{M}_{\lambda,k}^{\varnothing'}$ , defined by the number density  $f_{\lambda,k,0}^{\varnothing'}(\mathbf{h}')$  must be added to the initial population at the boundary of  $\mathcal{M}_\lambda$ . For this, the number density  $f_{\lambda,k}^{\varnothing'}(\mathbf{h}', t)$  is lifted to the full state space according to Eq. (2.90):

$$f_{\lambda,k}^{\varnothing'}(\mathbf{h}, t) = f_{\lambda,k}^{\varnothing'}(\mathbf{h}', t) \delta(\mathbf{b}_{\lambda,k}^{i \rightarrow \varnothing} \cdot \mathbf{h}), \quad (4.80)$$

still being defined on  $\mathcal{M}_{\lambda,k}^{\varnothing'}$ . The shift to the domain  $\mathcal{M}_{\lambda,k}^\varnothing$  is obtained with the help of the jump function, relating points on  $\mathcal{M}_{\lambda,k}^\varnothing$  with their counterparts on  $\mathcal{M}_{\lambda,k}^{\varnothing'}$ :

$$\mathbf{h}|_{\mathcal{M}_{\lambda,k}^{\varnothing'}} = \Xi_{\lambda,k} \mathbf{h}|_{\mathcal{M}_{\lambda,k}^\varnothing}, \quad (4.81)$$

where

$$\Xi_{\lambda,k} = [\mathbf{e}_1, \dots, \mathbf{e}_{i-1}, \mathbf{b}_{\lambda,k}^{i \rightarrow \varnothing}, \mathbf{e}_{i-1}, \dots, \mathbf{e}_n]^\top, \quad (4.82)$$

with the basis vectors  $\mathbf{e}_j$  containing zeros on all positions except on the  $j$ -th one. For the present case, the transfer from  $\mathcal{M}_{\lambda,k}^{\varnothing'}$  to  $\mathcal{M}_{\lambda,k}^\varnothing$  is needed, i.e., the inverse function to the one given in Eq. (4.81):

$$\mathbf{h}|_{\mathcal{M}_{\lambda,k}^\varnothing} = \Xi_{\lambda,k}^{-1} \mathbf{h}|_{\mathcal{M}_{\lambda,k}^{\varnothing'}}. \quad (4.83)$$

In view of Eq.s (2.91), the number density  $f_{\lambda,k}^{\varnothing'}(\mathbf{h}, t)$  is shifted to  $\mathcal{M}_{\lambda,k}^\varnothing$  by

$$f_{\lambda,k}^\varnothing(\mathbf{h}|_{\mathcal{M}_{\lambda,k}^\varnothing}, t) = f_{\lambda,k}^{\varnothing'}(\mathbf{h}|_{\mathcal{M}_{\lambda,k}^{\varnothing'}}, t) \det(\Xi_{\lambda,k}^{-1}). \quad (4.84)$$

Inserting Eq. (4.80), and adding this number density to the initial number density of  $\mathcal{M}_\lambda$ , we arrive at:

$$f_\lambda(\mathbf{h}, t=0) = f_{\lambda,0}(\mathbf{h}) + f_{\lambda,k}^{\varnothing'}(\mathbf{h}', t) \delta(\mathbf{b}_{\lambda,k}^{i \rightarrow \varnothing} \cdot \mathbf{h}) \det(\Xi_{\lambda,k}^{-1}). \quad (4.85)$$

### 4.3.2 Case 2 – Jump into Stable Surface

As for Case 1, the interior of the morphology cones is determined by continuous evolution. For the regions  $\mathcal{M}_\lambda$  and  $\mathcal{M}_{\lambda+1}$  the population balances are equivalent to the previous case, stated in Eq.s (4.77) and coupled by Eq. (4.79). The dynamics in  $\mathcal{M}_{\lambda,k}^{\varnothing'}$  is coupled to the number density in  $\mathcal{M}_\lambda$ , because particles reaching  $\mathcal{M}_{\lambda,k}^\varnothing$  are trans-

ferred to  $\mathcal{M}_{\lambda,k}^{\emptyset'}$  instantaneously by a jump, see Fig. 4.18, i.e. feeding the population in  $\mathcal{M}_{\lambda,k}^{\emptyset'}$ . Using Eq. (2.89) and the jump function (4.81), the evolution of the number density is given by

$$\frac{\partial f_{\lambda,k}^{\emptyset'}}{\partial t} + \nabla_{\mathbf{h}'} \cdot (\mathbf{G}' f_{\lambda,k}^{\emptyset'}) = (\mathbf{G} f_{\lambda}(\mathbf{h}, t))|_{\mathcal{M}_{\lambda,k}} \cdot \mathbf{b}_{\lambda,k}^{i \rightarrow \emptyset} \det(\Xi_{\lambda,k}), \quad \text{for } \mathbf{h} \in \mathcal{M}_{\lambda,k}^{\emptyset'}, \quad (4.86)$$

where  $\mathbf{G}' = (G_1, \dots, G_{i-1}, G_{i+1}, \dots, G_n)^T$ .

## 4.4 Summary

In this chapter the multivariate population balances accounting for crystal shape have been derived. At first, the example of potassium dihydrogen phosphate has been studied, where the conditions have been restricted such that no faces on the crystals can disappear. In this sense, it is a rather simple case which nonetheless captures the basic concept of multidimensional modeling. The more challenging case of disappearing faces, leading to the possible reduction of the dynamic part of the state space to morphological manifolds on the facets of the morphology cone, was then addressed in order to exemplify the derivation of population balances in subspaces. Clearly, the general mechanisms studied in Ch. 2 enabled for a rather straightforward development of the equations. In the last section this concept was extended to  $n$ -dimensional state spaces. The universal and detailed treatment of the state space structure for arbitrary convex crystals taken out in Ch. 3 together with the tools provided by Ch. 2 made it possible to master the complexity by providing the generic cases.



*I call our world Flatland, not because we call it so, but to make its nature clearer to you, my happy readers, who are privileged to live in Space.*

---

Edwin Abbott Abbott  
*Flatland – A romance of many dimensions*  
§1 – Of the Nature of Flatland

## Chapter 5

# Observation of Crystal Shape

Modeling of the evolving shape distribution in a crystallization process as delineated in the previous chapter is only useful when it can be equipped with proper kinetic expressions. If this is available, the shape distribution can be (pre)computed for different process conditions. For example, based on a population balance model, the shape distribution could be reconstructed from the evolution of the supersaturation and seed distribution. Due to the complexity of numerous interacting process variables governing the dynamics of crystallizers, the quantitative knowledge of kinetic parameters as a function of a full set of process variables is usually not available. Particularly crystal shape can be perturbed dramatically by minor changes in impurity concentration or simply through the switching to a different supersaturation level, see for instance the review by Sangwal (1998), or different original research articles by Boerrigter et al. (2004); Gilmer (1980); Weissbuch et al. (1991, 1995) and others. Because of the high sensitivity, it is necessary to *observe* a crystallization process with regard to the shape features. However, compared to size analysis, the monitoring of shape is far less developed for good reasons of which to our opinion the most important ones are: (i) Sensors enabling the quantification of the full 3D shape, examples are given below, require thorough sample preparation and are costly; (ii) In situ and ex situ microscopes deliver a 2D information from which it is rather difficult to extract quantitative information.

The aim of this chapter is to develop a scheme with which the 3D shape in terms of the geometrical state vector  $\mathbf{h}$  can be estimated from a 2D photograph of the crystal. The acquisition of these images can be performed with different commercial devices of which the probe QICPIC, built and sold by the company Sympatec GmbH (Clausthal, Germany) has been chosen because it yields high quality images with regard to sharpness of the particle projection boundary. The only information which is extracted from the photo to estimate the 3D shape is the boundary curve (contour) of the 2D particle projection. If the 3D crystal is not attached to others, i.e., it is a single, convex crystal, the projection from any orientation is a convex region as well. If the face orientations are known, the set of projection shapes from different directions of a crystal with fixed geometrical state, can be precomputed. This knowledge can in turn be used conversely to relate the 2D projection to the 3D object. Of course, this inversion is not always unique, that is, the estimation is subject to possibly large – but quantifiable – errors.

The following Chapter is organized as follows. In Sec. 5.1 basic techniques for the measurement and estimation of 3D structures are presented in order to clearly classify the techniques discussed in the then following sections. The specification of the form of 2D projections in terms of parameters, so called shape descriptors, is part of the Sec. 5.2. From the shape descriptors of the 2D projection, the 3D shape shall be obtained which is subject to Sec. 5.3 which includes the especially important analysis on the error of this estimation scheme. In Sec. 5.4 an image processing procedure is sketched and the proposed estimation scheme is applied to the so treated images recorded in experiments. Finally, Sec. 5.5 summarizes the chapter.

## 5.1 Crystal Observation

The information we are aiming for in order to be able to compare a real experiment to a simulation is the 3D crystal shape, at best expressed in terms of the orientations of the crystal faces and their distances to the crystal center, see Ch. 3. However, there does not exist a probe with which this information can be obtained directly, neither for an individual crystal, nor for a full population. Different techniques are available to determine the real 3D crystal shape or in general the 3D structures of objects under investigation, namely *tomography* and *sectioning*. These two major directions are shortly explained in order to differentiate it from a third approach – in the following called *estimation from projection* – to which this work contributes in major parts of this chapter.

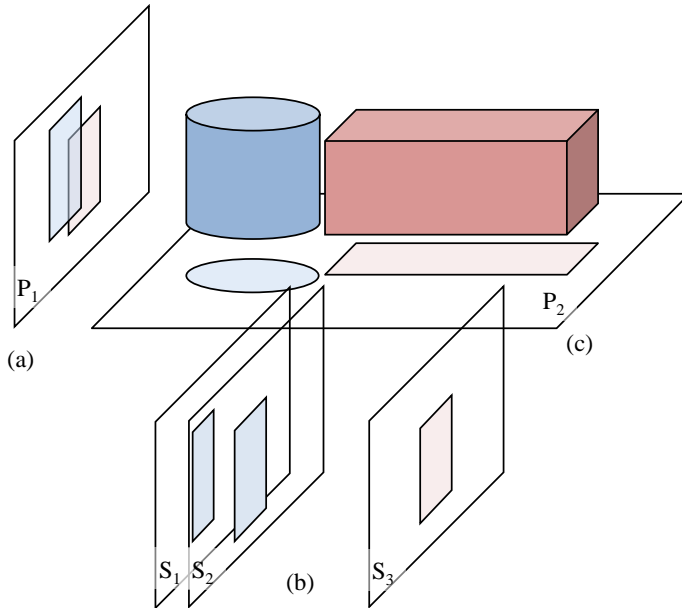


**Figure 5.1:** Techniques to elucidate 3D structures. (a) Tomography uses a number of images, e.g.  $P_1$ , of the object generated with a penetrating wave from different angles. (b) Optical sectioning relies on images which have been recorded in different focal planes ( $S_{1-3}$ ). (c) The estimation approach followed in this work is based on a single projection of the object to a 2D plane ( $P_2$ ).

### 5.1.1 Tomography

The 3D geometry of a crystal can be represented by a 3D array of voxels<sup>1</sup> to which a numerical value (grayscale level) is assigned allowing for the distinction between (possibly different kinds of) solid material and other surrounding matter. Such a precise, non-parametric description of the crystal can be obtained with the help of tomography. Tomography reconstructs a 3D object from a set of images taken from different directions. For this, a wave is generated that penetrates through the object and is partially absorbed, depending on the density and kind of material present within the sample. From every perspective, a different image is obtained since the absorption pattern of the waves varies for different directions for a nonhomogeneous and nonspherical object. Hence, the set of grayscale images collected in this way contains information about the inner structure of the sample. The Radon transform captures this concept mathematically, and by using the inverse Radon transform, the photographed 3D structure can be restored from the set of images (Gonzalez and Woods, 2008). Nowadays, more advanced tomographic restoration algorithms superior to the Radon transform exist, for example the direct Fourier reconstruction, backprojection methods and iterative reconstruction algorithms (Midgley et al., 2007; Gonzalez and Woods, 2008; Buzug, 2008). Tomographs are in first order classified by the wave which is sent through the object. For medical applications X-Rays (CT), radio waves (MRI) and positrons (PET) and combinations thereof are most commonly used. The resolution currently reaches about 10  $\mu\text{m}$  with commercially available devices (Buzug, 2008) and can be used to determine size distributions (Jerram et al., 2009). Specialized X-Ray microscopes yield resolutions down to 15 nm (Midgley et al., 2007; Chao et al., 2005). For even smaller structures, the electromagnetic wave is replaced by a penetrating electron as used in transmission electron microscopy (TEM). This technique is thus called 3D TEM or electron tomography (Koster et al., 2000; Midgley and Weyland, 2003; Weyland et al., 2001; Midgley et al., 2007). The resolution achieved with this technique, for example for studying of catalyst structures, lies in the sub-nanometer range (Ward et al., 2005; Tariq et al., 2011).

Tomography offers promising applications with regard to shape characterization and quantification of dispersed phase systems in general. However, its utilization is costly and specialized staff must be trained to ensure correct and efficient operation. The major disadvantage is that it requires a thorough, time intensive sample preparation, which may alter the sample. Furthermore, with current devices it is not possible to image 3D structures (e.g. crystal suspensions) in motion with the necessary spatiotemporal resolution eligible for dynamic shape distribution measurements. This is primarily due to the fact that a large number of images must be taken from different directions if a high-quality image shall be obtained. By the virtue of the ever evolving tomographic techniques with regard to speed and spatial precision and as the devices may become less costly, one can expect it to be applied as a powerful and widespread method to investigate dispersed phase systems in the future.

---

<sup>1</sup>In 3D the equivalent to a pixel in 2D.

### 5.1.2 Optical Sectioning

By dissecting a crystal population – at best fixed in a glassy solid – mechanically into thin slices, one obtains an immediate impression of the inner and outer geometry of the crystals. Re-stacking of the measured quasi 2D shapes of the slices to a 3D object, the crystal geometry can be reconstructed accurately. Serial sectioning is used in volcanology to analyze the spatial spreading and the shape- and size distributions of mineral grains in igneous rocks (Jerram et al., 2009). This approach is experimentally much more expensive than using a single 2D slice with which one usually tries to determine the size distribution with the help of a shape model, for example as described by Higgins (2000) and Holden et al. (2009) for olivine in kimberlite. Though useful in volcanology, mechanical slicing does not come into question to analyze samples of industrial crystallizers because they are not fixed in a glassy phase and the process of mechanical slicing is too expensive. Instead, non-destructive slicing, making use of optical means only is better suited to obtain shape information.

For transparent crystals, suspended at a low density, images can be acquired in different focal planes with a classical optical bright field microscope. The so obtained image stack is combined to a 3D array which reproduces the underlying 3D structure. For example, Castro et al. (2003) use this technique to measure size distributions of microlites in volcanic glass. Modern microscopic techniques, heavily used in 3D imaging of biological structures, namely laser confocal microscopy, allow for the acquisition of detailed structure information of at least partly transparent samples (Conchello and Lichtman, 2005; Wilson, 2011). Roughly speaking, this method does not record the fully exposed object at one instant but sends light waves of a defined wavelength to a particular part of the object. The region can be controlled in all three spatial directions. Sending light waves to a particular point, only a small region is illuminated and the emitted wave is observed with the microscope. A further development of this technique causes – in the specially prepared sample – fluorescence of markers adhering at particular substances. The lightening and recording of the sample is performed point by point, which avoids the interference of light emitted from different parts of the sample. Combining the recorded information to one 3D array, yields a high-quality image of the object. Biological structures can be observed with this technique with a spectacular clarity, see for instance the book by Pawley (2006). The application of this method to crystals is in principle possible as shown by Vivares et al. (2007) and Fukura et al. (2004). The recorded geometry data could be used to identify different crystal planes and the geometrical state vector as Singh et al. (2010) presented in an in-silico study.

Optical sectioning and particularly laser scanning microscopy is a promising method to elucidate the 3D shape of crystals. However, the recording of 3D images currently takes a few minutes for a crystal of a few 100  $\mu\text{m}$  in size. Thus, it is unrealistic that a crystal population in a moving suspension can be imaged with the necessary accuracy in a short time. As with tomography, optical devices still undergo a vast evolution and the temporal resolution should in the future reach a level that makes true 3D structure information available in large quantities at a high sampling rate.

### 5.1.3 2D Observation

Though the full 3D shape information is desirable to be available in future devices, this work is focused on extracting useful information from a single 2D projection of the particle. The main advantage is the comparatively easy probe operation and handling. In principle, three sampling techniques can be distinguished:

**Offline Imaging of Dry Samples** A sample of the crystal suspension is taken, filtered, dried, dispersed on a microscope slide and imaged with a standard laboratory microscope. Classical optical microscopes, available as standard equipment in the lab, offer the least costly method to implement this means of image acquisition. The manual scanning of the microscope slide and image acquisition can be automatized using programmable stages, e.g. from Prior Scientific Inc. (Rockland, MA)<sup>2</sup>. Malvern (Houston, TX)<sup>3</sup> offers also a ready-to-use optical microscope, for instance MORPHOLOGI G3 from Nikon, equipped with an automatized stage, a dispersing unit for dry samples and image processing software especially designed for particle analysis. Alternatively to dispersing the crystal onto a microscope stage, systems with a vibratory feeder are offered (QICPIC from Sympatec GmbH (Clausthal, Germany)<sup>4</sup> and CAMSIZER from Retsch GmbH (Haan, Germany)), which transports the crystals to a free fall imaging shaft with a light source and a camera, see Patchigolla and Wilkinson (2009) and Brown et al. (2005). However well developed the automation and thus possibilities to increase the number of measured crystals is, a careful sample preparation is necessary, particularly involving drying, which may alter the crystals (Puel et al., 1997). Further, for direct process control it is desirable to record and process crystal images in-line or even in situ within the suspension.

**In-line Imaging of Suspension** The crystal suspension is pumped through a cuvette which is installed on a microscope stage. The crystals within the suspension are imaged while flowing through the cuvette which is possible due to a powerful light source enabling a very short exposure time. This technique can in principle be installed on a standard microscope in the lab with custom-made cuvettes as presented for instance by Patience and Rawlings (2001a); Eggers et al. (2008); Kempkes et al. (2010) and Ferreira et al. (2011). However, this kind of ex situ sensor is also available on the commercial market, for instance the QICPIC system of Sympatec GmbH (Clausthal, Germany) equipped with a flow-through cuvette. In-line imaging of the suspension usually yields a higher image quality than in situ probes because the particles are better aligned within the focal plane of the optical system. However, this comes at the cost of an additional sampling loop subject to the risk of clogging and selective sampling. Crystals possessing low hardness may undergo breakage within the pump which is necessary to convey the suspension into the flow cell. Also aggregation may occur preferentially within feed pipes to the microscope. A further disadvantage occurs for high-density suspensions which must be diluted with clear solution in order to keep the suspension density low so that within an image, crystals that are not merged in an aggregate do not overlap.

---

<sup>2</sup><http://www.prior.com/>

<sup>3</sup><http://www.malvern.com/>

<sup>4</sup><http://www.sympatec.com/>

**In Situ Imaging of Suspension** A camera is directly installed within the crystallizer, thus taking images of the suspension directly in the growth environment. Commercially available in situ sensors, e.g. PVM from Mettler-Toledo AG (Greifensee, Switzerland)<sup>5</sup> or PARTICLEEYE from HiTec Zang GmbH (Herzogenrath, Germany)<sup>6</sup>, can be installed directly in standard laboratory crystallizers. The in situ microscope III-XTF by Sartorius Stedim Biotech GmbH (Göttingen, Germany)<sup>7</sup> is particularly developed for dispersed phase applications in biotechnology (Bluma et al., 2009; Prediger et al., 2011). An alternative to placing the camera directly within the vessel is to install it outside the reactor at an imaging window, e.g. Li et al. (2006); Larsen et al. (2006). The advantage of setting the camera outside of the crystallizer is that it does not influence the growth environment, particularly with respect to the flow-field. A disadvantage, however, is that only crystals at the wall of the vessel can be seen. Clearly, in situ (or quasi in situ) probes deliver the most immediate impression of the crystal population since they can be observed directly in their growth environment without being pumped through a sampling loop or even dried. Compared to in line imaging, however, the quality of the acquired images is lower in the sense that only few particles pass the window within the focal plane of the camera and thus possess the desired sharpness necessary for quantitative, single particle based image processing. Furthermore, if the suspension is of a high density, different overlapping particles can hardly be distinguished and opposite to in-line imaging it is not even possible to dilute the photographed suspension.

The further processing of images obtained with which method whatsoever, can be distinguished in two directions. The first one deduces shape and size measures from the 2D projection and uses this information for further applications, for instance for process monitoring, model calibration or quality control. This utilization of imaging techniques is a rather simple but powerful means to gain better insight in a crystallization process. The next section shall give a short overview on this. The second direction which can be identified aims at reconstructing the true 3D shape from the 2D projection. In a further section, the relevant work on this – far less developed – path is discussed.

### 5.1.3.1 Simple 2D Observation

Imaging or better to say visual inspection of particles is the oldest and most trusted analysis practice in mechanical process engineering in general and specifically in crystallization. The automated observation of the evolving crystal morphology has been of interest to researchers for years over a widespread class of substances. Hence, the following survey cannot be comprehensive but claims to give a representative selection.

Size distribution analysis is of course the most prevalent task in particle image processing. Monnier et al. (1996) use automatic image analysis in order to determine the size distribution of samples which are taken online for adipic-acid crystallization. The observed size distribution along with a calorimetric supersaturation measure-

---

<sup>5</sup><http://www.mt.com/>

<sup>6</sup><http://www.hitec-zang.de/>

<sup>7</sup><http://www.sartorius-stedim.de/>

ment has been used to identify a full population balance model of the crystallization process. Puel et al. (1997) measure hydroquinone crystals dispersed on a microscope slide in length and width to obtain 2D shape distributions of the population. They discuss particularly the transient behavior of crystal habits in an industrial crystallizer. Patchigolla and Wilkinson (2009) use images of  $\alpha$  and  $\beta$  L-glutamic acid and monosodium glutamate monohydrate obtained with CAMSIZER to measure size and shape distributions. They compare the measured size distribution with results obtained from manual microscopic image analysis, ultrasonic attenuation spectroscopy and laser diffraction spectroscopy and find all measurements in reasonable agreement. Alander et al. (2004, 2003) investigate the agglomeration behavior of paracetamol (acetaminophen) in different solvents with the help of off-line microscopic images. Not only scalar shape measures of the identified particles are taken but also the intensity variation of the grayscale within the particle region. For the image analysis they used commercial software, namely *Image-Pro-Plus*<sup>®</sup> by MEDIACYBERNETICS<sup>8</sup>. Sucrose crystallization from water has been investigated with regard to crystal morphology by Ferreira et al. (2011) with a custom flow-cell equipped with a microscope camera. The recorded data is used for a mass-based growth rate determination at different impurity concentrations (calcium chloride and D-fructose). Similarly to the aforementioned study of Alander et al. (2004) also the agglomeration behavior in chemically differently environments is studied.

A couple of papers with qualitative image analysis studies has been published by the groups of Wang and Roberts: In De Anda et al. (2005) the segmentation of images obtained from Mettler-Toledo's PVM-probe and subsequent identification of particle regions is discussed. In De Anda et al. (2005) and De Anda et al. (2005) a pragmatic approach is used to distinguish  $\alpha$  and  $\beta$  polymorphs of L-glutamic acid on the basis of Fourier descriptors together with a neural network. In Wang et al. (2007), the length- and width growth rates of needle shaped L-glutamic acid crystals are estimated over a small supersaturation range (0.47 – 0.51) taken at seemingly arbitrary instances. In Wang et al. (2008) growth laws are presented on this small data basis of six measurements at virtually the same supersaturation level. Furthermore, the titles of their work, e.g. 'Real-Time Measurement of the Growth Rates of Individual Crystal Facets Using Imaging and Image Analysis – A Feasibility Study on Needle-shaped Crystals of L-Glutamic Acid', pretend that face specific growth rates are measured. However, within the text the authors withdraw the announcement from the title and admit that with their method only growth rate in length and width have been measured by neglecting for instance the influence of crystal orientation. Though from studying the titles of a number of publications particularly those by the above mentioned groups it may seem that detailed crystal shape evolution measurements on a population basis have reached a mature status but in fact the authors themselves recognize the fact that this is not the case.

### 5.1.3.2 Estimation of the 3D State from the 2D Projection

When the 3D geometrical state of the crystal has to be reconstructed from a single 2D image, only model based methods can be used in contrast to non-parametric shape quantifications of true 3D sensors. The model is needed because features of the pro-

---

<sup>8</sup><http://www.mediacy.com/>

jection can then be used as an indicator for the 3D shape, that is, the space of possible objects throwing the projection is confined to those which are as well obtainable by the shape model. Shape recognition in grayscale in-situ images of a crystal suspension has for instance been discussed by Larsen et al. (2007) and Larsen (2007). The method presented therein mainly relies on the detection of linear features in the grayscale image and is designed for well faceted high aspect-ratio crystals. A further development is capable of reconstructing wire frame models of the crystals with which crystal morphologies can be estimated (Larsen et al., 2006). Mazzotti and coworkers developed a flow-through microscope in which the passing particles can be seen from two different directions (Kempkes et al., 2010). Based on former work (Eggers et al., 2008) which estimated the height and width of needle-like crystals from a photograph from a single direction which was also applied to ascorbic acid crystallization, they estimate the height, width and depth distribution, i.e., a 3D property distribution, for glutamic acid and ascorbic acid crystals using a 4D axis length distribution (Eggers et al., 2009). The strength of the approach followed by Mazzotti and coworkers is the validation against simulated measurements in order to verify the correctness of the applied estimation scheme which relates the projected data to the full 3D shape. Clearly, this verification problem does not arise in the context of the previously discussed 'simple 2D observation' since it is not the aim of that approach to identify the 3D shape. One weakness of the work of Mazzotti and coworkers is the fact that only the major and minor axis lengths of the projections are used to assess the 3D shape model. In this sense, the present work can in a certain sense be seen to further develop the proposed approach on a larger data basis. Another disadvantage of the work of Mazzotti and coworkers is that the orientation distribution must be known in order to achieve correct results. In the hereafter proposed method, this is not necessary, i.e. the method can be applied regardless of possibly existing preferential orientations.

**Estimation in this work** In order to identify the shape, the crystal geometry model in terms of the state vector  $\mathbf{h}$  is used. Clearly,  $\mathbf{h}$  is the quantity we wish to measure. An additional difficulty to this is that the orientation of the crystal in space has a decisive influence on the shape of the photoprojection but is, depending on the sensor, a more or less stochastic process. In practice, the acquisition of images is performed with flow-through microscope as discussed above. For the design and evaluation of the estimation scheme, however, synthetic images have been generated so that the measured state and orientation can be directly and quantitatively compared to the actual state.

The matching of a crystal projection with the actual crystal shape constitutes a highly nonlinear optimization problem which is tractable by different means. Using continuous, gradient-based optimization techniques in orientation and geometrical state space would be a possibility, but the starting point must be chosen well beneath the true values in order to avoid the solver to run into a local minimum. Global optimizers using heuristic or stochastic techniques require a large number of relatively costly function evaluations and thus the estimation of a large number of crystal shapes becomes infeasible. Therefore, in this work a lookup table is used in which the shape descriptors as functions of state and orientation are precomputed. With this it is also possible to go the inverse way: the determination of state and orientation which corresponds to a specific descriptor. This is a commonly used approach in



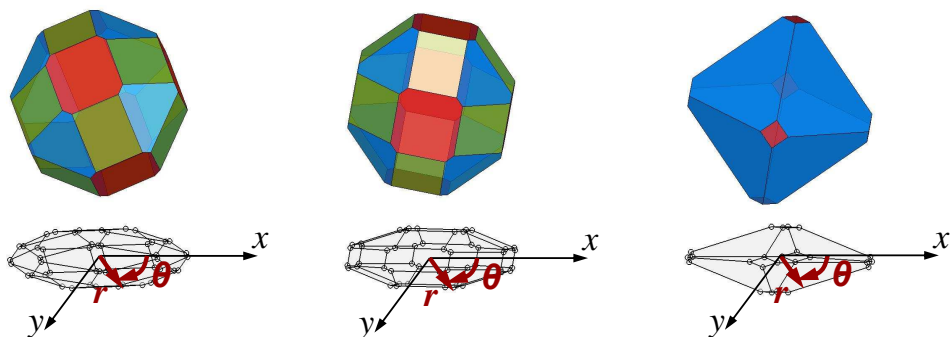


**Figure 5.2:** The projection of a 3D convex crystal to a 2D plane produces a convex region on the plane whose shape depends on the shape of the crystal (essentially the geometrical state vector  $\mathbf{h}$  and the orientation of the crystal relative to the plane. The same crystal shape projected from different perspectives (left and middle). Different shapes photographed from the same direction (middle and right).

object recognition (DeMenthon and Davis, 1995, 1992) and has for instance been used to distinguish crystal polymorphs (De Anda et al., 2005; Li et al., 2006).

Before the estimation method is described in detail, the next Sec. gives an introduction to shape descriptors which shall be used to quantify a projection of a 3D particle.

## 5.2 Shape Descriptors

Crystals that are observed with microscopes are viewed from one perspective and essentially a projection of the particle can be seen, see Fig. 5.2. Though there is a huge information content in the grayscale landscape within a particle, see for instance Fig. 5.20, this information is particularly sensitive to the system under consideration, complex to analyze and difficult to interpret by quantitative means. Therefore, we focus on the shape of the projection which is given by its boundary curve; also referred to as contour. This curve is determined by the shape of the crystal and its orientation in space, see Fig. 5.2. The same crystal shape can produce clearly different contours depending on the orientation from which the projection is taken. However, different crystal shapes, projected onto the 2D plane from the same direction usually produce distinct projections. Hence, the projection can be used as an indicator for the shape of the original 3D crystal shape. But the inversion from the 2D to the 3D shape is usually not unique.

For a convex crystal, the boundary curve is determined by the convex hull of the projection of the crystal vertices which are connected by straight lines. I.e., the crystal projection exhibits characteristic features reflecting features of the original 3D state. Essentially, scalar and vector-valued shape descriptors are distinguished. Scalar measures for the shape of the projection are for example :

- Solidity, the ratio between actual and convex area
- Aspect ratio, the ratio between maximum and minimum Feret diameter

- Convexity, the ratio between convex perimeter to perimeter
- Circularity, the ratio between actual area to the area of a circle with the same perimeter
- Eccentricity, the ratio between major and minor axis lengths or the ratio between the major and minor side length of the smallest box containing the particle.

Definitions of these descriptors can for instance be found in Gonzalez and Woods (2008); Alander et al. (2003); Burger and Burge (2008) and also in the Matlab manual under the help document for the function `regionprops` (MathWorks, 2011). Helpful are also manuals of microscopes and image processing software, e.g. Sympatec (2006); MathWorks (2009); Cybernetics (2005). Note that shape descriptors tend to be defined in different ways by different authors/companies. For a comparison between measurements taken by different devices and computer programs, it is thus always necessary to agree on one definition of the shape descriptor. Scalar shape descriptors are of course very useful in quantifying the shape of a projection in a pragmatic and simple way. Particularly shape distributions can be produced in a straightforward way and the structure evolution of particles can be observed in such a manner, as for example shown in Borchert and Sundmacher (2011a). Multiple scalar shape descriptors can be assembled to a descriptor vector which is a point in the descriptor space involving for example also a quantity for size. Therein, a number density can be identified whose evolution reveals the structure evolution in a rather detailed way (Borchert and Sundmacher, 2011a).

Though scalar shape descriptors can be helpful for classification, they are a rather coarse measure compared to the rich information that is exhibited by the full projected shape. For the identification of the 3D state, a descriptor carrying a more detailed shape information is requisite. Inevitably, vector valued shape descriptions have to be employed. Clearly, this information must be extracted from the boundary curve whose detailed deduction from the 3D object is discussed next. In the then following section the signature and the abstraction of the same – making up the information-rich descriptor vector we are aiming for – is introduced.

### 5.2.1 2D Boundary Curve

The shape of the crystal is given by a point set defined by the geometrical state  $\mathbf{h}$  and the orientation  $\mathbf{N}$  of the planes, or – which is a more appropriate terminology in crystallography – the crystal faces, see Ch. 3:

$$\mathcal{S} = \{\mathbf{r} : \mathbf{N} \mathbf{r} \leq \mathbf{h}\} . \quad (3.1)$$

Alternatively, this set can be expressed as the convex domain bound by the crystal vertices, the so called  $\mathcal{V}$ -representation, see Ziegler (2006):

$$\mathcal{S} = \left\{ \mathbf{r} : \mathbf{r} = \sum_{j=1}^{n_S} \alpha_j \mathbf{v}_j, \sum_{j=1}^{n_S} \alpha_j = 1 \right\} , \quad (5.1)$$

where the crystal vertices,  $\mathbf{v}_j$ , can be calculated from the plane orientations,  $\mathbf{N}$ , and the geometrical state vector,  $\mathbf{h}$ , using Eq. (3.6). As discussed in Sec. 3.1, the number

of vertices, denoted by  $n_S$ , is a function of the geometrical state and thus varies in different domains of the morphological state space. The projection of  $S$  onto the photoplane is given by

$$\mathcal{P} = \left\{ \mathbf{x} : \mathbf{x} = \sum_{j=1}^{n_P} \alpha_j \mathbf{p}_j, \sum_{j=1}^{n_P} \alpha_j = 1 \right\}, \quad (5.2)$$

where  $\mathbf{x} = (x, y)^T \in \mathbb{R}^2$  is the coordinate vector on the projection plane and  $\mathbf{p}_j$  are projected vertices of the crystal:

$$\mathbf{p}_j = \mathbf{P} \mathbf{v}_j. \quad (5.3)$$

The projection matrix is composed of a true projection matrix and a product of rigid body rotation matrices specifying the relative orientation between the crystal and plane in terms of the Euler angles  $\boldsymbol{\psi} = (\psi, \theta, \phi)$  (Bronstein et al., 2001; Eggers, 2008):

$$\mathbf{P} = \mathbf{P}_P \mathbf{P}_\psi \quad (5.4a)$$

$$\mathbf{P}_P = \begin{bmatrix} 1 & 0 & 0 \\ 0 & 1 & 0 \end{bmatrix} \quad (5.4b)$$

$$\mathbf{P}_\psi = \begin{bmatrix} \cos \psi & -\sin \psi & 0 \\ \sin \psi & \cos \psi & 0 \\ 0 & 0 & 1 \end{bmatrix} \times \begin{bmatrix} 1 & 0 & 0 \\ 0 & \cos \theta & -\sin \theta \\ 0 & \sin \theta & \cos \theta \end{bmatrix} \times \begin{bmatrix} \cos \phi & -\sin \phi & 0 \\ \sin \phi & \cos \phi & 0 \\ 0 & 0 & 1 \end{bmatrix}, \quad (5.4c)$$

see also Fig. 5.3, which depicts a projected KDP crystal. In Eq. (5.2) not all  $n_S$  vertices of the crystal are used but only the  $n_P$  ones which form the convex hull of the projection, i.e., which lie on the boundary of the projection. Let the projected vertices, as Fig. 5.3 depicts, be ordered in a counterclockwise direction, that is, the boundary of the projection is composed of linear sections between two successive projected vertices. With this, the boundary can be expressed as

$$\mathcal{B} = \left\{ \mathbf{x} : \mathbf{x} = (1 - \lambda) \mathbf{p}_j + \lambda \mathbf{p}_{j+1}, 0 \leq \lambda \leq 1, j = 1 \dots n_P \right\}. \quad (5.5)$$

Properties of the projection which can be computed from the projected vertices efficiently and turn out to be useful later are area (Burger and Burge, 2008):

$$A = \frac{1}{2} \sum_{j=1}^{n_P} \det[\mathbf{p}_j \mathbf{p}_{j+1}] \quad (5.6)$$

and centroid (Eggers, 2008; Burger and Burge, 2008):

$$\mathbf{x}_c = \frac{1}{6A} \sum_{j=1}^{n_P} (\mathbf{p}_j + \mathbf{p}_{j+1}) \det[\mathbf{p}_j \mathbf{p}_{j+1}]. \quad (5.7)$$

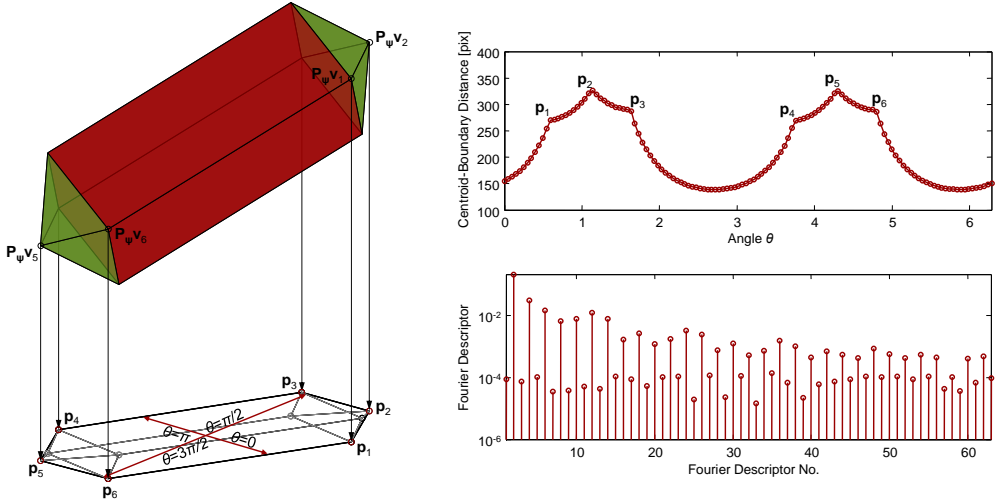


**Figure 5.3:** Relationship between 3D crystal shape and Fourier descriptors. Left: Projection of a KDP crystal onto a projection plane. The orientation of the crystal in terms of the Euler angles is  $\psi = [1.12, 2, 1]$ , the geometrical state is  $\mathbf{h}^T = [0.177, 0.464]$ . The crystal is projected on an array simulating a CCD chip whose pixel size is  $5 \times 10^{-6}$  in both directions. The overall number of pixels of the boundary is 1485 which is a value comparable to well developed crystals as recorded in experiments. Right: The signature function 'centroid to boundary versus angle' of the projection evaluated for a sequence of 128 angles. Major features like corners can be clearly identified (top). The absolute values of the Fourier coefficients of the signature yield a description that is independent of rotations on the projection plane (bottom).

## 5.2.2 Signature

In principle, the boundary surrounding the 2D object is a 1D curve and thus can be represented by a 1D functional which can be defined in different ways (Gonzalez and Woods, 2008). The simplest of these so called signature functions is obtained by measuring the distance between the centroid of the object to the boundary curve as a function of the angle, see Fig. 5.3. This signature function is referred to as *centroid-to-boundary distance* (Loncaric, 1998). It is transformed to polar coordinates whose origin is the centroid of the projection (Bronstein et al., 2001):

$$r = |\mathbf{x} - \mathbf{x}_c| \quad (5.8a)$$

$$\theta = \begin{cases} +\arctan \frac{x-x_c}{r} & \text{for } (y-y_c) \geq 0 \\ -\arctan \frac{x-x_c}{r} & \text{for } (y-y_c) < 0 \end{cases} \quad (5.8b)$$

For a convex polygon defined by the edges  $\mathbf{p}_1, \dots, \mathbf{p}_n$ , the function  $r(\theta)$  is composed of linear connecting lines between the edges:

$$r(\theta) = -\frac{\det[\mathbf{p}_j \mathbf{p}_{j+1}]}{(\mathbf{p}_j^T - \mathbf{p}_{j+1}^T) \mathbf{q}} \quad \text{for } 0 \leq -\frac{\mathbf{p}_j^T \mathbf{q}}{(\mathbf{p}_j^T - \mathbf{p}_{j+1}^T) \mathbf{q}} \leq 1, \quad (5.9a)$$

where

$$\mathbf{q} = \begin{pmatrix} -\sin \theta \\ \cos \theta \end{pmatrix}, \quad 0 \leq \theta \leq 2\pi. \quad (5.9b)$$

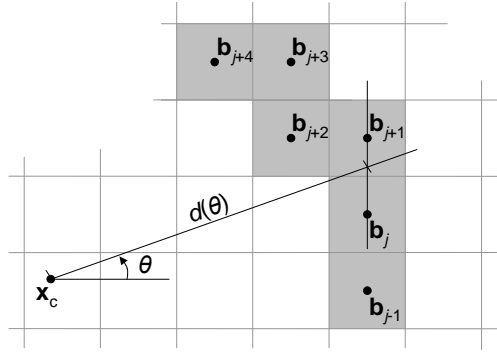


**Figure 5.4:** Evaluation of the signature functional at defined angles for pixelated images.

The functional  $r(\theta)$  is invariant under translation of the object on the projection plane but clearly depends on the orientation. This can be remedied by a transformation which displaces  $r(\theta)$  such that it starts at a characteristic feature, for instance at the maximum. Such an operation corresponds to a shape-preserving rotation on the photoplane. A typical example of the centroid to boundary signature is shown in Fig. 5.3: The signature of the projection which can be seen in the left part is depicted in the upper right corner. It exhibits two maxima which correspond to the projected apices of the pyramids and two minima reflecting the drawn-out prismatic part of the crystal. Points of high curvature of the signature function are associated with corners in the projection.

Alternatives to the centroid-to-boundary approach use the tangent angle versus arc length function, directly a complex function in the  $x - y$ -plane, or the distance between the centroid and special feature points on the boundary, for instance points of high curvature which are usually associated with corners as can be seen in Fig. 5.3 (Loncaric, 1998; Gonzalez and Woods, 2008). However, these variants require additional processing steps (e.g. an algorithm to detect high curvature points) which reduces the robustness compared to the centroid-to-boundary distance signature as used in the following.

### 5.2.3 Sampled Signature

So far the signature of the projection contour has been discussed in continuous terms, i.e., the form given in Eq. (5.9) can be evaluated with an arbitrary accuracy. In practice the boundary can be recorded only at a finite resolution on a CCD-chip. For example, the flow-through microscope QICPIC which is used for the observation of experiments presented below, has a resolution of  $5\mu\text{m}$  (or  $1\mu\text{m}$  depending on the chosen measurement range) in the vertical and horizontal direction. That is, the boundary is in practice given as a set of mean pixel coordinates,  $\mathbf{b}_j = (x_j, y_j)^T \in \mathbb{R}^2$ , which make up the discretized boundary,

$$\mathbf{B} = [\mathbf{b}_1, \dots, \mathbf{b}_b], \quad (5.10)$$

see also Fig. 5.4. The sampling of the signature obtained from the discrete digital image is obtained by measuring the distance from the centroid to the boundary in the respective direction

$$\mathbf{r}(\mathbf{B}) = [\text{dist}(\mathbf{x}_c, \mathbf{B}, \theta_1), \dots, \text{dist}(\mathbf{x}_c, \mathbf{B}, \theta_N)]^T \in \mathbb{R}^N, \quad (5.11)$$

where  $\text{dist}(\cdot)$  is the Euclidian distance between  $\mathbf{x}_c$  and the intersection between (i) the ray with angle  $\theta$  starting at  $\mathbf{x}_c$  and (ii) the straight line connecting the two boundary points  $\mathbf{b}_j$  and  $\mathbf{b}_{j+1}$  which are closest to the ray, see Fig. 5.4.  $N$  is the number of sampling points of the signature which was in all studies in this work set to  $N = 128$ .

The sampled signature function not taken from a discretized image but directly from the analytical form of the boundary, Eq. (5.8), evaluated at predefined angles  $\theta_1, \dots, \theta_n$  is simply obtained from solving Eq. (5.9) at the respective angles:

$$\mathbf{r}(\mathcal{B}) = [r(\theta_1), \dots, r(\theta_N)]^T \in \mathbb{R}^N. \quad (5.12)$$

Of course, this sampling of the signature function is not used for the analysis of images but will be utilized to build up a database with which images shall be analyzed.

## 5.2.4 Abstraction of the Signature: The Fourier Transform

The centroid-to-boundary distance is in principle a good representation form of the projection shape. It characterizes the boundary in any detail and in an identification scheme for the 3D state it would be possible to take all these details into account. However, the boundaries in real crystal images are subject to noisy variations since in general, the crystal shape is not ideally formed but featured with irregular bumps for instance caused through smaller crystals attached to the surface or growth irregularities. Also the real projection boundary is not recorded with an infinitely well resolving plane but on a finitely resolving CCD-chip. That is, recording the boundary of a real crystal with a digital microscope, the discretization allows only for a limited accuracy of subtle boundary features. For this reason, it is desirable to transfer the centroid-to-boundary function to a representation in which slight variations are captured with descriptors that assume values of a magnitude well below those descriptors which carry the principal shape data.

Since the centroid-to-boundary function is a 1D signature of the 2D projection contour, the well developed 1D signal processing tools can be used in order to analyze and classify the projection. The Fourier transform is the most widely used concept in signal processing and has in fact been used for shape analysis some fifty years ago for the first time in a research group of the Ohio State University, see Zahn and Roskies (1972) and references therein. From the seventies onwards Fourier descriptors have been employed for pattern recognition. Of the numerous applications, the identification of handwritten characters has been the most vividly studied problem, see for example the papers by Granlund (1972); Zahn and Roskies (1972); Persoon and Fu (1977). A major difference – whether advantageous or disadvantageous – is that Fourier descriptors do not resolve the contour locally but all major and minor details are distributed globally onto the Fourier coefficients. Thus, a small number of Fourier coefficients suffices to reconstruct the gross shape (Gonzalez and Woods,

2008). The Fourier transform of the sampled signature is given by (Bronstein et al., 2001):

$$R_{k+1} = \sum_{n=0}^{N-1} r(\theta_{n+1}) e^{-\frac{2\pi i kn}{N}}, \quad k = 0, \dots, N-1, \quad (5.13)$$

where  $i$  denotes the imaginary unit. The Fourier coefficients  $R_j$  are in general complex valued and specify amplitude and phase of periodic components in the original sequence  $\mathbf{r}$ , see Eq.s (5.11) and (5.12). That is, a shift of the signature function, corresponding to a rotation on the projection plane, is reflected in the phase of the Fourier transformed signal. Therefore, a rotation-invariant shape description is obtained by the magnitude of the Fourier coefficients:

$$|R_k| = \sqrt{\text{Re}(R_k) + \text{Im}(R_k)}. \quad (5.14)$$

In order to achieve scale invariance, the Fourier coefficients are resized by division through the largest coefficient. The so obtained values make up the shape descriptor vector

$$\mathbf{d} = (d_1, \dots, d_N)^T = s (R_1, \dots, R_N)^T, \quad s = \max_j (R_j). \quad (5.15)$$

which shall be used in the subsequent section for the identification of the 3D shape. As described in the Sec.s 5.2.1-5.2.4, see also Fig. 5.5, the descriptor is obtained from the 3D state quantified for a particular crystal system by the geometrical state vector  $\mathbf{h}$  and the orientation  $\psi$ , i.e., the descriptor vector can be seen as a function of these inputs:

$$\mathbf{d} = \mathbf{f}_{\text{descr}}(\mathbf{h}, \psi). \quad (5.16)$$

In principle, other descriptor vectors can be used as well. Of course, the direct use of the sampled signature would be possible which must be scaled for scale-invariance and shifted in order to achieve rotation invariance as presented by Borchert and Sundmacher (2009). In Borchert and Sundmacher (2011b) yet another alternative is used in which the linear features of the boundary curve are extracted with the help of a Hough transformation. The linear boundary segments are ordered according to their lengths and the angle between them is measured. The descriptor vector is made up by the lengths of linear segments and the angles between them. Borchert and Sundmacher (2011b) show that this vector is a useful, however, relatively compact indicator to relate to the 3D geometry.

## 5.3 Shape Estimation Scheme

It is obvious that a loss of information is caused by the projection and in general there is not a unique mapping from the descriptor vector  $\mathbf{d}$  to the state vector  $\mathbf{h}$ . I.e., the same set of descriptors can be produced from different states and orientations so that the inverse operation to Eq. (5.16)

$$(\mathbf{h}, \psi) = \mathbf{f}_{\text{descr}}^{-1}(\mathbf{d}) \quad (5.17)$$

must not necessarily be unique. However, when the geometrical state is given, it is an easy task to project the vertices on a plane and determine the descriptor vector  $\mathbf{d}$ . The

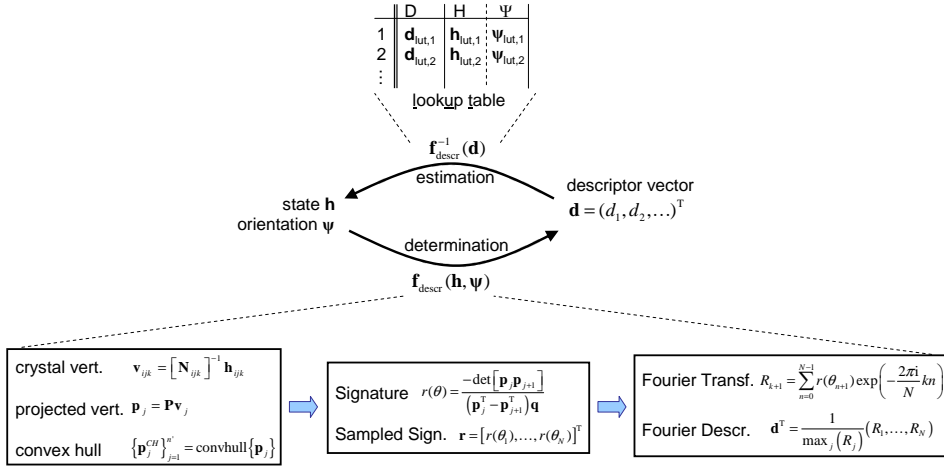


Figure 5.5: Shape estimation scheme.

main idea of the following part is to build up a lookup table or database of descriptors for which the geometrical state is known. By comparing a measured descriptor vector to this data set, a guess can be made which crystal shape is at hand.

### 5.3.1 Shape Estimator Setup

In principle, it is possible to formulate an optimization problem that estimates the state and orientation on the basis of the measured descriptor vector,  $\hat{\mathbf{d}}$ , by minimizing the difference to the descriptor obtained from the model:

$$\min_{\mathbf{h}, \psi} (\hat{\mathbf{d}} - \mathbf{f}_{\text{descr}}(\mathbf{h}, \psi))^T (\hat{\mathbf{d}} - \mathbf{f}_{\text{descr}}(\mathbf{h}, \psi)). \quad (5.18)$$

However, this optimization problem must be solved for every single particle that is extracted from an image. The objective, though continuous, exhibits several local minima and thus a global optimization strategy has to be employed which is computationally expensive. Since the dimensionality of the problem is not too high, the joint  $(\mathbf{h}, \psi)$ -space can be screened previously in order to calculate the descriptor vectors in different regions of the state and orientation space. The descriptor vectors are stored in a lookup table which is compiled from numerical experiments: The descriptor vectors  $\mathbf{d}_{\text{lut},j}$  are acquired for boundary curves of crystals with randomly chosen, uniformly distributed states  $\mathbf{h}_{\text{lut},j}$  and orientations  $\psi_{\text{lut},j}$ . The random choice of the orientation is achieved with random numbers, which are equally distributed for the Euler angles  $\phi$  and  $\psi$  and for  $\theta$  the arcsine of random number in the interval  $-1$  to  $1$  is taken:

$$0 \leq \phi < 2\pi \quad (5.19a)$$

$$\theta = \arcsin(m), \quad -1 \leq m < 1 \quad (5.19b)$$

$$0 \leq \psi < 2\psi, \quad (5.19c)$$



see for details Eggers (2008) and Eisenschmidt (2009). The whole set of (random) states and therefrom determined descriptors:

$$D = \{\mathbf{d}_{\text{lut},1}, \dots, \mathbf{d}_{\text{lut},n_{\text{lut}}}\} \quad (5.20a)$$

$$H = \{\mathbf{h}_{\text{lut},1}, \dots, \mathbf{h}_{\text{lut},n_{\text{lut}}}\} \quad (5.20b)$$

$$\Psi = \{\boldsymbol{\psi}_{\text{lut},1}, \dots, \boldsymbol{\psi}_{\text{lut},n_{\text{lut}}}\} \quad (5.20c)$$

is the boundary descriptor lookup table, see Fig. 5.5. The number of entries in the lookup table is denoted by  $n_{\text{lut}}$  and is made up of  $n_{\text{lut},h}$  different random state vectors which are each imaged from  $n_{\text{lut},\psi}$  different orientations, i.e.,  $n_{\text{lut}} = n_{\text{lut},h} n_{\text{lut},\psi}$ . An estimator uses this database and compares a measured descriptor  $\hat{\mathbf{d}}$  to those given in the table:

$$\text{dist}(\hat{\mathbf{d}}, \mathbf{d}_{\text{lut},j}) = (\hat{\mathbf{d}} - \mathbf{d}_{\text{lut},j})^T (\hat{\mathbf{d}} - \mathbf{d}_{\text{lut},j}), \quad \mathbf{d}_{\text{lut},j} \in D, \quad j = 1, \dots, n_{\text{lut}}. \quad (5.21)$$

Finally, the entry in the database that deviates least from the measured one is taken as the hit and the geometry of the crystal can be identified:

$$\mathbf{h}_{\text{est,sc}}(\hat{\mathbf{d}}) = \mathbf{h}_{\text{lut},j} : \text{dist}(\hat{\mathbf{d}}, \mathbf{d}_{\text{lut},j}) \leq \text{dist}(\hat{\mathbf{d}}, \mathbf{d}_{\text{lut},k}) \quad \forall \mathbf{d}_{\text{lut},k} \in D, \quad (5.22)$$

where  $\mathbf{h}_{\text{est,sc}}$  must be rescaled to original dimensions reversing the scaling as introduced in Eq. (5.15):

$$\mathbf{h}_{\text{est}} = \mathbf{f}_{\text{est}}(\hat{\mathbf{d}}) = s \mathbf{h}_{\text{est,sc}}. \quad (5.23)$$

The accuracy of this estimation scheme depends on the complexity of the crystal, the quality of the images and the degree of consistency with which the real crystals are reflected in the polyhedral crystal model. The following section assesses the quality of the estimates under various circumstances ranging from the theoretical situation of a descriptor acquisition from a CCD chip with infinite resolution to pixelated images of asymmetric crystals photographed with poor boundary resolution. The following case studies are based on synthetic images, i.e., they serve to compare the measured with the actual state to test the estimation quality which can in principle and in practice be achieved.

### 5.3.2 Performance of the Estimator

A population consisting of three subpopulations of KDP crystals is examined which are all normally distributed with means and variances

$$\begin{aligned} \mu_1^T &= (2, 6) \times 10^{-4} & \sigma_{1,11} &= 2 \times 10^{-5} & \sigma_{1,22} &= 2 \times 10^{-5} \\ \mu_2^T &= (4, 3) \times 10^{-4} & \sigma_{2,11} &= 5 \times 10^{-6} & \sigma_{2,22} &= 1.25 \times 10^{-5} \\ \mu_3^T &= (2, 3) \times 10^{-4} & \sigma_{3,11} &= 1 \times 10^{-5} & \sigma_{3,22} &= 1 \times 10^{-5} \end{aligned} \quad (5.24)$$

and vanishing covariances. From each subpopulation 200 samples are generated, see Fig. 5.7 (top left), randomly oriented according to Eq. (5.19), and the descriptor vector  $\hat{\mathbf{d}} = \mathbf{f}_{\text{descr}}(\mathbf{h}, \boldsymbol{\psi})$  is determined. The procedure described in Sec. 5.3.1 is used to reestimate the geometrical state. An exemplary result is depicted in Fig. 5.7 (bottom left): The features of the original population (top left) can be reconstructed well. Especially

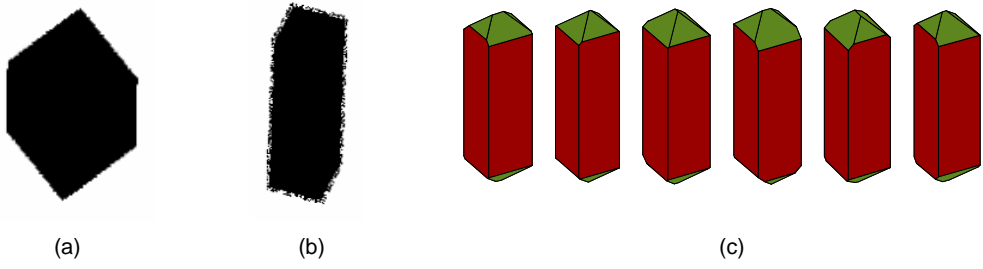


**Figure 5.6:** Real world effects considered in the assessment of the estimation scheme: pixelated image (a), blurred crystal boundary (b) and asymmetric crystals (c).

the distinction between different subpopulations is possible in a reliable way. The error of the estimate of the  $j$ -th particle with respect to the quantity  $h_k$  is measured by

$$e_{jk,est} = \frac{h_{k,est} - h_{k,true}}{h_{k,true}}. \quad (5.25)$$

The assessment of the estimation scheme is carried out in several steps in which successively several 'real world effects' are added which make the estimation more difficult due to the resulting lower data quality. At first, the images are taken on a plane with infinite resolution, i.e., the Fourier descriptors are directly computed from the analytical (but sampled) contour (Eq.s (5.9) and (5.12)), see Sec. 5.3.2.1. The first effect to assess the performance under more practical circumstances is the finite resolution (discretization) of the projection plane as depicted in Fig. 5.6 (a), see Sec. 5.3.2.2. The projection of the crystal can in practice become diffuse as depicted in Fig. 5.6 (b) due to two effects: (i) small crystals adhering to the 'actual' large crystal or (ii) crystals are imaged out of focus, see Sec.s 5.3.2.3 and 5.3.2.5. The crystal model that shall be identified is in a particular point highly idealized: In stirred systems the crystals rarely grow perfectly symmetric but the distances of individual faces of one form usually fluctuate around a mean value, see Fig. 5.6 (c). This effect is discussed in Sec. 5.3.2.4 and jointly with the diffuse boundary in Sec. 5.3.2.5.

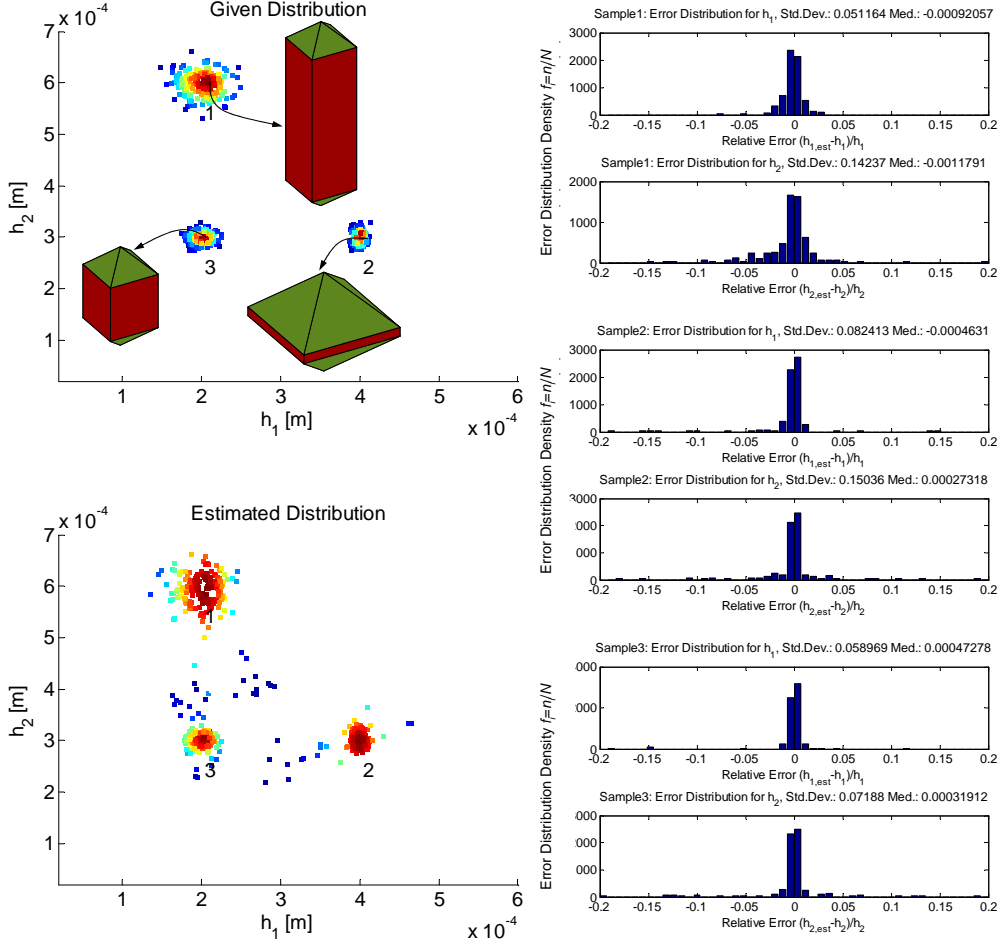
### 5.3.2.1 Projection on Plane with Infinite Resolution

Fig. 5.7 (right) shows the error distribution for each of the three populations for both quantities  $h_1$  and  $h_2$ . It can be seen that the majority of the estimates comes with an error well below 5%. The standard deviation of the error distribution ranges from  $5.12 \times 10^{-2}$  to  $1.50 \times 10^{-1}$  as specified in the titles of the error distributions shown in Fig. 5.7. Note also that the standard deviation of the error distribution is relatively high because erratic outliers for which the estimate is very poor exist in all populations. This is due to the fact that it is not always possible to reconstruct the 3D shape from the projection uniquely. For instance, if the three representative shapes shown in 5.7 (top left) are viewed from top, i.e., only pyramidal faces can be seen, the state of the pyramidal faces cannot be determined. Such outliers can thus only be eliminated by analyzing the inner structure of the particle region or increasing the number of perspectives from which the crystal is imaged, see the works of Larsen (2007) and Kempkes (2009). Both approaches are not further pursued in this work. The median as well as the mean of the error distribution is for all error distributions below  $1 \times 10^{-2}$ , i.e., below 1%, that is, the *mean* value of a population – wherever located in the state space – can be measured with a good accuracy. But the *error distribution* indicates that the estimation scheme is not working equally well in all areas of the state space (but the mean value of the population being estimated well). Particularly the distribution of population 3 can be identified with a better quality than populations 1 and 2. The accuracy of the estimates of  $h_2$  in populations 1 and 2 is rather poor compared to estimates of  $h_1$ . In population 1 this is due to the lower prominence of the  $h_2$  faces on the crystal surface, see examples of these shapes in Fig. 5.7 (top left). Therefore, features of  $h_2$  faces are less expressed in the projections and thus the distinction between subtle differences in  $h_2$  requires highly resolved lookup tables to achieve better results. However, a standard deviation of the error, denoted by  $\sigma_{e_k}$ , of less than 10% shall be considered sufficient for our purposes especially with regard to the well measurable mean values of the population. This result has been achieved with a lookup table which was made up of  $n_{\text{lut},h} = 300$  different state vectors whose resulting crystal shapes are each photographed from  $n_{\text{lut},\psi} = 150$  different random directions.

Assessing the improvement of the estimation quality with varying configurations of the lookup table can be done by considering the standard deviation of the error distribution  $\sigma_{e_k}$ . This is depicted for population 1 in Fig. 5.8 with a variation of the lookup table size from  $n_{\text{lut},h} = 100 \dots 1000$  and  $n_{\text{lut},\psi} = 100 \dots 300$ . As expected, a blow-up of the table size improves the accuracy of the estimates. Particularly an increase in the number of states,  $n_{\text{lut},h}$ , reproduces the population in a better way while the effect of increasing the number of orientation variations  $n_{\text{lut},\psi}$  is weak. It is clear now that the estimation scheme as described in 5.3.1 works in principle if the shape descriptors  $\hat{\mathbf{d}}$  can be measured with a high accuracy (infinite resolution of the CCD chip). At next the case of pixelated images is presented.

### 5.3.2.2 Crystals Projected on Plane with Finite Resolution

The estimation performance for descriptors obtained from a pixelated synthetic image, see Fig. 5.6 (a), is shown in Fig. 5.9. The major characteristics of the population are again well reproducible (bottom left). The characteristics of the error distributions



**Figure 5.7:** Estimator performance tested on a KDP population being concentrated in three different areas of the state space. Each 'island' consists of 200 individual crystals which have been photographed in silico from a random perspective. The images are taken with infinite resolution, i.e., the contour is given in an analytical form, Eq. (5.9), and subsequently sampled according to Eq. (5.12). Left column: Given shape distribution with sketches of representative shapes for each region (top). Estimated distribution on the basis of synthetic images from which Fourier descriptors are extracted and used to match them with the closest entry in a precomputed database (bottom). Right column: Distributions of the relative error of the estimated values for  $h_1$  and  $h_2$  separately for all three regions in which the crystals are concentrated, i.e., sample 1 (top), sample 2 (middle) and sample 3 (bottom). The size of the database used was  $n_{\text{lut}} = 45,000$  ( $n_{\text{lut},h} = 300$  and  $n_{\text{lut},\psi} = 150$ ).

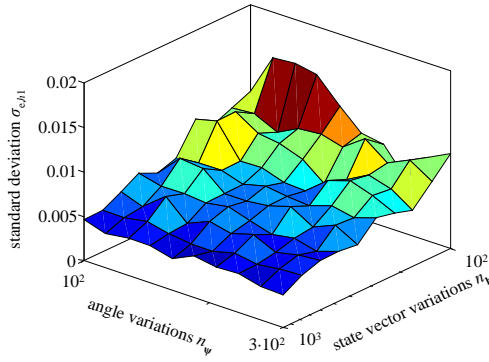


**Figure 5.8:** Standard deviation of the error distribution for varying database size.

are similar to the case of infinite resolution, however, as expected, the distributions become wider due to the additional data coarsening as a result of the pixelization. As discussed for the previous case already, the enlargement of the lookup table which resolves the joint state and orientation space finer, enhances the quality of the estimates to a certain degree as is exemplary shown in Fig. 5.10. The higher estimation quality can be seen immediately from the scatter plots of the estimated populations in Fig.s 5.9 and 5.10 (bottom left). Also the error distribution is clearly narrowed for the estimation with a larger database.

Yet another effect which usually improves the accuracy of the estimation is the preferential orientation of the crystals. For instance, elongated shapes as they typically appear in population 1 tend to be oriented such that the prismatic edges are parallel to the projection plane, see the microscopic photo in Fig. 5.20 and the sketched view directions in Fig. 5.11. The error distributions for an estimate is depicted in Fig. 5.11. It can be clearly seen that the estimation performance is far better than even for the case of an infinitely resolving plane on which the crystals are projected from a purely random perspective. Especially outliers cannot be observed because in this particular case all faces can be clearly seen and the inversion from the projection contour to the 3D state is in principle possible from this perspective. That is, the error that is still present, as can be seen in the error distributions, is only due to the finite resolution of the image and lookup table.

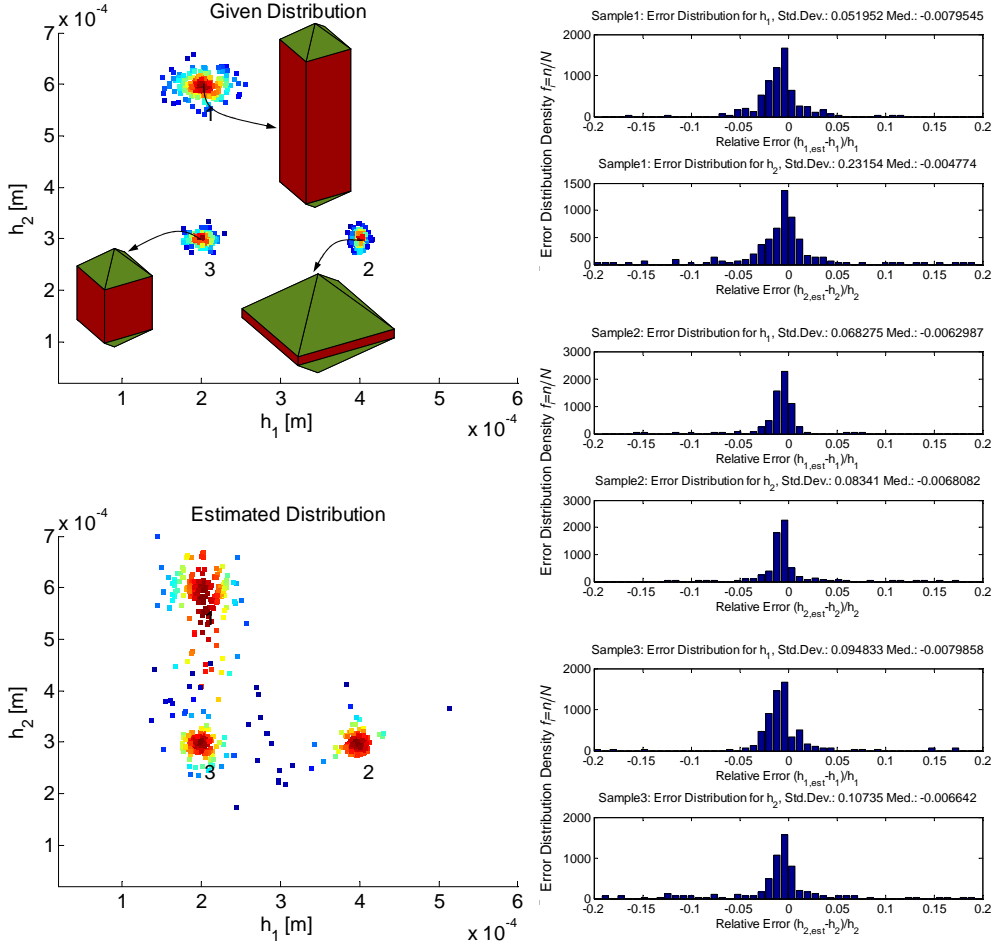


**Figure 5.9:** Estimator performance tested on a KDP population similar to Fig. 5.7. The images are taken on an array with finite resolution. Left column: Given shape distribution (top). Estimated distribution on the basis of synthetic images (bottom). Right column: Distributions of the relative error of the estimated values for samples 1 (top), 2 (middle) and 3 (bottom). The size of the lookup table was  $n_{lut} = 45,000$  ( $n_{lut,h} = 300$  and  $n_{lut,psi} = 150$ ).

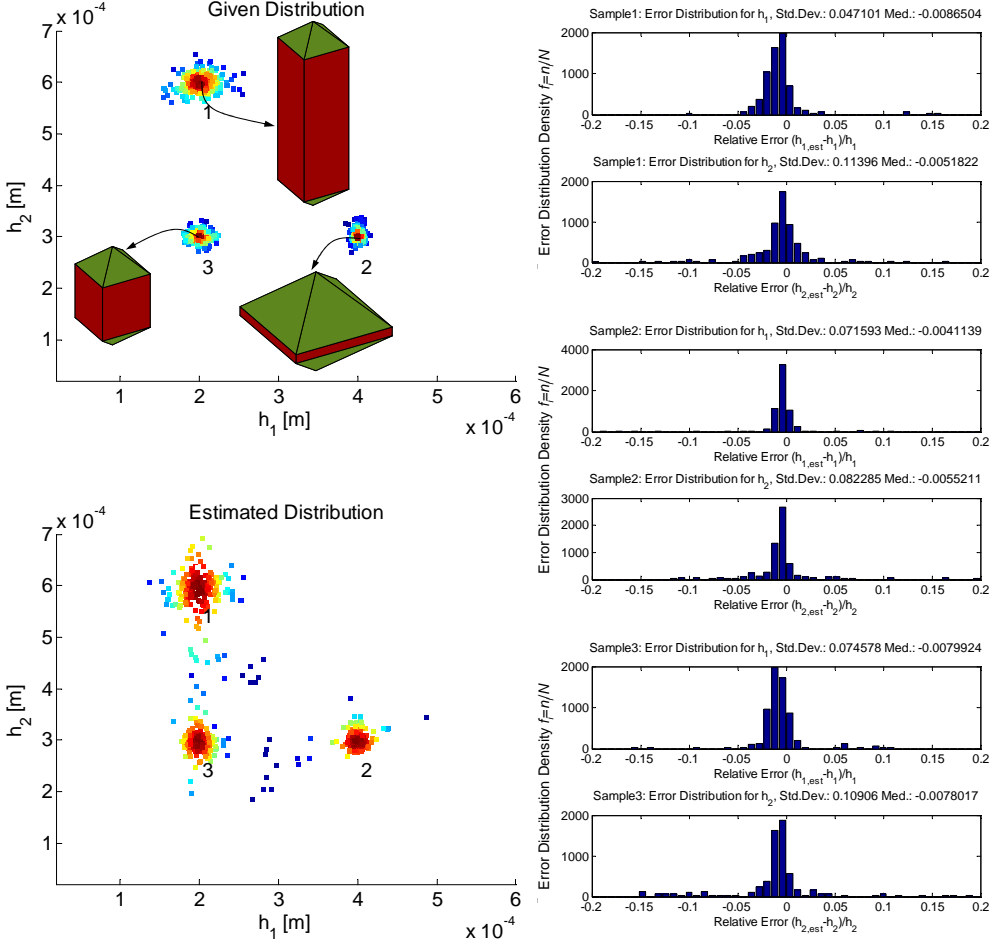


**Figure 5.10:** Estimator performance tested on a KDP population similar to Fig. 5.7. The images are taken on an array with finite resolution. Left column: Given shape distribution (top). Estimated distribution on the basis of synthetic images (bottom). Right column: Distributions of the relative error of the estimated values for samples 1 (top), 2 (middle) and 3 (bottom). The size of the lookup table was  $n_{\text{lut}} = 300,000$  ( $n_{\text{lut},h} = 1000$  and  $n_{\text{lut},psi} = 300$ )

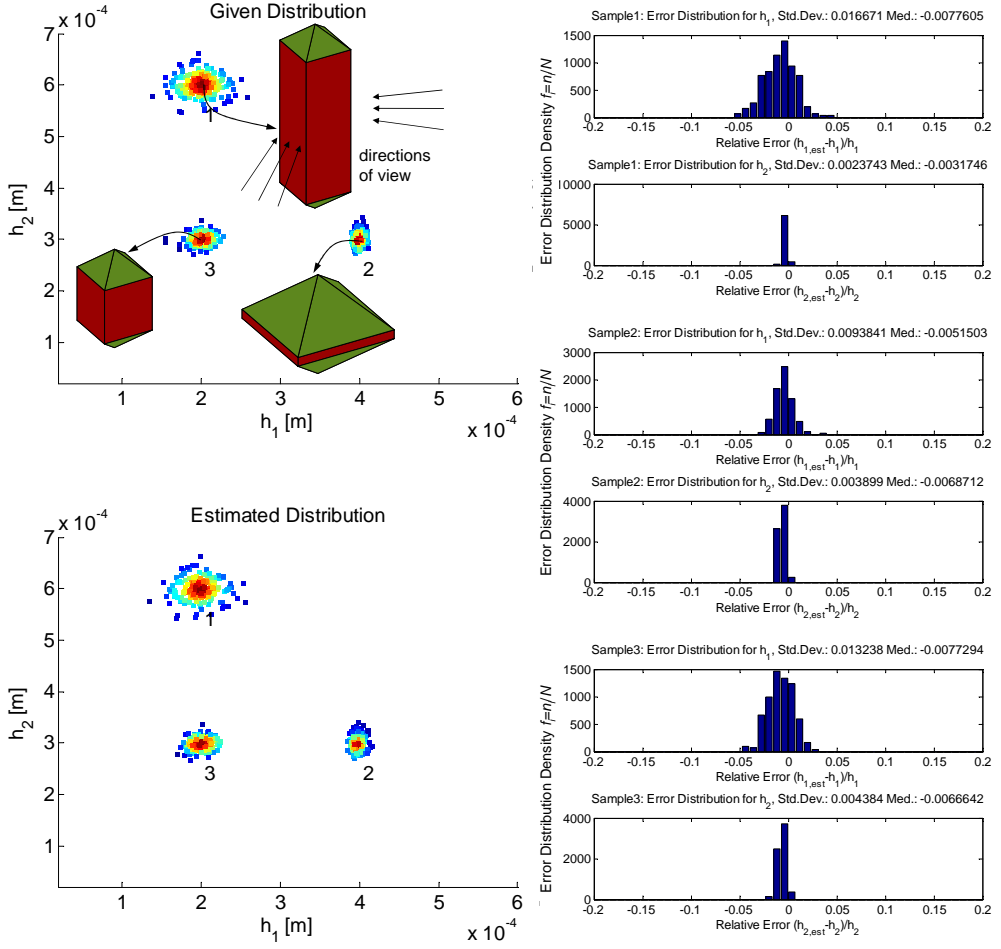


**Figure 5.11:** Estimator performance tested on a KDP population similar to Fig. 5.9 but with a preferred orientation from which the crystals are viewed as indicated at the example shape in the upper left region. The images are taken on an array with finite resolution. Left column: Given shape distribution (top). Estimated distribution on the basis of synthetic images (bottom). Right column: Distributions of the relative error of the estimated values for samples 1 (top), 2 (middle) and 3 (bottom). The size of the lookup table was  $n_{lut} = 45,000$  ( $n_{lut,h} = 300$  and  $n_{lut,psi} = 150$ ).



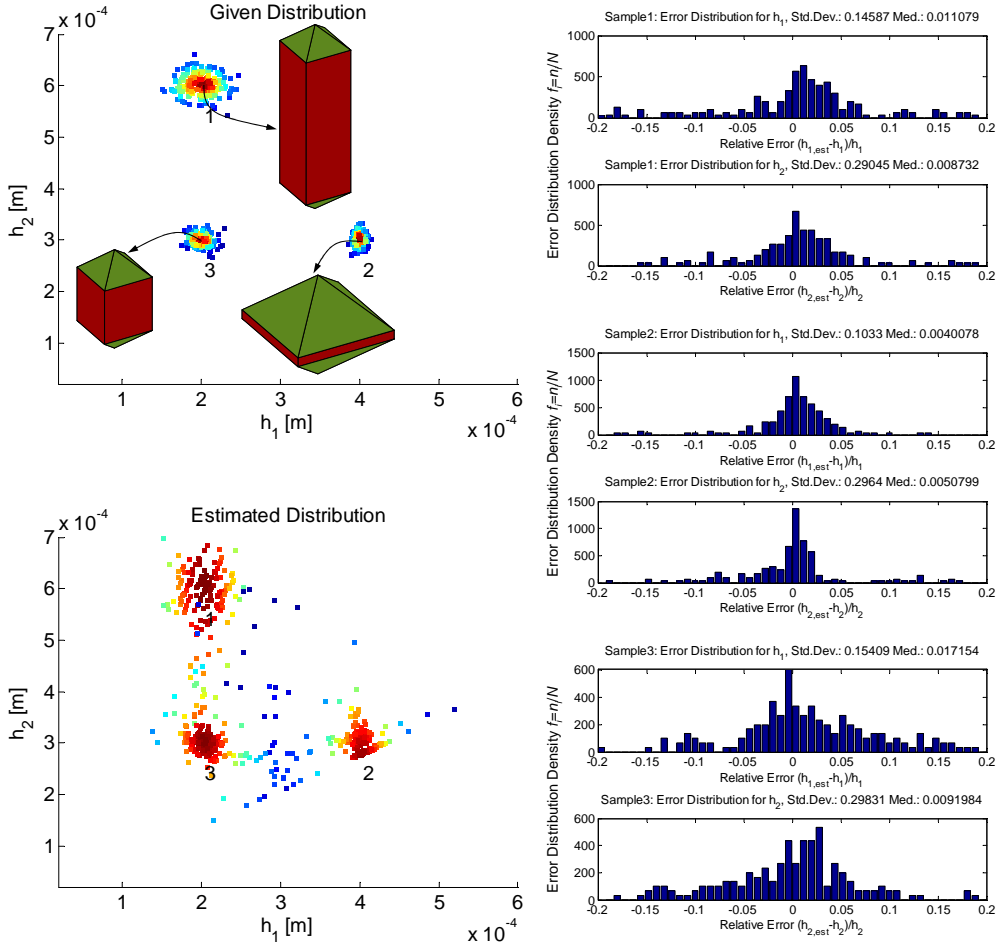


**Figure 5.12:** Estimator performance tested on a KDP population similar to Fig. 5.7. The images are taken on an array with finite resolution and the projection boundaries have been blurred as shown in Fig. 5.6 (b). Left column: Given shape distribution (top). Estimated distribution on the basis of synthetic images (bottom). Right column: Distributions of the relative error of the estimated values for samples 1 (top), 2 (middle) and 3 (bottom). The size of the lookup table  $n_{lut} = 45,000$  ( $n_{lut,h} = 300$  and  $n_{lut,psi} = 150$ ).

### 5.3.2.3 Projection on Plane with Finite Resolution and Blurred Boundaries

If the boundary of the projection is not mapped onto the projection plane perfectly as depicted in Fig. 5.6 (b), the quality of the sampled signature and thus also of the Fourier descriptors is of course lower, which deteriorates the achievable estimation accuracy. The result of a case study following the previous ones is shown in Fig. 5.12. The error distributions are clearly wider compared to the estimation test in which the boundaries have not been diffused but all other parameters, particularly the lookup table size, are kept constant (Fig. 5.9).

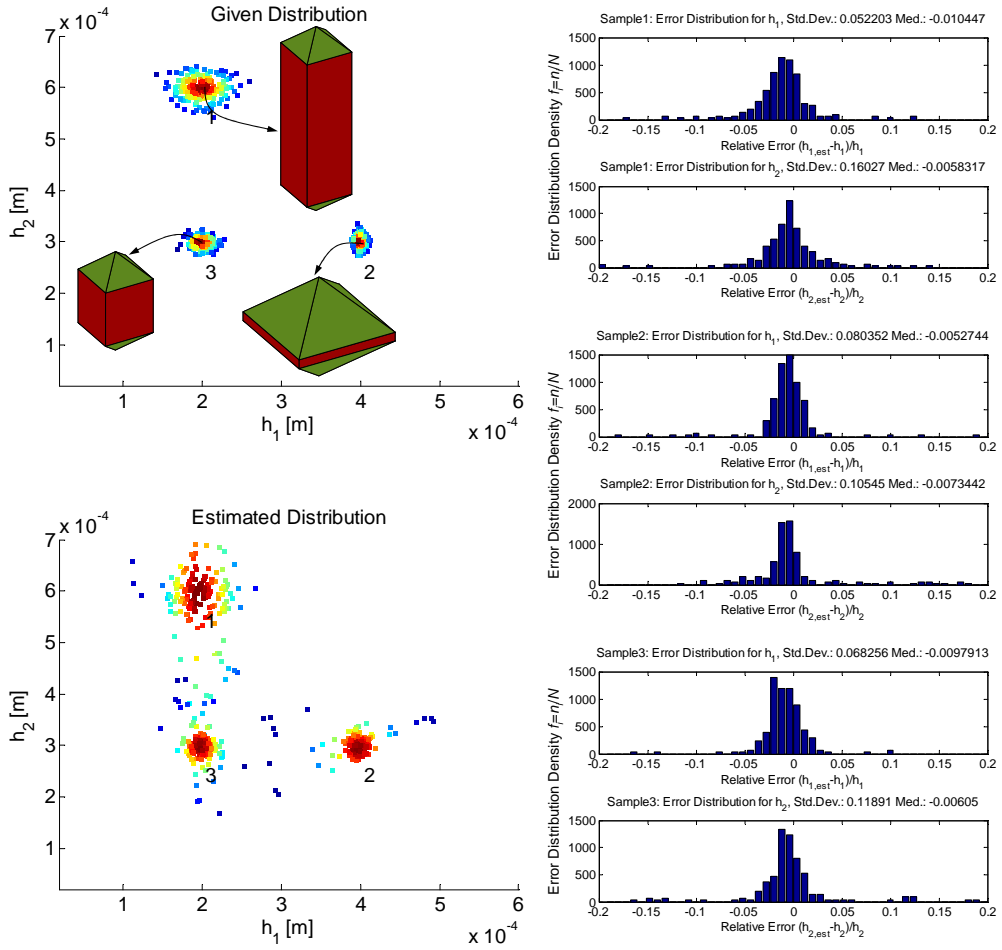


**Figure 5.13:** Estimator performance for a KDP crystal population, equivalent to Fig. 5.9, see the figure caption there. The boundary of the crystal region is – contrary to the results shown in Fig. 5.12 – clear but now the original 3D crystal can exhibit asymmetries (see Fig. 5.6 (c)) which are actually not reflected in the model used for the database employed for the state estimation. This imperfection shall show the applicability of the estimation scheme for real crystals which are seldom grown perfectly symmetrical.

### 5.3.2.4 Asymmetric Crystals Projected on Plane with Finite Resolution

The case of asymmetrically grown crystals, see Fig. 5.6 (c), for which the distance of individual faces of one form fluctuates within in interval of 5% around a mean value randomly (uniformly distributed) is depicted in Fig. 5.13. The performance should be directly compared to Sec. 5.3.2.2 (Fig. 5.9). The estimation performance and error distribution is worse – as expected – but still the features of the population can be clearly identified and especially the mean values of the three distributions are well reproducible.

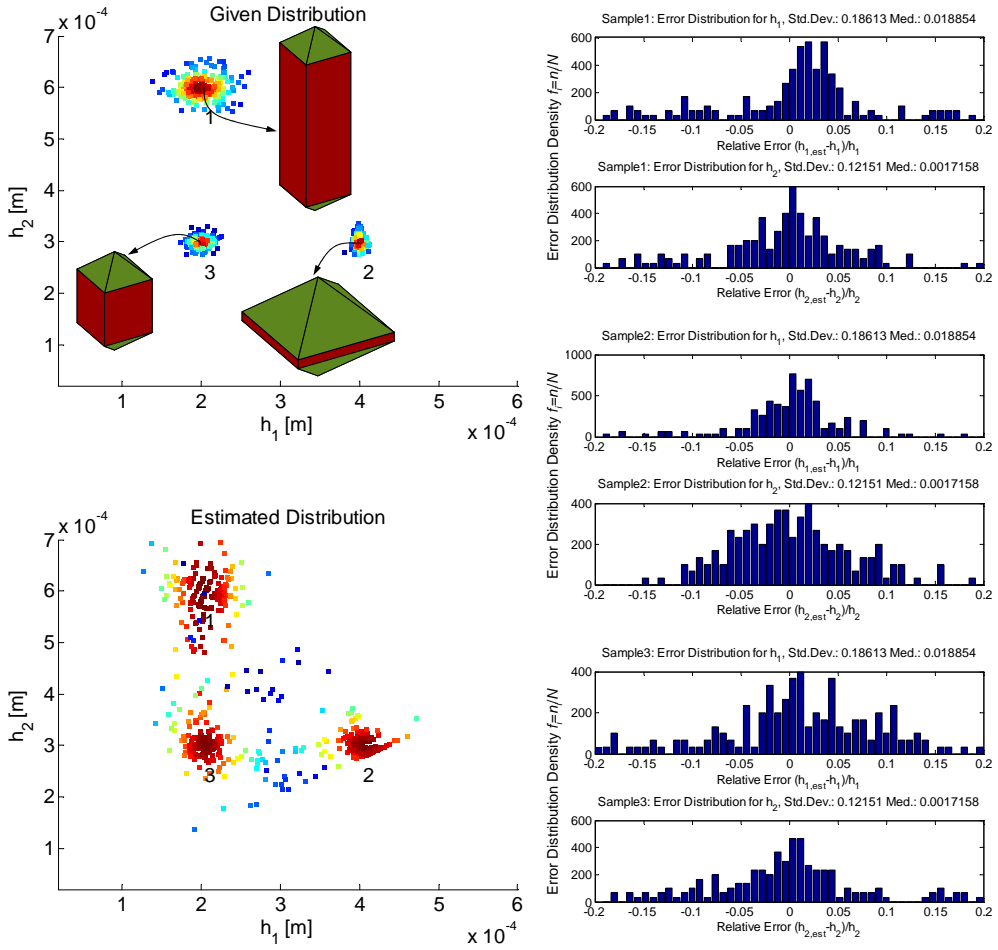


**Figure 5.14:** Estimator performance for a KDP crystal population, equivalent to Fig. 5.9, see the figure caption there. The noise effects of a blurred boundary as separately studied in Fig. 5.12 and of asymmetric crystals as included in Fig. 5.13 have been added.

### 5.3.2.5 Asymmetric Crystals Projected on Plane with Finite Resolution and Blurred Boundaries

The joint impact of blurred projection boundaries and asymmetric crystals is shown in Fig. 5.14. The error distributions are further widened compared to the previously presented case studies. It is this magnitude of error that we shall in the worst case be concerned with in experiments. As will be shown later, the blurring of the crystal boundary as used in these studies (Fig. 5.6 (b)) is well worse than for the processed experimental images. The standard deviation of the error can reach values as high as 20%, however, the mean values of the populations (quantified by the almost zero median) are still surprisingly well reproducible.

## 5.4 Application to Real Images

The shape estimation method that has been developed and examined in the previous sections of this chapter shall now be applied to real images rather than testing it only on synthetic ones. The apparatus for the image acquisition is presented in Sec. 5.4.1. Since the so obtained images cannot be fed directly to the shape estimation scheme, several image processing steps have to be taken out which are shortly sketched in Sec. 5.4.2. After this, two case studies on evolving KDP crystal populations are presented in Sec. 5.4.3.

### 5.4.1 Image Acquisition

Of the numerous methods and devices with which crystals could be imaged, the microscope QICPIC has been selected as discussed in detail in Sec. 5.1.3. This instrument records up to 25 grayscale images per second of the passing suspension in a flow cell of 2 mm width, see Fig. 5.15. The field of view is 5000-by-5000  $\mu\text{m}$  (also other modes are available but have not been used in our experiments) and projected onto a CCD chip with a resolution of 1024-by-1024 pixel. The objects are illuminated with laserlight which is transmitted through the suspension in the flow cell. Due to the uniformity of the distance to the camera, the particles are relatively well focused, see Fig. 5.16 (left), see also the discussion in Sec. 5.1.3.

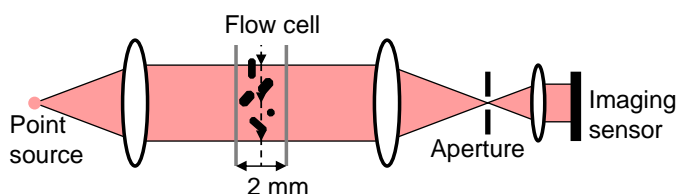


**Figure 5.15:** Working principle of the flow-through microscope QICPIC.

The suspension which flows through the microscope's cuvette is continuously withdrawn from a vessel in which the suspension is well stirred in order to minimize biasing of the sampling with respect to crystal size, see Fig. 5.19. The peristaltic pump is operated at 200 – 250 ml/min. In principle it is possible that the crystals break due to mechanical stressing in the pump. However, since the crystal system under consideration, KDP, has a relatively high Vickers hardness of 150 in contrast to comparable model substances such as potassium alum (56) or sucrose (64) (Mullin, 2001), breakage could not be observed even for prolonged continuous pumping.

### 5.4.2 Image Analysis

For the quantitative analysis of the images which are acquired with the QICPIC-probe, an image processing routine has been assembled which accounts for the special requirements due to the relatively dark background and partly transparent crystals, see Fig. 5.16. The advantage over the software that comes with the probe is full access to all image abstraction parameters necessary to identify particle regions and

full access to all single-particle measures and their user-defined manipulation. Also the analysis of multivariate distribution data with respect to number or mass density can be performed.

To extract quantitative information – and especially the contours of single crystals for the shape identification – from the images, the following main steps are taken out and discussed in subsequent sections:

1. Image enhancement, Sec. 5.4.2.1 ,
2. Thresholding and region filling, Sec.s 5.4.2.2 and 5.4.2.3 ,
3. Particle identification and measurement, Sec. 5.4.2.4 .

The algorithm has been implemented in Matlab 2009b which was equipped with the Image Processing Toolbox V6.4.

### 5.4.2.1 Image Enhancement

The data obtained from the camera are 8 bit intensity images, i.e., they can be represented by a matrix  $I_{x,y} \in 0, \dots, 255$ , where the pixel positions  $x$  and  $y$  can assume values between 1 and 1024 (1 MP CCD chip). The intensity level of 0 represents a black pixel and 255 is a white one. In Fig. 5.16 (left) an example image is shown with its histogram. On the first sight, crystals are clearly distinguishable since they appear darker. However, the background has relatively dark grayscale values which can be found also in particle regions. This is because the crystals are partly transparent. The background is practically constant in a series of images because the crystals flow through the cell and images are taken in front of the same scenery. The background and its histogram is shown in Fig. 5.16 (middle). The result of the procedure described below is anticipated: consider the histogram of the image in Fig. 5.16 (right) in which the background has been brightened and the intensity of particle regions was kept constant. The histogram of the background, Fig. 5.16 (middle), and the histogram of the particles in Fig. 5.16 (right) overlap in the range 70-130, i.e., background pixels cannot be separated from crystal pixels reliably by the grayscale level and thus segmenting the image by direct, global thresholding (as performed in the original QICPIC software) fails. This can be seen also in the histogram of the as-recorded image, Fig. 5.16 (left), because the two histogram peaks of the (usually brighter) background pixels and (usually darker) particle pixels are not fully differentiated. An extreme, though not exceptional case is highlighted in Fig. 5.16 by the red and green circles. On closer inspection, it becomes clear that the dark spot within the red circle belongs to the background (probably a dust particle on the outer face of the flow-cell) whereas the relatively bright structure within the green circle is a crystal.

In order to fade out background features, the image  $I_{x,y}$  is compared to the background image  $B_{x,y}$ . Pixels of the original image whose intensity is at least 50 units darker than the corresponding pixel of the background image are classified to belong to the projection of a crystal. If the grayscale value between original and background image is comparable, it is identified as a background pixel and brightened, i.e., the

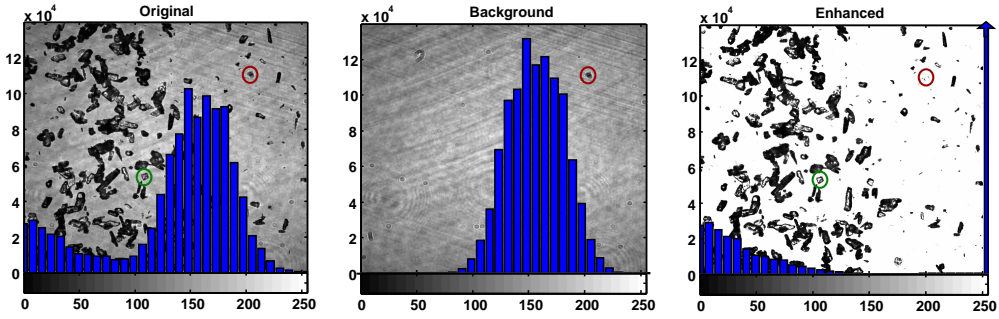


**Figure 5.16:** Image enhancement: well populated image and its histogram as obtained from the microscope (left). About 20 % of the projection area is occupied by particles. The background image is rather dark and exhibits features which cannot be distinguished from particles directly by their intensity (middle). The enhanced image emphasizes particles and suppresses background characteristics (right).

difference between original and background image is used. That is, the enhanced image  $E_{x,y}$  is given by

$$E_{x,y} = \begin{cases} I_{x,y} & \text{if } B_{x,y} - I_{x,y} > 50 \\ 255 - (B_{x,y} - I_{x,y}) & \text{otherwise} \end{cases} \quad (5.26)$$

The result is shown in Fig. 5.16 (right). Crystals are far better distinguishable from the background than in the original image. The encircled dark spot in the upper-right corner belonging to the background has been erased whereas the subtle crystal shadow marked by the green circle is still visible.

#### 5.4.2.2 Adaptive Background Image

Since the photos are taken from within the flow cell, it can happen that a crystal adheres to the glass walls and is continuously photographed. If the background is assumed to be static and the same background image is used over the course of a whole experiment, the adhering crystal is continuously identified as a particle, although it should be eliminated because once it is a static part of the image, it belongs to the background. The experiment is conducted in such a way that in the beginning only clear solution is pumped through the flow cell, i.e., only images of the background are recorded. Therefore, the average of the first 20 particle-free frames is taken as the initial background image:

$$B_{x,y}^1 = \frac{1}{20} \sum_{j=1}^{20} I_{x,y}^j \quad (5.27)$$

From then on the current background is calculated as the weighted sum of the current image and of the background of the previous image:

$$\tilde{B}_{x,y}^n = \alpha_B B_{x,y}^{n-1} + \alpha_I I_{x,y}^n, \quad \alpha_B + \alpha_I = 1. \quad (5.28)$$

Because images with particles are darker, the so obtained background image is biased towards darker than actual grayscale values the more particles flow through the system. Therefore, the average grayscale level of the background

$$g(\tilde{B}_{x,y}^n) = \frac{1}{n_{\text{pix}}} \sum_{x,y} \tilde{B}_{x,y}^n \quad (5.29)$$

is adjusted such that it matches with the average grayscale level of the reference background  $B_{x,y}^1$ :

$$B_{x,y}^n = \frac{g(\tilde{B}_{x,y}^1)}{g(\tilde{B}_{x,y}^n)} \tilde{B}_{x,y}^n, \quad (5.30)$$

which is the background image used to enhance the original image  $I$  according to Eq. (5.26).

In Eq. (5.28) the weight  $\alpha_B$  of the previous background image should be a couple of times higher than the weight  $\alpha_I$  of the current image because otherwise a (dark) particle occurring in  $I_{x,y}^n$  would leave a considerable footprint on the new background image. In fact, particles passing through the microscope and thus appearing only once at a location in a series of images should have only a differential impact on the background image. However, if a particle stays, e.g., glues to the cell's glass wall, it must be accumulated into the background image. Of course, this should be as fast as possible which is in opposition to the demand that flowing particles should only have a minor impact. Some case studies showed that with  $\alpha_B = 0.9 \dots 0.95$  new static background features are erased from the enhanced image relatively fast and the adapted background image is practically unaltered from bypassing particles.

#### 5.4.2.3 Binarization and Region Filling

In the enhanced image, see Fig. 5.16 (right), dark regions can reliably be identified as belonging to a particle. Binarization converts the enhanced image into a logical (or binary) image by simple, global thresholding

$$L_{x,y} = \begin{cases} 0 & \text{for } E_{x,y} < I_{\text{thres}} \rightarrow \text{black, particle} \\ 1 & \text{for } E_{x,y} \geq I_{\text{thres}} \rightarrow \text{white, background} \end{cases} \quad (5.31)$$

where  $I_{\text{thres}}$  was set to 100 which gave good results for all crystal systems we have tested (KDP, urea, paracetamol, threonin), see also the histogram in Fig. 5.16 (right). With a morphological closing operation, using a 3-by-3 square structuring element, smaller gaps in the particle countours are closed and smaller holes are eliminated, see also Gonzalez and Woods (2008). Since some crystals have transparent sectors, the true particle areas can comprise parts in the interior which are white, called holes. A hole is a set of pixels not directly assigned to a particle region that cannot be reached from the background without crossing a particle region. Therefore, hole regions most probably belong to a partially transparent crystal and thus a filling operation is taken out. The resulting binary image is shown in Fig. 5.17. In this image, black pixels are directly identified to belong to a crystal, that is, particle regions are extracted and measured with respect to different scalar quantities. Particles touching the border are ignored (gray regions in Fig. 5.17).

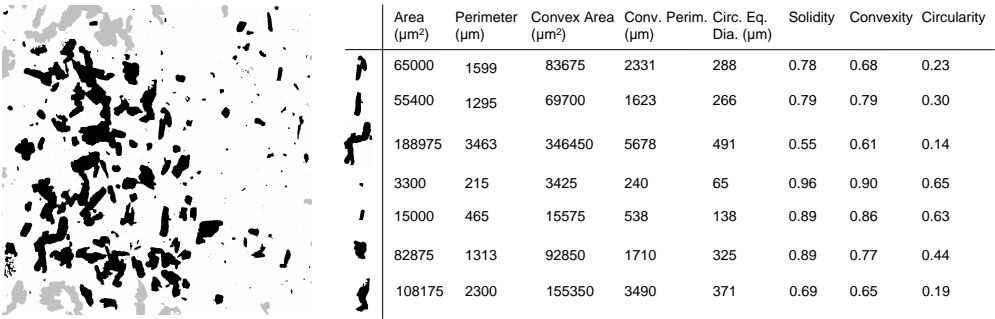


Figure 5.17: Binary image and scalar measures of some particles.

Table 5.1: Shape and size descriptors.

Descriptor	Explanation	Symbol
Area ( $\mu\text{m}^2$ )	Area of pixels occupied by a particle	$A$
Perimeter ( $\mu\text{m}$ )	Perimeter of the particle region	$P$
Convex Area ( $\mu\text{m}^2$ )	Area of the particle area's convex hull	$A_{\text{CH}}$
Convex Perimeter ( $\mu\text{m}$ )	Perimeter of the particle's convex hull	$P_{\text{CH}}$
Circle Equivalent Diameter ( $\mu\text{m}$ )	Diameter of a circle with the same area	$D = 2\sqrt{\frac{A}{\pi}}$
Solidity	Ratio of area to convex area	$S = \frac{A}{A_{\text{CH}}}$
Convexity	Ratio of convex perimeter by perimeter	$O = \frac{P_{\text{CH}}}{P}$
Circularity	Ratio of area to area of a circle with the same perimeter	$C = \frac{4\pi A}{P^2}$

5.4.2.4 Feature Extraction and Distributions

The measures, which are easily calculated and interpretable but suffice to distinguish between single crystals and the type of aggregates we found in our experiments, are enlisted in Tab. 5.1. In Fig. 5.17 (right) some example particles from the binary image on the left are picked out and their property values are given. It can be seen that particles which are compact and correspond to single particles have higher values for all three shape measurements, that is solidity, convexity and circularity. On the other hand, formations which are built of attaching primary particles tend to have lower values for the aforementioned quantities. For the experiments that are discussed below we chose solidity as the only measure which is used to separate the single crystals fed to the shape identification scheme of Sec. 5.3:

$$S = \frac{\text{Area}}{\text{Convex Area}} \begin{cases} < 0.95 \rightarrow \text{Aggregate} \\ \geq 0.95 \rightarrow \text{Single Particle} \end{cases} \quad (5.32)$$

see also the discussion in Sec. 5.4.3 on the data processed for a real experiment.



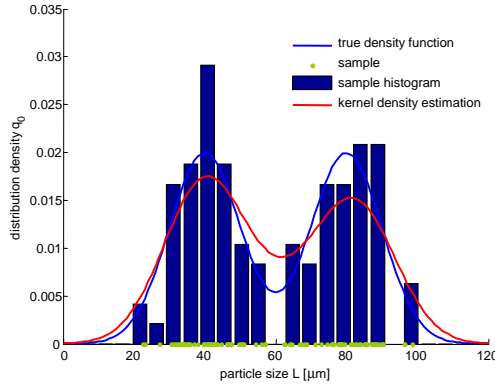


**Figure 5.18:** Example of a 1D kernel histogram based on 100 datapoints compared to a classical histogram.

#### 5.4.2.5 Density Estimation with Kernel Functions

Classical histograms are a useful implement to estimate distributions based on a sufficiently large number of measurements taken on representative individuals of a population. They can be viewed as sums of (discontinuous) step functions. Thus, they may not be adequate when a continuously differentiable density should be observed. A nearby solution to this problem would be the application of filter functions to smooth the coarser original histogram. However, so called kernel histograms overcome this difficulty and spare out the intermediate step of firstly generating a classical histogram. The kernel histogram (or kernel density estimation) technique assigns each sample point a kernel function, for instance a Gaussian distribution. The resulting kernel histogram is the average of all kernel functions assigned to every data point. A 1D example is shown in Fig. 5.18: The individual measures (here: particle size) are samples obtained using the true density function and indicated by dots on the abscissa. The classical histogram gives a rough impression about the shape of the underlying distribution, whereas the kernel density estimation allows a relatively good approximation to the true density based on the measurements. Compared to ordinary histograms for which the class width must be specified, the application of kernel histograms requires the specification of kernel function parameters (bandwidth). In the following the main ideas of this method is briefly sketched. More detailed information can for instance be found in Wand (1995); Silverman (1986) or Ledl (2004).

Let  $\mathbf{x}_i \in \mathfrak{R}^n$ ,  $i = 1 \dots N$  be vector-valued measurements, for example a crystal's geometrical state  $\mathbf{h}$  and time at which it is recorded,  $t$ , i.e.:

$$\mathbf{x}_i = \begin{pmatrix} \mathbf{h}_i \\ t_i \end{pmatrix}, \quad i = 1 \dots N. \quad (5.33)$$

From the  $N$  samples we aim at determining the estimated number density function. The kernel density estimator is given by (Wand, 1995; Silverman, 1986)

$$\hat{f}(\mathbf{x}; \mathbf{H}) = \frac{1}{N} \sum_{j=1}^N K_{\mathbf{H}}(\mathbf{x} - \mathbf{x}_j), \quad (5.34)$$

where  $\mathbf{x}$  is an arbitrary point in  $\mathbf{x}$ -space and

$$K_{\mathbf{H}}(\mathbf{x}) = \frac{1}{\sqrt{\det \mathbf{H}}} K\left(\mathbf{H}^{-\frac{1}{2}} \mathbf{x}\right) \quad (5.35)$$

the  $n$ -variate kernel function  $K$ . The parameters of this functions are contained in the positive definite  $n$ -by- $n$  so called bandwidth matrix  $\mathbf{H}$ . For instance, a multivariate normal distribution can be used:

$$K(\mathbf{x}) = \frac{1}{(2\pi)^{n/2}} \exp\left(-\frac{1}{2} \mathbf{x}^T \mathbf{x}\right), \quad (5.36)$$

which fulfills the necessary conditions for kernel density functions which says that the integral of the kernel function over the whole support domain (for a gaussian distribution  $\mathfrak{R}^n$ ) is unity (Silverman, 1986). For the practical implementation of this technique in Matlab we refer to a freely available code package, made available by Ihler (2007), which has been used also throughout this work.

### 5.4.3 Two Case Studies on KDP Crystal Populations

Up to now the theoretical background of the image processing and shape identification has been discussed which is in this section applied to real experimental data.<sup>9</sup> A seeded batch cooling crystallization has been taken out for the system potassium dihydrogen phosphate (KDP) (crystalline phase) and water (solvent). Basic physical properties, in particular its solubility and crystal shape have been presented in Sec. 4.1. In Fig. 5.19 the experimental setup is sketched. The jacketed crystallization vessel has a volume of about 3l and a thermostat allows the application of temperature profiles to the vessel content. Crystal suspension is continuously pumped through the microscope's cuvette in which the suspension is imaged with QICPIC, see Sec. 5.4.1 and particularly Fig. 5.15. The hardness of the crystals is relatively high (Mullin, 2001) so that disintegration of single crystals due to mechanical stressing in the peristaltic pump was not observable at the chosen flow rate of 250 ml/min.

In order to track the composition of the fluid phase, clear solution is continuously withdrawn through a frit, heated to a reference temperature (here 40°C) and subsequently fed to a densitometer (Model: Mettler Toledo DE 40 Density Meter) in which the density of the clear mother liquor is measured. After the measurement pipe, the solution is fed back to the vessel. Since the fluid phase consists of water and KDP only which is, furthermore, relatively well soluble in water, the current composition can be determined from the density. Before the start of the experiment, the densitometer was fed with clear solution of known composition in order to obtain a calibration curve with which the time series of the density evolution – recorded during the course of crystallization – can be converted to a composition time series. With the help of the temperature that is measured in the vessel, the equilibrium composition is calculated using Eq. (4.15). The supersaturation is subsequently obtained by Eq. (4.20).

<sup>9</sup>The experiments shown in this work have been performed by Erik Temmel of the group Physical and Chemical Foundations of Process Engineering at the Max Planck Institute in Magdeburg. The recorded data (QICPIC videos and supersaturation measurements) have kindly been made available to the author. It is, however, self-evident that the author assumes the full responsibility for the correctness of the material presented in the following.

Crystal suspension was continuously photographed at a rate of 10 Hz in order to track the state of the crystalline phase. An example image is shown in Fig. 5.20. Colored lines are traced around identified particles. Red stands for particles that have been classified as aggregates ( $\text{Solidity} < 0.95$ , see Eq. (5.32)) and green refers to areas which have been identified as single crystals ( $\text{Solidity} \geq 0.95$ , see Eq. (5.32)). Additionally, a list of numbers beside or within each particle is added which are in the depicted image from top to bottom: Circle equivalent diameter, major and minor axes lengths, solidity and eccentricity. All these descriptors can be calculated using the MATLAB IMAGE PROCESSING TOOLBOX's command `regionprops`. The numbers drawn onto the processed image as well as the particle boundaries serve to check for the consistent operation of the algorithm. Though for storing the acquired information it is not necessary to endorse the data onto the image that has been processed, we have continuously filed every tenth so prepared image for visual inspection.

The identified single crystals in Fig. 5.20 are numbered from 1 to 7. It can be seen that the distinction between single crystals and aggregates works well but not perfectly. The as such identified single crystal 1 consists of two crystals which are grown together. However, the remaining six tagged single crystals are consistent with what a human operator would classify as single crystals as well. It can also be observed that the crystal boundaries can be seen clearly and are far less diffused than for the reliability study of the identification scheme on synthetic images as carried out in Sec. 5.3.2. Only small swells at particles 4, 6 and 7 cause the real shape to not perfectly fit the assumed model shape. However, due to the high frequency of these deviations in the spectrum of the Fourier descriptors, their impact is small and does not – like the diffused boundaries in the reliability studies – hinder the identification of the geometrical state. Further characteristics of the image processing routine are indicated by arrows a-c in Fig. 5.20: (a) If not only the interior of the crystal but also its boundary is transparent, it can occur that an object that is by visual inspection easily recognized as a contiguous region is separated by the algorithm. (b) Small particles which could be classified by visual inspection as single crystals are usually not recognized as such due to the low resolution in that size range. The area of the convex hull relative to the actual area of such pixelated convex objects is usually considerably larger than for objects photographed at a higher resolution. Therefore, their solidity is smaller and thus they are not recognized as single particles. But this effect is advantageous because a low resolution is not eligible for quantitative 3D shape identification. Furthermore, in order to obviate the processing of small crystals for shape identification, the minimum size for assigning it to be a single crystal is set to  $30\ \mu\text{m}$ . (c) Objects recognized at the image border are not counted since in principle no reliable evidence about their size and shape is given.

The experiments we have taken out have been inspired by the ones reported by Yang et al. (2006). They have shown that the shape of the KDP crystals grown from water-KDP solution strongly varies with the temperature profile and seed load – and thus supersaturation – that is applied. We have performed two experiments to verify their finding that at high supersaturations KDP assumes a more compact shape, see Sec. 5.4.3.1, and that for lower supersaturations the form becomes more elongated, see Sec. 5.4.3.2. Before the experiments are further discussed in a more technical detail, the unsurprising major results – confirming the results of Yang et al. (2006) – can be seen in the evolution of the mean states depicted in Figs 5.26 and 5.32. The sharper temperature profile of the first experiment, see Fig. 5.21, yields higher super-

saturation values which produce relatively compact crystals (Fig. 5.26). The relatively gentle temperature decrease of the second experiment, see Fig. 5.27, leads to a lower supersaturation level producing more elongated crystals than in the first experiment (Fig. 5.32).

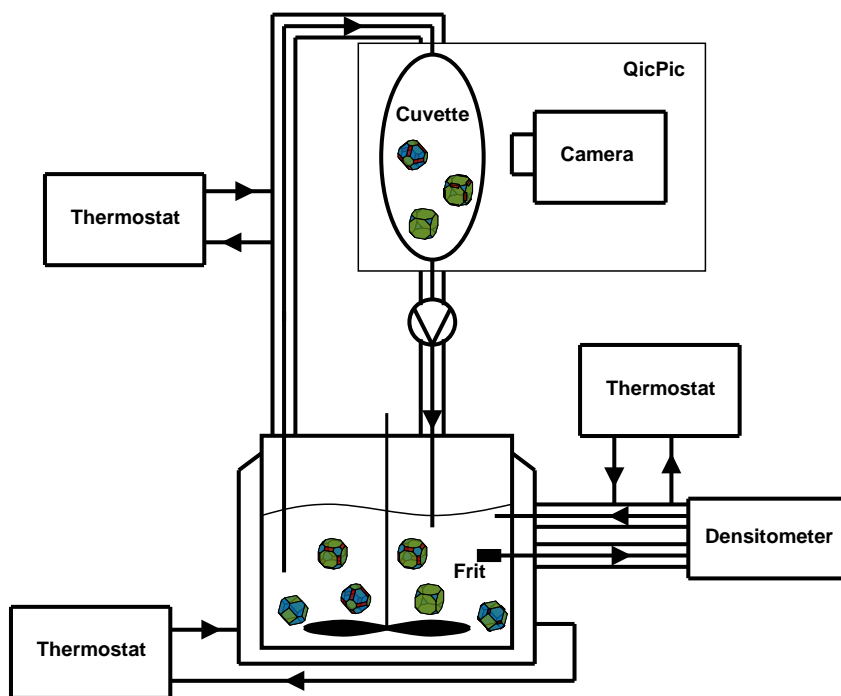


**Figure 5.19:** Sketch of the experimental setup: From the batch crystallizer the suspension is continuously pumped through the cuvette in which the crystals are imaged. The suspension vessel can be tempered which allows to take out cooling crystallization experiments.

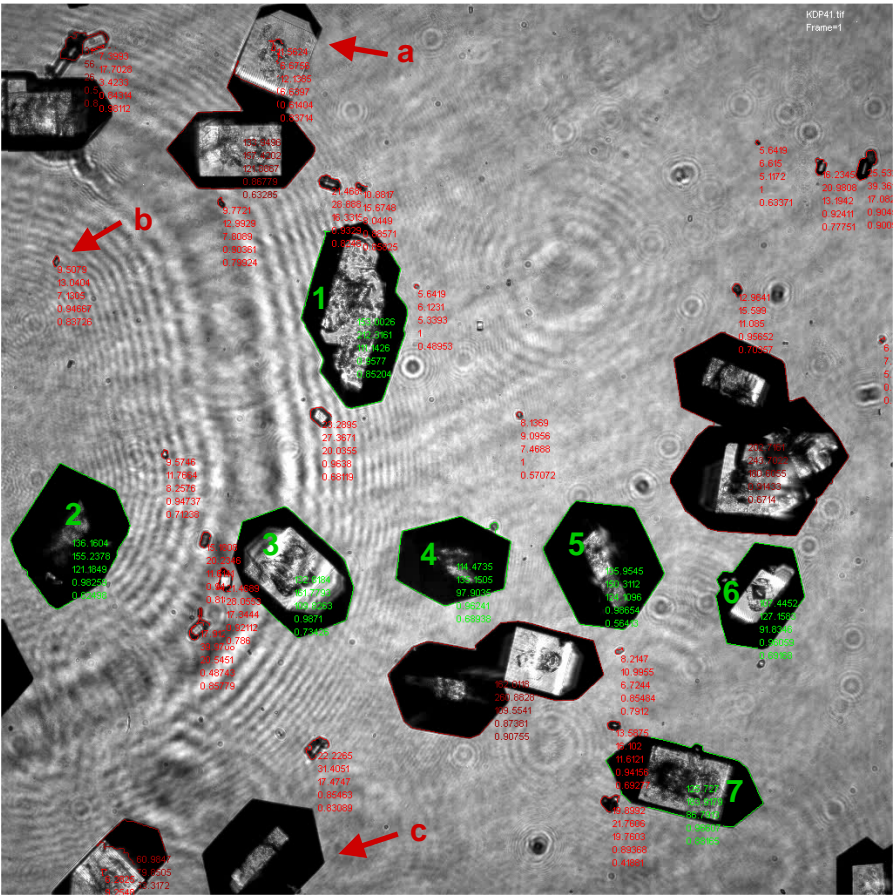


Figure 5.20: Example of a processed image of Exp. 1 at  $t \approx 1500$  s.

### 5.4.3.1 KDP Growth at High Supersaturations (Exp. 1)

Basic technical data of Exp. 1 can be found in Tab. 5.2. The temperature profile was set to linear cooling at  $-20\text{ K/h}$  which was not fully achieved as can be seen in Fig. 5.21 (left). The seed crystals were added when the solution was slightly undercooled at  $t \approx -60\text{ s}$ . Due to the increasing undercooling of the solution, the suspension becomes supersaturated, reaching a level slightly below  $\sigma = 0.12$ , see Fig. 5.21 (right). The increase of the supersaturation is retarded by the transfer of KDP from the dissolved to the crystalline state by growth and nucleation. However, the amount of nucleated particles is rather low as it can already be seen by visual inspection of the suspension images (Fig. 5.20). In terms of the mass fraction of nucleated crystals, this is quantitatively illustrated in Fig. 5.22 (right). It can be observed that the mass of nuclei remains well below 2%. However, this should be seen only as a rough estimate obtained by the following pragmatic approach. The number-based average sphere-equivalent diameter of that part of the (seed) population is taken which has been identified as single crystals, see Fig. 5.22 (left). Initially, the average size is about  $210\text{ }\mu\text{m}$ , therefore particles whose size is lower than the average diameter minus  $200\text{ }\mu\text{m}$  are classified as nuclei. The mass of a particle is assumed to be proportional to the power of  $3/2$  of the measured particle area for all particles regardless of particle shape, that is, the estimated mass-ratio between nuclei and all particles is obtained as

$$\frac{m_{\text{nuc}}}{m_{\text{particles}}} = \frac{\sum_i^{n_{\text{nuc}}} A_i^{3/2}}{\sum_i^{n_{\text{particles}}} A_i^{3/2}}, \quad (5.37)$$

where  $n_{\text{nuc}}$  and  $n_{\text{particle}}$  is the number of nucleated and the number of all particles, respectively. Though this approach is rather simple, it can for instance be seen that the slope of the nuclei mass fraction reaches its maximum at about  $t \approx 1000\text{ s}$ , see Fig. 5.22 (right), which corresponds to the maximum supersaturation level depicted in Fig. 5.21 (right). This supports the commonly used hypothesis that the major driving force for nucleation is supersaturation.

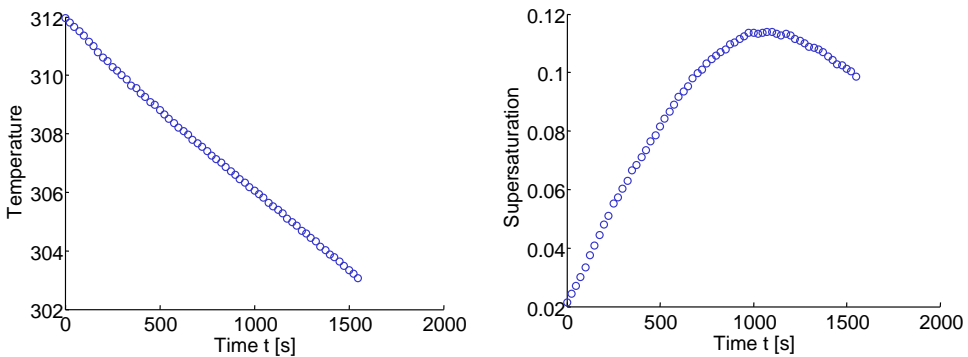


**Figure 5.21:** State of the continuous phase for Exp. 1. Due to the relatively high cooling rate, the supersaturation becomes large.

The result of the application of the image processing routines discussed in detail in Sec. 5.4 and the subsequent identification of the geometrical state vector using the routines developed in Sec. 5.3 is depicted in Fig. 5.24: The contours of the normal-

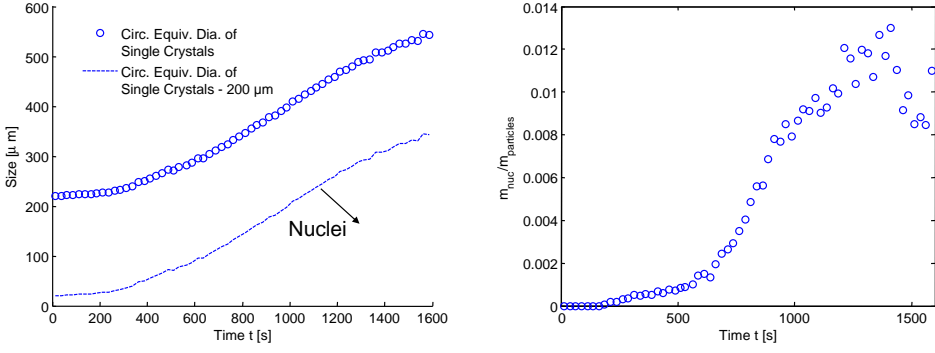


**Figure 5.22:** Evaluation of the amount of nuclei produced over the course of the experiment. Left: Particles which are smaller than the average sphere equivalent diameter of the single crystals minus  $200 \mu\text{m}$  are classified as nuclei. Right: Nuclei mass-fraction.

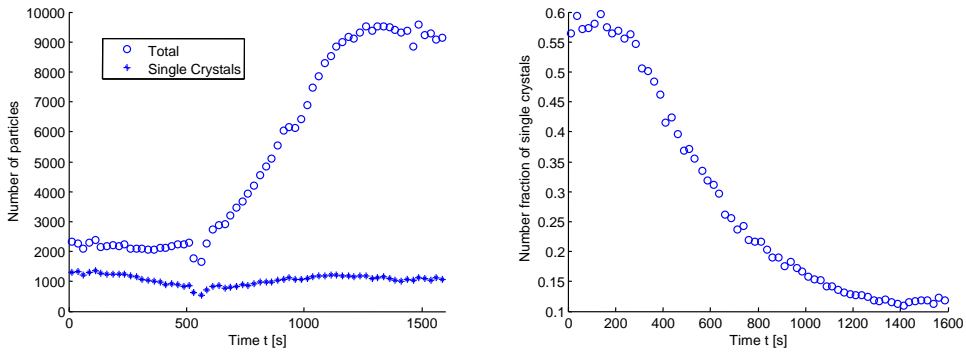


**Figure 5.23:** Total number of particles and number of particles classified as single crystals, measured within a sampling interval of 25s for Exp. 1.

ized number density function in  $\mathbf{h}$ -space estimated using the kernel density estimator, Eq. (5.34), is shown at eight different instances starting at  $t = 0$ . The bandwidth of the Gaussian kernel was set to

$$\mathbf{H} = \begin{bmatrix} 20 \mu\text{m}^2 & 0 & 0 \\ 0 & 20 \mu\text{m}^2 & 0 \\ 0 & 0 & 60 \text{s}^2 \end{bmatrix}, \quad (5.38)$$

i.e. the influence domain of a single measurement (one particle) in terms of the variance of the Gaussian kernel function is  $20 \mu\text{m}$  in each direction of the  $\mathbf{h}$ -space and  $60 \text{s}$  in time-direction, see also the composition of the  $\mathbf{x}$  vector given in Eq. (5.33). In Fig. 5.24, beside the number density, the trajectory of the mean state of the seed crystals is drawn as a thick black line. This mean is calculated as follows: Firstly, the location of the maximum,  $\mathbf{h}_{\text{max}}$ , of the estimated number density is determined. Then the first moment of the density function in the window of  $h_{1,\text{max}} \pm 100 \mu\text{m}$ ,  $h_{2,\text{max}} \pm 100 \mu\text{m}$  is calculated and taken as the mean of the seed population. At  $t = 0$  the population (and seed) mean is  $h_1 \approx 80 \mu\text{m}$  and  $h_2 \approx 110 \mu\text{m}$ . The seed crystals spread around this value where the standard deviation in  $h_1$ - and  $h_2$ -direction is about  $20 \mu\text{m}$  in all

**Table 5.2:** Parameters of Exp. 1 and 2.

Quantity	Unit	Symbol	Value Exp 1	Value Exp 2
mass of solvent	kg	$m_{\text{H}_2\text{O}}$	2	2
mass of dissolved KDP	kg	$m_{\text{KDP,diss}}$	0.682	0.682
mass of seeds	kg	$m_{\text{KDP,seed}}$	$5 \times 10^{-4}$	$5 \times 10^{-4}$
temperature gradient	K/h	$\Delta T$	-20	-5
Qicpic frame rate	Hz	10	10	10
source of KDP seed preparation	Merck, CAS-No. 7778-77-0 sieve fraction 150 – 200 $\mu\text{m}$ taken from the as-delivered crystal population			

directions. Keep in mind that not all crystals are used to estimate the  $\mathbf{h}$ -distribution but only those which have been identified as single crystals and thus are eligible to be fed to the shape estimation scheme. For this reason, the unquestionable presence of aggregation producing considerably larger particles than can be seen here is not observable. On the right side of the distribution snapshots, the geometry of the population mean of the single crystals is drawn. As time progresses and supersaturation is built up by undercooling (Fig. 5.21), the population moves to the upper right in state space. Clearly, the height and width of the population distribution increases, which may be attributed to growth dispersion.

Clearly the relatively wide kernel (5.38) may obscure some of the underlying structure of the number density function. In order to verify the application of the kernel density estimator yet another estimation has been taken out with a more narrow kernel:

$$\mathbf{H} = \begin{bmatrix} 10 \mu\text{m}^2 & 0 & 0 \\ 0 & 10 \mu\text{m}^2 & 0 \\ 0 & 0 & 30 \text{s}^2 \end{bmatrix}, \quad (5.39)$$

which yields of course not as smooth contours as for the wider kernel, see Fig. 5.25. However, the trajectory of the seed's mean state remains practically unchanged. The evolution of the mean state over time is additionally depicted in Fig. 5.26: The ratio between  $h_1$  and  $h_2$  remains almost constant which is reflected also in the sketched, quite compact shapes at  $t = 250 \text{ s}$  and  $t = 1500 \text{ s}$ .



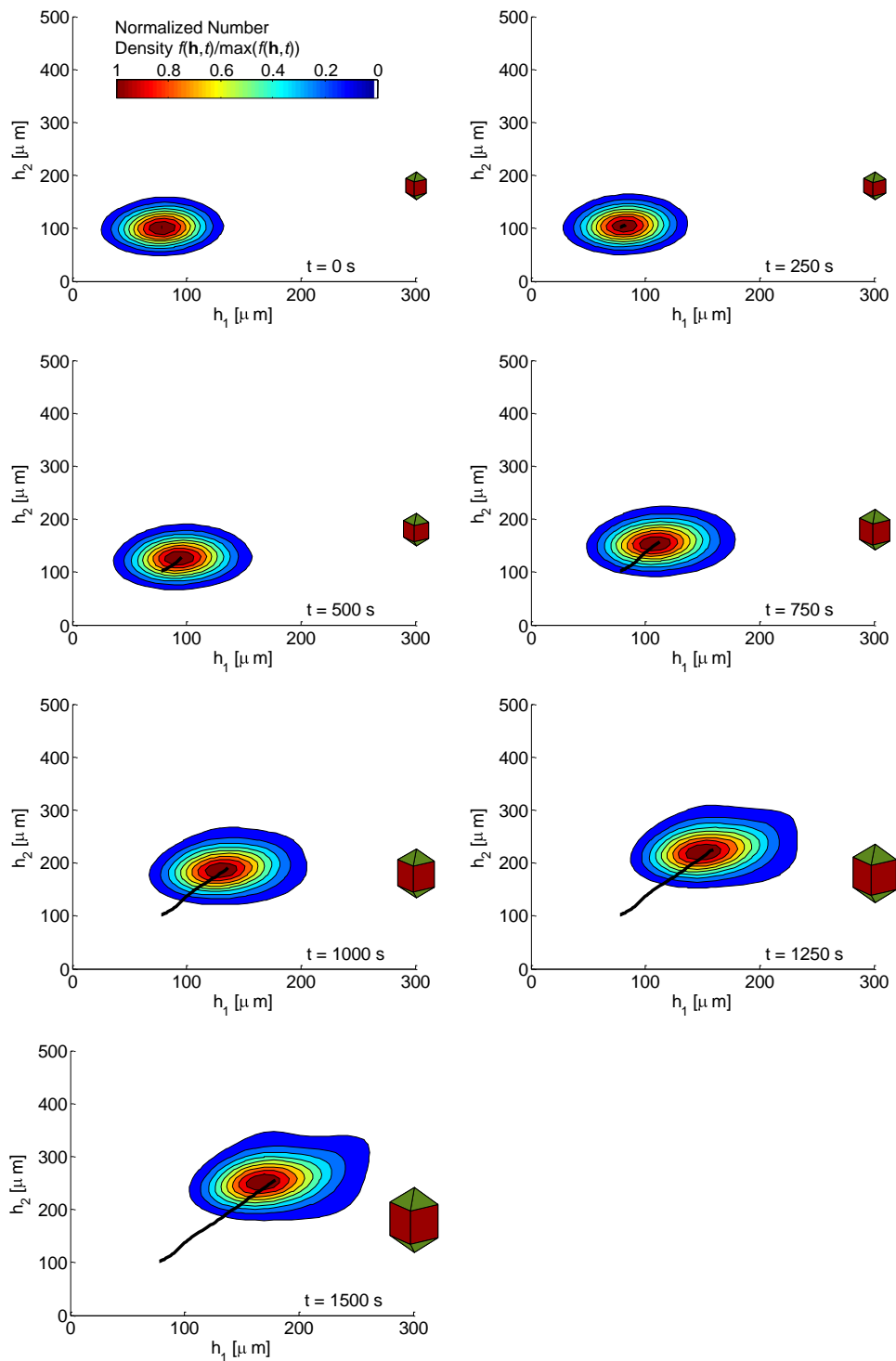
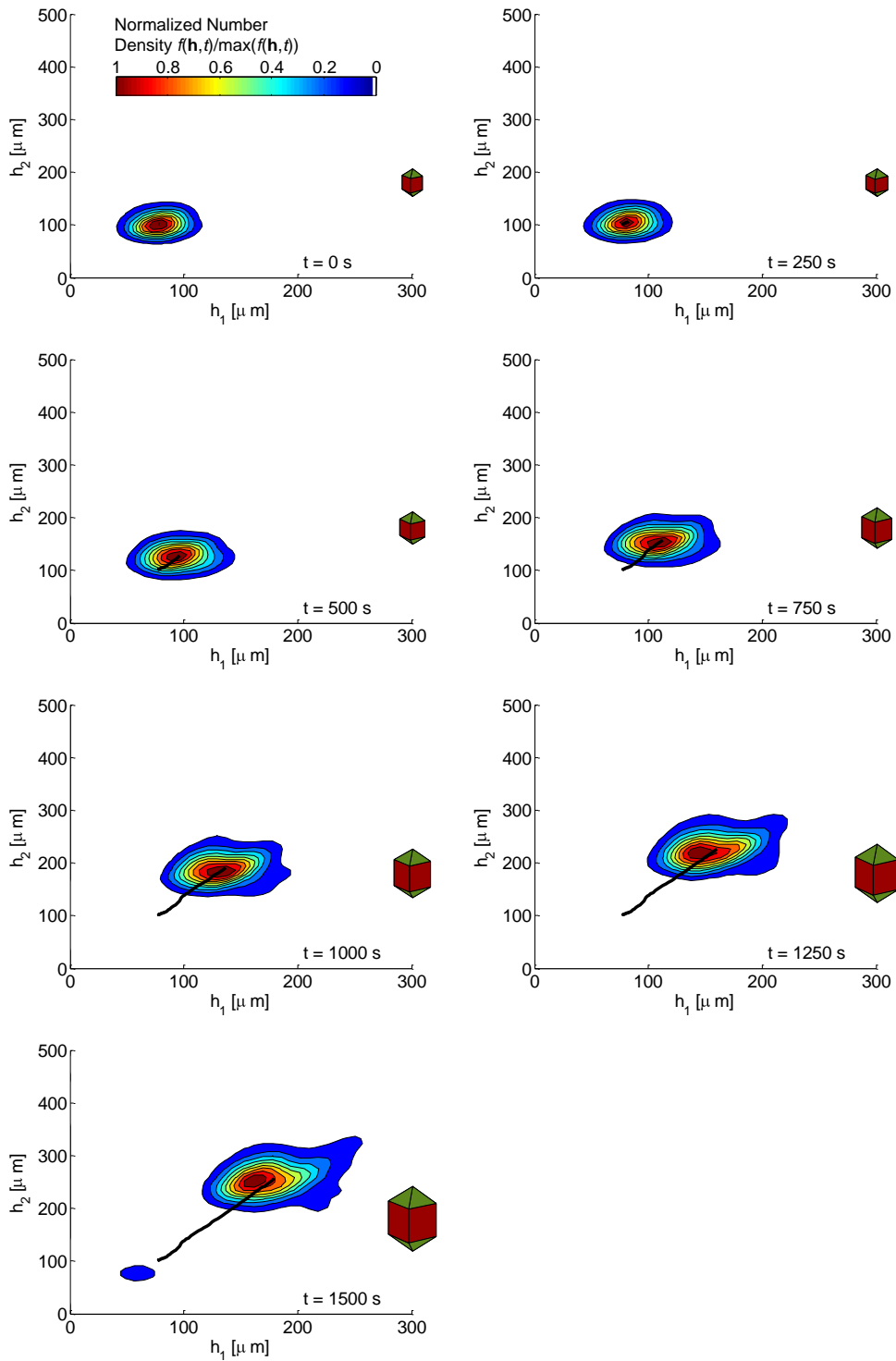
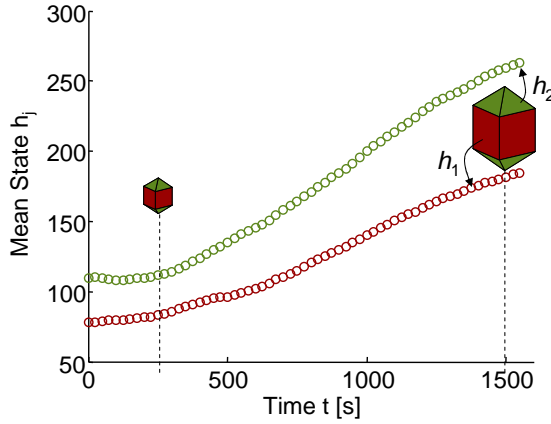


Figure 5.24: Evolution of the shape distribution of Exp. 1.



**Figure 5.25:** Evolution of the shape distribution of Exp. 1 estimated using a tighter kernel function than in Fig. 5.24.



**Figure 5.26:** Mean geometry of the crystals that are recognized as single crystals in Exp. 1.

#### 5.4.3.2 KDP Growth at Low Supersaturations (Exp. 2)

In the preceding Exp. 1 we have seen that at high supersaturation the crystals keep their compact shape. Yang et al. (2006) report that crystals grown at low supersaturation assume a more elongated shape. Therefore, we performed Exp. 2 under practically equal conditions like Exp. 1, see Tab. 5.2, except for the cooling rate which was with  $-5\text{ K/h}$  set to a value of a quarter of that chosen in Exp. 1. The resulting temperature and supersaturation profiles are shown in Fig. 5.27. The supersaturation remains below  $\sigma = 0.08$ . Fig. 5.28 (left) depicts the overall number of particles and the number of detected single crystals which are recorded within a sampling interval of 25 s. It can be seen that the number of particles which are observed remains over the course of the whole experiment at around 7000 and the number of single crystals decreases from around 2000 to about 200 at the end of the batch. In terms of the number fraction this is a decrease from about 25% to below 5%. This is mainly due to crystal aggregation which is – compared to Exp. 1, see Fig. 5.23 – better noticeable owed to the longer processing time. In the interval 3000 – 3400 s the total number of particles drastically increases and the fraction of single crystals significantly drops. At this time problems with the feeding of the QICPIC-probe occurred, that is, smaller particles clogged the supply piping which was dispensed during that interval. After 4000 s similar problems issues occurred which finally led to the abortion of the experiment. As in the previous case, also in this experiment nucleation was relatively low as can be seen in Fig. 5.29. The drastic increase of the nucleated crystals after about 3000 s is attributed to sampling problems due to clogging which caused the preferential sucking of smaller particles.

The lower supersaturation caused the seed crystals to grow to a more elongated shape which means that the values for  $h_2$  (pyramidal faces) become significantly larger than for the prismatic  $h_1$ -faces as depicted in an image of the suspension in Fig. 5.31. In Fig. 5.30 this can be seen on the basis of the  $\mathbf{h}$ -distribution evolution but even clearer in the time series of the mean state shown in Fig. 5.32 (compare to Fig. 5.26 of Exp. 1).

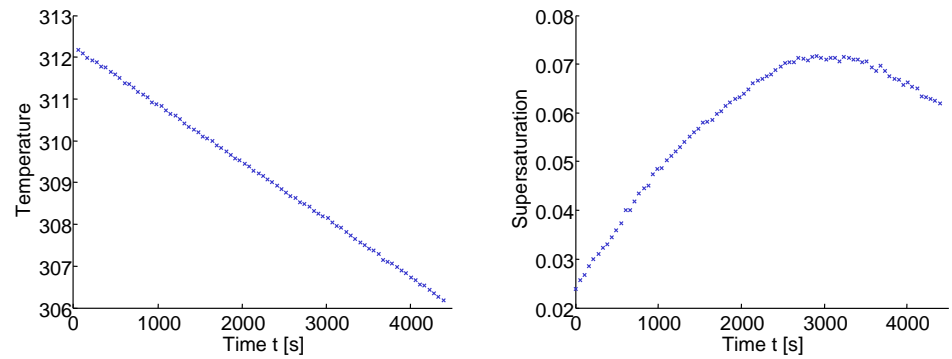


**Figure 5.27:** State of the continuous phase for experiment 2. Due to the moderate cooling rate, the supersaturation is lower than in Exp. 1, see Fig. 5.21.

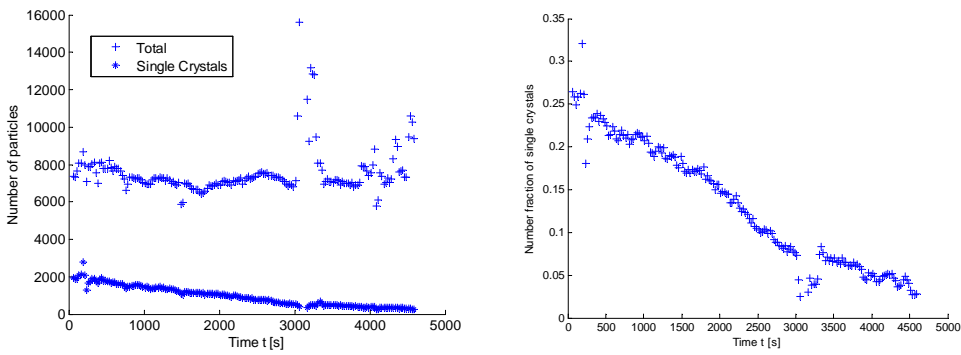


**Figure 5.28:** Total number of particles and number of particles classified as single crystals, measured within a sampling interval of 25 s for Exp. 2.

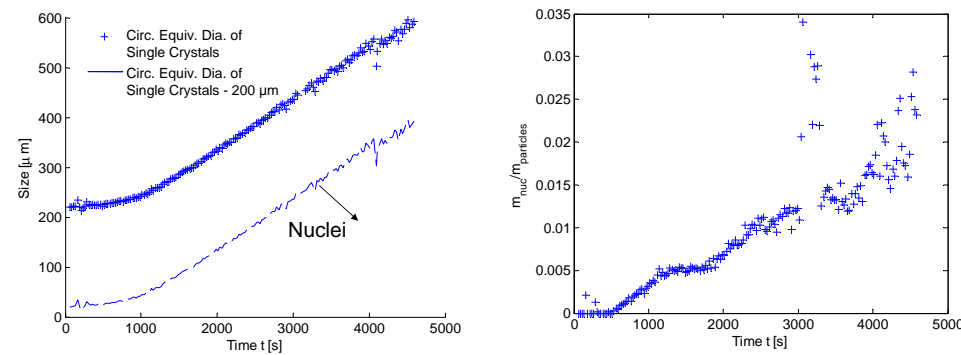


**Figure 5.29:** Evaluation of the amount of nuclei produced over the course of Exp. 2. Left: Particles which are smaller than the average sphere equivalent diameter of the single crystals minus 200  $\mu$ m are classified as nuclei. Right: Mass-ratio of the nuclei.

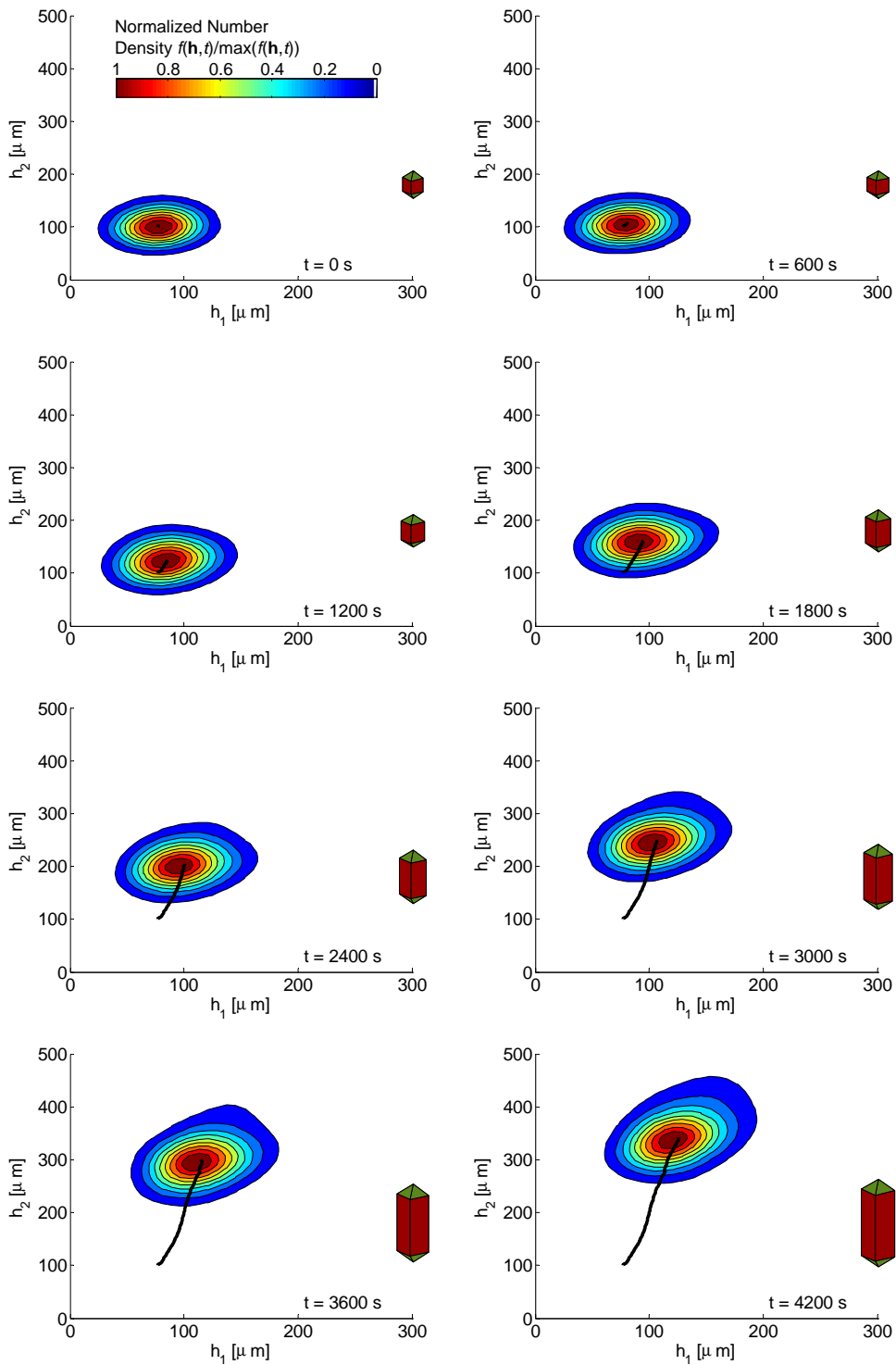


**Figure 5.30:** Evolution of the number density function in  $\mathbf{h}$ -space, estimated using a kernel density estimator.

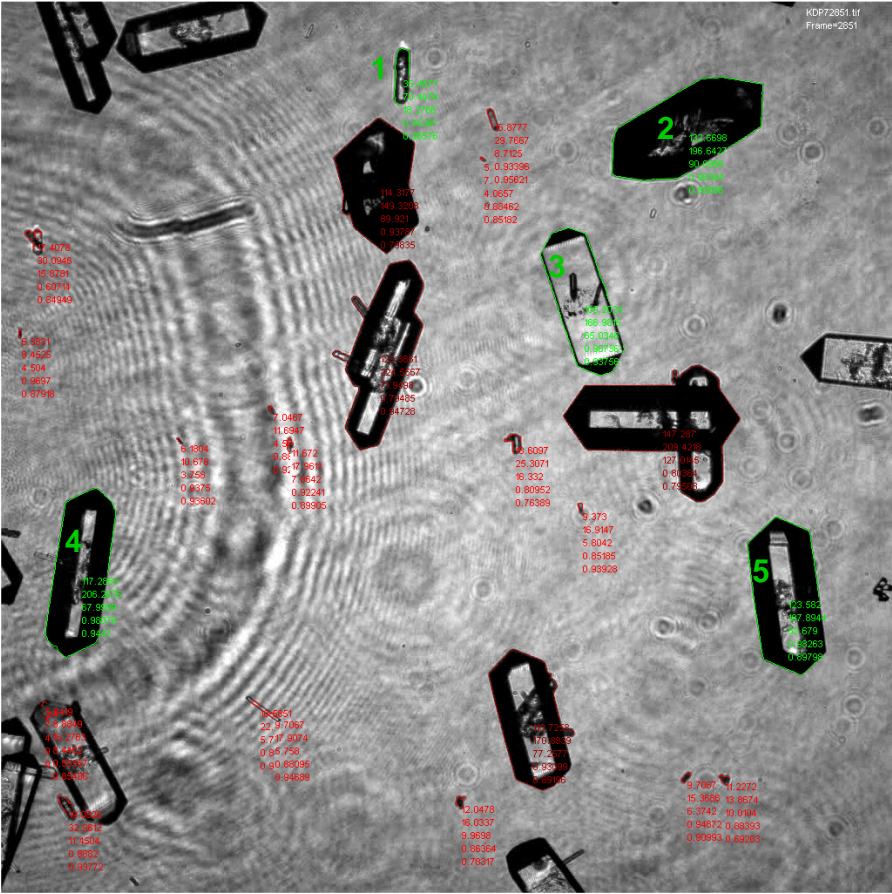


Figure 5.31: Example of a processed image of Exp. 2 at  $t \approx 4000$  s.

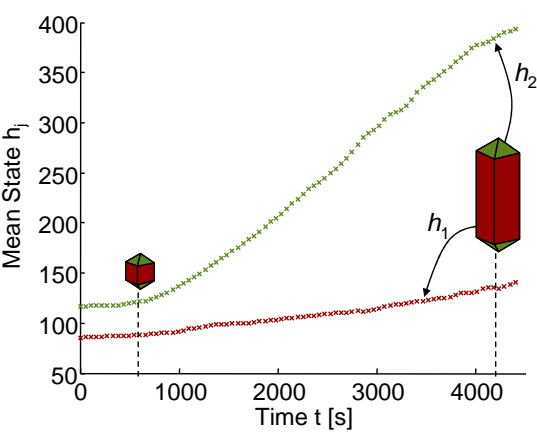


Figure 5.32: Mean geometry of the crystals that have been classified as single crystals in Exp. 2.

## 5.5 Summary

This chapter started with an overview on measurement techniques for crystal shapes. It has been pointed out that a direct 3D measurement is possible only using true 3D sensors which return a set of voxels with which a visual impression on the 3D shape can be gained. Reconstruction of the 3D shape on the basis of a shape model that rationally confines the variety of possible projections thrown by an object has been identified as the method of choice. Relatively easy collection of crystal image data, recording within suspension and justifiable image processing effort are the major arguments supporting this decision. After this, the identification scheme has been introduced that serves to match the boundary of a particle projection to its true 3D shape. Instead of the original collection of boundary pixels, a Fourier transform of its signature function is taken as an information-rich descriptor vector. Such descriptor vectors can be obtained also from computer experiments, which simulate the imaging process of the shape. With this implement, a database was built, which tabulates Fourier descriptor vectors together with the state vector of the shape from which it has been produced. The database then serves to determine the state vector for descriptor vectors which have been extracted from images. This identification process has been validated against synthetic data in order to show its robustness and reliability. For practical applications the raw grayscale images which were in this work acquired using the flow-through microscope QICPIC, must be preprocessed in order to render them adequate to be fed to the shape identification scheme. Finally, the scheme has been applied to real experimental image data of two crystallization experiments (system KDP-water). It has been shown that the identification scheme is applicable on large data sets and suited to quantitatively capture the shape evolution of growing crystal populations on the basis of a huge number of single-particle measurements.





## Chapter 6

# Connecting Observation and Simulation

In the preceding parts of this work, the modeling of crystallization processes with regard to shape has been discussed in Ch. 3 on the single crystal level and in Ch. 4 on the population level. The observation of crystals was the major topic in Ch. 5. This chapter aims at extracting kinetic data from the observed shape evolution that furnishes the model equations in order to describe real processes. At first, in Sec. 6.1, the population's number density of a simulated experiment is artificially sampled. That is, at different instants, a number of representative crystal state vectors is generated. Based on these state vectors, the shape is calculated and imaged (in-silico) from a random perspective as it has been done for the reliability analysis of the shape estimation scheme in Sec. 5.3.2. The obtained shape distribution data is used to re-estimate the evolution of the population distribution and particularly the mean state. This is done in order to assess the reliability of the data that is obtained with the shape estimation scheme on the basis of a simulated experiment. After this has been shown, the mean state evolution is used to estimate the face-specific growth rates as a function of supersaturation. Again, only synthetic data is used so that the reliability of the estimation of the kinetic data can be validated. In Sec. 6.2, the procedure is applied to the experiments that have been presented in Sec. 5.4.3 in order to determine the growth rates. Further validation experiments show that the growth rate data that has been extracted from the two experiments of Sec. 5.4.3 are applicable to predict the outcome of differently conducted experiments. Though, we strongly conjecture that the method that is developed can be applied directly to other crystallization systems, it is only applied to crystallizing potassium dihydrogen phosphate (KDP) with water as solvent; a model substance which is employed in this work for simulation studies as well as in experiments. Finally, Ch. 6.3 concludes this short chapter in brief.

### 6.1 Identifiability Analysis

This section develops the implements that are used to estimate the growth rates of the previously used example system potassium dihydrogen phosphate (KDP) (simulations in Sec. 4.1 and experiments in Sec. 5.4.3). In Sec. 6.1.1 the sampling of a simu-

lated number density function evolution is described. Because the kinetics are known which are fed to the simulation, this synthetic data is used to verify the technique to find the kinetic data as described in Sec. 6.1.2.

### 6.1.1 Synthetic Data

The computation of the shape distribution evolution has been discussed in Ch. 4 and particularly Sec. 4.1.4 contains one of the simulation results that are subsequently used to generate in-silico synthetic image data. In Sec. 4.1.4, only Exp. 1, see Fig. 4.13 has been simulated. A similar computation is set up for Exp. 2. The shape distribution has been sampled at a number of instants, where each sample comprises of  $n_c = 200$  crystals. An example is depicted in Fig. 6.1 which shows 200 samples for the seven instants which have also been selected for the illustration of the solution of the population balance model in Fig. 4.13. The crystal shape of each sample is computed and imaged from a random perspective like for the reliability analysis of the shape estimation scheme in Sec. 5.3.2. The shape estimation scheme is applied using a lookup table with  $n_h = 300$  different state vectors for which the shape descriptor, taken from  $n_\psi = 150$  random perspectives, is recorded. From the 200 samples taken at every instant, the mean state of the estimated population is calculated. The result can be seen for the simulation of Exp. 1 in Fig. 6.2 (left). The mean state of the simulation (dashed line) can be reproduced well by the mean value of measurements but small disturbances occur. For each of the 41 sampling points, the state of 200 synthetically imaged crystals is estimated and the mean value of the 200 measurements is calculated. Using a 7-degree moving average filter, the variations of around the simulated data is filtered out (solid line) and hence, the state measured from synthetic data matches the simulated one very closely. Unsurprisingly, the quality of the measured curve is further improved if the number of sample points is increased, see Fig. 6.2 (right). Of course, the measurement assessment using synthetic data generated with the simulation of Exp. 2 producing more compact crystals, yields similar results, which are depicted in Fig. 6.3.

It has been sketched that the time evolution of a crystal population can be tracked accurately, the measurement data can in principle be used to recover the kinetic parameter that have been used in the simulation.

### 6.1.2 Parameter Estimation and its Verification Using Synthetic Data for Potassium Dihydrogen Phosphate

The quantitative observation of a crystallization process is of value in its own right. But even more desirable is the extraction of kinetic data from an observed process. Since only crystal growth has been taken into account, we aim at restoring the growth rates, which have been used in the simulation. One could also apply the estimation techniques directly to real experiments and determine growth rates. However, we find it essential to test an observation and estimation scheme against artificial experiments to gain information on the reliability of the applied technique.

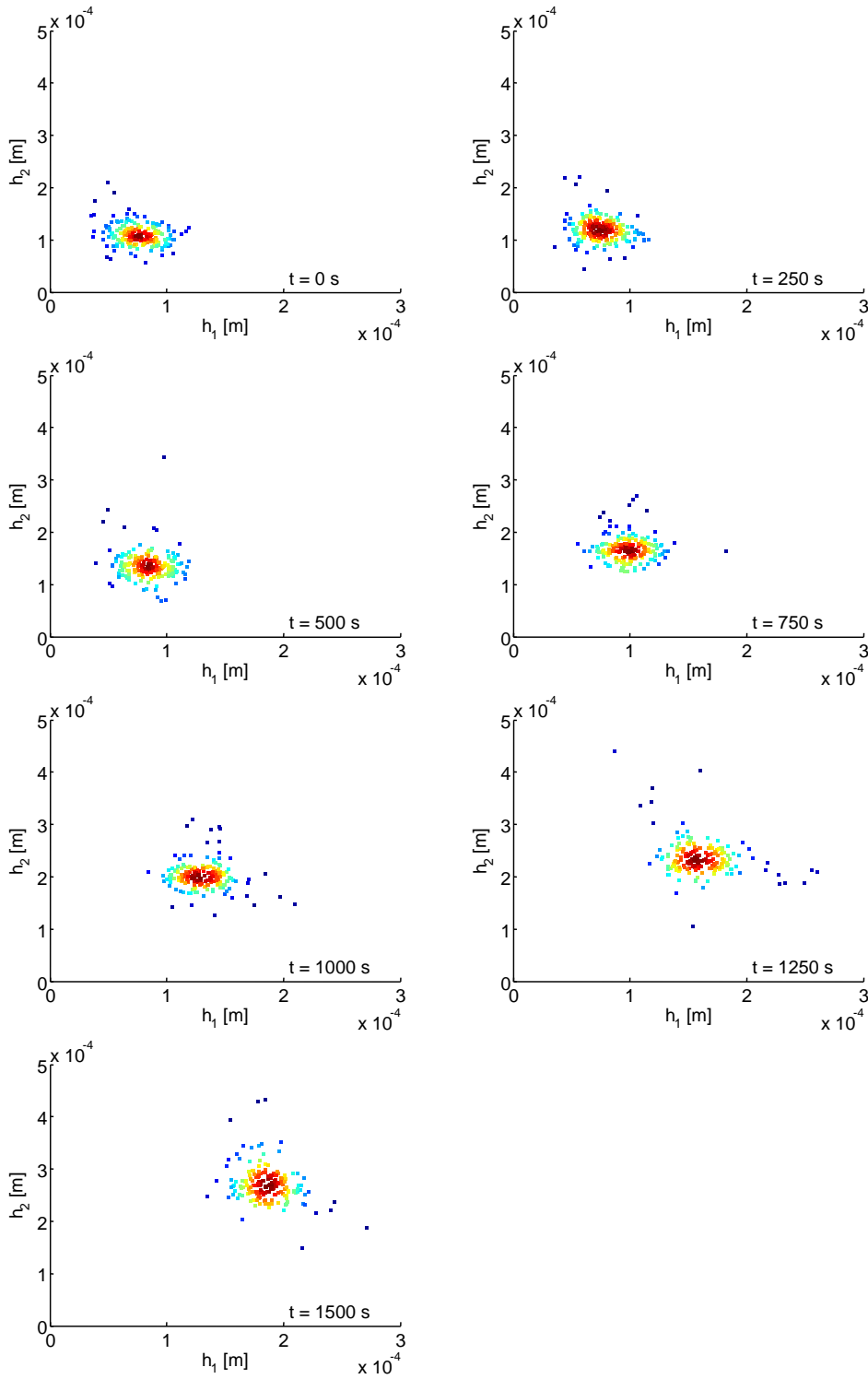


**Figure 6.1:** Sampling of the simulated shape distribution evolution shown in Fig. 4.13.

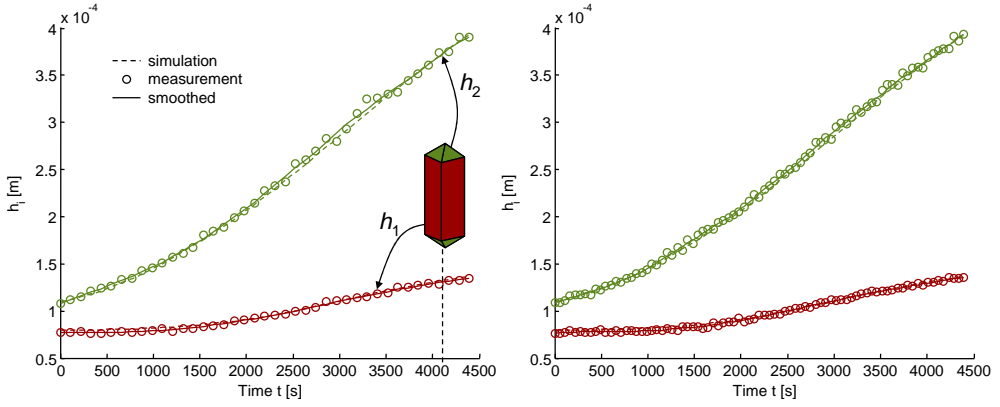


**Figure 6.2:** Mean states of the sampled evolution of  $h_1$  and  $h_2$  from synthetic image data generated using the simulation of Exp. 1 at 41 (left) and 82 instants (right). For each measurement, the images of 200 particles are included.

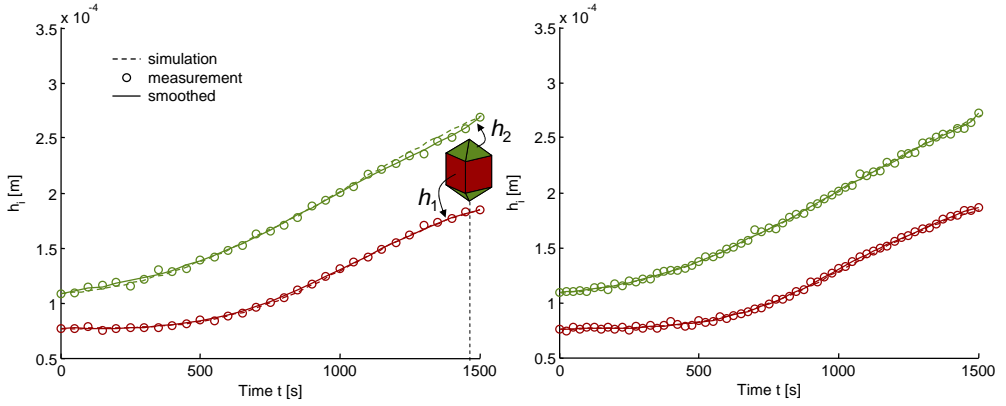


**Figure 6.3:** Mean states of the sampled evolution of  $h_1$  and  $h_2$  from synthetic image data generated using the simulation of Exp. 2 at 31 (left) and 61 instants (right). For each measurement, the images of 200 particles are included.

If an exponential growth model (Eq. (4.11)) is assumed, the measured evolution of the mean crystal shape  $\bar{\mathbf{h}}_j$  can be compared to the mean crystal size following from the growth law together with supersaturation measurements:

$$\bar{\mathbf{h}}_{\text{mod}}(t) = \bar{\mathbf{h}}_0 + \int_0^t \mathbf{k}_g \sigma^g dt, \quad \mathbf{k}_g = (k_1, k_2)^T, \quad \mathbf{g} = (g_1, g_2)^T. \quad (6.1)$$

The deviation between measured and modeled mean size evolution is quantified by the objectives

$$e_1 = \sum_{j=1}^{n_s} (\bar{h}_{1,j} - \bar{h}_{1,\text{mod},j})^2 \quad (6.2a)$$

$$e_2 = \sum_{j=1}^{n_s} (\bar{h}_{2,j} - \bar{h}_{2,\text{mod},j})^2. \quad (6.2b)$$

In Fig. 6.4 the estimated growth laws obtained by the minimization of the objective functions using only the synthetic data of the simulation of Exp. 1 are depicted. It can be seen that with increasing number of samples the accuracy of the estimates increases not significantly. A similar result is obtained from the growth rate estimation from the other simulation depicted in Fig. 6.5: The estimation accuracy of the parameters for  $G_1$  become even worse for a larger number of samples where the estimates for  $G_2$  improve. Even though the parameter of the growth law may not be found perfectly, the evolution of the mean state is reproduced well using the estimated kinetics and also the supersaturation-dependent growth law is matched almost perfectly with better results for an increasing number of samples. The objective shows, independent of the number of samples, stretched valleys which are undesirable when optimization algorithms are applied. Also, if it comes to the measurement of real data, the acquisition of images and measurement of shape distributions is further complicated by crystal shapes which are not as ideally formed as in the simulation. This can involve deviations from symmetry, formation of aggregates or broken crystals which all lead to more complex (that is, a wider variety of) crystals. That is, the stochastic process of crystal orientation, which has been thoroughly included in our analysis is further superimposed by other stochastic processes. Some of these phenomena have been shown to have a negligible influence on the estimation of the mean state, see Sec. 5.3.2, where other particles, like aggregates, are systematically obviated to be passed to the shape estimation scheme, see Sec. 5.4.2.4. Hence, the data quality in real experiments may decrease to a certain degree compared to synthetic data and therefore stretched valleys of the objective in the parameter space further complicate the judgment over the quality of the estimated parameters. However, since the shape of the growth laws could be recovered accurately, the method is eligible to extract kinetic parameters from experiments with satisfactory precision.

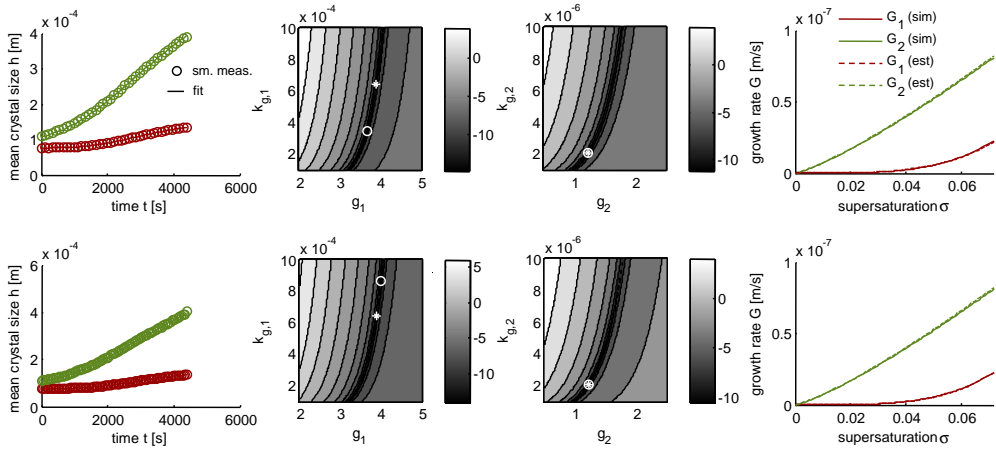


**Figure 6.4:** Estimation of growth rates with underlying model using a varying number of samples of the simulation of Exp. 1. Upper row: 41 samples, bottom row: 81 samples. Left column: evolution of mean crystal size estimated from synthetic image data and fitted evolution. Middle columns: contour plots of the objective  $e_j$  as a function of growth parameters. The true parameter used in the simulation is indicated by a star, whereas the minimum of the objective is marked by a circle. Right column: true (-) and estimated (- -) growth laws.

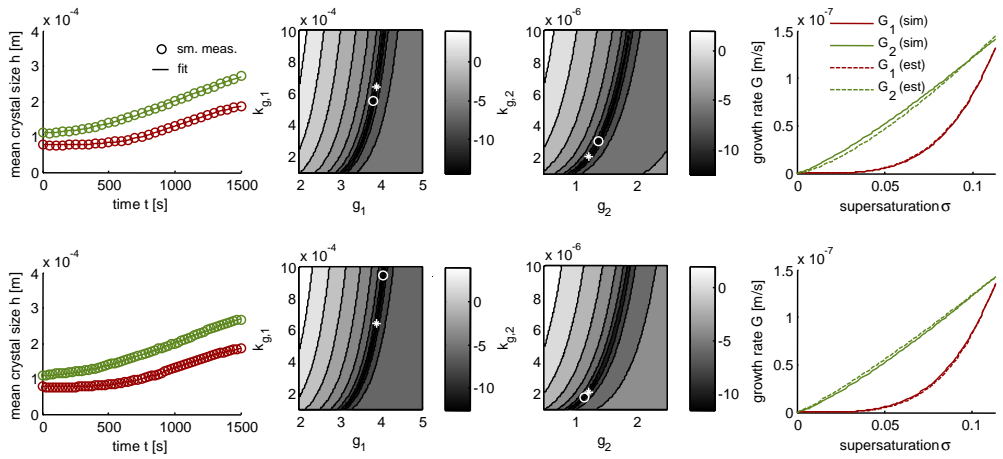


**Figure 6.5:** Estimation of growth rates with underlying model using a varying number of samples of the simulation of Exp. 2. Upper row: 31 samples, bottom row: 61 samples. Left column: evolution of mean crystal size estimated from synthetic image data and fitted evolution. Middle columns: contour plots of the objective  $e_j$  as a function of growth parameters. The true parameter used in the simulation is indicated by a star, whereas the minimum of the objective is marked by a circle. Right column: true (-) and estimated (- -) growth laws.

## 6.2 Application to Potassium Dihydrogen Phosphate Crystallization

So far the recovering of growth laws has been taken out for simulated dynamic shape distributions that were sampled and imaged in silico. In this section the estimation of growth laws from grayscale images recorded in batch crystallizations of potassium dihydrogen phosphate (KDP) is performed, see Exp.s 1 and 2, presented in Sec. 5.4.3. This is based on the mean shape evolution for two kinds of crystal faces that are present on KDP-shapes. The mean geometry evolution of Exp. 1 which was conducted with a relatively fast undercooling is depicted in Fig. 5.26, the associated temperature and supersaturation profile is shown in Fig. 5.21. For the second experiment (Exp. 2), the measured mean geometry evolution can be found in Fig. 5.32 and the temperature and supersaturation profiles in Fig. 5.27. The comparison of the mean state with a model approach that uses the measured supersaturation profile directly, see Eq. (6.1), under the variation of the growth rate parameters, yields the contours of the objectives for both growth laws, Eq.s (6.2), as depicted in Fig. 6.6. At the minimum of the objectives (circles), the growth rate parameter are found that reflect the measured shape evolution best which are concretely:

$$G_1 = k_1 \sigma^{g_1}, \quad k_1 = 643.2 \times 10^{-6} \text{ m/s}, \quad g_1 = 3.89, \quad (6.3a)$$

$$G_2 = k_2 \sigma^{g_2}, \quad k_2 = 2.07 \times 10^{-6} \text{ m/s}, \quad g_2 = 1.23. \quad (6.3b)$$

The evolution of the mean state obtained from Eq. (6.1) (together with the measure supersaturation) in comparison to the measured values is shown in Fig. 6.7. The growth laws are validated in two different ways. Firstly, the simulation of a process model using the parameters is taken out, see Sec. 4.1.2. This process model comprises a mass balance from which the supersaturation is calculated. The estimation of the growth rates does not involve a mechanism to match the mass uptake, as a result of crystal growth, with the measured supersaturation. Therefore, the precision with which the supersaturation curve is reproduced by the simulation is an indicator for the correctness of the estimated growth laws. It can be seen from Figs 4.11 and 4.12 that the computed and the measured supersaturation profile are very close. Secondly, further experiments have been conducted with temperature and supersaturation curves, see Fig. 6.8, different from the ones applied in Exp.s 1 and 2 (from which the parameters had been determined). Fig. 6.9 shows that also these four experiments are reproducible using the estimated growth laws. Even though the evolution is not as accurately matched as for Exp.s 1 and 2, the principle trend can be predicted with a satisfactory precision. Both practical test on the estimated kinetics, that is, the achievement of the mass balance as well as the application to other experiments, confirm that the determined parameters produce sensible results.

## 6.3 Conclusions

In this short chapter the experiments presented in Ch. 5 are used to derive growth laws from the observed shape evolution. In order to assess the reliability of the developed procedure, it has been tested with the help of synthetic data. The tests show

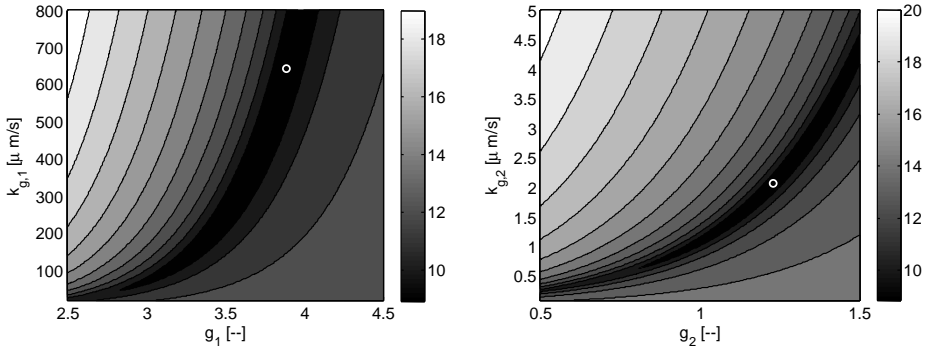


**Figure 6.6:** Contours of the objective functions, Eq.s 6.2, for the identification of the growth parameters. Points: Least squares estimates.

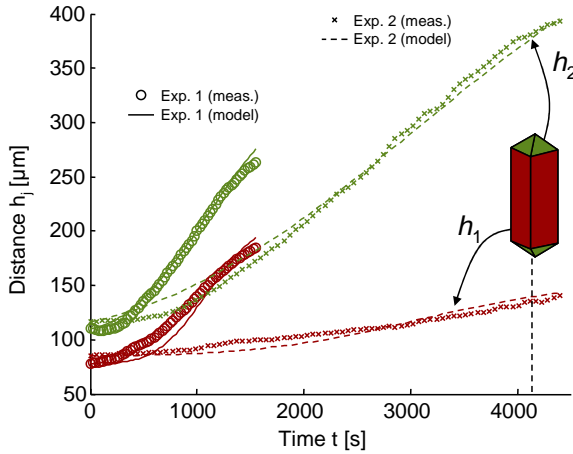


**Figure 6.7:** Mean geometry of the crystals which have been classified as single crystals in Exp. 1 and 2 with model fits.

that the kinetics used for the generation of synthetic data could be reproduced with sufficient precision. Having confidence in the method, it has been applied to experimental data. The identified growth laws were tested in two different ways: firstly, it has been proven that the supersaturation profile, calculated in simulations, meets the measured one and secondly, the shape evolution observed in validation experiments could be reproduced.



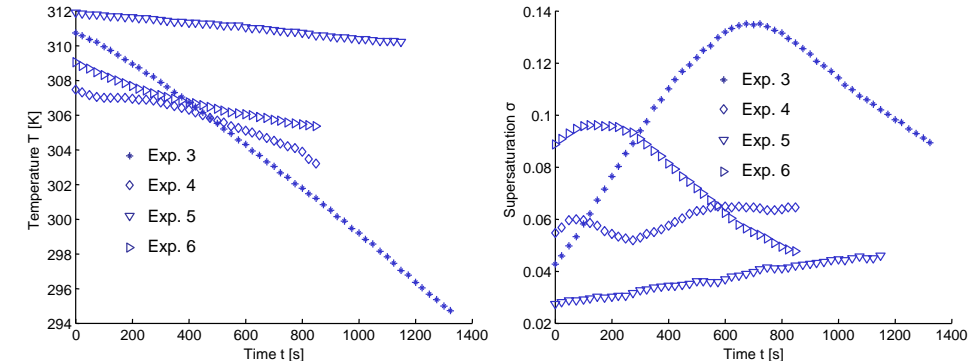


Figure 6.8: Temperature and supersaturation profiles of validation experiments.

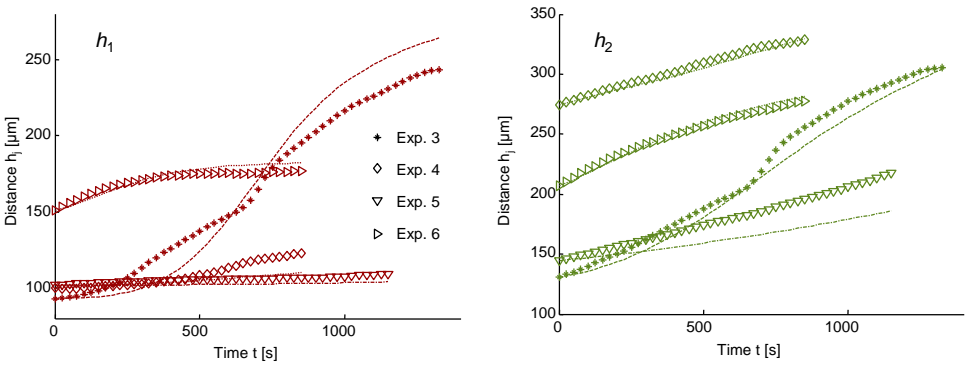


Figure 6.9: Validation of the growth kinetics against four further experiments.



*The game of science is, in principle, without end. He who decides one day that scientific statements do not call for any further test, and that they can be regarded as finally verified, retires from the game.*

Karl Popper

*The Logic of Scientific Discovery*

Chapter 2 - On the Problem of a Theory of Scientific Method

## Chapter 7

# Summary, Conclusion, and Outlook

### 7.1 Summary

The topics of this thesis are primarily set in the field of crystal shape dynamics. In the foreground stands the model-based description and identification of crystal growth on the particle level and its integration to process-level models using population balances. That is, the underlying physico-chemical process of the attachment of molecular layers is not considered. It is assumed that the crystals grow as polyhedra and that secondary phenomena like breakage and aggregation are not prevalent. The advancement of a crystal face on the macroscopic particle level is assumed to be determined by face-specific growth rates defining the velocity normal to the crystal planes. The growth rate depends on environmental conditions, in particular supersaturation. In this work, a methodology is developed to identify crystal shapes from microscope images of the suspension. With a simultaneous supersaturation measurement, it is possible to identify the kinetic parameters of crystal growth from laboratory experiments. The chosen approach also allows the validation of the measurement and identification processes on the basis of simulated, also called *in-silico*, experimental data. A major difficulty in the model building is the possibly varying number of independently growing crystal faces. This phenomenon stipulates a structure on the crystal state space that confines the accessible region to the morphology cone. The boundary of the morphology cone is made up by surfaces of different co-dimensions on which the shape evolution is qualitatively different. For crystallizers in which many crystals exist, the dynamics of the shape distribution shall be described by a population balance. With the aforementioned structure of the state space, however, it is rather challenging to formulate the population balance in a rigorous way. The detailed summary is given below.

Ch. 2 dissects the incorporation of special structures for spatially lumped systems that describe the evolution of a single entity. These structures are for instance surfaces at which the velocity field switches instantaneously, boundaries which capture trajectories to continue in a lower-dimensional subspace or surfaces inducing state jumps in the individual's evolution. Such mechanism are well known from the theory of hybrid dynamical systems. This part is followed by the introduction of model equations that describe the evolution of a whole population in state spaces exhibiting the above mentioned structures. For that purpose, classical balancing in state space from the

continuum mechanical perspective is employed. The results are of a rather general nature and shall be seen as a population balance framework for hybrid dynamical systems.

More specific and concrete explanations with regard to shape evolution are given in Ch. 3. The aim of the single crystal analysis is the development of a general framework for the description of single, convex, and polyhedral crystals taking face appearance and disappearance (morphological changes) into account. Previously published techniques require the tracking of morphological switches in shape evolution models by the computation of the crystal polyhedron in every time step. With the shape analysis derived in this work it is possible to deduce regions and boundaries in the state space where morphological changes occur. For this, simple linear algebra in 3D (for the dissection of the crystal polyhedron) and in  $n$ D Cartesian spaces (for the derivation of morphology regions in state space) and heuristic search strategy is sufficient. The applicability of the proposed technique is demonstrated for two example systems of which one can be reassessed quickly by pencil-and-paper geometry and another one (paracetamol) for which the exposed systematic method is practically inevitable.

Because in large scale crystallization crystals do not grow isolated from each other but are embedded into a continuous phase as a whole population, process models must capture the variability of the crystal shapes. The most flexible and elegant framework for this is enabled by a number density function in the property state space. Population balances track the evolution of that number density and thus allow the assessment of property distributions for large collections of crystals. For systems that do not undergo morphological transitions, this is performed in a straightforward way. A simple model system for which this is the case because not faces or edges appear or disappear is potassium dihydrogen phosphate (KDP). Specifically, the population balance for the system KDP is formulated and solved numerically. The determination of the kinetic parameters is discussed in Ch. 6. The comparison to experimental data, presented in Ch. 5, shows very good agreement. Using kinetic data from the literature, however, it is not possible to retrace the outcome of the conducted experiments. A more complex population balance model that captures morphological changes is presented for a simple 2D system (cubic crystal with cubic and octahedral faces). This example demonstrates the incorporation of hybrid structures for the concrete case of shape evolution as it has been introduced from a rather general perspective in Ch. 2. In a further section the concept is generalized to  $n$ D state spaces of populations of arbitrary but convex and polyhedral crystals.

Sensors cannot directly measure the shape of a crystal. Hence, Ch. 5 is dedicated to the extraction of shape information from images of the crystal suspension. After a general idea of different techniques for the quantification of crystal shapes is given, the focus is laid on matching projections of crystals on a 2D surface. That is in practical terms the imaging of crystals on a CCD-chip. The crystal projection is reduced to its boundary curve of which a signature function is calculated. The Fourier transform of that signature is taken as a descriptor vector of the projection. By simulating the imaging process, in-silico image data is generated. From these artificial images, descriptor vectors are collected for which the original 3D shape of the crystal is known. In a rather simple – but therefore robust – scheme, the descriptor vectors of crystal projections recorded from real experimental images of the crystal suspension are compared to that database. This allows to inversely look up the original state of the

crystal. Albeit mismatches occur, the main features, in particular the evolution of the average shape, of a population can be reconstructed. This is validated by the application of the scheme to in-silico data that also simulates imperfections as they can be seen in experimental images of the crystal suspension.

Furthermore, shape distributions can be observed with this technique over time as discussed in Ch. 6. Using synthetic experimental data, the reliable determination of crystal growth rates is developed and validated. On the basis of the shape distribution evolution of two experiments with different temperature – and thus different supersaturation – profiles, kinetic expressions for the growth rate of potassium dihydrogen phosphate have been extracted. The validity of the obtained parameters is confirmed in two ways. Firstly, the mass balance, which was not included in the estimation procedure, is fulfilled in simulations using the parameters. Secondly, the outcome of experiments, with different temperature and supersaturation profiles than the ones used for the estimation, could be predicted with a satisfactory accuracy.

## 7.2 Conclusion

The major contributions of this work are:

1. Derivation of population balances for populations of hybrid dynamical systems.
2. Determination of existence domains of crystal morphologies in shape space.
3. Connection of these two implements and a rigorous derivation of multivariate population balance models capable of incorporating morphology switches.
4. Development and employment of an image-based shape observation scheme, used for tracking the evolution of the shape distribution in crystallization experiments from which the growth kinetics can be identified.

Whilst the first chapters contribute to the theory of population balances and to the general model formulation for shape dynamics on the single-crystal and population level, later chapters mainly address the practical monitoring of shape evolution and the identification of the growth kinetics leading to shape changes. Though the level of the modeling tools goes well beyond the complexity that is necessary for the description of the system that is actually (potassium dihydrogen phosphate, KDP) used in the experiments, a major achievement of this work is the connection between more sophisticated models and reliable identification of kinetic parameters from experiments. That is not to say that this is the first and foremost effort in this direction but it is – in contrast to some of the earlier work – characterized by:

1. Generality and rigorousness of the model equations.
2. Systematic validation of the shape identification scheme and the technique to estimate the growth rates with the help of synthetic data.

Hence, the most important achievements of this work are:

1. The widening of the class of crystallization systems which can be modeled with population balances accounting for crystal shape. That is, all convex, polyhedral crystals are analyzed and modeled in a generalized, consistent framework.

2. Shape identification using image-based techniques has been further developed with an additional validation of the robustness with regard to imperfections that typically occur in experiments.

Though some progress has been achieved, clearly, this work is only a modest contribution to master the herculean task of shape control.

## 7.3 Outlook

Despite the fact that the modeling and experimental tools to describe and observe crystal shape distributions have gone through quite a development over the last years, general methods for shape control in crystallization processes are still missing. Much effort has been invested in additive and solvent screening to support the desired shape evolution. This work shall not be seen as an antithesis to such efforts that are mainly taken out on the single crystal level or possibly only on isolated faces. Rather, the non-dissipative incorporation of information gained on the smaller scale of single crystals or facets into process-level models is pursued. Such models can in principle be used for model-based feedforward or even feedback control strategies. The model system that has been chosen in this work has some advantages which most industrial substances probably not exhibit. For instance, a sufficiently high number of single crystals, eligible for shape estimation could be found in the images. For denser suspensions, this task becomes more difficult if not impossible. Also the number of symmetric faces is low in the presented experiments, i.e., the identification of features was relatively easy which may not be the case for crystals with a larger number of faces. On the other hand, multi-perspective imaging systems can deliver a wealth of additional information which can counterbalance the additional complexity.

In summary, it remains to be stated that the tools of this work ought to be used in the future for the optimization of the process control of simple, well behaving materials such as the chosen model system potassium dihydrogen phosphate. This can involve supersaturation profiles, systematic feed of additives or changing the solvent composition or other methods. Concerning the model building, a further development towards the rigorous incorporation of crystal aggregation without neglecting the notion of crystal shape poses a challenging task. This is due to the inherent involvement of different scales, i.e., the single crystal scale which characterizes the shape of the individual crystal and the relative position between single crystals within an aggregate. Breakage is of course a challenging problem as well but less relevant for shape evolution because broken crystals that grow, often heal and may even reach a fully symmetric state after a while. But first and foremost, the observation of crystals – whether single crystals in a population or aggregates – under more complicated situations, i.e., in dense suspension and for a large number of facets – is the field in which successful methodologies and techniques will have the largest impact. Crystal observation is the enabling technology for crystal shape control in practice.

## Bibliography

- Alander, E. M., M. S. Uusi-Penttilä, and A. C. Rasmuson (2003). Characterization of paracetamol agglomerates by image analysis and strength measurement. *Powder Technology* 130, 298–306.
- Alander, E. M., M. S. Uusi-Penttilä, and A. C. Rasmuson (2004). Agglomeration of paracetamol during crystallization in pure and mixed solvents. *Industrial & Engineering Chemistry Research* 43, 629–637.
- Aris, R. (1989). *Vectors, Tensors, and the Basic Equations of Fluid Mechanics*. New York: Dover.
- Aulbach, B. (1997). *Gewöhnliche Differentialgleichungen*. Heidelberg: Spektrum Akademischer Verlag.
- Bajcinca, N., V. de Oliveira, C. Borchert, J. Raisch, and K. Sundmacher (2010). Optimal control solutions for crystal shape manipulation. In S. Pierucci and G. Buzzi Ferraris (Eds.), *20th European Symposium on Computer Aided Process Engineering ESCAPE 20*, Volume 29 of *Computer Aided Chemical Engineering*, pp. 751–756.
- Barnard, A. S. (2009). Shape-dependent confinement of the nanodiamond band gap. *Crystal Growth & Design* 9, 4860–4863.
- Bird, R. B., W. E. Stewart, and E. N. Lightfoot (2002). *Transport Phenomena*. New York: Wiley.
- Blagden, N., M. de Matas, P. T. Gavan, and P. York (2007). Crystal engineering of active pharmaceutical ingredients to improve solubility and dissolution rates. *Advanced Drug Delivery Reviews* 59, 617–630.
- Bluma, A., T. Höpfner, G. Rudolph, P. Lindner, S. Beutel, B. Hitzmann, and T. Scheper (2009). Adaptation of in-situ microscopy for crystallization processes. *Journal of Crystal Growth* 311, 4193–4198.
- Boerrigter, S. X. M., H. M. Cuppen, R. I. Ristic, J. N. Sherwood, P. Bennema, and H. Meekes (2002). Explanation for the supersaturation-dependent morphology of monoclinic paracetamol. *Crystal Growth & Design* 2, 357–361.
- Boerrigter, S. X. M., G. P. H. Josten, J. van de Streek, F. F. A. Hollander, J. L. H. M. Cuppen, P. Bennema, and H. Meekes (2004). MONTY: Monte Carlo crystal growth on any crystal structure in any crystallographic orientation; Application to fats. *Journal of Physical Chemistry A* 108, 5894–5902.
- Borchardt, R. and S. Turowski (1999). *Symmetriehre der Kristallographie*. München: Oldenbourg.
- Borchardt-Ott, W. (2009). *Kristallographie*. Berlin: Springer.
- Borchert, C., N. Nere, D. Ramkrishna, A. Voigt, and K. Sundmacher (2009). On the prediction of crystal shape distributions in a steady-state continuous crystallizer. *Chemical Engineering Science* 64, 686–696.
- Borchert, C. and K. Sundmacher (2009). Statistical modeling of image-based crystallization observation. In *Proceedings of AIChE Annual Meeting 2009*.
- Borchert, C. and K. Sundmacher (2011a). Crystal Aggregation in a Flow Tube: Image-Based Observation. *Chemical Engineering & Technology* 34, 545–556.

- Borchert, C. and K. Sundmacher (2011b). Morphology evolution of crystal populations: Modeling and observation analysis. *Chemical Engineering Science* 70, 87–98.
- Bremner, D., K. Fukuda, and A. Marzetta (1998). Primal-dual methods for vertex and facet enumeration. *Discrete & Computational Geometry* 20, 333–357.
- Briesen, H. (2006). Simulation of crystal size and shape by means of a reduced two-dimensional population balance model. *Chemical Engineering Science* 61, 104–112.
- Briesen, H. (2007). Aggregate Structure Evolution for Size-Dependent Aggregation by Means of Monte Carlo Simulations. *Kona Powder and Particle* 25, 180–189.
- Bronstein, I. N., K. A. Semendjajew, G. Musiol, and H. Mühlig (2001). *Taschenbuch der Mathematik*. Frankfurt: Deutsch.
- Brown, D. J., G. T. Vickers, A. P. Collier, and G. K. Reynolds (2005). Measurement of the size, shape and orientation of convex bodies. *Chemical Engineering Science* 60, 289–292.
- Burger, W. and M. J. Burge (2008). *Digital Image Processing – An Algorithmic Introduction Using Java*. New York: Springer.
- Buzug, T. M. (2008). *Computed Tomography – From Photon Statistics to Modern Cone-Beam CT*. Berlin: Springer.
- Cardew, P. T. (1985). The growth shape of crystals. *Journal of Crystal Growth* 73, 385–391.
- Carrica, P. M., D. Drew, F. Bonetto, and R. T. Lahey (1999). A polydisperse model for bubbly two-phase flow around a surface ship. *International Journal of Multiphase Flow* 25, 257–305.
- Castro, J. M., K. V. Cashman, and M. Manga (2003). A technique for measuring 3D crystal-size distributions of prismatic microtites in obsidian. *American Mineralogist* 88, 1230–1240.
- Chakraborty, J. and S. Kumar (2007). A new framework for solution of multidimensional population balance equations. *Chemical Engineering Science* 62, 4112–4125.
- Chakraborty, J., M. R. Singh, D. Ramkrishna, C. Borchert, and K. Sundmacher (2010). Modeling of crystal morphology distributions. Towards crystals with preferred asymmetry. *Chemical Engineering Science* 65, 5676–5686.
- Chao, W. L., B. D. Harteneck, J. A. Liddle, E. H. Anderson, and D. T. Attwood (2005). Soft X-ray microscopy at a spatial resolution better than 15nm. *Nature* 435, 1210–1213.
- Charpentier, J.-C. (2009). Perspective on multiscale methodology for product design and engineering. *Computers & Chemical Engineering* 33, 936–946.
- Chemseddine, A. and T. Moritz (1999). Nanostructuring titania: control over nanocrystal structure, size, shape, and organization. *European Journal of Inorganic Chemistry* 2, 235–245.
- Chen, P., M. P. Dudukovic, and J. Sanyal (2005). Three-dimensional simulation of bubble column flows with bubble coalescence and breakup. *AIChE Journal* 51, 696–712.



- Chow, E. K., X. Q. Zhang, M. Chen, R. Lam, E. Robinson, H. H., S. D., E. Osawa, A. Goga, and D. Ho (2011). Nanodiamond therapeutic delivery agents mediate enhanced chemoresistant tumor treatment. *Science Translational Medicine* 3(73), 73ra21.
- Christopher, P. and S. Linic (2008). Engineering selectivity in heterogeneous catalysis: Ag nanowires as selective ethylene epoxidation catalysts. *Journal of the American Chemical Society* 130, 11264+.
- Conchello, J. A. and J. W. Lichtman (2005). Optical sectioning microscopy. *Nature Methods* 2, 920–931.
- Coulaloglou, C. A. and L. L. Tavlarides (1977). Description of interaction processes in agitated liquid-liquid dispersions. *Chemical Engineering Science* 32, 1289–1297.
- Cybernetics, M. (2005). *Image-Pro Plus, Version 6.0 for Windows, Start-Up Guide*. Media Cybernetics, Inc.
- Damm, C., D. Segets, G. A. Yang, B. F. Vieweg, E. Spiecker, and W. Peukert (2012). Shape transformation mechanism of silver nanorods in aqueous solution. *Small* 7, 147–156.
- Davey, R. J., J. W. Mullin, and M. J. I. Whiting (1982). Habit modification of succinic acid crystals grown from different solvents. *Journal of Crystal Growth* 58, 304–312.
- De Anda, J. C., X. Z. Wang, X. Lai, and K. J. Roberts (2005). Classifying organic crystals via in-process image analysis and the use of monitoring charts to follow polymorphic and morphological changes. *Journal of Process Control* 15, 785–797.
- De Anda, J. C., X. Z. Wang, X. Lai, K. J. Roberts, K. H. Jennings, M. J. Wilkinson, D. Watson, and D. Roberts (2005). Real-time product morphology monitoring in crystallization using imaging technique. *AIChE Journal* 51, 1406–1414.
- De Anda, J. C., X. Z. Wang, and K. J. Roberts (2005). Multi-scale segmentation image analysis for the in-process monitoring of particle shape with batch crystallisers. *Chemical Engineering Science* 60, 1053–1065.
- Decker, S. (2005). *Zur Berechnung von gerührten Suspensionen mit dem Euler-Lagrange-Verfahren*. Ph. D. thesis, Martin Luther University Halle-Wittenberg.
- Dellamorte, J. C., J. Lauterbach, and M. A. Barteau (2009). Promoter-Induced morphological changes of Ag catalysts for ethylene epoxidation. *Industrial & Engineering Chemistry Research* 48, 5943–5953.
- DeMenthon, D. F. and L. S. Davis (1992). Exact and approximate solutions of the perspective-3-point problem. *IEEE Transactions on Pattern Analysis and Machine Intelligence* 14, 1100–1105.
- DeMenthon, D. F. and L. S. Davis (1995). Model-based object pose in 25 lines of code. *International Journal of Computer Vision* 15, 123–141.
- Deuffhard, P. and F. Bornemann (2002). *Numerische Mathematik 2: Gewöhnliche Differentialgleichungen*. Berlin: de Gruyter.
- Eggers, J. (2008). *Modeling and Monitoring of Shape Evolution of Particles in Batch Crystallization Processes*. Ph. D. thesis, ETH Zurich.

- Eggers, J., M. Kempkes, J. Cornel, M. Mazzotti, I. Koschinski, and E. Verdurand (2009). Monitoring size and shape during cooling crystallization of ascorbic acid. *Chemical Engineering Science* 64, 163–171.
- Eggers, J., M. Kempkes, and M. Mazzotti (2008). Measurement of size and shape distributions of particles through image analysis. *Chemical Engineering Science* 63, 5513–5521.
- Eisenschmidt, H. (2009). Analyse der bildbasierten Beobachtung komplexer Kristallformen. Master's thesis, Otto-von-Guericke-Universität Magdeburg.
- Engell, S., G. Frehse, and E. Schnieder (Eds.) (2002). *Modelling, Analysis, and Design of Hybrid Systems*. Springer.
- Ferreira, A., N. Faria, F. Rocha, and J. A. Teixeira (2011). Using an Online Image Analysis Technique to Characterize Sucrose Crystal Morphology during a Crystallization Run. *Industrial & Engineering Chemistry Research* 50, 6990–7002.
- Fillippov, A. F. (1988). *Differential Equations with Discontinuous Righthand Sides*. Dordrecht: Kluwer Academic Publishers.
- Fredrickson, A. G., D. Ramkrishna, and H. M. Tsuchiya (1967). Statistics and dynamics of procaryotic cell populations. *Mathematical Biosciences* 1, 327–374.
- Fredrickson, A. G. and H. M. Tsuchiya (1963). Continuous propagation of microorganisms. *AIChE Journal* 9(4), 459–468.
- Friedlander, S. K. (2000). *Somke, Dust and Haze: Fundamentals of Aerosol Dynamics*. New York: Oxford University Press.
- Fujiwara, M., P. S. Chow, D. L. Ma, and R. D. Braatz (2002). Paracetamol crystallization using laser backscattering and ATR-FTIR spectroscopy: Metastability, agglomeration, and control. *CRYSTAL GROWTH & DESIGN* 2, 363–370.
- Fukura, S., F. Tsunomori, T. Iwai, H. Shibata, and H. Kagi (2004). Confocal fluorescence spectrometry for observation of crystal dissolution kinetics. *Journal of Crystal Growth* 269, 580–591.
- Gadewar, S. B. and M. F. Doherty (2004). A dynamic model for evolution of crystal shape. *Journal of Crystal Growth* 267, 239–250.
- Garekani, H. A., J. L. Ford, M. H. Rubinstein, and A. R. Rajabi-Siahboomi (1999). Formation and compression characteristics of prismatic polyhedral and thin plate-like crystals of paracetamol. *International Journal of Pharmaceutics* 187, 77–89.
- Gelbard, F. and J. H. Seinfeld (1978). Numerical solution of dynamic equation for particulate systems. *Journal of Computational Physics* 28, 357–375.
- Gelbard, F. and J. H. Seinfeld (1980). Simulation of multicomponent aerosol dynamics. *Journal of Colloid and Interface Science* 78, 485–501.
- Gelbard, F., Y. Tambour, and J. H. Seinfeld (1980). Sectional representations for simulating aerosol dynamics. *Journal of Colloid and Interface Science* 76, 541–556.
- Gerstlauer, A. (1999). *Herleitung und Reduktion populationsdynamischer Modelle am Beispiel der Flüssig-Flüssig-Extraktion*. Ph. D. thesis, University of Stuttgart.
- Gilmer, G. H. (1980). Computer-models of crystal growth. *Science* 208, 355–363.

- Glicksman, M. E., M. B. Koss, V. E. Fradkov, M. E. Rettenmayr, and M. S. S. (1994). Quantification of crystal morphology. *Journal of Crystal Growth* 137, 1–11.
- Gonzalez, R. C. and R. E. Woods (2008). *Digital Image Processing*. Upper Saddle River: Pearson Prentice Hall.
- Granlund, G. H. (1972). Fourier preprocessing for hand print character recognition. *IEEE Transactions on Computers* C 21, 195–200.
- Gunawan, R., D. L. Ma, M. Fujiwara, and R. D. Braatz (2002). Identification of kinetic parameters in multidimensional crystallization processes. *International Journal of Modern Physics B* 16, 367–374.
- Gupta, A. K. and M. Gupta (2005). Synthesis and surface engineering of iron oxide nanoparticles for biomedical applications. *Biomaterials* 26, 3995–4021.
- Higgins, M. D. (2000). Measurement of crystal size distributions. *American Mineralogist* 85, 1105–1116.
- Hojjati, H. and S. Rohani (2006). Measurement and prediction of solubility of paracetamol in water-isopropanol solution. Part 1. Measurement and data analysis. *Organic Process Reserach & Development* 10, 1101–1109.
- Holden, E. J., S. Moss, J. K. Russell, and M. C. Dentith (2009). An image analysis method to determine crystal size distributions of olivine in kimberlite. *Computational Geosciences* 13, 255–268.
- Hounslow, M. J., J. M. K. Pearson, and T. Instone (2001). Tracer studies of high-shear granulation: II. population balance modeling. *AIChE Journal* 47, 1984–1999.
- Hulburt, H. M. and S. Katz (1964). Some problems in particle technology – a statistical mechanical formulation. *Chemical Engineering Science* 19, 555–574.
- Ihler, A. (2007). Kernel density estimation toolbox for Matlab.
- Imura, J. and A. van der Schaft (2000). Characterization of well-posedness of piecewise-linear systems. *IEEE Transactions on Automatic Control* 45, 1600–1619.
- Iskandar, F. (2009). Nanoparticle processing for optical applications - A review. *Advanced Powder Technology* 20, 283–292.
- Jakobsen, H. A. (2008). *Chemical Reactor Modeling*. Berlin: Springer.
- Jerram, D. A., A. Mock, G. R. Davis, M. Field, and R. J. Brown (2009). 3D crystal size distributions: A case study on quantifying olivine populations in kimberlites. *Lithos* 112, 223–235.
- Jischa, M. F. (1982). *Konvektiver Impuls-, Wärme- und Stoffaustausch*. Vieweg Verlagsgesellschaft.
- Johnsen, A. (1910). *Wachstum und Auflösung der Kristalle*. Leipzig: Engelmann.
- Kempkes, M. (2009). *Monitoring of Particle Size and Shape in Crystallization Processes*. Ph. D. thesis, ETH Zurich.
- Kempkes, M., T. Vetter, and M. Mazzotti (2010). Measurement of 3D particle size distributions by stereoscopic imaging. *Chemical Engineering Science* 65, 1362–1373.
- Kofman, E. (2004). Discrete event simulation of hybrid systems. *Siam Journal on Scientific Computing* 25, 1771–1797.

- Kolev, N. I. (1993). Fragmentation and coalescence dynamics in multiphase flows. *Experimental Thermal and Fluid Science* 6, 211–251.
- Kolev, N. I. (2002). *Multiphase Flow Dynamics 2: Mechanical and Thermal Interactions*. Berlin: Springer.
- Körner, R., B. Butz, and W. Spiecker, E. & Peukert (2012). Crystal shape engineering of silicon nanoparticles in a thermal aerosol reactor. *Crystal Growth and Design* 12, 1330–1336.
- Koster, A. J., U. Ziese, A. J. Verkleij, A. H. Janssen, and K. P. de Jong (2000). Three-dimensional transmission electron microscopy: A novel imaging and characterization technique with nanometer scale resolution for materials science. *Journal of Physical Chemistry B* 104, 9368–9370.
- Kumar, S. and D. Ramkrishna (1996a). On the solution of population balance equations by discretization .2. A moving pivot technique. *Chemical Engineering Science* 51, 1333–1342.
- Kumar, S. and D. Ramkrishna (1996b). On the solution of population balance equations by discretization .1. A fixed pivot technique. *Chemical Engineering Science* 51, 1311–1332.
- Kumar, S. and D. Ramkrishna (1997). On the solution of population balance equations by discretization - III. Nucleation, growth and aggregation of particles. *Chemical Engineering Science* 52, 4659–4679. 1995 AIChE Annual Meeting, MIAMI BEACH, FLORIDA, NOV 12-17, 1995.
- Lahav, M. and L. Leiserowitz (2001). The effect of solvent on crystal growth and morphology. *Chemical Engineering Science* 56, 2245–2253.
- Larsen, P. A. (2007). *Computer Vision and Statistical Estimation Tools for In Situ, Imaging-based Monitoring of Particulate Populations*. Ph. D. thesis, University of Wisconsin-Madison.
- Larsen, P. A. and J. B. Rawlings (2009). The potential of current high-resolution imaging-based particle size distribution measurements for crystallization monitoring. *AIChE Journal* 55, 896–905.
- Larsen, P. A., J. B. Rawlings, and N. J. Ferrier (2006). An algorithm for analyzing noisy, in situ images of high-aspect-ratio crystals to monitor particle size distribution. *Chemical Engineering Science* 61, 5236–5248.
- Larsen, P. A., J. B. Rawlings, and N. J. Ferrier (2007). Model-based object recognition to measure crystal size and shape distributions from in situ video images. *Chemical Engineering Science* 62, 1430–1441.
- Lavalle, G., P. M. Carrica, A. Clausse, and M. K. Qazi (1994). A bubble number density constitutive equation. *Nuclear Engineering and Design* 152, 213–224.
- Ledl, T. (2004). Kernel density estimation: Theory and application in discriminant analysis. *Austrian Journal of Statistics* 33, 267–279.
- Lee, I., F. Delbecq, R. Morales, M. A. Albitzer, and F. Zaera (2009). Tuning selectivity in catalysis by controlling particle shape. *Nature Materials* 8, 132–138.
- Lehr, F. and D. Mewes (2001). A transport equation for the interfacial area density applied to bubble columns. *Chemical Engineering Science* 56, 1159–1166.

- Li, R. F., G. B. Thomson, G. White, X. Z. Wang, J. C. De Anda, and K. J. Roberts (2006). Integration of crystal morphology modeling and on-line shape measurement. *AIChE Journal* 52, 2297–2305.
- Loncaric, S. (1998). A survey of shape analysis techniques. *Pattern Recognition* 31, 983–1001.
- Lovette, M. A., A. R. Browning, D. W. Griffin, J. P. Sizemore, R. C. Snyder, and M. F. Doherty (2008). Crystal shape engineering. *Industrial & Engineering Chemistry Research* 47, 9812–9833.
- Lunze, J. (2002). *What Is a Hybrid System?*, pp. 3–14. Lecture Notes in Control and Information Sciences. Berlin: Springer.
- Ma, C. Y., X. Z. Wang, and K. J. Roberts (2008). Morphological population balance for modeling crystal growth in face directions. *AIChE Journal* 54, 209–222.
- Ma, D. L. and R. D. Braatz (2000). Robust batch control of crystallization processes. In *Proceedings of the 2000 American Control Conference*, Volume 1-6, pp. 1737–1741.
- Ma, D. L. and R. D. Braatz (2001). Worst-case analysis of finite-time control policies. *IEEE Transactions on Control Systems Technology* 9, 766–774.
- Ma, D. L., D. K. Tafti, and R. D. Braatz (2002a). High-resolution simulation of multidimensional crystal growth. *Industrial & Engineering Chemistry Research* 41, 6217–6223.
- Ma, D. L., D. K. Tafti, and R. D. Braatz (2002b). Optimal control and simulation of multidimensional crystallization processes. *Computers & Chemical Engineering* 26, 1103–1116.
- Mathew, M. and W. Wong-Ng (1995). Crystal structure of a new monoclinic form of potassium dihydrogen phosphate containing orthophosphacidium ion,  $[\text{H}_4\text{PO}_4]^+1$ . *Journal of Solid State Chemistry* 114, 219–223.
- MathWorks (2009). *Image Processing Toolbox 6*. Natick: The MathWorks, Inc.
- MathWorks (2011). *Matlab 7 Mathematics*. Natick: MathWorks, Inc.
- Matthews, H. B. and J. B. Rawlings (1998). Batch crystallization of a photochemical: Modeling, control, and filtration. *AIChE Journal* 44, 1119–1127.
- Matveev, A. S. and A. V. Savkin (2000). *Qualitative theory of hybrid dynamical systems*. Boston: Birkhäuser.
- McWeeny, R. (1963). *Symmetry – An introduction to group theory and its applications*. The International Encyclopedia of Physical Chemistry and Chemical Physics. Oxford: Pergamon Press.
- Meldrum, F. C. and H. Coelfen (2008). Controlling mineral morphologies and structures in biological and synthetic systems. *Chemical Reviews* 108, 4332–4432.
- Midgley, P. A., E. P. W. Ward, A. B. Hungria, and J. M. Thomas (2007). Nanotomography in the chemical, biological and materials sciences. *Chemical Society Reviews* 36, 1477–1494.
- Midgley, P. A. and M. Weyland (2003). 3D electron microscopy in the physical sciences: the development of Z-contrast and EFTEM tomography. *Ultramicroscopy* 96, 413–431.

- Monnier, O., G. Fevotte, C. Hoff, and J. P. Klein (1996). An advanced calorimetric approach for population balance modelling in batch crystallization processes. *Thermochimica Acta* 289, 327–341.
- Mullin, J. A. (2001). *Crystallization*. Oxford: Butterworth-Heinemann.
- Mullin, J. W., A. Amataviv, and M. Chakraborty (1970). Crystal habit modification studies with ammonium and potassium dihydrogen phosphate. *Journal of Applied Chemistry of the USSR* 20, 153–&.
- Patchigolla, K. and D. Wilkinson (2009). Crystal shape characterisation of dry samples using microscopic and dynamic image analysis. *Particle & Particle Systems Characterization* 26, 171–178.
- Patience, D. B. and J. B. Rawlings (2001a). Particle-shape monitoring and control in crystallization processes. *AIChE Journal* 47, 2125–2130.
- Patience, D. B. and J. B. Rawlings (2001b). Particle-shape monitoring and control in crystallization processes. *AIChE Journal* 47, 2125–2130.
- Pawley, J. B. (Ed.) (2006). *Handbook of Biological Confocal Microscopy*. New York: Springer.
- Peglow, M. (2005). *Beitrag zur Modellbildung von eigenschaftsverteiltern dispersen Systemen am Beispiel der Wirbelschicht-Sprühagglomeration*. Ph. D. thesis, University of Magdeburg.
- Peltier, R., C. W. Evans, A. L. DeVries, M. A. Brimble, A. J. Dingley, and D. E. Williams (2010). Growth habit modification of ice crystals using antifreeze glycoprotein (AFGP) analogues. *Crystal Growth & Design* 10, 5066–5077.
- Persoon, E. and K. S. Fu (1977). Shape discrimination using fourier descriptors. *IEEE Transactions on Systems Man and Cybernetics* 7, 170–179.
- Persson, P. O. and G. Strang (2004). A simple mesh generator in Matlab. *Siam Review* 46, 329–345.
- Prediger, A., A. Bluma, T. Höpfner, P. Lindner, S. Beutel, J. J. Müller, L. Hilterhaus, A. Liese, and T. Scheper (2011). In-situ-Mikroskopie zur Online-Überwachung von Enzymträgern und Zweiphasenprozessen. *Chemie Ingenieur Technik* 83, 884–887.
- Prywer, J. (1996). Three-dimensional model of the disappearance of triangular faces in the crystal habit. *Journal of Crystal Growth* 165, 335–340.
- Prywer, J. (2002). Morphological importance of crystal faces in connection with growth rates and crystallographic structure of crystal. *Crystal Growth & Design* 2, 281–286.
- Prywer, J. (2005). Kinetic and geometric determination of the growth morphology of bulk crystals: Recent developments. *Progress in Crystal Growth and Characterization of Materials* 50, 1–38.
- Puel, F., P. Marchal, and J. Klein (1997). Habit transient analysis in industrial crystallization using two dimensional crystal sizing technique. *Chemical Engineering Research & Design* 75, 193–205.
- Radenovic, N., W. van Enkevort, P. Verwer, and E. Vlieg (2003). Growth and characteristics of the {111} NaCl crystal surface grown from solution. *Surface Science* 523,

307–315.

Ramkrishna, D. (2000). *Population Balances*. San Diego: Academic Press.

Randolph, A. D. (1964). Population balance for countable entities. *Canadian Journal of Chemical Engineering* 42, 280–281.

Randolph, A. D. and P. A. Larsen (1988). *Theory of Particulate Processes: Analysis and Techniques of Continuous Crystallization*. London: Academic Press.

Randolph, A. D. and M. A. Larson (1962). Transient and steady state size distributions in continuous mixed suspension crystallizers. *AIChE Journal* 8, 639–645.

Rasenack, N. and B. W. Muller (2002). Crystal habit and tableting behavior. *International Journal of Pharmaceutics* 244, 45–57.

Ristic, R. I., S. Finnie, D. B. Sheen, and J. N. Sherwood (2001). Macro- and micromorphology of monoclinic paracetamol grown from pure aqueous solution. *Journal of Physical Chemistry B* 105, 9057–9066.

Rollié, S. (2010). *Heteroaggregation processes in colloidal particle and cell systems*. Ph. D. thesis, Otto von Guericke University Magdeburg.

Sangwal, K. (1998). Growth kinetics and surface morphology of crystals grown from solutions: Recent observations and their interpretations. *Progress in Crystal Growth and Characterization of Materials* 36, 163–248.

Schwarzenbach, D. (2001). *Kristallographie*. Berlin: Springer.

Selloni, A. (2008). Anatase shows its reactive side. *Nature Materials* 7, 613–615.

Shampine, L. F. (1994). *Numerical solution of ordinary differential equations*. New York: Springer.

Shekar, S., W. J. Menz, A. J. Smith, and W. Kraft, M. & Wagner (2012). On a multivariate population balance model to describe the structure and composition of silica nanoparticles. *Computers and Chemical Engineering* 43, 130–147.

Shekar, S., M. Sander, R. C. Riehl, A. J. Smith, and M. Braumann, A. & Kraft (2012). Modelling the flame synthesis of silica nanoparticles from tetraethoxysilane. *Chemical Engineering Science* 70, 54–66.

Silverman, B. W. (1986). *Density estimation for statistics and data analysis*. Boca Raton: CRC Press.

Singh, J., M. Balthasar, M. Kraft, and W. Wagner (2005). Stochastic modeling of soot particle size and age distributions in laminar premixed flames. *Proceedings of the Combustion Institute* 30, 1457–1465.

Singh, M. R., J. Chakraborty, D. Ramkrishna, S. Boerrigter, C. Borchert, and K. Sundmacher (2010). Morphological measurements of faceted crystals using image analysis. In *Conference Proceedings of AIChE Annual Meeting*, Salt Lake City.

Sizemore, J. P. and M. F. Doherty (2009). A new model for the effect of molecular imposters on the shape of faceted molecular crystals. *Crystal Growth & Design* 9, 2637–2645.

Slattery, J. C. (1999). *Advanced Transport Phenomena*. Cambridge: Cambridge University Press.

- Slattery, J. C., L. Sagis, and E.-S. Oh (2007). *Interfacial Transport Phenomena*. New York: Springer.
- Smoluchowski, M. (1917). Grundriß der Koagulationskinetik kolloider Lösungen. *Kolloid Zeitschrift* 21, 98–104.
- Snyder, R. C. and M. F. Doherty (2007). Faceted crystal shape evolution during dissolution or growth. *AIChE Journal* 53, 1337–1348.
- Snyder, R. C., S. Studener, and M. F. Doherty (2007). Manipulation of crystal shape by cycles of growth and dissolution. *AIChE Journal* 53, 1510–1517.
- Sun, C. and D. J. W. Grant (2001). Influence of crystal shape on the tableting performance of L-lysine monohydrochloride dihydrate. *Journal of Pharmaceutical Sciences* 90, 569–579.
- Sympatec (2006). *Qicpic Operating Instructions*. Clausthal-Zellerfeld: Sympatec GmbH.
- Tariq, F., R. Haswell, P. D. Lee, and D. W. McComb (2011). Characterization of hierarchical pore structures in ceramics using multiscale tomography. *Acta Materialia* 59, 2109–2120.
- Taylor, J. E., J. W. Cahn, and C. A. Handwerker (1992). Geometric models of crystal growth. *Acta Metallurgica Materialia* 40, 1443–1474.
- Tiwary, A. K. (2007). *Encyclopedia of Pharmaceutical Technology*, Chapter Crystal Habit Changes and Dosage Form Performance, pp. 820–833. Informa Healthcare.
- Tomlin, J. C. (2005). Analysis and control of hybrid systems (aa278a).
- van der Schaft, A. and H. Schumacher (2000). *An introduction to hybrid dynamical systems*. London: Springer.
- Variankaval, N., A. S. Cote, and M. F. Doherty (2008). From form to function: Crystallization of active pharmaceutical ingredients. *AIChE Journal* 54, 1682–1688.
- Vivares, D., E. W. Kaler, and A. M. Lenhoff (2007). Polyhedral instability of glucose isomerase crystals as revealed by confocal scanning fluorescence microscopy. *Crystal Growth & Design* 7, 1411–1415.
- Wand, M. P. & Jones, M. C. (1995). *Kernel Smoothing*. London: Chapman & Hall.
- Wang, X. Z., J. C. De Anda, and K. J. Roberts (2007). Real-time measurement of the growth rates of individual crystal facets using imaging and image analysis - A feasibility study on needle-shaped crystals of L-glutamic acid. *Chemical Engineering Research & Design* 85, 921–927.
- Wang, X. Z., K. J. Roberts, and C. Ma (2008). Crystal growth measurement using 2D and 3D imaging and the perspectives for shape control. *Chemical Engineering Science* 63, 1173–1184.
- Ward, E. P. W., I. Arslan, P. A. Midgley, A. Bleloch, and J. M. Thomas (2005). Direct visualisation, by aberration-corrected electron microscopy, of the crystallisation of bimetallic nanoparticle catalysts. *Chemical Communications*, 5805–5807.
- Webster, M. (Ed.) (2003). *Merriam-Webster Collegiate Dictionary*. Merriam Webster Dictionaries.



- Weissbuch, I., L. Addadi, M. Lahav, and L. Leiserowitz (1991). Molecular recognition at crystal interfaces. *Science* 253, 637–645.
- Weissbuch, I., R. Popovitzbiro, M. Lahav, and L. Leiserowitz (1995). Understanding and control of nucleation, growth, habit, dissolution and structure of 2-dimensional and 3-dimensional crystals using tailor-made auxiliaries. *Acta Crystallographica Section B – Structural Science* 51, 115–148.
- Weyland, M., P. A. Midgley, and J. M. Thomas (2001). Electron tomography of nanoparticle catalysts on porous supports: A new technique based on Rutherford scattering. *Journal of Physical Chemistry B* 105, 7882–7886.
- Williams, M. M. R. and S. K. Loyalka (1991). *Aerosol Science: Theory and Practice*. Oxford: Pergamon.
- Wilson, T. (2011). Optical sectioning in fluorescence microscopy. *Journal of Microscopy* 242, 111–116.
- Wintermantel, K. (1999). Process and product engineering - achievements, present and future challenges. *Chemical Engineering Science* 54, 1601–1620.
- Wu, J., S. Hao, J. Lin, M. Huang, Y. Huang, Z. Lan, and P. Li (2008). Crystal morphology of anatase titania nanocrystals used in dye-sensitized solar cells. *Crystal Growth & Design* 8, 247–252.
- Wulkow, M. (1990). *Numerical Treatment of Countable Systems of Ordinary Differential Equations*. Ph. D. thesis, Konrad-Zuse-Zentrum fr Informationstechnik Berlin.
- Yang, G., N. Kubota, Z. Sha, M. Louhi-Kultanen, and J. Wang (2006). Crystal shape control by manipulating supersaturation in batch cooling crystallization. *Crystal Growth & Design* 6, 2799–2803.
- Yang, H. and Z.-H. Liu (2009). Facile synthesis, shape evolution, photocatalytic activity of truncated cupros oxide octahedron microcrystals with hollows. *Crystal Growth and Design* 10, 2064–2067.
- Yang, H. G., C. H. Sun, S. Z. Qiao, J. Zou, G. Liu, S. Campbell Smith, H. M. Cheng, and G. Q. Lu (2008). Anatase tio<sub>2</sub> single crystals with a large percentage of reactive facets. *Nature* 453, 638–641.
- Yong, P. K. and J. H. Seinfeld (1992). Simulation of multicomponent aerosol dynamics. *Journal of Colloid and Interface Science* 149, 425–449.
- Zahn, C. T. and R. Z. Roskies (1972). Fourier descriptors for plane closed curves. *IEEE Transactions on Computers* C 21, 269–&.
- Zhang, D., G. Li, H. Wang, K. M. Chan, and J. C. Yu (2010). Biocompatible anatase single-crystal photocatalysts with tunable percentage of reactive facets. *Crystal Growth & Design* 10, 1130–1137.
- Zhang, Y. C. and M. F. Doherty (2004). Simultaneous prediction of crystal shape and size for solution crystallization. *AIChE Journal* 50, 2101–2112.
- Zhang, Y. C., J. P. Sizemore, and M. F. Doherty (2006). Shape evolution of 3-dimensional faceted crystals. *AIChE Journal* 52, 1906–1915.
- Ziegler, G. M. (2006). *Lectures on polytopes*. Berlin: Springer.

Zinser, A. (2010). Modellierungs- und Simulationswerkzeuge für Kristallisationsprozesse in Matlab/Simulink. Master's thesis, Otto von Guericke University.

Zurmühl, R. and S. Falk (1996). *Matrizen 1*. Berlin: Springer.

# List of Figures

1.1	Dissertation guide. . . . .	5
2.1	Property and environmental state. . . . .	13
2.2	Collision of a cart to an elastic wall. . . . .	16
2.3	Division of the state space. . . . .	17
2.4	Velocity fields in state space. . . . .	18
2.5	Bouncing ball . . . . .	24
2.6	State space division for jumping systems . . . . .	25
2.7	Surface intrinsic coordinates $\mathbf{z}$ . . . . .	28
2.8	Balancing in state space. . . . .	31
2.9	Control area $S_\Sigma$ within the dividing surface. . . . .	34
2.10	Population balance modeling for jumping systems . . . . .	38
3.1	Morphologies of NaCl. . . . .	42
3.2	Edge $\mathcal{E}_{ij,kl}^{i \rightarrow \emptyset}$ . . . . .	44
3.3	Edge $\mathcal{E}_{ij,kl}^{\sim}$ . . . . .	44
3.4	Morphology cones in $\mathbf{h}$ -space. . . . .	49
3.5	Workflow of the computation of the morphology cone. . . . .	53
3.6	Potassium alum. . . . .	54
3.7	Morphologies of potassium alum. . . . .	56
3.8	Shape evolution of a cubic crystal. . . . .	60
3.9	The shape evolution as a hybrid system. . . . .	61
3.10	Crystal decomposition for volume determination. . . . .	64
3.11	The 13 C-morphologies of Paracetamol. . . . .	65
3.12	Facets of the paracetamol morphology cone. . . . .	65
3.13	Simulation of paracetamol growth . . . . .	71
4.1	Quantification of the crystal shape. . . . .	74
4.2	Morphology cone of KDP. . . . .	75
4.3	Comparison of the KDP growth kinetics. . . . .	77
4.4	Solubility of KDP in water. . . . .	79
4.5	Numerical scheme. . . . .	80
4.6	Meshing of the population region. . . . .	82
4.7	Nucleation scheme. . . . .	83
4.8	Continuous state evolution (sim. Exp. 1, par. from literature). . . . .	85
4.9	Crystal mass over time (sim. Exp. 1, par. from literature). . . . .	86

4.10	Evolution of the shape distribution (sim. Exp. 1, par. from literature).	87
4.11	Continuous state evolution (sim. Exp. 1, par. from Ch. 6).	88
4.12	Continuous state evolution (sim. Exp. 2, par. from Ch. 6).	89
4.13	Evolution of the shape distribution (sim. Exp. 1, par. from literature).	90
4.14	State space partitioning for example system.	92
4.15	Growth rates for example system.	93
4.16	Single crystal trajectory for example system.	95
4.17	Single crystal trajectory for example system with state jumps.	96
4.18	Generic cone configuration for $n$ -dimensional state spaces.	104
5.1	Techniques to elucidate 3D structures.	108
5.2	Projection of a 3D convex crystal to a 2D plane.	115
5.3	Relationship between 3D crystal shape and Fourier descriptors.	118
5.4	Evaluation of the signature functional.	119
5.5	Shape estimation scheme.	122
5.6	Real world effects.	124
5.7	Estimator performance.	126
5.8	Standard deviation of the error distribution	127
5.9	Estimator performance.	128
5.10	Estimator performance.	129
5.11	Estimator performance.	130
5.12	Estimator performance.	131
5.13	Estimator performance.	132
5.14	Estimator performance.	133
5.15	Flow-through microscope QICPIC.	134
5.16	Image enhancement.	136
5.17	Binary image and scalar measures.	138
5.18	Kernel histogram example.	139
5.19	Experimental setup.	142
5.20	Example of a processed image of Exp. 1.	143
5.21	State of the continuous phase for Exp. 1.	144
5.22	Evaluation of the amount of nuclei produced.	145
5.23	Total number of particles and number of single crystals.	145
5.24	Evolution of the shape distribution of Exp. 1.	147
5.25	Evolution of the shape distribution of Exp. 1 with different kernel.	148
5.26	Evolution of the mean state in Exp. 1.	149
5.27	State of the continuous phase for Exp. 2.	150
5.28	Total number of particles and number of single crystals in Exp. 2.	150
5.29	Evaluation of the amount of nuclei produced in Exp. 2.	150
5.30	Evolution of the shape distribution of Exp. 2.	151
5.31	Example of a processed image of Exp. 2.	152
5.32	Evolution of the mean state in Exp. 2.	152
6.1	Sampling of the simulated shape distribution evolution.	157
6.2	Samling of the mean states from synthetic experimental data.	158
6.3	Samling of the mean states from synthetic experimental data.	158
6.4	Growth rate estimation at low supersaturation from synthetic data.	159
6.5	Growth rate estimation at high supersaturation from synthetic data.	160
6.6	Objective contours.	162

6.7	Mean geometry, measured and fitted. . . . .	162
6.8	Temperature and supersaturation profiles of validation experiments. .	163
6.9	Validation of growth kinetics. . . . .	163



# List of Tables

3.1	Boundary matrices of the joint morphology cone. . . . .	67
3.2	Coefficients of the tensor $C_{ijk}$ . . . . .	68
3.3	Parameters for the simulation. . . . .	69
4.1	Dynamic characteristics of the shape domains. . . . .	98
4.2	Characteristics of the $n$ -dimensional shape domains. . . . .	104
5.1	Shape and size descriptors. . . . .	138
5.2	Parameters of Exp. 1 and 2. . . . .	146





# Publications

Major parts of this work have been published in the following articles and conference contributions.

## Journal Articles

- Borchert, C., N. Nere, D. Ramkrishna, A. Voigt, and K. Sundmacher (2009). On the prediction of crystal shape distributions in a steady state continuous crystallizer. *Chemical Engineering Science* 64, 686–696.
- Borchert, C. and K. Sundmacher (2011a, April). Crystal aggregation in a flow tube: Image-based observation. *Chemical Engineering and Technology* 34(4), 545–556.
- Borchert, C. and K. Sundmacher (2011b). Morphology evolution of crystal populations: Modeling and observation analysis. *Chemical Engineering Science* 70, 87–98.
- Borchert, C. and K. Sundmacher (2012). Efficient formulation of crystal shape evolution equations. *Chemical Engineering Science* 84, 85–99.
- Borchert, C., E. Temmel, H. Eisenschmidt, A. Seidel-Morgenstern, and K. Sundmacher. Image-based identification of a multivariate crystallization model. *in preparation*.
- Chakraborty, J., M. Singh, D. Ramkrishna, C. Borchert, and K. Sundmacher (2010). Modeling of crystal morphology distributions. towards crystals with preferred asymmetry. *Chemical Engineering Science* 64, 5676–5686.
- Krasnyk, M., C. Borchert, and M. Mangold (2011). Model reduction techniques for the simulation of particle populations in fluid flow. *Mathematical and Computer Modelling of Dynamical Systems* 18, 427–438.

## Conference Proceedings

- Bajcinca, N., V. de Oliveira, C. Borchert, J. Raisch, and K. Sundmacher (2010, June). Optimal control solutions for crystal shape manipulation. In S. Pierucci and G. Buzzi Ferraris (Eds.), *20th European Symposium on Computer Aided Process Engineering*, Volume 28 of *Computer Aided Chemical Engineering*, pp. 751–756. Elsevier.
- Bajcinca, N., R. Perl, J. Raisch, C. Borchert, and K. Sundmacher (2010). Convex optimization for crystal shape manipulation. In *16th Nordic Process Control Workshop*,

*Lund, Sweden*, pp. 130–131.

Borchert, C., N. Nere, A. Voigt, Sundmacher, K., and D. Ramkrishna (2007, September). On the prediction of crystal shape distribution through multidimensional population balances. In *Proceedings of the 3rd International Conference on Population Balance Modeling, Quebec, Canada*.

Borchert, C. and K. Sundmacher (2009a). Dynamische Modellierung und Simulation von Kristallformverteilungen. In *Chemie Ingenieur Technik, ProcessNet Jahrestagung, Mannheim, Germany*, Volume 81, pp. 1147.

Borchert, C. and K. Sundmacher (2009b). A new method for the determination of crystallization kinetics. In *World Congress of Chemical Engineering Program Book, Montreal, Canada*.

Borchert, C. and K. Sundmacher (2010a). Experimentelle Untersuchung von Aggregation im Strömungsrohr. In *Chemie Ingenieur Technik, ProcessNet Jahrestagung, Aachen, Germany*, Volume 82, pp. 1464–1465.

Borchert, C. and K. Sundmacher (2010b). Morphology evolution of crystal populations: Population balance model predictions versus experimental data. In *Proceedings of the 4th International Conference on Population Balance Modeling, Berlin, Germany*, pp. 351–371.

Borchert, C., K. Sundmacher, and D. Ramkrishna (2009, June). Model based prediction of crystal shape distributions. In J. Jezowski and J. Thullie (Eds.), *19th European Symposium on Computer Aided Process Engineering, Cracow, Poland*, Volume 26 of *Computer Aided Chemical Engineering*, pp. 141–146. Elsevier.

Borchert, C., A. Voigt, and K. Sundmacher (2008, September). Evolution of crystal shape distributions and morphology classification. In J. Jansens and J. Ulrich (Eds.), *Proceedings of the 17th International Symposium on Industrial Crystallization, Maastricht, The Netherlands*.

Eisenschmidt, H., C. Borchert, and K. Sundmacher (2010). Image-based measurement of crystal shape distributions. In J. Stelzer and J. Ulrich (Eds.), *BIWIC 2010 17th International Workshop on Industrial Crystallization, Halle, Germany, Göttingen*, pp. 241–249. Cuvillier.

## Other Conference Talks and Posters

Borchert, C., N. Nere, A. Voigt, K. Sundmacher, and D. Ramkrishna (2007, 4-9 November). Prediction of crystal shape and size distributions using multidimensional population balances. AIChE Annual Meeting, Salt Lake City, USA. (Oral presentation).

Borchert, C., N. Nere, A. Voigt, K. Sundmacher, and D. Ramkrishna (2008, 15-20 November 2008). Modeling the manipulation of crystal morphology distributions. AIChE Annual Meeting, Philadelphia, USA. (Oral Presentation).

Borchert, C., D. Ramkrishna, and K. Sundmacher (2010, 27 - 29 April). Towards tailor-made crystal shape distributions – a model-based analysis. World Congress on Particle Technology, Nuremberg, Germany. (Oral Presentation).

- Borchert, C. and K. Sundmacher (2009, November 7-13). Statistical modeling of image-based crystallization observation. AIChE Annual Meeting, Nashville, USA. (Oral Presentation).
- Borchert, C. and K. Sundmacher (2010a, November 7-12). Image-based experimental investigation of crystal aggregation along a pipe. AIChE Annual Meeting, Salt Lake City, USA. (Oral Presentation).
- Borchert, C. and K. Sundmacher (2010b, March 11-12). Modellbasiertes Messen von Kristallformverteilungen. ProcessNet-Fachausschuss Kristallisation, Magdeburg, Germany. (Poster Presentation).
- Borchert, C., A. Voigt, and K. Sundmacher (2008, March). Evolution of crystal shape distributions. ProcessNet-Fachausschüsse Trocknungstechnik und Kristallisation, March 5-7, 2008 Halle-Wittenberg. (Oral Presentation).
- Fricke, M., A. Zinser, C. Borchert, and K. Sundmacher (2009, November, 7-13). Numerical simulation of spatially distributed population balances. AIChE Annual Meeting, Nashville, USA. (Poster Presentation).
- Singh, M. R., S. X. M. Boerrigter, C. Borchert, K. Sundmacher, and D. Ramkrishna (2011, October). Experimental investigation of crystal shape evolution during growth and dissolution. AIChE Annual Meeting, October 16, 2011 Minneapolis, MN. (Oral Presentation).
- Singh, M. R., J. Chakraborty, D. Ramkrishna, S. X. M. Boerrigter, C. Borchert, and K. Sundmacher (2010, November). Morphological measurements of faceted crystals using image analysis. AIChE Annual Meeting, November 11, 2010 Salt Lake City, UT. (Oral Presentation).



# Curriculum Vitae

## Personal Details

Name	Christian Willi Borchert
Date of birth	25 April 1983 in Cloppenburg
Address	Geibelstr. 51, D-67063 Ludwigshafen

## Education

08/1995-05/2002	<b>Clemens-August-Gymnasium</b> , Cloppenburg University-entrance Diploma
10/2002-06/2007	<b>Otto-von-Guericke-University</b> , Magdeburg Studies of Engineering Cybernetics
09/2005-05/2006	<b>Institute of Chemical Technology</b> , Prague Studies of Chemical Engineering and Pre-Diploma Thesis
09/2006-05/2007	<b>Purdue University</b> , West Lafayette Studies of Chemical Engineering and Diploma Thesis
06/2007	<b>Otto-von-Guericke-University</b> , Magdeburg Diplom-Ingenieur in Engineering Cybernetics

## Work Experience

07/2007-10/2011	<b>Max-Planck-Institute</b> , Magdeburg Research Assistant
since 11/2011	<b>BASF SE</b> , Ludwigshafen Polymer Reaction Engineer

## Scholarships and Awards

06/2002	<b>Deutsche Physikalische Gesellschaft</b> , Bad Honnef Free membership
01/2006-05/2006	<b>Ernest-Solvay-Stiftung</b> , Essen Scholarship
09/2006-04/2007	<b>Deutscher Akademischer Austauschdienst</b> , Bonn Scholarship
06/2009	<b>19 Eur. Symp. on Computer Aided Process Eng.</b> , Cracow Best Lecture Award